

TECHNICAL REPORT 97-05

Grimsel Test Site

Further Development of Seismic Tomography

March 1999

W. Albert, J. Bühnemann, K. Holliger
H.R. Maurer, G. Pratt, I. Stekl

TECHNICAL REPORT 97-05

Grimsel Test Site

Further Development of Seismic Tomography

March 1999

W. Albert ¹⁾, J. Bühnemann ²⁾, K. Holliger ³⁾,
H.R. Maurer ³⁾, G. Pratt ⁴⁾, I. Stekl ⁵⁾

1) Formerly Nagra, Wettingen;
presently Albert-Donié Geo-Consult Ltd., Wettingen.

2) Formerly Institute of Geophysics, ETH, Zurich;
presently RWE-DEA, Hamburg, D.

3) Institute of Geophysics, ETH, Zurich

4) Formerly Dept. of Geology, Imperial College, London, UK.;
presently Dept. of Geological Science, Queen's University,
Kingston, Ontario, CAN.

5) Dept. of Geology, Imperial College, London, UK.

This report was prepared on behalf of Nagra. The viewpoints presented and conclusions reached are those of the author(s) and do not necessarily represent those of Nagra.

ISSN 1015-2636

"Copyright © 1999 by Nagra, Wettingen (Switzerland) / All rights reserved.

All parts of this work are protected by copyright. Any utilisation outwith the remit of the copyright law is unlawful and liable to prosecution. This applies in particular to translations, storage and processing in electronic systems and programs, microfilms, reproductions, etc."

FOREWORD

Concepts which envisage the storage of radioactive waste in geological formations are crucially dependent on a thorough knowledge of the host rock and neighbouring rock strata. Since 1984, NAGRA has been operating the Grimsel underground rock laboratory (Felslabor Grimsel - FLG), which complements NAGRA's work on repositories. This laboratory, which provides a generic test rock environment, lies 450 m below the eastern flank of the Juchlistock. It is located in the granitic rock of the Aar-Massif, at a height of 1730 m and can be reached via a horizontal access tunnel.

The most important purposes of the Grimsel underground rock laboratory are:

- The accumulation of know-how in planning, execution and interpretation of underground experiments in various scientific and technical fields.
- Acquisition of practical experience in the development and use of those experimental methods, measurement procedures and equipment which could be used in the search for potential sites.
- Experimental investigation of processes crucial to the safety of a radioactive waste repository.

In 1984, as part of a German/Swiss collaboration, various experiments were initiated by NAGRA and its German partner, the Federal Institution for Geoscience and Raw Materials (Bundesanstalt für Geowissenschaft und Rohstoffe - BGR) together with the Research Centre for Environment and Health (Forschungszentrum für Umwelt und Gesundheit - GSF¹).

Work performed by the German partner was sponsored by the Federal Ministry for Education, Science, Research and Technology (Bundesministerium für Bildung, Wissenschaft, Forschung und Technologie - BMBF²).

International collaboration in the FLG has been strengthened through the years by collaboration agreements with the following partner organisations: ANDRA (France), ENRESA (Spain), EU (European Union), PNC³ (Japan), SKB (Sweden) and US-DOE (United States).

By 1985, NAGRA had already tested seismic tomography at the Grimsel underground rock laboratory. During the project, several areas (up to a max. of 250 x 250 m) were measured (Gelbke C. 1988). It is planned that much larger areas, of up to approx. 1 km², will be explored as part of NAGRA's repository projects. The fundamentals of future research should be defined during the "Further Development of Seismic Tomography" tests.

Experience gained by NAGRA and its partner organisations (e.g., SKB, Nirex) has led to the identification of the following main areas of investigation:

- The evaluation and testing of underground seismic sources suitable for large measurement distances.
- Improvement of the evaluation process with respect to stability, quality and resolution possibilities.

The experiment was carried out in close co-operation with the Department of Geology, Imperial College, London and the Institute for Geophysics at the University of Zurich.

¹ Now: Society for Plant and Reactor Safety (Gesellschaft für Anlagen und Reaktorsicherheit - GRS)

² Now: Bundesministerium für Wirtschaft (BMWi)

³ Now: Japan Nuclear Cycle Development Institute, Japan (JNC)

VORWORT

Bei Konzepten, welche die Endlagerung radioaktiver Abfälle in geologischen Formationen vorsehen, ist die Kenntnis des Wirtgesteins und der angrenzenden Gesteinsschichten von entscheidender Bedeutung. Seit 1984 betreibt die NAGRA ein standortunabhängiges Felslabor das die endlagerspezifischen Arbeiten der NAGRA ergänzt. Das Felslabor Grimsel (FLG) liegt 450 Meter unter der Ostflanke des Juchlistock in den granitischen Gesteinen des Aar-Massivs auf einer Höhe von 1730 m und ist durch einen horizontalen Zugangstollen erreichbar.

Das Felslabor Grimsel dient folgenden übergeordneten Zielsetzungen:

- Aufbau von Know-how in der Planung, Ausführung und Interpretation von Untertageversuchen in verschiedenen wissenschaftlichen und technischen Fachgebieten
- Erwerb praktischer Erfahrung in der Entwicklung und der Anwendung von Untersuchungsmethoden, Messverfahren und Messgeräten, die für die Erkundung von potentiellen Standorten in Frage kommen
- Experimentelle Untersuchungen von Prozessen die für die Sicherheit eines Endlagers für radioaktive Abfälle entscheidend sind.

Auf der Basis eines deutsch-schweizerischen Zusammenarbeitsvertrages begannen 1984 verschiedene Versuche der NAGRA und der deutschen Partner, der Bundesanstalt für Geowissenschaften und Rohstoffe (BGR) und dem Forschungszentrum für Umwelt und Gesundheit (GSF¹). Die Arbeiten der deutschen Partner sind durch das Bundesministerium für Bildung, Wissenschaft, Forschung und Technologie (BMBF²) gefördert worden.

Die internationale Zusammenarbeit im FLG wurde im Verlauf der Jahre durch Zusammenarbeitsverträge mit folgenden Partnerorganisationen ANDRA (Frankreich), ENRESA (Spanien), EU (Europäischen Union), PNC³ (Japan), SKB (Schweden) und US-DOE (Vereinigte Staaten) ausgebaut.

Die seismische Tomographie wurde von der Nagra im Felslabor Grimsel bereits 1985 getestet. In dem damaligen Projekt wurden mehrere Messfelder (bis max. 250 x 450 m) tomographisch vermessen (Gelbke C. 1988). Im Rahmen der Endlagerprojekte der Nagra sollen auch wesentlich grössere Felder (bis ca. 1 km²) erkundet werden. Mit dem Versuch "Weiterentwicklung der seismischen Tomographie" sollen die Grundlagen für die zukünftigen Arbeiten gelegt werden.

Aufgrund der bisherigen Erfahrungen der Nagra und ihrer Partnerorganisationen (z.B. SKB, Nirex) ergaben sich für das Projekt folgende Schwerpunkte:

- die Evaluation und der Test von seismischen Untertagequellen für grosse Messdistanzen
- die Verbesserung der Auswerteverfahren in bezug auf Stabilität, Qualität und Auflösungsvermögen.

Der Versuch wurde in enger Kooperation mit dem Department of Geology, Imperial College, London und dem Institut für Geophysik der ETH, Zürich durchgeführt.

¹ heute: Gesellschaft für Anlagen und Reaktorsicherheit (GRS)

² heute: Bundesministerium für Wirtschaft (BMWi)

³ heute: Japan Nuclear Cycle Development Institute, Japan (JNC)

PRÉFACE

Avec des concepts prévoyant le stockage final des déchets radioactifs dans des formations géologiques, il est capital de bien connaître la roche d'accueil et ses roches environnantes. Pour compléter ses travaux spécifiques au dépôt final, la CEDRA exploite depuis 1984 un laboratoire souterrain indépendant d'un site. Le laboratoire souterrain du Grimsel (LSG) a été aménagé à 450 mètres au-dessous du flanc est du Juchlistock, dans les roches granitiques du massif de l'Aar, à une altitude de 1730 m ; il est accessible par une galerie horizontale.

Le laboratoire souterrain du Grimsel poursuit les principaux objectifs suivants :

- Elaboration d'un savoir-faire en matière de planification, de réalisation et d'interprétation d'essais souterrains réalisés dans différentes branches techniques et scientifiques.
- Acquisition d'une expérience pratique dans le développement et l'application de méthodes d'investigation, de procédures et d'instruments de mesure entrant en question pour étudier des sites potentiels.
- Analyse expérimentale de processus déterminants pour la sûreté d'un dépôt final pour déchets radioactifs.

Sur la base d'un accord de coopération germano-suisse, la CEDRA et ses partenaires allemands l'Office fédéral BGR, Bundesanstalt für Geowissenschaften und Rohstoffe, et le Centre de recherche GSF¹, Forschungszentrum für Umwelt und Gesundheit, ont commencé différents essais en 1984. Les travaux des partenaires allemands ont été soutenus par le Ministère allemand de l'éducation, de la science, de la recherche et de la technologie (BMBF²).

Au cours des années, la coopération internationale au LSG s'est enrichie d'autres accords de coopération avec les organisations partenaires suivantes : l'ANDRA (France), l'ENRESA (Espagne), l'UE (Union Européenne), la PNC³ (Japon), la SKB (Suède) et le US-DOE (Etats-Unis).

C'est en 1985 déjà que la Cédra a testé la tomographie sismique au laboratoire souterrain du Grimsel. Dans l'ancien projet, on avait procédé à la mesure tomographique de plusieurs champs de mesure (250 à 450 m maximum) (Gelbke C. 1988). Dans le cadre des projets de dépôt final de la CEDRA, on étudiera aussi des champs bien plus grands (jusqu'à 1 km² environ). L'essai relatif au perfectionnement de la tomographie sismique permettra de jeter les bases des futurs travaux.

En raison des expériences acquises jusqu'à présent par la Cédra et ses organisations partenaires (par ex. SKB, Nirex), le projet s'articule maintenant autour des importants points suivants :

- Evaluation et test de sources sismiques souterraines sur de grandes distances de mesure.
- Amélioration des méthodes d'évaluation de la stabilité, de la qualité et de la résolution.

L'essai a été réalisé en étroite collaboration avec le Département de géologie de l'Imperial College de Londres et l'Institut de géophysique de l'EPF de Zurich.

¹ aujourd'hui: Gesellschaft für Anlagen und Reaktorsicherheit (GRS)

² aujourd'hui: Bundesministerium für Wirtschaft (BMWi)

³ aujourd'hui: Japan Nuclear Cycle Development Institute, Japon (JNC)



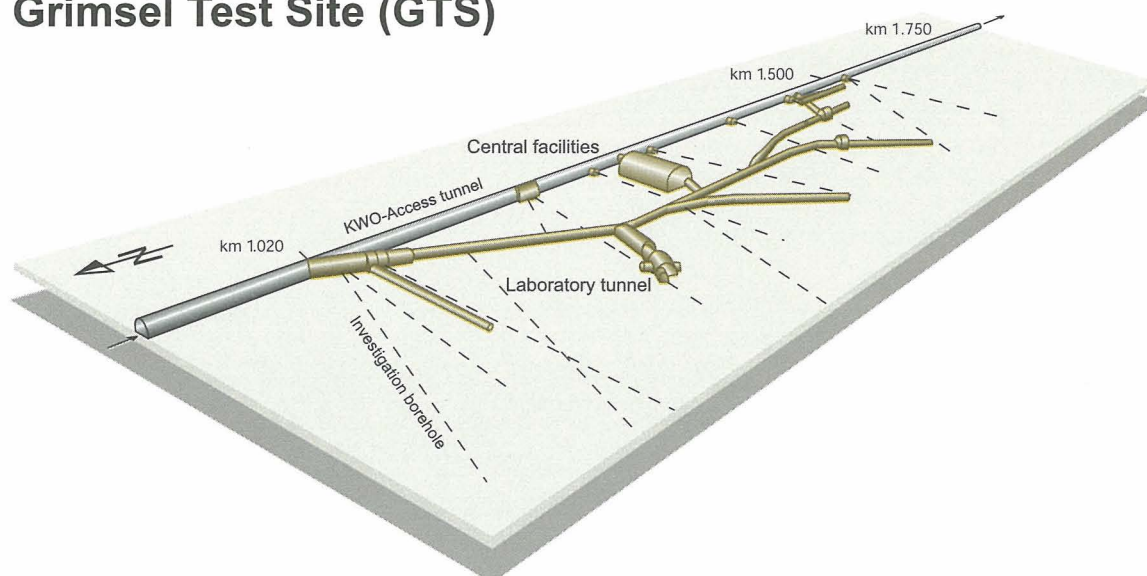
Location of Nagra's underground test facility at the Grimsel Pass in the Central Alps (Bernese Alps) of Switzerland

Grimsel area (view to the west)



1 Grimsel Test Site 2 Lake Raeterichsboden 3 Lake Grimsel 4 Juchlistock

Grimsel Test Site (GTS)



Grimsel Test Site GTS

 KWO-Access tunnel

 Laboratory tunnel

 Central Aaregranite (CAGR)
High biotite content CAGR

 Grimsel-Granodiorite

 Shear zone

 Lamprophyre

 Investigation borehole

ZB Central facilities

BK Fracture system flow

GS Rock stresses

MI Migration

VE Ventilation test

WT Heater test

GTS Phase IV 1994-1996

BOS Borehole Sealing

TOM Further Development of
Seismic Tomography

EDZ Excavation Disturbed Zone

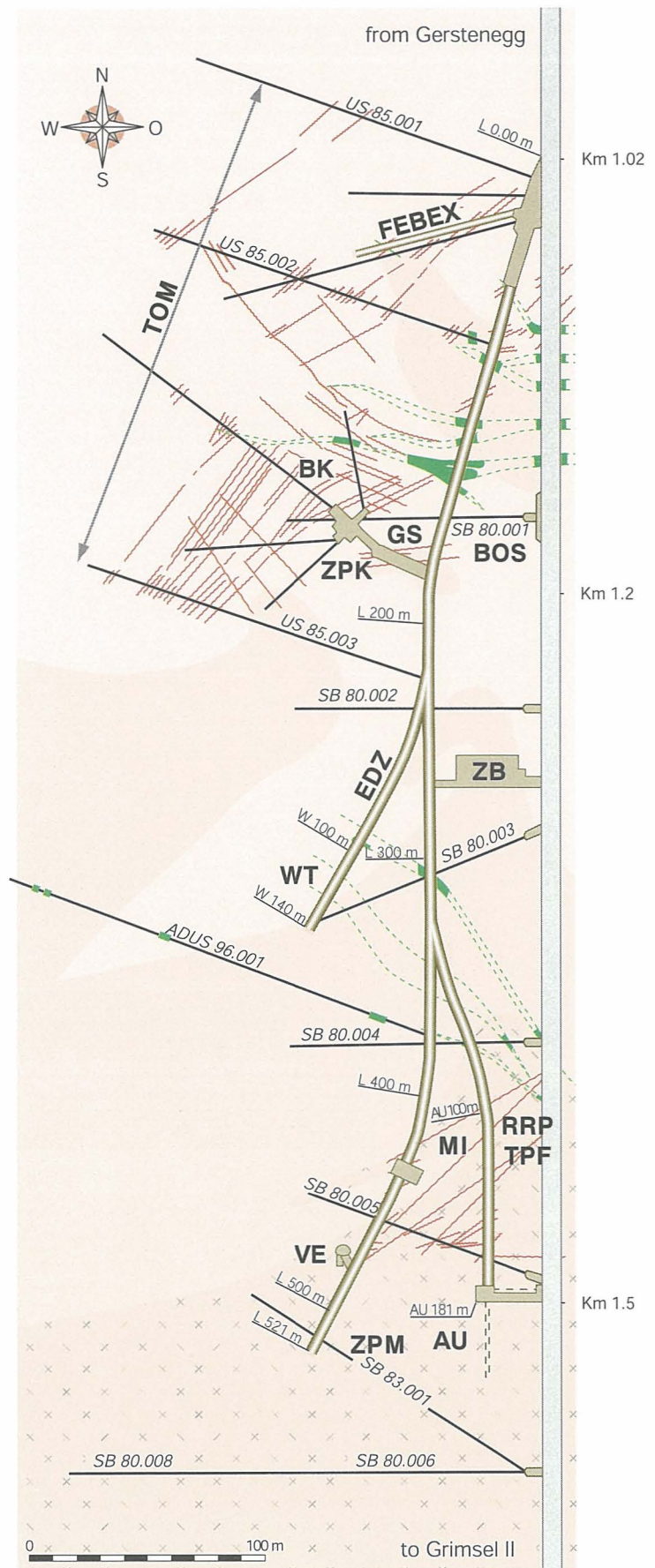
TPF Two-Phase Flow

RRP Radionuclide Retardation
Project

ZPK Two-Phase Flow in Fracture Net-
works of the Tunnel Near-field

ZPM Two-Phase Flow in the Unsat-
urated Matrix of Crystalline Rocks

FEBEX 1:1 EBS – Demonstration (HLW)



SUMMARY

The project entitled "Further Development of Seismic Tomography" has two components: evaluating and testing underground seismic sources for use over large measuring distances and improvement of analysis (inversion) methods in terms of stability, quality and resolution.

Various high-frequency seismic sources have been tested at the Grimsel Test Site (GTS) (Bühnemann, 1996; Bühnemann & Holliger, 1998). The tests were designed to facilitate future tomographic studies of potential radioactive waste disposal sites. A key objective was to identify borehole and tunnel seismic sources capable of generating and sustaining high-frequency signals over distances of up to 1000 m. Seismic sources were located in both water-filled boreholes (sparker, two piezo-electric sources, explosives) and at the tunnel wall (accelerated weight drop, minivibrator, bolt gun, buffalo gun, explosives). In order to evaluate and compare the source characteristics, the direct P-wave generated by the various sources was investigated for decay of its signal-to-noise ratio and dominant frequency with offset and for the maximum distance at which pickable first arrivals could be recognised. Of the seismic sources tested, small explosive charges (5-100 g) were found to have the most favourable energy and frequency characteristics. At the GTS, the target distance of around 1000 m was reached with explosive charges of around 50 g or more. None of the sources tested was capable of sustaining frequencies of 1000 Hz over distances in excess of 100 to 200 m.

The seismic waves are strongly attenuated in the region of the GTS. Q values estimated using the spectral ratio and rise time methods range from about 20 to 60, with a median value of 35 and a standard error of 20% or less (Holliger & Bühnemann, 1996). This explains the observed rapid depletion of high frequencies with increasing offset. In the investigation areas Zürcher Weinland (Opalinus Clay) and Wellenberg (marl) a similar attenuation is expected (Schön, 1996; Tonn, 1989). In the crystalline basement of Northern Switzerland, the attenuation should be lower and the propagation characteristics of the seismic waves should be correspondingly better.

Even when small amounts of explosives (5 g) are used as seismic source, it is to be expected that there will be damage to the borehole wall. This was confirmed by televiwer measurements performed after blasting in borehole BOGS 84.041a.

In the component of the project dealing with improvement (and development) of analysis techniques in terms of stability, quality and resolution, 3 inversion techniques were tested and developed using the dataset US85 (Gelbke, 1988). Two traveltimes inversions - anisotropic velocity tomography - AVT (Pratt & Chapman, 1992) and coupled inversion - CI (Maurer, 1996; Maurer & Green, 1997) - and a wavefield inversion (WFI - Song et al., 1995) were used.

Several problems occurred in the first inversion of the US85 dataset using the Simultaneous Iterative Reconstruction Technique (SIRT); these were due to the velocity anisotropy of the rock, the triggering inaccuracy of the shots and uncertainties regarding the source/receiver locations in the boreholes. In the AVT, the velocity anisotropy of the rock is taken into account as a free parameter. In addition to an "isotropic" velocity image, this involves producing tomograms of anisotropy. Taking into account the anisotropy of the rock allows the artefacts of the SIRT inversion to be explained and the traveltimes inversion to be stabilised.

A fundamental assumption of tomographic inversion techniques currently in use is that the coordinates of the boreholes and tunnels containing the seismic sources and receivers are accurately known. By inverting both synthetic and observed traveltimes data, it can be demonstrated that relatively minor coordinate errors (1-2%) in the deeper sections of long boreholes (> 100 m) may produce artefacts in the tomographic images that are comparable in extent and amplitude to true velocity anomalies. To address this problem, the coupled inversion method (Maurer, 1996) commonly used in earthquake studies is introduced as a means for simultaneously determining borehole coordinate adjustments and an estimate of the tomographic image. Coupled inversions of two independent subsets of traveltimes data (Field US1 and Field US2) that involve a common central borehole (BOUS85.002), together with a coupled inversion of the entire dataset (Field US1, Field US2 and Field US3), yield consistent coordinate adjustments for all boreholes. This also allows the artefacts of the SIRT inversion to be explained and the traveltimes inversion to be stabilised.

Further investigations using synthetic datasets showed that, for the US85 data, it is impossible to draw a distinction between a weak anisotropy and borehole uncertainties based on traveltimes only. However, given the inversion results, it is likely that both effects are present.

The WFI was fully tested on synthetic data before processing the real data. Two synthetic datasets were used: the first was generated using the same (acoustic) wave equation software used in the wavefield inversion process. The second was generated by Professor M. Korn's group at the University of Leipzig. The data from Professor Korn comprised a full, 2D elastic wave simulation.

The synthetic data were fully processed with the sequence used for the field data. This sequence includes:

- i) Traveltimes tomographic imaging
- ii) Data pre-processing (projection of multi-component data, time windowing and amplitude normalisation)
- iii) Frequency domain wavefield inversion

The results obtained using the synthetic data confirmed that a dramatic increase in resolution relative to traveltimes tomography can potentially be obtained when wavefield inversion is used. The use of synthetic data allowed an optimum pre-processing sequence to be designed with confidence and also confirmed that amplitude normalisation, which is necessary for the real data, does not adversely affect the final velocity images - on the contrary it can improve the convergence rate.

The real data differ from the synthetic data in two major respects. First, the field data contain a higher noise level. The noise consists of random background acoustic noise, systematic problems with source static time shifts and spurious trace-to-trace amplitude variations. The second major effect in the real data, which is not present in the synthetic data, is a small but consistent level of P-wave anisotropy. These problems led to the following modifications being incorporated into the wavefield inversion algorithm:

- i) A constraint on the images that enforces a degree of "smoothness"
- ii) Including the source function in the inverse problem. The data were divided into a number of "groups", each having an approximately consistent source static.

- iii) Accounting for a background level of anisotropy by applying a "stretch" to the geometry that simulates anisotropy. In order to account for the apparent angle of the principal anisotropy axis, a coordinate transformation, stretch and retransformation procedure was successfully implemented.

All three were critical in obtaining reliable and interpretable images. The final images show the expected improvement in resolution and enhance the detailed characterisation of the test site.

The resulting tomograms were then validated in three steps. The first step involved an internal consistency check which compared the velocity images for the separately inverted Fields US1 and US2 at the field boundary (borehole BOUS85.002). A good agreement of the velocities along borehole BOUS85.002 was achieved for all the inversion techniques.

In the second step, the agreement between the tomograms and the results of seismic velocity measurements performed in boreholes (sonic logs) was assessed. Sonic logs were available for 9 boreholes in the investigation area (BOUS85.001, BOUS85.002, BOUS85.003, BOBK85.004/BOBK86.001, BOBK85.008, BOBK86.003, FEX95.001 and FEX95.002). In the third and final step, the tomograms were compared with a geological model based on all the geological and hydrogeological data from the US, BK and FEBEX zones. Compared with the SIRT inversion, both the new travelttime inversions (AVT and CI) provide a more stable image with less artefacts which coincides better with the measured sonic velocities and geological structures. The difference between the AVT and CI inversions is minimal. The WFI has the best resolution and the best agreement with the sonic results and geological evidence but it also produces the image with the most artefacts. The reliability of the interpretation is reduced both by strong oscillations mainly at the field boundaries and the extent to which it depends on the selected global anisotropy corrections. More certainty in interpretation can be achieved only by further developing this algorithm for the elastic wave equation, taking into account anisotropy.

ZUSAMMENFASSUNG

Das Projekt "Weiterentwicklung der seismischen Tomographie" ("Further Development of Seismic Tomography") setzt sich aus zwei Untersuchungsschwerpunkten zusammen: die Evaluation und der Test von seismischen Untertagequellen für grosse Messdistanzen und die Verbesserung von Auswerteverfahren (Inversionsverfahren) in Bezug auf Stabilität, Qualität und Auflösungsvermögen.

Verschiedene hochfrequente seismische Quellen wurden im Felslabor Grimsel (FLG) getestet (Bühnemann, 1996; Bühnemann & Holliger, 1998). Ziel dieser Tests war es, zukünftige grossflächige, tomographische Untersuchungen an potentiellen Endlagerstandorten zu ermöglichen. Wesentlich hierfür sind Stollen- und Bohrlochquellen, die hochfrequente seismische Signale über Distanzen von bis zu 1000 m propagieren können. Die getesteten Quellen wurden in wassergefüllten Bohrungen (Sparker, zwei piezoelektrische Quellen, Sprengstoff) und an der Stollenwand (Presslufthammer, Minivibrator, Bolzenschussgerät, Bohrlochgewehr (sog. Gun), Sprengstoff) eingesetzt. Zur Analyse der Charakteristiken der verschiedenen Quellen wurde die direkte P-Welle auf folgende Punkte hin untersucht: die Abnahme des Nutz-/Störsignalverhältnisses mit zunehmenden Abstand von der Quelle, die Abnahme der dominanten Frequenz mit zunehmenden Abstand von der Quelle, sowie die maximale Distanz, bei der erkennbare Einsätze angerissen werden können. Kleine Sprengstoffladungen (5 - 100 g) erzeugen am meisten Energie und weisen das breiteste Frequenzspektrum auf. Im FLG wurde die Zieldistanz von ca. 1000 m nur mit Sprengladungen ab 50 g erreicht. Keine der getesteten Quellen konnte Frequenzen von 1000 Hz über Distanzen von mehr als 100 bis 200 m propagieren.

Im FLG werden die seismischen Wellen sehr stark gedämpft. Aus den gemessenen Daten wurden Q-Werte mit der Spectral-Ratio- und der Rise-Time-Methode bestimmt und reichen von ca. 20 bis 60 bei einem Median von 35 und einer Standardabweichung von bis zu 20% (Holliger & Bühnemann, 1996). Damit kann man die beobachtete rasche Abnahme der hohen Frequenzen mit zunehmendem Abstand gut erklären. In den Untersuchungsgebieten Zürcher Weinland (Opalinuston) und Wellenberg (Mergel) wird eine vergleichbare Dämpfung der seismischen Wellen erwartet (Schön, 1996; Tonn, 1989). Im kristallinen Grundgebirge der Nordschweiz dürfte die Dämpfung der seismischen Wellen geringer sein.

Auch bei kleinen Sprengladungen (5 g) muss mit Schäden an der Bohrlochwand gerechnet werden. Dies wurde durch Televiever-Messungen vor und nach Sprengungen in der Bohrung BOGS 84.041a bestätigt.

In dem Teilprojekt, das sich mit der Verbesserung (und Weiterentwicklung) von Auswerteverfahren in Bezug auf Stabilität, Qualität und Auflösungsvermögen vom Tomogrammen befasst, wurden drei Inversionsverfahren unter Verwendung des US85-Datensatz (Gelbke, 1988) weiterentwickelt und getestet. Zwei Laufzeitinversionen - "Anisotropic Velocity Tomography AVT", (Pratt & Chapman, 1992) und "Coupled Inversion CI" (Maurer, 1996; Maurer & Green, 1997) – sowie eine Wellenforminversion (WFI, Song et al., 1995) wurden eingesetzt.

Bei der ersten Inversion des US85-Datensatzes mit der Simultaneous Iterative Reconstruction Technique (SIRT) traten mehrere Probleme auf, die auf die Geschwindigkeitsanisotropie des Gesteins, auf Triggerungenauigkeiten bei den einzelnen Schüsse, sowie auf Ungenauigkeiten bei der Lagevermessung der Bohrungen zurückgeführt

werden können. Bei der AVT-Inversion wird die Geschwindigkeitsanisotropie des Gesteins als freien Parameter berücksichtigt, d.h. zusätzlich zu den Tomogrammen der "isotropen" Geschwindigkeit werden Abbildungen der Anisotropie erzeugt. Durch die Berücksichtigung der Anisotropie können die Artefakte der SIRT-Inversion erklärt und die Inversion stabilisiert werden.

Bei den heute eingesetzten Inversionsverfahren wird im Prinzip angenommen, dass die Schuss- und Aufnehmerkoordinaten in den Bohrungen und im Stollen genau bekannt sind. Bei Inversionen von synthetischen und gemessenen Laufzeitdaten konnte nachgewiesen werden, dass relativ kleine Koordinatenfehler (1 – 2 %) in grösseren Teufen (> 100 m) Artefakte in den Tomogrammen erzeugen, die im Hinblick auf Umfang und Amplitude mit echten Geschwindigkeitsanomalien vergleichbar sind. Dieses Problem wurde mit der gekoppelten Inversion (Maurer, 1996) gelöst, bei der zusätzlich zu den seismischen Geschwindigkeiten die Lage der Schuss- und Geophonpositionen bestimmt wird. Diese Methode wird häufig in der Seismologie eingesetzt. Mit gekoppelten Inversionen von den zwei unabhängigen Datensätzen Feld US1 und US2 (mit der gemeinsamen Bohrung BOUS85.002), und einer gekoppelten Inversion aller drei Datensätze (Feld US1, US2 und US3) konnten konsistente Koordinatenanpassungen für alle Bohrungen bestimmt werden. Auch die Artefakte der SIRT-Inversion konnten dabei erklärt und die Inversion stabilisiert werden.

Weitere Untersuchungen an synthetischen Datensätzen haben gezeigt, dass es für die US85-Daten unmöglich ist, basierend nur auf Laufzeitdaten zwischen einer schwachen Anisotropie und Bohrlochvermessungsungenauigkeiten zu unterscheiden. Angesichts der Resultate der Laufzeitinversionen sind wohl beide Effekte in den Datensätzen vorhanden.

Die WFI wurde vor der Verarbeitung der Felddaten ausführlich an synthetischen Daten getestet. Zwei synthetische Datensätze wurden eingesetzt: der erste wurde mit dem gleichen Algorithmus erzeugt, wie er in der akustischen Wellenforminversion verwendet wird. Der zweite Datensatz wurde an der Universität von Leipzig (Gruppe Prof. Korn) erzeugt und beruht auf der zweidimensionalen elastischen Wellengleichung.

Die synthetischen Daten wurden mit der gleichen Sequenz bearbeitet, die für die Felddaten eingesetzt wurde. Diese Sequenz besteht aus:

- (i) Laufzeittomographie
- (ii) Bearbeitung der Wellenzüge (Projektion der Mehrkomponentendaten, Time Windowing der Wellenzüge und Amplitudennormierung).
- (iii) Wellenforminversion im Frequenzbereich

Die Resultate an den synthetischen Daten bestätigen, dass eine deutliche Erhöhung des Auflösungsvermögens mit der Wellenforminversion erreicht werden kann. Es konnte eine optimale Bearbeitungssequenz der Wellenzüge vor der Wellenforminversion erarbeitet werden und es konnte bestätigt werden, dass die Normierung der Amplituden, die für die Felddaten notwendig ist, keine negativen Auswirkungen auf die endgültigen Geschwindigkeitsabbildungen hat. Die Normierung führt sogar zu einer Verbesserung der Konvergenz.

In zwei wesentlichen Punkten unterscheiden sich die Felddaten von den synthetischen Daten. Der Störenergiepegel der Felddaten, der vom Hintergrundrauschen, von Triggervariationen und eigenartigen Spur-zu-Spur-Amplitudenvariationen verursacht wird,

ist wesentlich höher. Zweitens enthalten die Felddaten eine kleine, aber konsistente Anisotropie der P-Welle, wohingegen die synthetischen Daten isotrop berechnet wurden. Beide Punkte führten zu folgenden Anpassungen des Wellenforminversions-Algorithmus:

- (i) Einschränkungen „smoothness constraints“ wurden in den Algorithmus eingebaut, die den Kontrast der Abbildungen reduzieren.
- (ii) Quellfunktionen wurden in das Inversionsverfahren integriert. Dazu wurden die Daten in verschiedene "Gruppen von seismischen Quellen" eingeteilt, die jede eine in sich einigermaßen konsistente Triggerzeit aufweisen.
- (iii) Die Anisotropie der untersuchten Felder wurde durch globale Streckung der Feldgeometrie berücksichtigt. Um den scheinbaren Winkel der Anisotropiehauptachse berücksichtigen zu können, wurde eine Koordinatentransformation, eine Streckung, sowie eine Koordinaten-Retransformation erfolgreich implementiert.

Alle drei Prozesse waren wesentlich für die Erzeugung von zuverlässigen und interpretierbaren Abbildungen. Die endgültigen Abbildungen zeigen die erwartete Erhöhung des Auflösungsvermögens und tragen zu einer verbesserten, detaillierten Charakterisierung des Untersuchungsgebiets bei.

Die neuen Laufzeit- und Wellenformtomogramme wurden in drei Schritten validiert. Zuerst wurde die interne Konsistenz überprüft, in dem die Abbildungen der Geschwindigkeit für die separat invertierten Felder US1 und US2 an der Feldgrenze (Bohrung BOUS85.002) verglichen wurden. Eine gute Übereinstimmung der Geschwindigkeiten entlang der Bohrung BOUS85.002 wurde für alle Inversionsverfahren erreicht.

Im zweiten Schritt wurde die Übereinstimmung zwischen den Tomogrammen und den seismischen Geschwindigkeiten (Sonic-Logs), die in Bohrungen gemessen wurden, untersucht. Für 9 Bohrungen im Untersuchungsgebiet standen Sonic-Logs zur Verfügung (BOUS85.001, BOUS85.002, BOUS85.003, BOBK85.004/BOBK86.001, BOBK85.008, BOBK86.003, FEX95.001 und FEX95.002). Im dritten und letzten Schritt wurden die Tomogramme mit einem geologischen Modell, das alle geologischen und hydrogeologischen Daten der US-, BK- und FEBEX-Zonen beinhaltet, verglichen. Im Vergleich mit der SIRT-Inversion liefern die zwei neuen Laufzeitinversionen (AVT und CI) eine stabilere Abbildung mit weniger Artefakten, die besser mit den gemessenen Sonic-Geschwindigkeiten und den geologischen Strukturen übereinstimmt. Der Unterschied zwischen dem AVT- und CI-Tomogramm ist gering. Die WFI weist das beste Auflösungsvermögen sowie die beste Übereinstimmung mit den Soniclogs und geologischen Befunden auf; aber ihre Abbildungen enthalten auch die meisten Artefakte. Die Zuverlässigkeit der Auswertung wird durch starke Oszillationen an den Feldgrenzen, sowie durch die Abhängigkeit der Ergebnisse von der gewählten globalen Anisotropie-Korrektur beeinträchtigt. Nur durch die Weiterentwicklung des Algorithmus für die elastische Wellengleichung und für die Anisotropie kann ein Artefakt-freieres Abbild erzeugt werden und damit mehr Sicherheit für die Interpretation erlangt werden.

RÉSUMÉ

Le projet « Further Development of Seismic Tomography » (perfectionnement de la tomographie sismique) comprend deux parties: d'une part, l'évaluation et le test de sources sismiques souterraines en vue d'applications sur de plus grandes distances; d'autre part, l'amélioration de la stabilité, de la qualité et de la résolution des méthodes d'analyse (inversion).

Diverses sources sismiques à haute fréquence ont été testées au laboratoire souterrain du Grimsel (LSG) (Bühnemann, 1996 ; Bühnemann & Holliger, 1998), dans le but de faciliter les futures études tomographiques de sites potentiels de dépôt final. Un objectif-clé a été l'identification de sources sismiques dans les forages et les galeries, susceptibles de générer et de maintenir des signaux à haute fréquence sur des distances allant jusqu'à 1000 m. Les sources sismiques ont été placées à la fois dans des forages remplis d'eau (dispositif à étincelles « sparker », deux sources piézo-électriques, explosif) et sur la paroi de la galerie (marteau à air comprimé, mini-vibreur, pistolet à chevilles, pistolet de forage, explosif). Pour évaluer et comparer les caractéristiques des différentes sources, on a analysé l'onde P directe ainsi générée, au niveau de la décroissance du rapport signal/bruit, de la fréquence dominante en fonction de la distance (offset), ainsi que de la distance maximale permettant d'identifier les premières arrivées. L'évaluation montre que les petites charges explosives (5 à 100 g) présentent les caractéristiques d'énergie et de fréquence les plus favorables. Au LSG, on a atteint la distance voulue d'environ 1000 m avec des charges explosives de 50g ou plus. Aucune des sources testées n'a pu propager des fréquences de 1000 Hz sur des distances dépassant 100 à 200 m.

Les ondes sismiques sont fortement amorties dans la zone du LSG. Les valeurs Q , estimées à l'aide du rapport spectral et du temps de croissance («rise time»), vont de 20 à 60, la moyenne étant de 35 et l'erreur standard de 20% ou moins (Holliger & Bühnemann, 1996). Cela explique la diminution rapide des hautes fréquences avec l'augmentation de l'offset. Dans les régions de recherche du «Zürcher Weinland» (Argiles à Opalinus) et du «Wellenberg» (marnes), on s'attend à un amortissement semblable (Schön, 1996; Tonn, 1989). Dans le socle cristallin du nord de la Suisse, on s'attend à ce que cet amortissement soit plus faible et à ce que la propagation des ondes sismiques soit d'autant meilleure.

La paroi du forage sera endommagée même si on recourt à de faibles charges explosives (5 g) comme source sismique. Cela a été confirmé par les mesures du televiever réalisées après les explosions dans le forage BOGS 84.041a.

Dans la partie du projet consacrée à l'amélioration et au perfectionnement des techniques d'analyse sur le plan de la stabilité, de la qualité et de la résolution, trois techniques d'inversion ont été testées et mises au point à l'aide des données US85 (Gelbke, 1988). On a recouru à deux inversions du temps de transit (Anisotropic Velocity Tomography - AVT, Pratt & Chapman, 1992, et Coupled Inversion - CI, Maurer, 1996), et à une inversion du champ d'ondes (Wavefield Inversion - WFI, Song et al., 1995).

Lors de la première inversion des données US85, plusieurs problèmes sont apparus avec la méthode SIRT (Simultaneous Iterative Reconstruction Technique), en raison de l'anisotropie des vitesses de propagation dans la roche et des incertitudes liées à l'emplacement des forages. Pour l'inversion AVT, on tient compte de l'anisotropie de vitesse de la roche en tant que paramètre libre: cela suppose la production de tomo-

grammes d'anisotropie en plus de la production d'une image de vitesse « isotrope ». Le fait de tenir compte de l'anisotropie de la roche permet d'expliquer les artefacts de l'inversion SIRT et de stabiliser l'inversion du temps de transit.

Concernant les techniques d'inversion tomographique actuellement utilisées, on suppose en principe que les coordonnées des forages et des galeries contenant les sources sismiques et les récepteurs sont précisément connues. En inversant les données synthétiques et les données de temps de transit observées, on peut démontrer que des erreurs de coordonnées relativement faibles (1 à 2%) dans les sections les plus profondes de longs forages (> 100 m) peuvent produire des artefacts dans les images tomographiques, dont l'étendue et l'amplitude sont comparables à de véritables anomalies de vitesse. Pour résoudre ce problème, on recourt normalement à la méthode d'inversion couplée CI (Couple Inversion, Maurer 1996), tant pour définir des ajustements de coordonnées de forage, que pour évaluer l'image tomographique. Cette méthode est utilisée couramment dans les études de tremblements de terre. Les inversions couplées de deux sous-ensembles de données de temps de transit indépendants (champ US1 et US2 comprenant un forage central commun BOUS85.003) et les inversions couplées de tout l'ensemble de données (champ US+, US2 et US3) permettent des ajustements de coordonnées cohérents pour tous les forages. On peut ainsi expliquer les artefacts de l'inversion SIRT et stabiliser l'inversion du temps de transit.

D'autres recherches à l'aide de données synthétiques ont montré qu'il est impossible, pour les données du LSG, de distinguer une anisotropie faible des incertitudes sur les forages, en se basant uniquement sur des temps de transit. Mais vu les résultats des inversions, les deux effets sont vraisemblablement présents.

Avant le traitement des données de terrain, l'inversion du champ d'ondes WFI a été testée à l'aide de données synthétiques. Deux ensembles de données synthétiques ont été utilisés: le premier a été créé avec le logiciel d'équation d'onde (acoustique) utilisé pour l'inversion d'ondes. Le second a été créé à l'Université de Leipzig, par le groupe du Professeur Korn. Les données du Professeur Korn comprennent toute une simulation 2D des ondes élastiques.

Les données synthétiques ont été entièrement traitées à l'aide de la séquence utilisée pour les données de terrain. Cette séquence se compose de :

- i) La représentation tomographique du temps de transit
- ii) Le traitement préalable des données (projection de données à plusieurs composantes, utilisation de fenêtres de temps des trains d'ondes - « time window » - et normalisation des amplitudes)
- iii) Inversion du champ d'ondes dans le domaine des fréquences.

Les résultats obtenus avec les données synthétiques confirment qu'une forte augmentation de la résolution, par rapport à la tomographie du temps de transit, est possible avec l'inversion du champ d'ondes. Les données synthétiques permettent la définition fiable d'une séquence optimale de traitement préalable et confirment aussi que la normalisation des amplitudes, qui est nécessaire pour les données réelles, n'a pas de répercussion négative sur les représentations définitives des vitesses. Cette normalisation permet au contraire une amélioration du taux de convergence.

Deux différences fondamentales séparent les données réelles des données synthétiques. Premièrement, les données réelles ont un niveau de bruit plus élevé, consistant en un bruit de fond aléatoire, des problèmes systématiques de décalage de temps source statique et de fausses variations d'amplitude piste-à-piste (« trace-to-trace »). Le second effet, identifié dans les données réelles mais pas dans les données synthétiques est une anisotropie de l'onde P faible mais toujours présente. Ces problèmes ont entraîné les adaptations suivantes dans l'algorithme d'inversion du champ d'ondes :

- i) Introduction d'une contrainte d'adoucissement des images, pour en réduire le contraste.
- ii) Intégration de la fonction source dans le problème inverse. Les données ont été réparties en un certain nombre de groupes, ayant chacun une source statique à peu près constante.
- iii) Introduction d'une anisotropie de base par étirement de la géométrie. Pour tenir compte de l'angle apparent du principal axe d'anisotropie, une procédure de transformation, étirement et retransformation des coordonnées a été appliquée avec succès.

Les trois adaptations se sont révélées significatives pour l'obtention de représentations fiables et interprétables. Les images définitives montrent l'amélioration de la résolution et augmentent le niveau de caractérisation du site de recherche.

Les tomogrammes qui en résultent ont été validés au cours de trois étapes. La première consiste en un contrôle de cohérence interne ; on y compare les représentations de vitesse pour les champs séparément inversés US1 et US2 à la limite du champ d'investigation (forage BOUS85.002). Une bonne concordance des vitesses le long du forage BOUS85.002 a été obtenue pour toutes les techniques d'inversion.

Dans la deuxième étape, on a évalué la concordance entre les tomogrammes et les résultats des mesures de la vitesse sismique réalisées dans les forages (diagraphies acoustiques). Des diagraphies acoustiques sont disponibles pour neuf forages du site de recherche (BOUS85.001, BOUS85.002, BOUS85.003, BOBK85.004/BOBK86.001, BOBK85.008, BOBK86.003, FEX95.001 et FEX95.002).

Dans la troisième et dernière étape, les tomogrammes ont été comparés à un modèle géologique comprenant toutes les données géologiques et hydrogéologiques des zones US, BK et FEBEX. Par rapport à l'inversion SIRT, les deux nouvelles inversions de temps de transit (AVT et CI) donnent une image plus stable avec moins d'artefacts, qui coïncide mieux avec les vitesses acoustiques mesurées et les structures géologiques. La différence entre les inversions AVT et CI est minime. L'inversion WFI fournit la meilleure résolution et la meilleure concordance avec les résultats acoustiques et les observations géologiques, mais produit aussi l'image contenant le plus d'artefacts. La fiabilité de l'interprétation est réduite, tant du fait de fortes oscillations, principalement aux limites du champ d'investigation, que du fait qu'elle dépend plus ou moins fortement des corrections de l'anisotropie globale sélectionnées. Cette situation ne peut être améliorée qu'en perfectionnant l'algorithme pour l'équation d'onde élastique prenant en compte l'anisotropie.

TABLE OF CONTENTS

SUMMARY	I
ZUSAMMENFASSUNG	IV
RESUME	VII
LIST OF FIGURES	XII
LIST OF TABLES	XIX
LIST OF ANNEXES	XX
1. INTRODUCTION	1
2. LARGE INVESTIGATION DISTANCES	4
2.1 Seismic sources	4
2.1.1 Borehole sources	4
2.1.2 Tunnel sources	6
2.2 Experimental set-up	9
2.3 Data analysis	10
2.3.1 Signal to noise ratio (S/N) as a function of offset	12
2.3.2 Seismic amplitude as function of explosive charge size	14
2.3.3 Dominant frequency as a function of offset	16
2.3.4 Maximum offset reached	18
2.4 Attenuation of seismic waves in the Grimsel Granite	21
2.4.1 Estimation of Q from seismic data	21
2.4.2 Q values of the Grimsel Granite	22
2.5 Analysis of the damage caused by explosive charges	26
2.5.1 Comparison of televiewer measurements from 1985 and July 1996	26
2.5.2 Comparison of televiewer measurements from July and November 1996	28
2.5.3 Evaluating the direction of damage	34
2.6 Conclusions on the source test	35
3. TRAVELTIME INVERSION METHODS	37
3.1 The US85 experiment	37
3.1.1 Results of the SIRT inversion	38
3.1.2 Problems of the SIRT inversion	40

3.2	Anisotropic velocity tomography	41
3.2.1	Method	41
3.2.2	Parameter test for anisotropic velocity tomography	44
3.2.3	Results of the anisotropic velocity tomography	45
3.3	Potential coordinate mislocation in crosshole tomography	53
3.3.1	Methodology	53
3.3.2	Feasibility studies on synthetic data	57
3.3.3	Inversion results from field data of the Grimsel Test Site	62
3.3.4	Possible three-dimensional effects and anisotropy	67
3.4	Coordinate errors versus anisotropy	71
4.	WAVEFIELD INVERSION	73
4.1	Methodology	73
4.2	Results with synthetic data	75
4.2.1	Acoustic synthetic data: imaging results	77
4.2.2	Elastic synthetic data: imaging results	79
4.3	Inversion of field data	82
4.3.1	Isotropic wavefield inversion	85
4.3.2	Anisotropic wavefield inversion	91
4.4	Conclusions on full wavefield inversion	95
5	VALIDATION OF TOMOGRAMS	97
5.1	Conformity of Field US1 and US2 tomograms at borehole BOUS85.002	97
5.2	Validation with new geometry data	98
5.3	Validation with sonic data	99
5.3.1	Summary of sonic velocities in the area of the tomography Fields US1 & US2	99
5.3.2	Correlation of sonic & tomogram velocity logs	102
5.3.3	Correlation of sonic & tomogram velocity images	105
5.4	Correlation tomogram <-> geological model	110
5.4.1	Correlation of sonic velocities with geological structures	110
5.4.2	Correlation of the tomograms with geological structures	113
5.5	Overall evaluation of the inversion techniques	115
6.	CONCLUSIONS ON NEW INVERSION METHODS	117
	REFERENCES	119

LIST OF FIGURES

Fig. 1.1:	Flow diagram for the project “Further Development of Seismic Tomography”.	3
Fig. 2.1:	Layout of the Grimsel Test Site showing the arrangement of the shot and geophone points used in the source test. The equipment used included two-component geophone sondes (spacing 50 m), 2 single geophone arrays (between 0 and 115 m with 5 m spacing and between 115 m and 350 m with 10 m spacing), a geophone chain (in borehole BOUS85.003) and a hydrophone chain (in borehole BOGS84.041a). The shotpoints were located every 50 m in the tunnel and in the boreholes BOUS85.003 (40, 75, 85, 95 m) and BOGS84.041a (20 and 100 m) (Bühnemann, 1996).	8
Fig. 2.2:	Seismic data generated by sources located (a) in a water-filled vertical borehole at 100 m depth (10 g explosive charge) and (b) along the tunnel wall (weight drop). Both datasets were recorded by vertical-component geophones firmly fixed in shallow vertical boreholes along the tunnel wall. Note that the offset scale is not linear (see Figure 2.1).	11
Fig. 2.3:	S/N of the direct P-wave as a function of offset for seismic signals generated by borehole seismic sources registered at the single geophone line. Solid: 5 g of explosives, dotted: sparker (vertically stacked 16 times), dash-dot: piezo source “Valerie” (16 pseudo-random impulse sequences vertically stacked), dashed: LBL piezo source (16 sweeps vertically stacked).	12
Fig. 2.4:	S/N of the direct P-wave as a function of offset for seismic signals generated by borehole seismic sources registered at the two-component geophone sondes. Dash-dot: 50 g of explosives, solid: 5 g of explosives, dotted: 1 g of explosives.	13
Fig. 2.5:	S/N of the direct P-wave as a function of offset for seismic signals generated by seismic sources located along the tunnel wall. Solid: 5 g of explosives, dotted: buffalo gun, dash-dot: minivibrator, dashed: weight drop, open circles: bolt gun. No S/N estimates are available at near offsets because the direct P-wave could not be separated from the shear and tunnel/surface wave trains.	14
Fig. 2.6:	Natural logarithm of the direct P-wave amplitudes generated by explosives set off in a water-filled vertical borehole at 100 m depth as a function of charge size and offset. The 1 g charge simply corresponds to the explosive cap and thus to a much faster burning type of explosive than the other charges. Open circles: 100 m offset, plus signs: 120 m offset, x-marks: 160 m offset; stars: 240 m offset; solid line: linear best-fits (excluding 1 g charge size) with slopes between 0.028 and 0.033.	15

- Fig. 2.7: Amplitude spectra of a 20 g explosive charge calculated for a 30 ms window around the first arrival at source-receiver offsets of a) 100 m, b) 144 m and c) 373 m. Note the varying scales of the amplitude axis and the rapid decrease of high-frequency amplitudes with propagation distance..... 16
- Fig. 2.8: Dominant frequency of the direct P-wave as a function of offset for seismic signals generated by borehole sources. Solid: 5 g of explosives, dotted: sparker (16 sparks vertically stacked), dash-dot: piezo-source "Valerie" (16 pseudo-random impulse sequences vertically stacked), dashed: LBL piezo-source (16 sweeps vertically stacked)..... 17
- Fig. 2.9: Dominant frequency of the direct P-wave as a function of offset for seismic signals generated by sources located along the tunnel wall. Solid: 5 g of explosives, dotted: buffalo gun, dash-dot: minivibrator, dashed: weight drop, open circles: bolt gun. No frequency estimates are available at near offsets because the direct P-wave could not be separated from the shear and tunnel/surface wave trains..... 18
- Fig. 2.10: Comparison of the maximum source-receiver offset at which the direct P-wave could be detected together with the dominant frequency of this part of the signal at these offsets. 19
- Fig. 2.11: Far offset seismic signals generated by a 100 g explosive charge a) before and b) after applying a 50 - 300 Hz bandpass filter. The explosive charge was located at shot position 24 (s. Fig. 2.1) in a short (3 m), sub-horizontal borehole..... 20
- Fig. 2.12: Q values and their standard errors estimated from amplitude spectra shown in Figure 2.7 by means of the spectral ratio method. Crosses: logarithmic ratio of observed amplitude spectra of a) 100 and 144 m (Figures 2.7a and 2.7b) and b) 144 and 373 m (Figures 2.7b and 2.7c) offsets; solid lines: least-squares estimate of the corresponding linear slopes. Standard errors are based on a least-squares error analysis of the slopes. Frequencies above 1200 Hz are rapidly attenuated below the ambient noise level and therefore were excluded from the analyses..... 23
- Fig. 2.13: Pulse width as a function of travelttime for seismic pulses generated by a) 50 g and b) 20 g explosive charges. Crosses: observed pulse widths defined by the first zero-crossing and the first maximum of the direct P-wave. Solid: linear least-squares best-fit. Corresponding estimates of Q range from about 20 to 40 (with an estimated standard error of about 10%) depending on the value of the proportionality constant c 24
- Fig. 2.14: Comparison of travelttime and amplitude images for the televiwer measurements of 1985 (Pahl et al., 1989) and July 1996 (Albert, 1997) in the depth interval 99.4 - 100.5 m..... 27

Fig. 2.15:	Comparison of traveltimes and amplitude images for televiewer measurements of July and November 1996 at the different shot positions between 10 and 30 m.....	29
Fig. 2.16:	Comparison of traveltimes and amplitude images for televiewer measurements from July and November 1996 at the different shot positions between 90 and 120 m.....	30
Fig. 2.17:	Caliber crossplots for shots at positions with small geological structures.	32
Fig. 2.18:	Caliber crossplots for shots at positions with no recognisable geological structures..	33
Fig. 3.1:	The underground seismic (US) area at the Grimsel Test Site. The areas between the boreholes BOUS85.001 and BOUS85.002, BOUS85.001 and BOUS85.003 and BOUS85.002 and BOUS85.003 have been scanned independently..	37
Fig. 3.2:	The ray distribution of Field US2 (between boreholes BOUS85.002/BOUS85.003). Only every fourth ray has been plotted. This geometry contains arrangements of a crosshole and two walkaway VSP measurements.....	38
Fig. 3.3:	The final result of the SIRT inversion for Fields US1 and US2 (Gelbke, 1988)	39
Fig. 3.4:	A suite of tomographic results, using variable roughness constraints (λ) for Field US1. a) As λ is increased, the images become less rough, but the data fit degrades. Isotropic images always have higher residuals. b) As λ is increased, the images become less rough and less noisy. The isotropic images are strongly corrupted by anisotropy. c) Traveltime residuals are shown for all source receiver pairs in relative colour code (red: positive residuals, blue: negative residuals). As λ is increased, the data residuals become larger. The isotropic data residuals display characteristic, systematic patterns. d) The anisotropy is not homogeneous and as λ is increased the images stabilise.	46/47
Fig. 3.5:	A suite of tomographic results, using variable roughness constraints (λ) for Field US2. a) As λ is increased, the images become less rough, but the data fit degrades. Isotropic images always have higher residuals. b) As λ is increased, the images become less rough and less noisy. The isotropic images are strongly corrupted by anisotropy. c) Traveltime residuals are shown for all source receiver pairs in relative colour code (red: positive residuals, blue: negative residuals). As λ is increased, the data residuals become larger. The isotropic data residuals display characteristic, systematic patterns. d) The anisotropy is not homogeneous, and as λ is increased the images stabilise.	48/49

- Fig. 3.6: Final velocity image from the anisotropy velocity tomography (AVT) for Fields US1 and US2. This image represents the distribution of the “isotropic” velocity (i.e., the mean velocity in each cell, averaged over all directions). 50
- Fig. 3.7: Final anisotropy image from the anisotropy velocity tomography (AVT) for Fields US1 and US2. This image represents the distribution of the ε factor, i.e. the fractional difference between the velocity in the tunnel direction (20°) and the velocity in the borehole direction (290°). 51
- Fig. 3.8: The direction of the principal axes of transverse isotropy symmetry from the anisotropy velocity tomography (AVT) for Fields US1 and US2. If the anisotropy were transverse isotropy, these arrows would indicate the symmetry direction in the plane of the survey. Each arrow is scaled by an amount proportional to the local ε factor; where ε is less than 2% no arrow is plotted. 52
- Fig. 3.9: Effects of systematic errors on a constant velocity model (5000 m/s): a) Artefacts produced by a slightly curved receiver borehole (shown in b). b) Assumed receiver borehole trace (solid straight line) and true borehole trace (dotted line). c) Artefacts produced by a constant delay of 0.5 ms for shots deeper than 200 m depth. d) Anomaly pattern obtained for an overall delay of 0.5 ms 54
- Fig. 3.10: Geometry of boreholes shown with a strong x-axis : y-axis exaggeration (~ 4.75) to highlight the curvature of the boreholes. Measured shot and receiver positions are shown by small circles (Gelbke, 1988), whereas shot and receiver positions used to compute synthetic traveltimes for the feasibility study are shown by solid lines. 57
- Fig. 3.11: Relocation results for the homogeneous velocity model. Different symbols represent results from the three fields: + = Field US1; x = Field US2; * = Field US3. Due to the good match, it is difficult to distinguish between the results of the individual fields. 58
- Fig. 3.12: Velocity model used for the second synthetic experiment of the feasibility study. Velocities are in m/s. 59
- Fig. 3.13: Tomograms for the second synthetic experiment of the feasibility study (input velocity model is shown in Fig. 3.12). The panels a to c show the results of the pure velocity inversions (i.e. no attempt to improve estimates of borehole locations), whereas the panels d to f depict the solutions of the coupled inverse problem. Velocities are in m/s. 60
- Fig. 3.14: Relocation results of the second synthetic experiment of the feasibility study. Different symbols represent results from the three fields: + = field 1; x = field 2; * = field 3. 61

- Fig. 3.15: Comparison of tomograms produced by the coupled inversion (CI) derived from the observed Grimsel datasets. The panels a to c show the results of the pure velocity inversions (i.e. no attempt to improve estimates of borehole locations), whereas the panels d to f depict the solutions of the coupled inverse problem. Velocities are in m/s..... 63
- Fig. 3.16: Relocation results of the observed data: + = Field US1, x = Field US2, * = Field US3..... 64
- Fig. 3.17: Refined and slightly smoothed version of the tomogram shown in Figure 3.15f. Field US1 lies between boreholes BOUS85.001 and BOUS85.002, Field US2 between boreholes BOUS85.002 and BOUS85.003, and Field US3 between boreholes BOUS85.001 and BOUS85.003. Velocities are in m/s. 66
- Fig. 3.18: Formal model resolutions (diagonal elements of the formal resolution matrix (Menke, 1984; Maurer, 1996)) of the tomograms shown in Figure 3.15. The values of the diagonal elements indicate whether a particular parameter can be resolved (1 = perfect resolution, 0 = unresolved)..... 68
- Fig. 3.19: Inversion results of synthetic traveltimes data that include an elliptical anisotropy of $\varepsilon = -0.05$ and four different azimuths ϕ of the fast axis: 20° , 65° , 110° and 155° , which correspond to angles of 0° , 45° , 90° and 135° relative to the x-axes of other figures. + = Field US1, x = Field US2..... 70
- Fig. 4.1: Acoustic wavefield inversion of synthetic acoustic data. a) Model of schematic velocity distribution in Field US2. b) Traveltimes tomography result obtained from manual picking of elastic synthetic time domain data. c) Acoustic wavefield inversion result, using 100 Hz data. d) Acoustic wavefield inversion result using 1000 Hz data..... 76
- Fig. 4.2: Acoustic wavefield inversion of synthetic acoustic data: Tests of survey geometry. a) Crosshole data, b) both VSP datasets, c) left-hand VSP d) right-hand VSP, all formed using 1000 Hz data, as in Figure 4.1d). 78
- Fig. 4.3: Acoustic wavefield inversion of synthetic elastic data. a) True model (same as in Figure 4.1a), b) traveltimes inversion, c) acoustic inversion of original data d) acoustic inversion of windowed, normalised data. 80
- Fig. 4.4: Two representative source gathers of VSP data from Field US2, as true amplitude displays. a) A VSP source gather with large offset. The spurious variation of amplitude from trace to trace is evident, as is the lack of consistency of alternate traces. The data were recorded in two passes, with intermediate traces recorded during a later "in-fill" survey. b) A near offset VSP source gather, on which the dramatic change in amplitude with receiver depth is evident.

- These variations in amplitudes cannot be modelled using the 2D acoustic method. As described in the text, in order to invert these data a normalisation was applied separately to each trace..... 83
- Fig. 4.5: A representative common receiver gather of the Field US2 data. The receiver was in borehole BOUS85.003. The first portion of the gather was recorded with sources in borehole BOUS85.002, and thus represents a portion of the crosshole data. The second section was recorded with sources in the tunnel, and thus represents a portion of the VSP data. The data have been windowed and trace-normalised. The random static shifts in the crosshole data and the systematic static shifts in the VSP data are evident. The labels indicate the VSP source groups that were identified, in order to solve for the source-consistent static shifts. 84
- Fig. 4.6: A small section of the Field US1 seismic wavefield data, from shot-point 121 (crosshole data). This demonstrates the data problems referred to in the text - every alternate trace contains a small phase shift, possibly due to slightly different instrumentation specifications between the initial and "in-fill" surveys 85
- Fig. 4.7: Isotropic full wavefield inversion results for Field US2, with various smoothing parameter values increasing from 0 to 100..... 86
- Fig. 4.8: Trade-off curve showing RMS roughness vs. RMS residuals for a suite of smoothing parameters (top panel is for Field US2, bottom panel is for Field US1)..... 87
- Fig. 4.9: Frequency domain data for Field US2, 900 Hz. a) Original data (following pre-processing and frequency transformation, b) residuals following isotropic wavefield inversion, c) residuals following correction for 2 % anisotropy. In all figures, each pixel represents the real part of the complex valued Fourier component for a single source - receiver pair in the survey, with sources arranged along the vertical axis and receivers arranged along the horizontal axis. Panel 1 corresponds to the crosshole data and panels 2 and 3 correspond to the two VSP surveys. The grey scale is a relative amplitude. 89
- Fig. 4.10: Frequency domain data for Field US1, 900 Hz. a) Original data (following pre-processing and frequency transformation, b) residuals following isotropic wavefield inversion, c) residuals following correction for 2 % anisotropy. In all figures, each pixel represents the real part of the complex valued Fourier component for a single source - receiver pair in the survey, with sources arranged along the vertical axis and receivers arranged along the horizontal axis. Panel 1 corresponds to the crosshole data and panels 2 and 3 correspond to the two VSP surveys. The grey scale is a relative amplitude. 90
- Fig. 4.11: Isotropic inversion of a synthetic dataset from a homogeneous, anisotropic model 91

Fig. 4.12:	Anisotropic full wavefield inversion results for Field US2 with 0, 1, 2 and 3 % elliptical anisotropy	92
Fig. 4.13:	Anisotropic full wavefield inversion results for Field US1 with 0, 1, 2 and 3 % elliptical anisotropy	93
Fig. 4.14:	RMS residuals for each of the tested anisotropy levels. Top panel is for Field US2, bottom panel is for Field US1	94
Fig. 4.15:	Final wavefield inversion images from Fields US1 and US2, using 2 % elliptical anisotropy	96
Fig. 5.1:	Geometry surveys in BOUS85.002 and relocalisation results from coupled inversion (Fig. 3.16).	99
Fig. 5.2:	Sonic logs from boreholes BOBK85.004/86.001, BOBK85.008, BOBK86.003, BOUS85.001, BOUS85.002, BOUS85.003, FEX95.001 and FEX95.002. The sonic logs were smoothed along the vertical projected trends of the boreholes onto the tomography plane; the colour code is the same as for the tomograms.....	101
Fig. 5.3:	Composite log for borehole BOBK85.008. Besides the sonic logs, the velocities read from the different tomograms along the projection of borehole BOBK85.008 are presented.	104
Fig. 5.4:	Comparison of the SIRT inversion with the sonic velocities. The velocity image was superimposed with the colour-coded sonic logs	106
Fig. 5.5:	Comparison of the AVT inversion with the sonic velocities. The velocity image was superimposed with the colour-coded sonic logs	107
Fig. 5.6:	Comparison of the CI inversion with the sonic velocities. The velocity image was superimposed with the colour-coded sonic logs.....	108
Fig. 5.7:	Comparison of WFI inversion with the sonic velocities. The velocity image (with an anisotropy correction of 2%) was superimposed with the colour-coded sonic logs	109
Fig. 5.8:	Comparison of geological structures (S-zone: red, K-zone: blue and lamprophyre: grey) with the sonic logs (waveform and velocity: V_p) for borehole FEX95.001	111
Fig. 5.9:	Plan with the geological interpretation of structural elements (S-zone: red, K-zone: blue and lamprophyre: grey). Projection of the borehole information onto the tomographic plane.	112
Fig. 5.10:	Interpretation of structural elements (S-zone: red, K-zone: blue and lamprophyre: grey) based on geological and hydrogeological data (Möri & Bossart, 1997).....	114
Fig. 5.11:	Geological interpretation of AVT, CI and WFI tomograms	116

LIST OF TABLES

Tab. 2.1:	Borehole and tunnel seismic sources.....	9
Tab. 2.2:	<i>Q</i> values calculated using the spectral ratio method and their standard errors for various sizes of explosive charge, offset ranges, S/N ratios and frequency ranges. <i>Q</i> values with standard errors < 20 are given in bold print.	25
Tab. 2.3:	Use of explosives in the source test.....	28
Tab. 2.4:	Explosive test of 13.11.1996	31
Tab. 2.5:	Analysis of preferential directions of damage to the borehole wall caused by using explosive charges.....	35
Tab. 5.1:	Overview of the results of sonic measurements performed in the boreholes BOBK 85.004/86.001, BOBK85.008, BOBK86.003, FEX95.001, FEX95.002, BOUS85.001, BOUS85.002 and BOUS85.003	100
Tab. 5.2:	Velocity anomalies with a lateral extent of more than 5 m and negative velocity deviations from the median value of at least 5% (corresponding to approx. 260 m/s). The depths in the boreholes and the percentage deviation in % are given.	103

LIST OF ANNEXES

- Annex 1: Composite log for borehole BOBK85.004/86.001. The composite log gives the sonic velocities, the tomogram velocities along the vertical projection of the borehole for the SIRT, AVT and CI traveltimes inversions and for the isotropic WFI inversion, 1%, 2% and 3% anisotropy correction, the sonic wavefields and the geological structures.
- Annex 2: Composite log for borehole BOBK85.008. The composite log gives the sonic velocities, the tomogram velocities along the vertical projection of the borehole for the SIRT, AVT and CI traveltimes inversions and for the isotropic WFI inversion, 1%, 2% and 3% anisotropy correction, the sonic wavefields and the geological structures.
- Annex 3: Composite log for borehole BOBK86.003. The composite log gives the sonic velocities, the tomogram velocities along the vertical projection of the borehole for the SIRT, AVT and CI traveltimes inversions and for the isotropic WFI inversion, 1%, 2% and 3% anisotropy correction, the sonic wavefields and the geological structures.
- Annex 4: Composite log for borehole BOUS85.001. The composite log gives the sonic velocities, the tomogram velocities along the borehole for the SIRT, AVT and CI traveltimes inversions and for the isotropic WFI inversion, 1%, 2% and 3% anisotropy correction, the sonic wavefields and the geological structures.
- Annex 5: Composite log for borehole BOUS85.002. The composite log gives the sonic velocities, the tomogram velocities along borehole for the SIRT, AVT and CI traveltimes inversions and for the isotropic WFI inversion, 1%, 2% and 3% anisotropy correction, the sonic wavefields and the geological structures.
- Annex 6: Composite log for borehole BOUS85.003. The composite log gives the sonic velocities, the tomogram velocities along the borehole for the SIRT, AVT and CI traveltimes inversions and for the isotropic WFI inversion, 1%, 2% and 3% anisotropy correction, the sonic wavefields and the geological structures.
- Annex 7: Composite log for borehole FEX95.001. The composite log gives the sonic velocities, the tomogram velocities along the vertical projection of the borehole for the SIRT, AVT and CI traveltimes inversions and for the isotropic WFI inversion, 1%, 2% and 3% anisotropy correction, the sonic wavefields and the geological structures.
- Annex 8: Composite log for borehole FEX95.002. The composite log gives the sonic velocities, the tomogram velocities along the vertical projection of the borehole for the SIRT, AVT and CI traveltimes inversions and for the isotropic WFI inversion, 1%, 2% and 3% anisotropy correction, the sonic wavefields and the geological structures.

- Annex 9: Overlay of the geological structures (Fig. 5.9) on the SIRT tomogram (Fig. 3.3).
- Annex 10: Overlay of the geological structures (Fig. 5.9) on the AVT tomogram (Fig. 3.6).
- Annex 11: Overlay of the geological structures (Fig. 5.9) on the CI tomogram (Fig. 3.17).
- Annex 12: Overlay of the geological structures (Fig. 5.9) on the WFI tomogram (Fig. 4.15).

1. INTRODUCTION

As part of demonstrating the safety of a repository for radioactive waste, it is necessary to characterise the potential host rock in detail. Investigations can be performed directly from tunnels or from exploratory boreholes. Since every borehole drilled into the potential host formation represents a weakening of the barrier function of the rock, it is attempted, when investigating and characterising such formations, to keep the number of boreholes to a minimum and to use non-invasive methods. One example of the latter is seismic tomography. The extent to which hydraulically relevant inhomogeneities can be detected by seismic tomography is of great interest in connection with repository exploration programmes.

The tomography investigation technique is known mainly from the field of medicine but it was tested successfully by Nagra at the Grimsel Test Site (GTS) in 1985. The programme (US85) consisted of tomographic surveys of several measurement fields (up to max. 225 m*450 m) carried out between a tunnel and three underground boreholes and the earth's surface (Blümling & Sattel, 1988; Gelbke, 1988).

As part of the disposal programmes for low- and intermediate-level waste (L/ILW) - marl/Wellenberg - and high-level waste (HLW) - crystalline basement/Mettau - it is planned to investigate larger fields up to around 1 square kilometre in extent using tomography. The aim of the project "Further Development of Seismic Tomography" described in this report is to develop tomographic methods for such applications.

Based on experience to date, the following focal points have been identified for the project:

- Evaluating and testing of underground seismic sources for use over large measurement distances
- Improvement of analysis (inversion) techniques in terms of stability, quality and resolution, including development of new methods if necessary.

Sensors and registration equipment are being developed in the industrial sector as part of an EU project (Asturiana de Zinc et al., 1998).

Evaluation and testing of underground seismic sources for use over large measurement distances

Planned site-specific investigations will have to cover large measurement distances (up to around 1000 metres). Up till now, tomographic surveys have not been tested sufficiently over such distances, either at the GTS or in similar programmes abroad. Normal distances for tomographic investigations (aside from earthquake studies) tend to be in the range of several decametres to a few hundred metres. In the earlier investigations at the GTS, the maximum distances covered were approximately 450 m (surface to tunnel).

The feasibility of carrying out tomographic field measurements over large distances (up to 1000 m) with sources which can be used repeatedly and without disturbance in an underground tunnel or borehole and which have a stable, sufficiently high-frequency signal characteristic is unclear and requires to be investigated further (cf. Chapter 2).

Improvement and development of analysis (inversion) techniques in terms of stability, quality and resolution

Various inversion algorithms which were available at the time were tested and compared for the purpose of analysing the measured data from the US85 programme. The best results were obtained with the SIRT (Simultaneous Iterative Reconstruction Technique) method (Blümling & Sattel, 1988; Gelbke, 1988). However, instability problems which arose during the inversion led, with an increasing number of iteration steps, to a number of different artefacts in the results. The root of these problems has not yet been identified. It is not clear whether it is a problem which is inherent to the dataset (e.g. surveying inaccuracies in the test boreholes) or to the algorithm (taking only the global anisotropy of the rock into account).

Thanks to the enormous advances in computer technology in recent years, and the associated increase in computing capacity, inversion algorithms have been developed in the meantime which allow a more comprehensive evaluation of tomographic field datasets which takes into account anisotropy, surveying inaccuracy, the whole wavefield and the three-dimensional radiation pattern of the source signals. The increase in interpretability of tomographic data, which is usually discussed in the literature for synthetic datasets, was verified using an existing field dataset (US85).

In terms of further developing inversion techniques, Nagra tried out two basically different procedures (travelttime and wavefield inversion). In the case of travelttime inversion, only the travelttime of the seismic wave from source to receiver is analysed; for wavefield inversion the whole seismic wave train is used.

The purpose of the new developments is to improve the stability and quality of imaging, as well as resolution. In most rocks, the velocity of a seismic wave depends on direction (anisotropy). If anisotropy is taken into account as an inversion parameter, travelttime inversion can be stabilised and image quality significantly improved (see Chapter 3.2). The accuracy of borehole path coordinates was also recognised as a problem. If the shot and receiver points are included as free parameters in the travelttime inversion, this also provides a stable inversion result and a relocalisation of the borehole source and receiver points (see Chapter 3.3).

Based on theoretical considerations, travelttime inversions can reach a maximum resolution corresponding to the first Fresnel zone (Williamson, 1991; Williamson & Worthington, 1993). The resolution is thus a function of wavelength and ray path and is approx. 20 - 30 m for Field US2 (Fig. 3.1). If the whole seismic wave train is used (wavefield inversion), information content is increased and resolution improved (see Chapter 4). A maximum achievable resolution of one wavelength (approx. 5 m) is given for the waveform inversion (Štekl & Pratt, 1998; Song & Worthington, 1995; Wu & Toksoz, 1987).

Finally, the results of the tomographic investigations were compared with borehole measurements (sonic logs) and geological data in order to assess the suitability of the inversion techniques for application in repository site investigation programmes (see Chapter 5).

Figure 1 gives a flow diagram for the project "Further Development of Seismic Tomography".

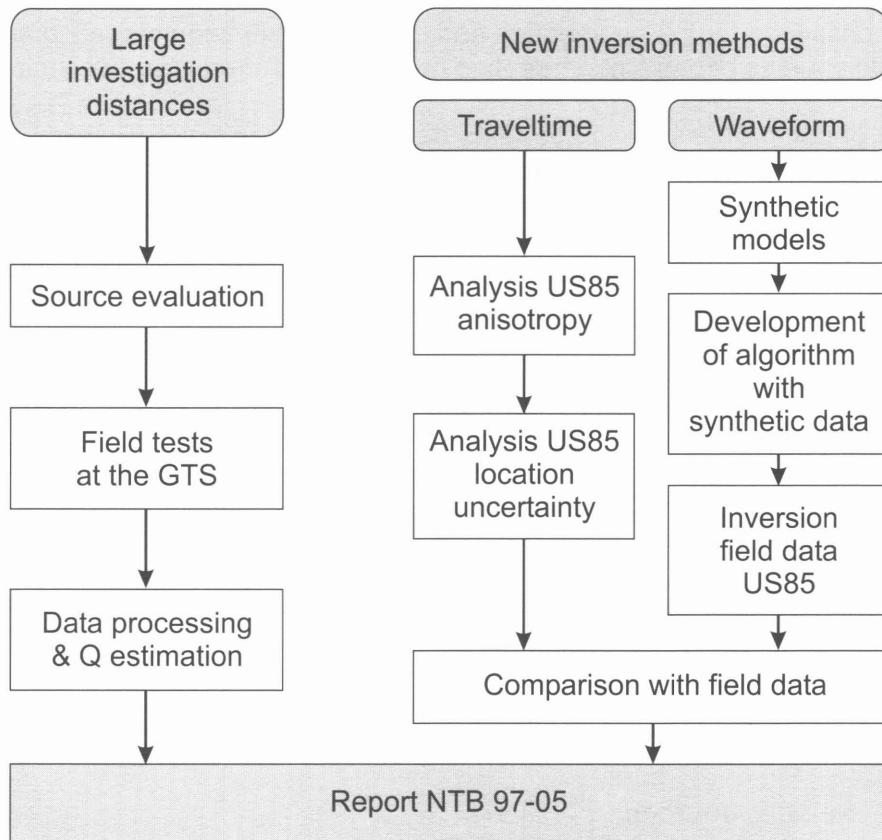


Fig. 1.1: Flow diagram for the project "Further Development of Seismic Tomography".

2. LARGE INVESTIGATION DISTANCES

An important task in environmental and engineering geophysics is the detailed seismic imaging of the subsurface by reflection, refraction and tomographic seismic methods. In many shallow geological formations, including some consolidated sediments and crystalline rocks, the high-frequency components of seismic signals may be strongly damped (e.g. Paulsson et al., 1985; Bourbié et al., 1987; Holliger & Bühnemann, 1996). Since seismic resolution is related directly to the dominant signal frequencies, it is a major challenge for the engineering and environmental geophysical communities to find seismic sources capable of generating powerful, high-frequency, seismic signals.

A number of comprehensive source tests have been carried out (Pullan & MacAulay, 1987; Miller et al., 1986, 1992; Parker et al., 1993; Rehtien et al., 1993). These efforts have been mostly geared towards shallow seismic reflection and refraction seismic applications, whereas this study deals with crosshole and crosstunnel tomographic characterisation of potential radioactive waste disposal sites (e.g. Hayles et al., 1996; Kragh et al., 1996). Corresponding scenarios are generally based on hard (i.e. crystalline or consolidated sedimentary) rock volumes with maximum extents of up to 1000 m and spatial resolutions of the order of 1 m (e.g. Green & Mair, 1983; Paulsson et al., 1985; Whitaker, 1987). Seismic sources and receivers for tomographic studies may be located in boreholes and along walls of exploratory tunnels. The primary objective of such tomographic seismic imaging of potential radioactive waste disposal sites is to locate fractures and shear zones as well as compositional and/or structural inhomogeneities.

Based on the objectives described above, borehole and tunnel seismic sources capable of generating seismic signals that sustain frequencies up to 1000 Hz over distances up to 1000 m were looked for. The sources used are described below and summarised in Table 2.1.

2.1 Seismic sources

The seismic sources considered in this study were selected for use at the tunnel wall and in water-filled boreholes (BOGS84.041a and BOUS85.003).

2.1.1 Borehole sources

The borehole sources considered comprised a sparker, two piezo-electric sources and small explosive charges ranging from 1 to 100 g in size (Bühnemann, 1996; Bühnemann & Holliger, 1998).

Explosives

Using explosives to generate seismic waves is a technique which is widely used in the field of exploration seismics to produce compact, energy-rich, wide-band signals. Depending on the investigation area and the desired depth range, the charge can be varied from a few grams to several hundred or thousand kilograms to produce signals with different ranges.

In the case of seismic exploration associated with identification of suitable repository sites, generation of seismic energy should not result in the formation of any new fractures and fault zones in the potential host rock. This places a restriction on the amount of explosive charge which can be used. In underground boreholes, charges of 1, 5, 10, 20 and 50 g were tested for signal range. The tests were carried out in two underground boreholes (Fig. 2.1): one almost horizontal (BOUS85.003: 75° inclination towards the vertical) and one vertical (BOGS84.041a).

In the vertical borehole, there was no problem with lowering the explosives to position using the ignition cable. In the other (almost horizontal) borehole, this operation proved to be much more time-consuming as the explosives had to be pushed into position using a plastic rod.

CSMA sparker Mark II

Sparkers are sources of seismic energy which are used primarily in high-resolution marine reflection seismics, although they are now finding increasing application in boreholes. Pulsed acoustic energy is generated by rapid electrical discharge in an arc (sparking) which forms between two electrodes in an electrolyte.

The Mark II sparker of the company Cambourne School of Mines Associates (CSMA, UK) was used for the test measurements. The discharge voltage of this source is ~ 4 kV, which is capable of releasing energies up to several kilojoules during one discharge. The Mark II sparker is particularly suited for use at high temperatures up to 200°C. The shot repetition rate is 2 - 10 impulses per minute (Dyer & Baria, 1994).

According to the manufacturer's information (Dyer & Baria, 1994), signals with frequencies of up to 2.5 kHz were registered over distances of 150 m during test measurements in Soultz (France). With a penetration over 850 m, direct P-waves with frequencies up to 1 kHz could be recognised in the unstacked data (Dyer & Baria, 1994).

Schlumberger 'Valerie'

'Valerie' is a high-frequency piezo-electric source developed by Schlumberger for crosshole measurements. The manufacturers recommend that, in the case of cross-hole measurements, a maximum distance between two boreholes of 500 m should not be exceeded. Results of test measurements at Sellafield (England), in which interpretable signals were registered between boreholes with an offset of 600 m (Emsley et al., 1994), prompted the decision to include 'Valerie' in the test.

According to the manufacturer, 'Valerie' generates the wavefield of a monopole, which is easy to reproduce and has a flat frequency response for frequencies between 0.2 to 2 kHz (Schlumberger, 1992).

The source signal is a 1.024 s long pseudo-random sequence of 64 single impulses. This signal is known in the fields of communication and measurement technology as the Goley code (Skolnik, 1990). Signal processing is similar to that for a vibroseis signal. By cross-correlating the registered data with the source signal registered on a pilot trace, the energy of the impulse sequence is compressed to a zero-phase signal (Yilmaz, 1987).

In contrast with the vibroseis technique, with 'Valerie' a Goley code signal is emitted in two separate shots - one positive and one negative. The autocorrelations of these two codes show complementary secondary lobes. On summation of the two autocorrelations, the secondary lobes are cancelled out and the central maxima, which correspond to the desired source signal, add together constructively (Skolnik, 1990).

LBL piezo-source

A second piezo-source to be tested was developed at the Lawrence Berkeley Laboratory (LBL) in California. The electrical energy supply for the source is a maximum of 500 V, whereby the largest seismic energy is generated with maximum voltage.

Various signal forms can be generated using the LBL piezo-source. The range covers single impulses and various sweeps and Barker codes of maximum 100 ms length. Barker codes, which have been borrowed from the field of radar technology, are monofrequency signals with phase shifts of 180° (Skolnik, 1990). Using this signal form has the same effect as the Goley sequence of 'Valerie' in that, in the autocorrelation of the signal, the ratio of central maximum to secondary maxima is as large as possible.

Two different upsweeps (sweep 1: 200-2000 Hz, sweep 2: 500-5000 Hz) and two different Barker codes (Barker code 9 and 17) were used in the test measurements (Bühnemann, 1996).

2.1.2 Tunnel sources

Seismic sources applied horizontally along the tunnel wall comprised a weight drop, a bolt gun, a minivibrator, a modified Buffalo gun and, again, explosive charges ranging from 1 to 100 g. In view of future applications to seismic exploration of potential radioactive waste disposal sites, all tunnel sources were designed to act more or less horizontally on the tunnel wall.

To be able to transmit through horizontal surfaces, energy release from the tunnel wall should be as horizontal as possible. For sources such as the weight drop and the minivibrator, special technical modifications were necessary; these were carried out during the preparation stage for the tests. Generation of signals using explosives and the shot gun was performed in 3 m deep, small-diameter (57 mm) boreholes which were inclined downwards (10° from the horizontal) and filled with water. The boreholes were located at intervals of 50 m along the tunnel wall.

Explosives

In addition to signal generation in underground boreholes, generation was also tested with various sizes of explosive charges (5, 20, 50 and 100 g) in tamped small-diameter boreholes at the tunnel wall.

'Vakimpak' weight drop

An accelerated weight drop, with signal generation as horizontal as possible, was also tested. Although such sources, which involve accelerating a body against a surface

using various acceleration mechanisms, are really designed for vertical generation, an attempt was made to achieve as horizontal a signal generation as possible. The 'Vakimpak' weight drop is accelerated by compressed air and allows signals to be generated up to an inclination of 60° from the vertical. In order to improve coupling, concrete wedges were used at every shotpoint to produce a flat impact surface at the tunnel wall. Despite this, the coupling conditions at the various generation points were very variable (Bühnemann, 1996).

Shot gun 'Sissy'

The shot gun used in the test (manufactured by 'Dynamit Nobel', Deisendorf, Germany) is known as 'Sissy' (seismic impulse source system). It can be anchored in a small-diameter (57 mm) borehole using a packer in such a way that no additional tamping is necessary to damp the backfire energy. Seismic energy is generated using electrically triggered blank cartridges (12 mm caliber). The gun was destroyed by the shots during the test measurements, meaning that signal generation using 'Sissy' had to be stopped at shotpoint 12. Based on this experience, it was recommended to use a more stable construction when working in intact crystalline rock (Bühnemann, 1996).

Minivibrator

The minivibrator (Industrial Vehicle International (IVI), Tulsa, Oklahoma, USA) was used to test generation of P-waves in a horizontal direction. As part of the experiment programme, a coupling element was developed to allow horizontal coupling of the hydraulically driven vibrator element with the tunnel wall. To improve coupling conditions, the element was mounted and fixed on nine metal bolts anchored in the rock. The signal used was a 7 s long upswing of 10 to 550 Hz. Frequencies over 550 Hz cannot be generated with this source.

'Hilti'

Based on an offer made by the company 'Hilti' (FL), the bolt-firing tool DX 750 from their standard production range was included in the test measurements. The bolt-firing tool is normally used to fix rivets, nails etc. on a steel background. When used as a seismic source, the rock was stamped with a bolt accelerated by a piston.

The impact power of the bolt is generated by the firing power of the four different-strength cartridges available. The strongest variant was used in the seismic test and achieved a maximum contact force of 110 N. The triggering of the registration equipment is done by an acceleration trigger attached to the impacting bolt of the tool. Horizontal generation of the seismic signal is caused by the impact on the tunnel wall.

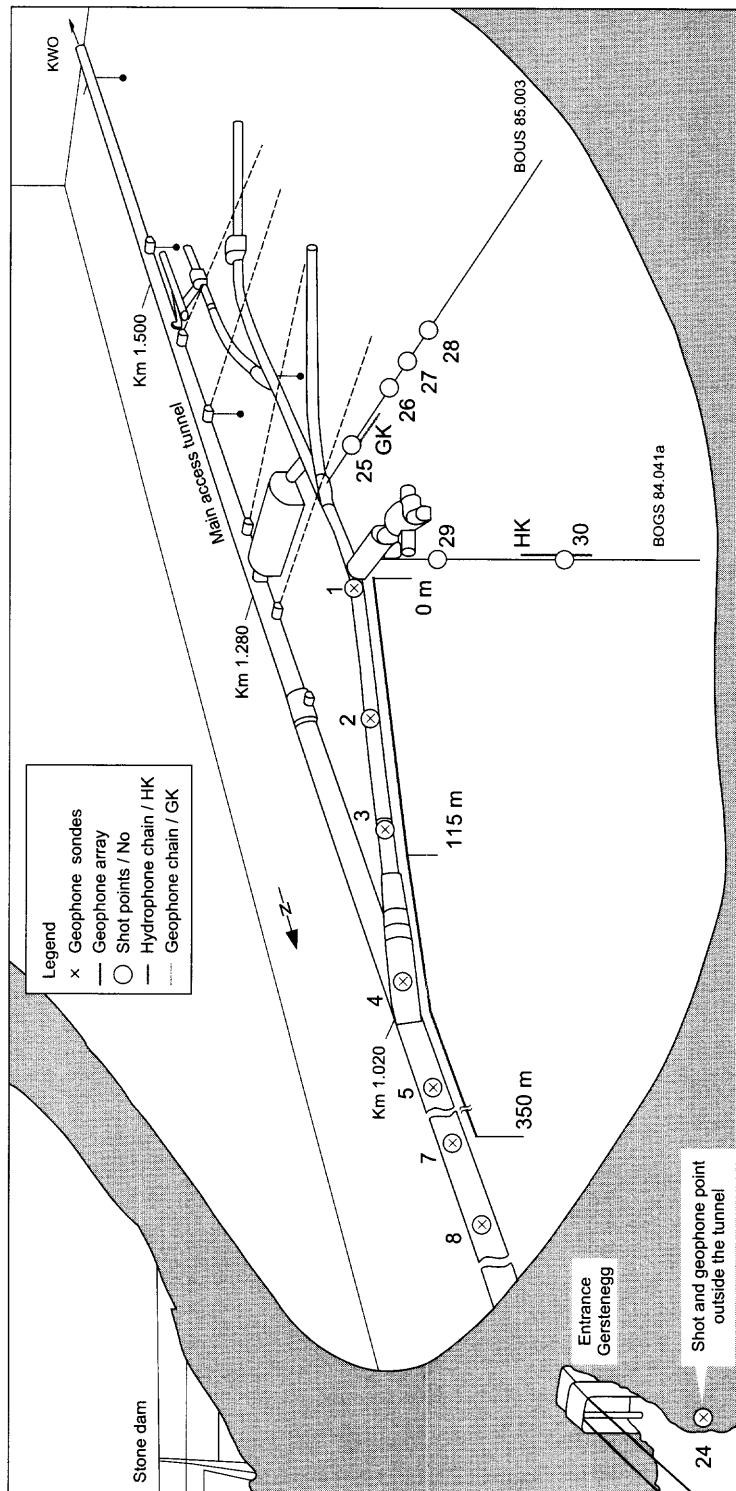


Fig. 2.1

Layout of the Grimsel Test Site showing the arrangement of the shot and geophone points used in the source test. The equipment used included two-component geophone sondes (spacing 50 m), 2 single geophone arrays (between 0 and 115 m with 5 m spacing and between 115 m and 350 m with 10 m spacing), a geophone chain (in borehole BOUS85.003) and a hydrophone chain (in borehole BOGS84.041a). The shotpoints were located every 50 m in the tunnel and in the boreholes BOUS85.003 (40, 75, 85, 95 m) and BOGS84.041a (20 and 100 m) (Bühnemann, 1996).

Tab. 2.1a: Borehole seismic sources

Source	Signal Type	Frequency Range (Hz)
Sparker	Impulse	100 - 1600
Piezo 'Valerie'	Pseudo-random impulse	150 - 600
	Sequence (Goley Code)	
LBL-Piezo	Sweep (Barker Code)	250 - 1600
Explosives	Impulse	50 - 1500

Tab. 2.1b: Tunnel seismic sources

Source	Signal Type	Frequency Range (Hz)
Weight Drop	Impulse	90 - 800
Bolt Gun	Impulse	120 - 1200
Minivibrator	Sweep	20 - 550
Buffalo Gun	Impulse	500 - 800
Explosives	Impulse	50 - 1500

2.2 Experimental set-up

Geophone array and shotpoint configuration

The source test was configured in such a way that the maximum possible shot-receiver distances could be registered using available instrumentation. Figure 2.1 shows the layout of the shot and receiver positions used in the test. Measurements were carried out in two phases.

In the first phase, various borehole sources were tested from a vertical (BOGS84.041a) and an almost horizontal (BOUS85.003, -15°) borehole with an arrangement of 96 channels. Both boreholes were completely filled with water.

48 28-Hz single component geophones were arranged along the tunnel wall. The first 24 were spaced at intervals of 5 m and the second 24 at intervals of 10 m. The spikes of the geophones were cemented into small boreholes in the rock and registered the vertical component of the ground speed.

The other 48 channels were used for recording 24 28-Hz, two-component geophones which were installed in 3 m deep small-diameter (57 mm) boreholes at intervals of 50 m along the tunnel wall. The two-component geophones are of the same type as the single geophones but are distinguished from the latter by the nature of their coupling. They were located in a casing which was pressed pneumatically onto the borehole wall. The array of the two-component geophones overlapped with that of the single component geophones for the first 350 m and then continued to the door of the

access tunnel. The last two-component geophone was thus located outside the tunnel at a distance of 1150 m from the beginning of the array. The two channels of each of these tools registered two horizontal components of ground speed parallel (in the direction of the wave propagation) and perpendicular to the tunnel wall. Placing the tools in 3 m deep boreholes was intended to eliminate any effect of the excavation disturbed zone (EDZ) on the signal.

In the second phase, seismic energy was generated at the tunnel wall and the signals were registered using a different receiver configuration (104 channels). Besides the single geophone array (48 channels) - which was the same as the first phase - a hydrophone chain (32 channels) was used in the vertical borehole (BOGS 84041a) and a geophone chain (24 channels) in the almost horizontal borehole (BOUS85003).

Signal generation at the tunnel wall with an interval of 50 m was carried out at the positions where the two-component geophones had been located in the first phase.

Data registration was performed with the 24-bit apparatus SUMMIT.

2.3 Data analysis

Figures 2.2a and 2.2b illustrate typical seismic signals generated by the seismic sources located in the vertical, water-filled borehole at 100 m depth and along the tunnel wall, respectively. In seismic data generated by the borehole sources, the direct P-wave is usually the only coherent signal. In contrast, in the seismic data generated by sources along the tunnel wall, much of the coherent seismic energy is concentrated in strong S- and tunnel or surface wave trains. The amount of coherent noise (shear, surface and air waves) generated by a variety of seismic sources has been investigated by Miller et al. (1992).

One of the primary objectives of this project was to compare the energy and frequency contents of the direct P-wave generated by the various sources as a function of offset. In order to preserve the original amplitude, phase and frequency information of the data, the only processing applied was a resampling of the data to 1/8 ms (using a standard anti-alias filter) and compensation for the geometric spreading of the wavefront. Since only the direct P-wave was of interest, and in order not to amplify noise in later parts of the data, the latter was achieved by multiplying the data with their source-receiver offsets rather than by their traveltimes.

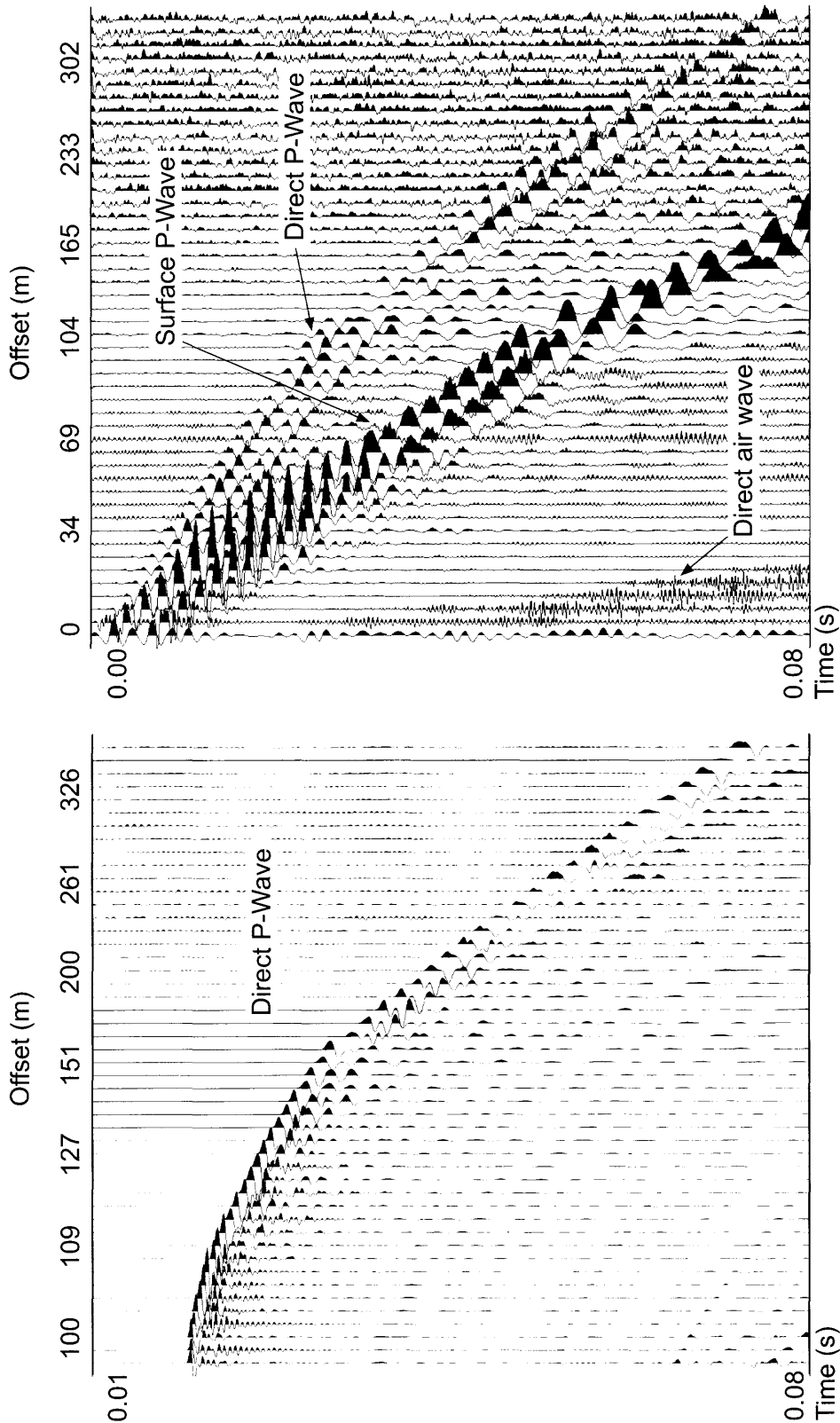


Fig. 2.2

Seismic data generated by sources located (a) in a water-filled vertical borehole at 100 m depth (10 g explosive charge) and (b) along the tunnel wall (weight drop). Both datasets were recorded by vertical-component geophones firmly fixed in shallow vertical boreholes along the tunnel wall. Note that the offset scale is not linear (see Figure 2.1).

2.3.1 Signal to noise ratio (S/N) as a function of offset

To obtain a robust estimate of the direct P-wave amplitude, the trace envelope was calculated by means of the Hilbert transform. For all traces, the maximum amplitude of the envelope was then picked in a 30 ms window including and following the direct P-wave. Variations of these amplitudes closely follow the maximum amplitudes of the first cycle of the direct P-waves. However, automatic picking of the maximum of the P-wave first cycle was determined to be more error-prone than picking the maximum of the envelope, particularly at lower S/N.

Due to technical difficulties, absolute amplitudes of source signals for borehole sources using sweeps or pseudo-random impulse sequences (piezo-sources) could not be reliably calibrated. Since ambient noise levels along the 48 vertical-component geophones (Figure 2.1) were relatively constant, the source strength in the following is mostly characterised by the S/N of the direct P-wave as a function of offset. The S/N was determined as follows: (i) pick the maximum amplitude of the envelope in the window containing and following the direct P-wave (as described above; this is assumed to

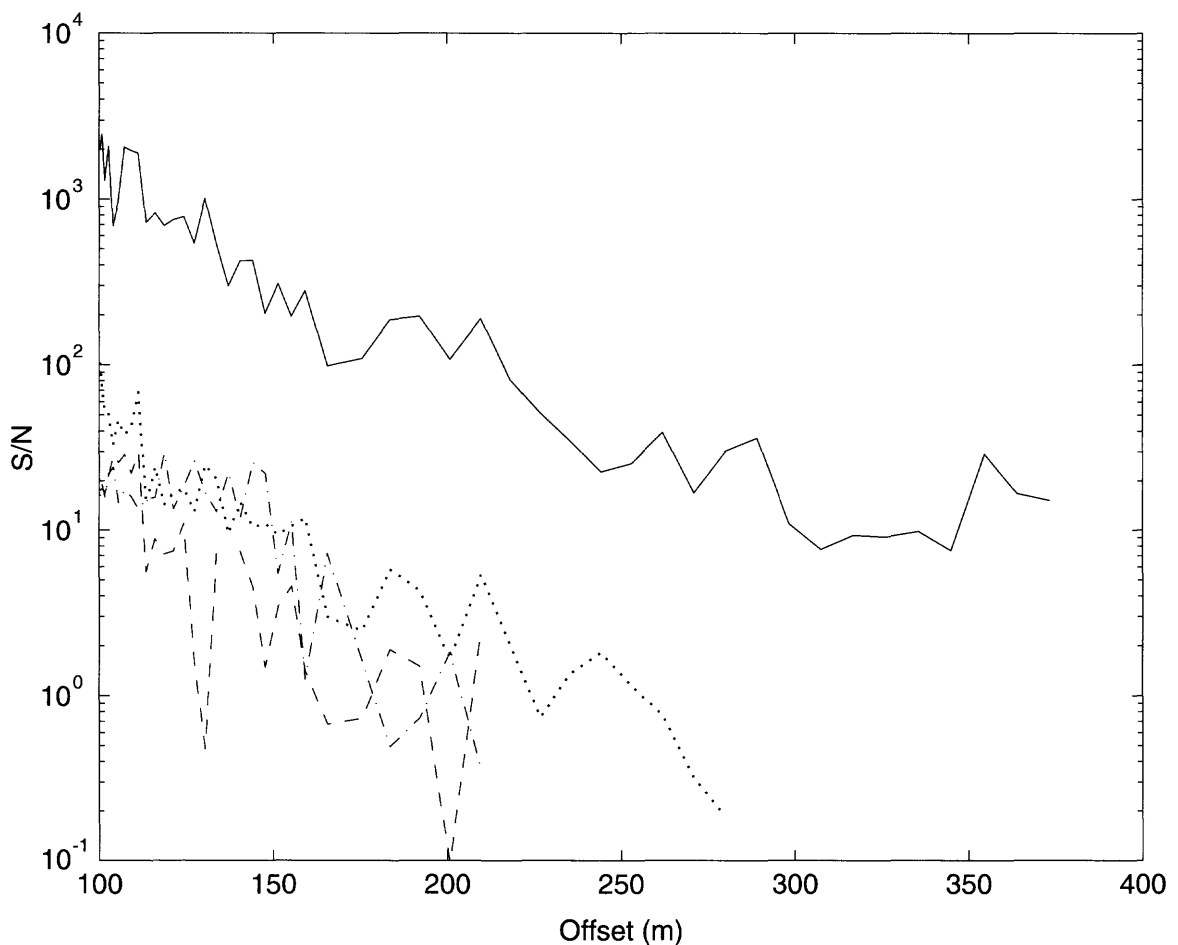


Fig. 2.3 S/N of the direct P-wave as a function of offset for seismic signals generated by borehole seismic sources registered at the single geophone line. Solid: 5 g of explosives, dotted: sparker (vertically stacked 16 times), dash-dot: piezo source "Valerie" (16 pseudo-random impulse sequences vertically stacked), dashed: LBL piezo source (16 sweeps vertically stacked).

correspond to signal plus noise); (ii) determine the average amplitude of the envelope in a 30 ms window preceding and excluding any part of the direct P-wave (this is assumed to correspond to the ambient noise present in the data).

Results for the borehole and tunnel seismic sources are illustrated in Figures 2.3, 2.4 and 2.5, respectively. An interesting result for the borehole seismic sources is that even small explosive charges (5 g) produce significantly more energetic seismic signals, as expressed by a significantly higher S/N, than the tested sparker and piezo-electric sources, even after substantial vertical stacking of the latter (Figure 2.3). Seismic signals generated by sources located along the tunnel wall show a more uniform and generally significantly lower S/N-versus-offset behaviour than the borehole sources. Although less pronounced than in the case of the borehole sources, the 5 g explosive charges detonated in a largely dry, shallow (<3 m) borehole again has the highest S/N, and thus the most favourable energy release, of all tunnel seismic sources considered (Figure 2.5).

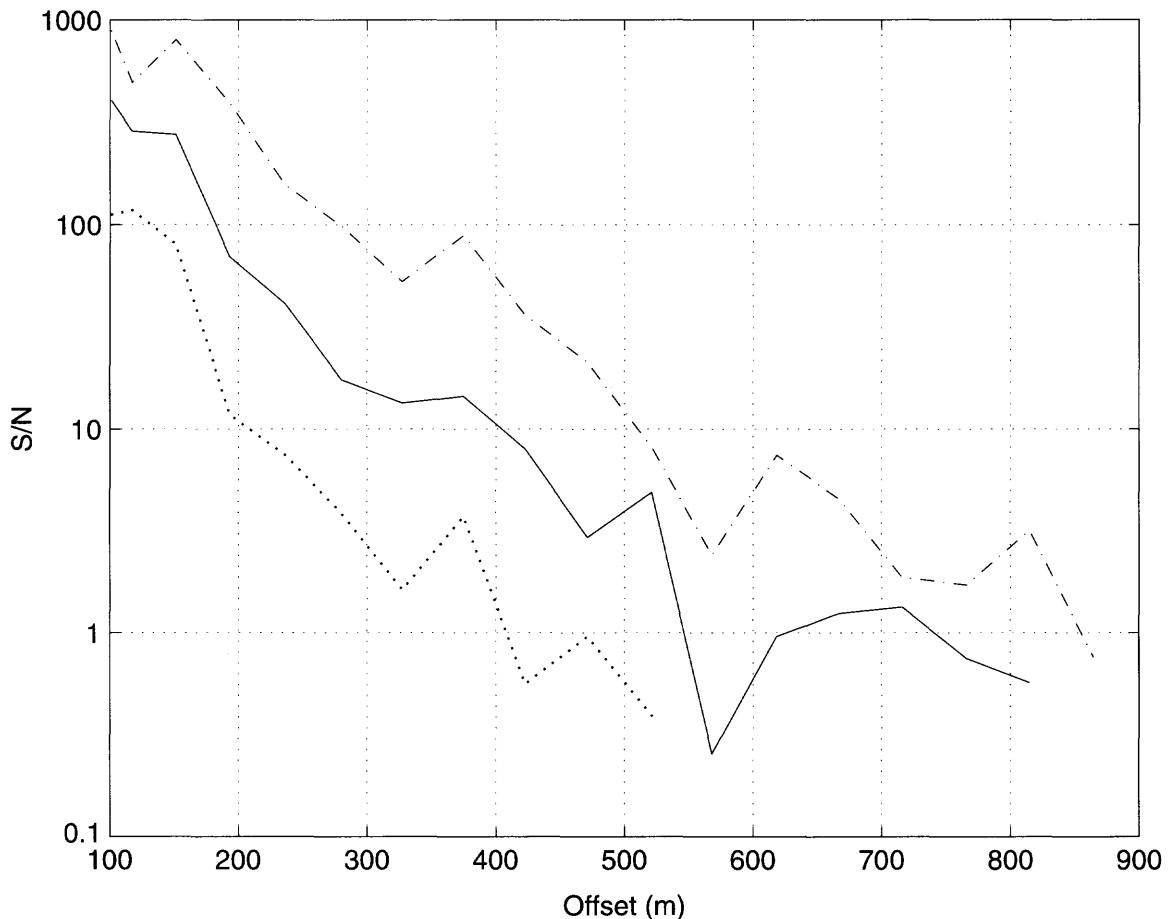


Fig. 2.4 S/N of the direct P-wave as a function of offset for seismic signals generated by borehole seismic sources registered at the two-component geophone sondes. Dash-dot: 50 g of explosives, solid: 5 g of explosives, dotted: 1 g of explosives.

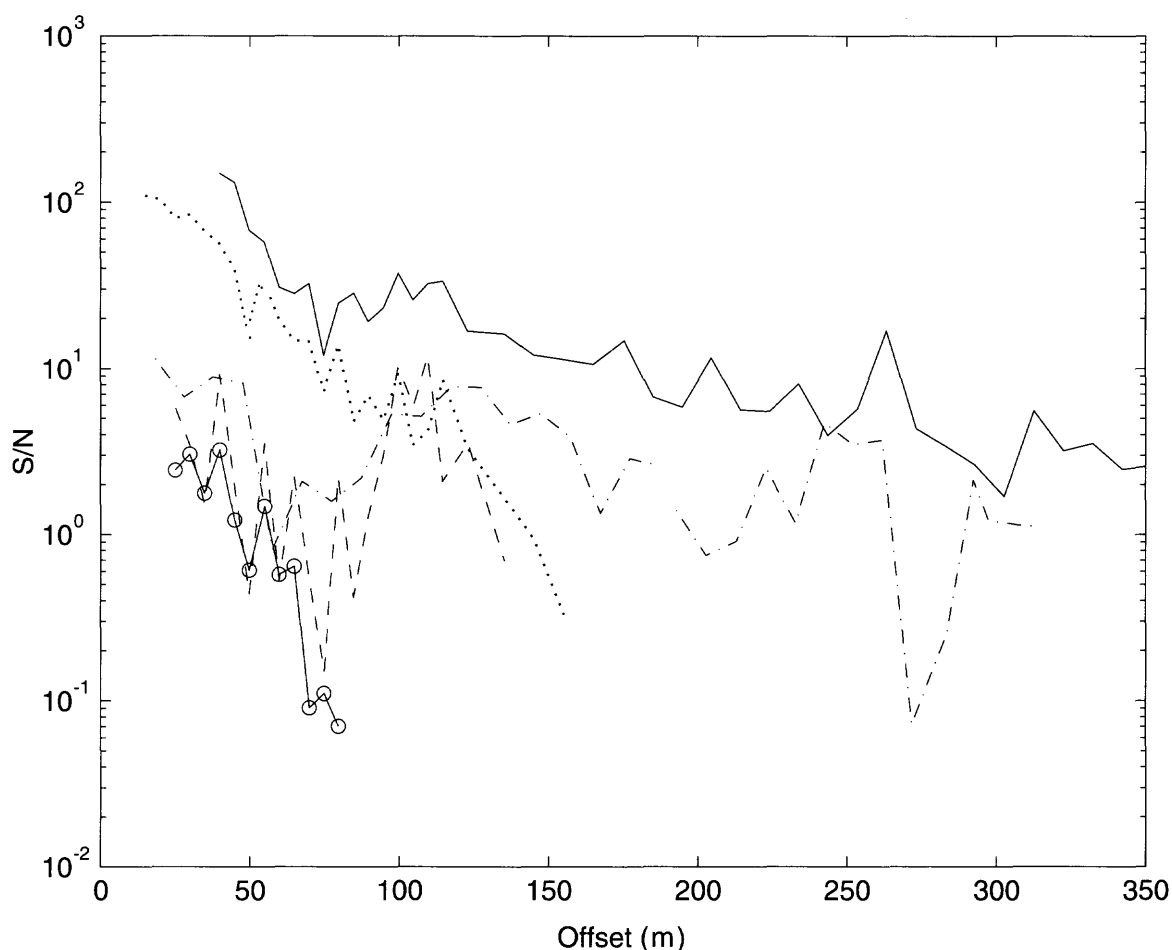


Fig. 2.5 S/N of the direct P-wave as a function of offset for seismic signals generated by seismic sources located along the tunnel wall. Solid: 5 g of explosives, dotted: buffalo gun, dash-dot: minivibrator, dashed: weight drop, open circles: bolt gun. No S/N estimates are available at near offsets because the direct P-wave could not be separated from the shear and tunnel/surface wave trains.

2.3.2 Seismic amplitude as function of explosive charge size

Based on the results presented above (Figures 2.3 - 2.5), it is concluded that small explosive charges, even when detonated in dry, shallow and poorly tamped boreholes, have superior energy characteristics to the other sources considered in this study. Of course, there are problems with using explosives as a seismic source. In particular, for radioactive waste disposal site exploration, it may be prudent to keep the charge size as small as possible in order to reduce the risk of fracturing the rock (Chapter 2.5). This implies that the individual seismic source signals should have a high degree of predictability and repeatability in order to allow accurate assessment of the charge size and/or vertical stacking that is required. In the following, a closer look will be taken at the predictability and repeatability of seismic amplitudes generated by explosive charges of various sizes.

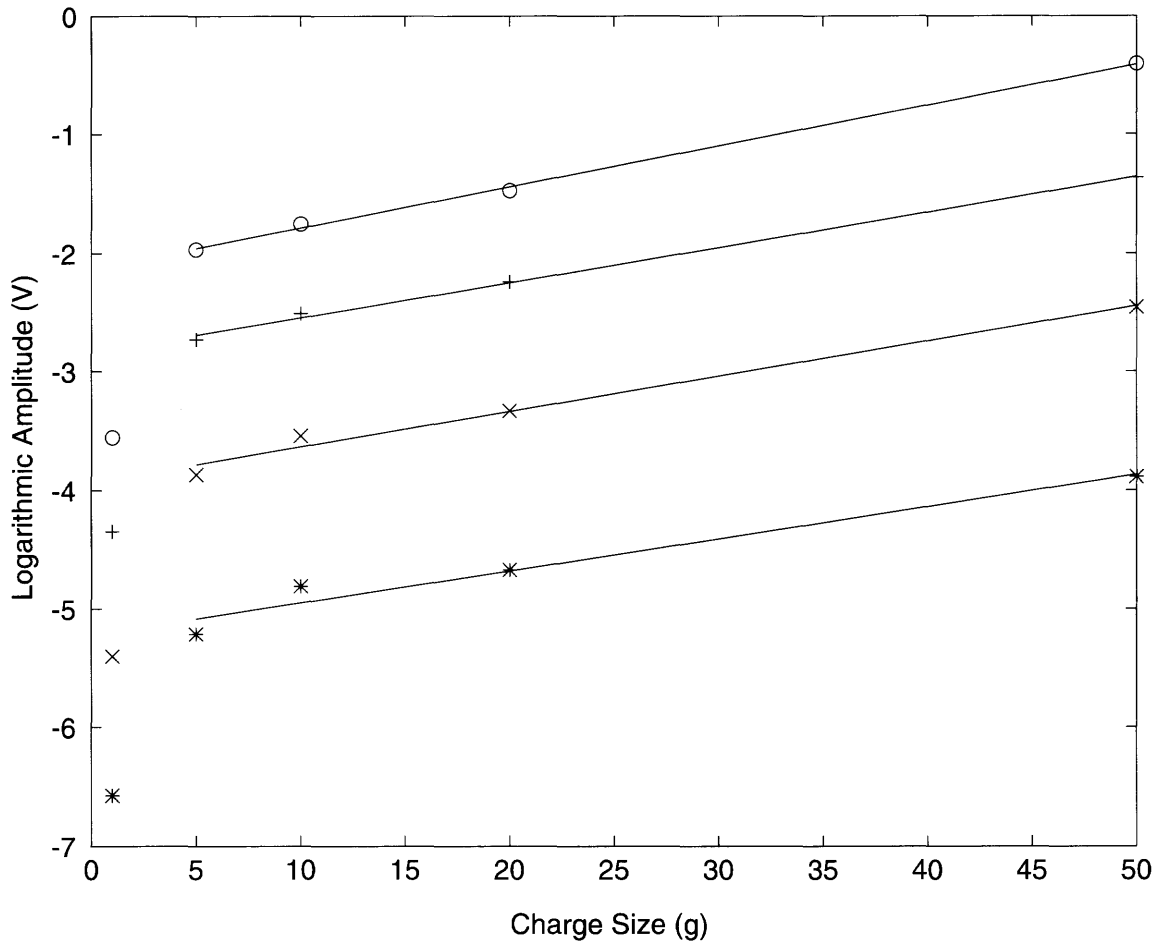


Fig. 2.6 Natural logarithm of the direct P-wave amplitudes generated by explosives set off in a water-filled vertical borehole at 100 m depth as a function of charge size and offset. The 1 g charge simply corresponds to the explosive cap and thus to a much faster burning type of explosive than the other charges. Open circles: 100 m offset, plus signs: 120 m offset, x-marks: 160 m offset; stars: 240 m offset; solid line: linear best-fits (excluding 1 g charge size) with slopes between 0.028 and 0.033.

At a given distance, the amplitude A of the seismic signal resulting from an explosives impulse source of mass m is expected to be given by (e.g. Thoenen & Windes, 1942):

$$\log A(m) = c_2 m + \log c_1, \quad (2.1)$$

where c_1 and c_2 are constants depending on the site conditions and the type of explosives used. In Figure 2.6 the natural logarithm of the direct P-wave amplitude is plotted as a function of the explosive charge size. All sources were located in the water-filled, vertical borehole at 100 m depth. The various symbols denote fixed source-receiver offsets at which amplitude measurements were taken. Evidently, the linear relationship in semi-logarithmic space predicted by equation (2.1) is fulfilled by these observations. The only systematic deviations are the seismic amplitudes generated by the 1 g charges, i.e. the explosive caps, which consisted of a different, much faster burning

type of explosives than the standard gelatine-type explosives used for the other charges. These results indicate that seismic amplitudes generated by small explosive charges at the GTS seem to have a relatively high degree of predictability and repeatability.

2.3.3 Dominant frequency as a function of offset

Approximate source frequency ranges of the seismic signals generated by the tested sources are given in Table 2.1. The change in frequency content of the direct P-wave as a function of offset was quantified by calculating the Fourier transform of the data contained in a 30 ms window including and following the first arrival. Figure 2.7 illustrates the changing frequency content with offset of the seismic data and Figures 2.8 and 2.9 show the dominant frequency (i.e. the frequency with the highest spectral amplitude) as a function of offset for the different sources.

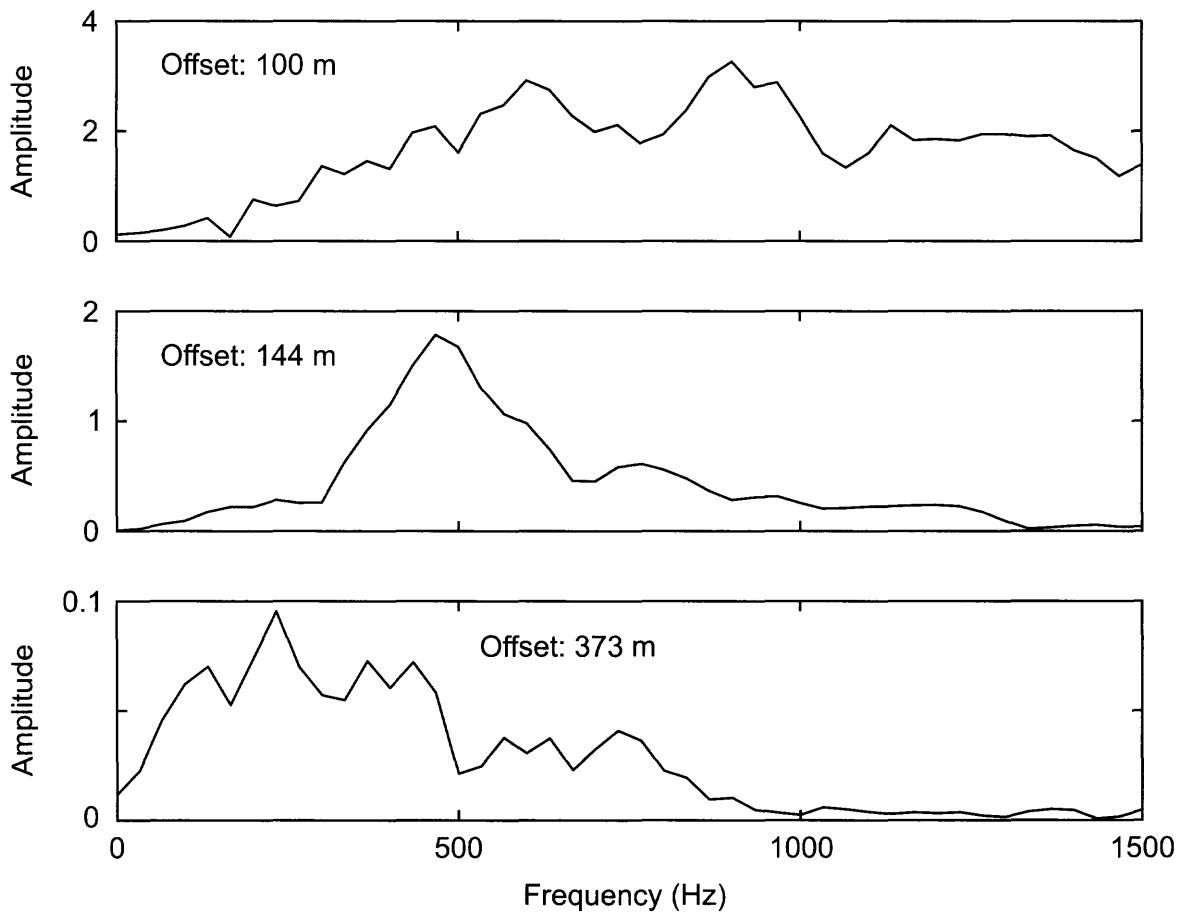


Fig. 2.7 Amplitude spectra of a 20 g explosive charge calculated for a 30 ms window around the first arrival at source-receiver offsets of a) 100 m, b) 144 m and c) 373 m. Note the varying scales of the amplitude axis and the rapid decrease of high-frequency amplitudes with propagation distance.

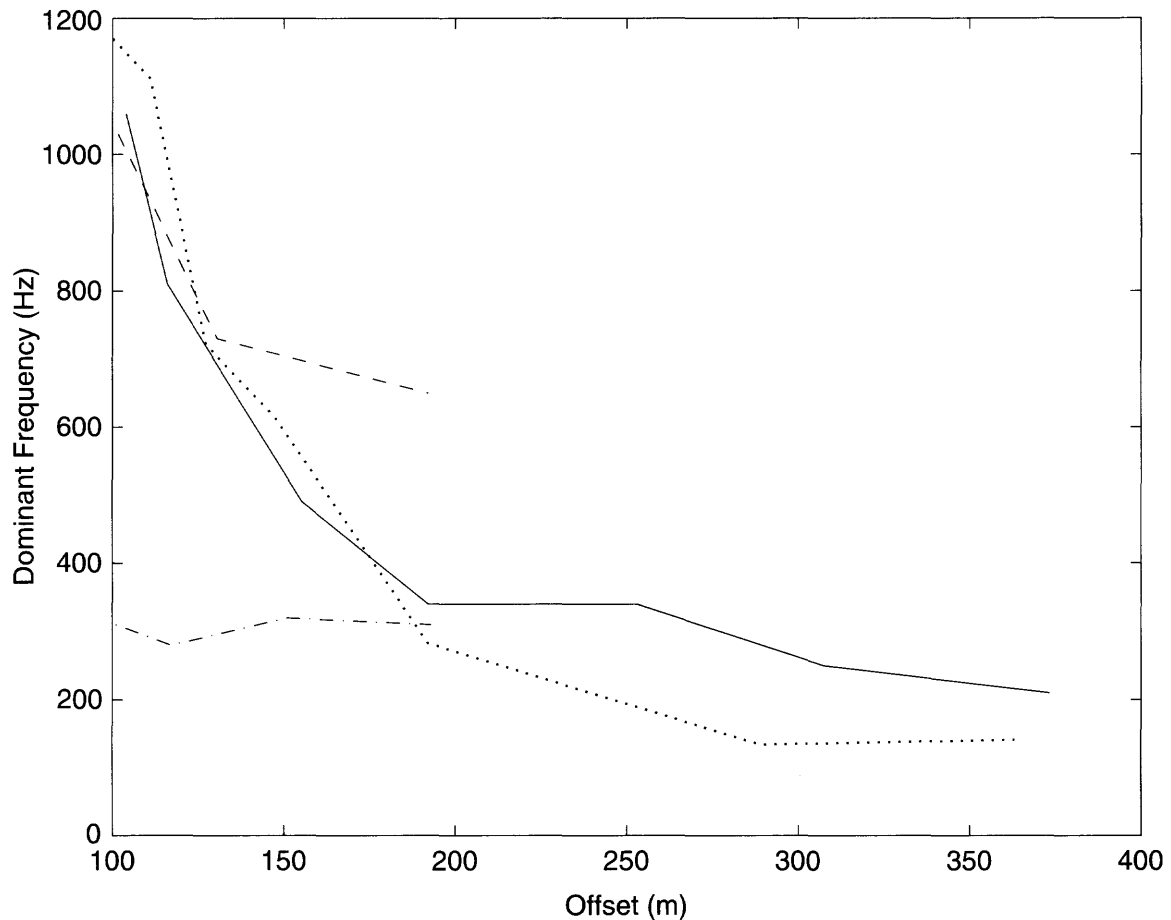


Fig. 2.8 Dominant frequency of the direct P-wave as a function of offset for seismic signals generated by borehole sources. Solid: 5 g of explosives, dotted: sparker (16 sparks vertically stacked), dash-dot: piezo-source "Valerie" (16 pseudo-random impulse sequences vertically stacked), dashed: LBL piezo-source (16 sweeps vertically stacked).

Seismic signals from the borehole sources are characterised by relatively uniform dominant frequency ranges of around 1000 to 1200 Hz at the top of the borehole (i.e. about 102 m from the source). One exception is the piezo-source "Valerie", for which the dominant source frequency is only about 300 Hz (Figure 2.8). The source signal was chosen to contain maximum frequencies up to about 600 Hz. This low frequency source signal was selected after preliminary testing showed extremely poor signal penetration for higher frequency source signals. Due to their low energy release, no data are available for the "Valerie" and LBL piezo-sources beyond offsets of some 200 m. For the sparker and explosive sources, the dominant frequency decays from about 1000 Hz at 100 m source-receiver offset to 100 to 200 Hz at 350 m offset (Fig. 2.8).

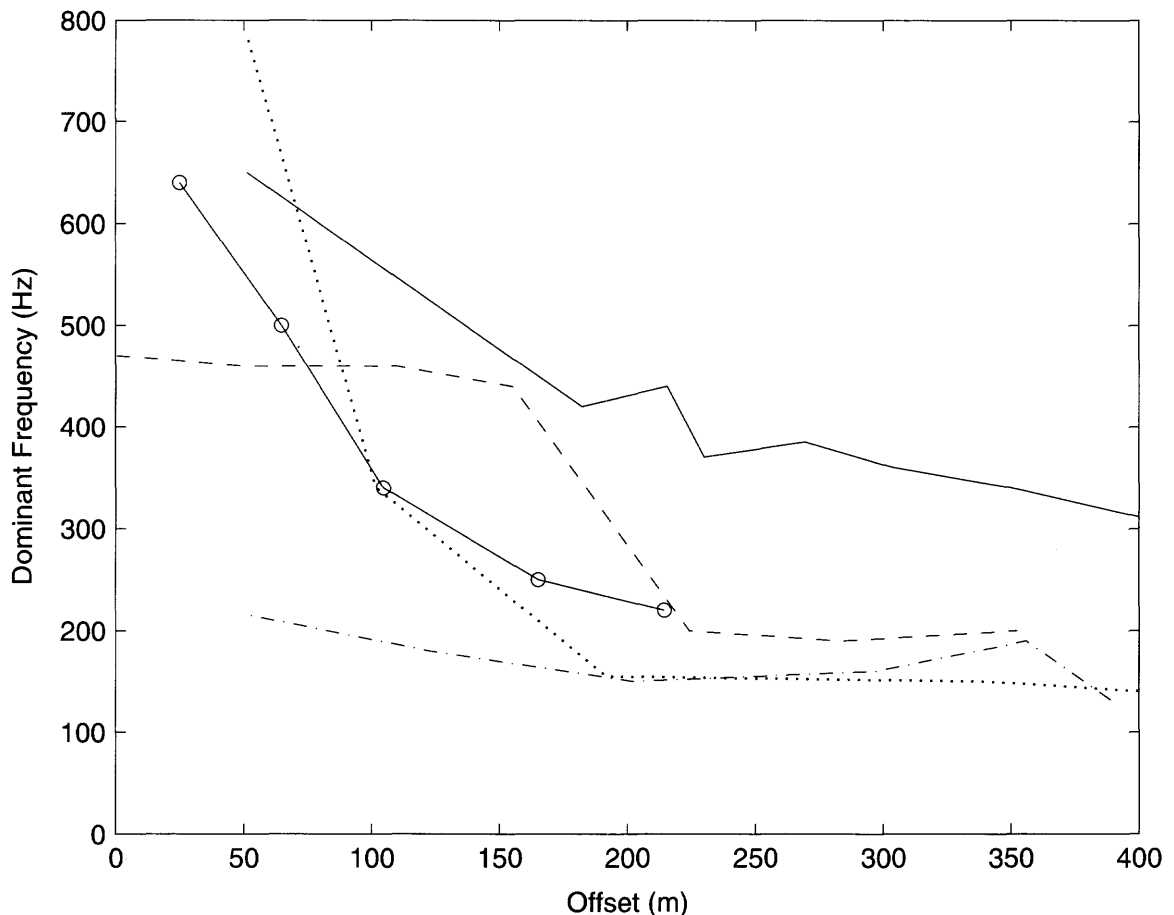


Fig. 2.9 Dominant frequency of the direct P-wave as a function of offset for seismic signals generated by sources located along the tunnel wall. Solid: 5 g of explosives, dotted: buffalo gun, dash-dot: minivibrator, dashed: weight drop, open circles: bolt gun. No frequency estimates are available at near offsets because the direct P-wave could not be separated from the shear and tunnel/surface wave trains.

Compared to the borehole sources, dominant frequencies at near offsets are more variable for the seismic sources located along the tunnel wall (Figure 2.9). They range from only about 200 Hz for the minivibrator to about 800 Hz for the modified buffalo gun. Seismic signals generated by the buffalo gun display similar frequency-versus-offset behaviour to those generated by small (5-20 g) explosive charges. As in the case of the borehole sources, the dominant frequencies of most tunnel wall seismic sources were reduced to about 300 Hz at offsets of around 400 m (Fig. 2.9).

2.3.4 Maximum offset reached

Some of the pertinent results of this study are summarised in Figures 2.10 and 2.11. Figure 2.11 shows the far offsets of a seismic signal generated by a 100 g explosive charge in a shallow, sub-horizontal borehole and Figure 2.10 illustrates, for various sources, the maximum offset at which a direct P-wave could be detected as well as the dominant frequency of this event.

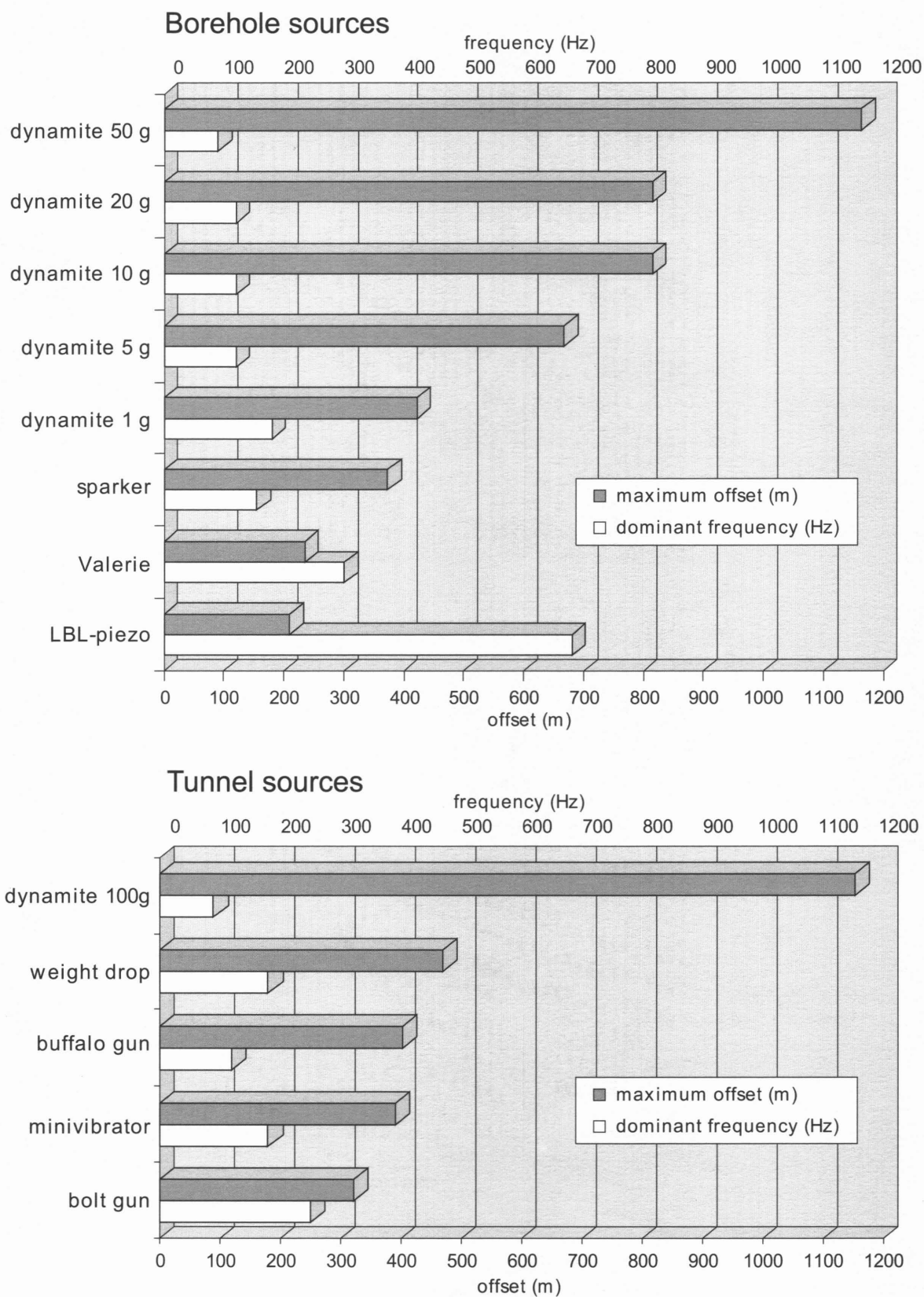


Fig. 2.10 Comparison of the maximum source-receiver offset at which the direct P-wave could be detected together with the dominant frequency of this part of the signal at these offsets.

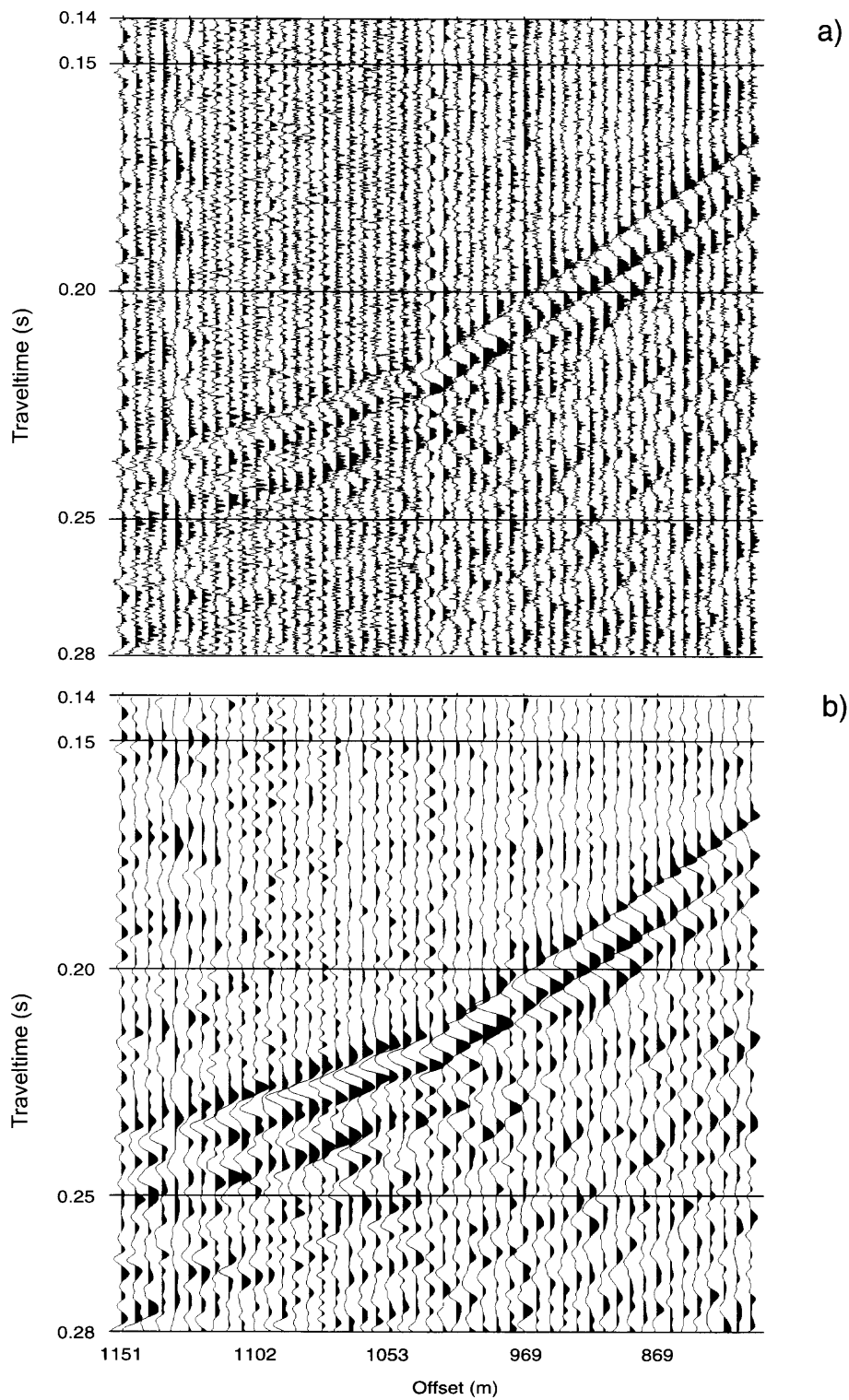


Fig. 2.11 Far offset seismic signals generated by a 100 g explosive charge a) before and b) after applying a 50 - 300 Hz bandpass filter. The explosive charge was located at shot position 24 (s. Fig. 2.1) in a short (3 m), sub-horizontal borehole.

The target distance of 1000 m was only reached by explosive charges of about 50 g or more (Figure 2.11). However, none of the sources tested managed to produce signals that sustained frequencies of the order of 1000 Hz over distances in excess of some 200 m. We found that small explosive charges (5-100 g) provided the best signal penetration, albeit at much lower frequencies than desired. The results presented here are based on analyses of essentially raw and bandpass filtered seismic data. Testing indicates that enhancing the high-frequency component of the data by signal processing does not significantly affect the general conclusions (Bühnemann, 1996). Furthermore, such processing could lead to distortions of the original phase and amplitude information. This could jeopardise subsequent tomographic investigations and thus defeat an important objective of this project.

The rapid depletion of high frequencies with distance for all sources is indicative of high attenuation for granite at the GTS. The attenuation will be calculated in Chapter 2.4.

2.4 Attenuation of seismic waves in the Grimsel Granite

Seismic waves travelling through the earth are attenuated due to scattering and various inelastic mechanisms (e.g. Bourbié et al., 1987). In a homogeneous medium, the attenuation of acoustic waves may be quantified as:

$$A(f, x_i) = A_0(f, x_{0i}) \exp\left[\frac{-\pi f (x_i - x_{0i})}{Q(f) \cdot v(f)}\right], \quad (2.2)$$

where f is the frequency, $Q(f)$ is the quality factor, $v(f)$ the velocity, and $A_0(f, x_{0i})$ and $A(f, x_i)$ the amplitude spectra at the locations x_{0i} and x_i ($i = 1, 2, 3$), respectively. $Q(f)$ corresponds to the number of cycles or wavelengths experienced by a harmonic wave of frequency f before its amplitude has decayed to $e^{-\pi}$, or about 4%, of its original value. The distribution of Q values within the earth thus determines how far seismic waves can propagate before their amplitudes drop below the noise level and is a measure of how their frequency content changes along the propagation path.

For problems relevant to environmental and engineering geophysics, it is usually desirable to achieve the highest resolution possible, and hence to use the highest seismic frequencies possible. Given the strong damping of high frequencies described by equation (2.2), approximate knowledge of the range of Q values expected in any target area is critical in the planning stage of a seismic experiment.

2.4.1 Estimation of Q from seismic data

The primary effect of attenuation described by equation (2.2) is that of a low-pass filter. Resulting systematic changes of both amplitude and shape of the propagating seismic signal are the basis for estimating Q values from observed seismic data. Common to most methods is the assumption that Q is independent of frequency (Tonn, 1989). In the following we shall estimate Q based on this assumption using the so-called spectral ratio method (e.g. Tarif & Bourbié, 1987). Taking the natural logarithm of a slightly modified version of equation (2.2) yields:

$$\ln\left(\frac{A(f, x_i)}{A_0(f, x_{0i})}\right) = -\frac{\pi(t-t_0)}{Q} \cdot f, \quad (2.3)$$

$$= b \cdot f$$

where $t-t_0 = (x_i - x_{0i})/v$ is the travelt ime of the seismic waves between locations x_{0i} and x_i for a constant velocity v . The assumption $v(f) = v = \text{constant}$ is generally considered to be appropriate for $Q \gg 1$. Q can thus be determined by calculating the amplitude spectra of the wavefield at two different source-receiver offsets, plotting the logarithmic ratio of the spectra as a function of frequency f , and estimating the slope b . Although the various methods for estimating Q from seismic data perform similarly for reasonable signal-to-noise ratios (S/N) (Tonn, 1989), the spectral ratio method has certain practical features: (1) errors in amplitude scaling, for example due to poorly constrained geometrical spreading corrections, only shift the data up or down with respect to the $y = \ln(A(f, x_i)/A_0(f, x_{0i}))$ -axis, but leave the slope b , and thus Q , unaffected; (2) by using a standard least-squares approach to estimate a best-fitting line through the data points, one also obtains a formal estimate of the error of the slope b and thus of Q (e.g. Taylor, 1982; White, 1992).

From equation (2.3) it is clear that the accuracy with which the slope b , and thus Q , can be determined depends on the bandwidth and S/N of the seismic data. The limited two to three octave bandwidth of most surface and borehole seismic data may restrict the accuracy of Q estimates to around 30 to 50% (White, 1992). The influence of S/N on the accuracy of Q is known to be similarly significant, but is harder to quantify (Bourbié et al., 1987; Tonn, 1989). Based on our tests, we judge that Q measurements on data with $S/N < 5$ are meaningless. Estimating Q within an acceptable error margin, say around 30% or less, thus requires seismic data that have overall high to very high S/N and broad frequency content. It is because of these restrictive a priori conditions that meaningful Q estimates in general, and for shallow crystalline rocks in particular, are relatively scarce.

2.4.2 Q values of the Grimsel Granite

Of the sources tested, explosives were found to have the best S/N and to generate the broadest and most uniform frequency spectrum, ranging from less than 50 to more than 1500 Hz near the source. For the 10 g explosive charge (Figure 2.2a) detonated in a 100 m deep vertical borehole, S/N ranged from about 4000 at the closest receiver (~100 m source-receiver offset) to less than 1 (Figure 2.4). The Q estimates presented here are based mainly on the data generated by explosive charges. For these data all receivers are located outside the near-field (minimum offset: 100 m; dominant wavelength: ~5 to 10 m) and hence damping effects are unlikely to depend on the strain amplitudes (e.g. Johnston et al., 1979).

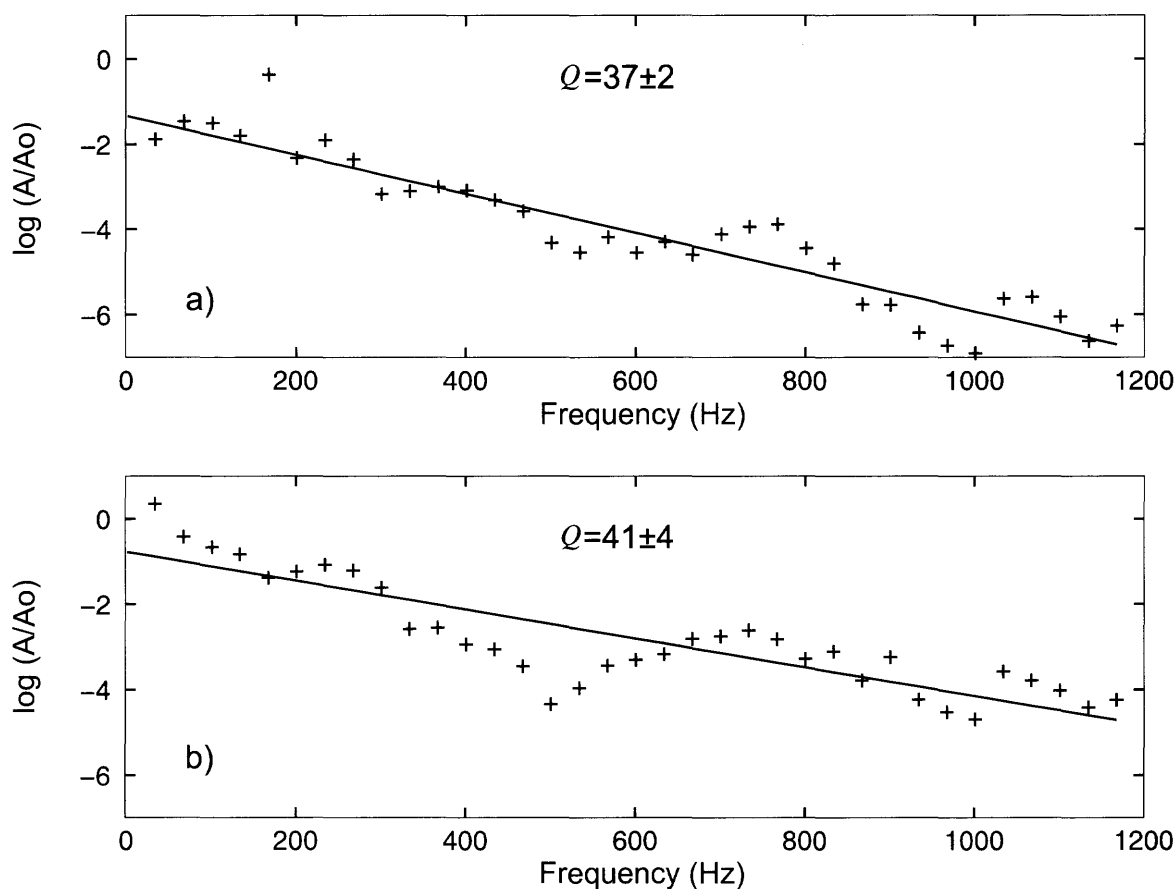


Fig. 2.12 Q values and their standard errors estimated from amplitude spectra shown in Figure 2.7 by means of the spectral ratio method. Crosses: logarithmic ratio of observed amplitude spectra of a) 100 and 144 m (Figures 2.7a and 2.7b) and b) 144 and 373 m (Figures 2.7b and 2.7c) offsets; solid lines: least-squares estimate of the corresponding linear slopes. Standard errors are based on a least-squares error analysis of the slopes. Frequencies above 1200 Hz are rapidly attenuated below the ambient noise level and therefore were excluded from the analyses.

Q values estimated from the data by means of the spectral ratio and conventional least-squares methods described above are listed in Table 2.2 (Bühnemann, 1996). Spectra were calculated at various shot-receiver offsets in a 20-30 ms window following the first arrival. The chosen window length results in a 33 to 50 Hz sampling interval in the frequency domain. Frequency spectra of data recorded from the 20 g explosive source at different source-receiver offsets illustrate well the rapid decay of high frequencies with propagation distance (Figure 2.7). Figure 2.12 shows logarithmic spectral ratios as functions of frequency for various offset ranges as well as their best-fitting slope, in a least-squares sense. Q -estimates from the entire dataset range from ~ 15 to 150 (with a median value of 37) and the standard errors from about 5 to 50 % (Table 2.2). Limiting the acceptable standard error to 20 % (White, 1992) yields Q values between ~ 20 and 60 (with a median value of 35), which we consider to be representative of the experimental site.

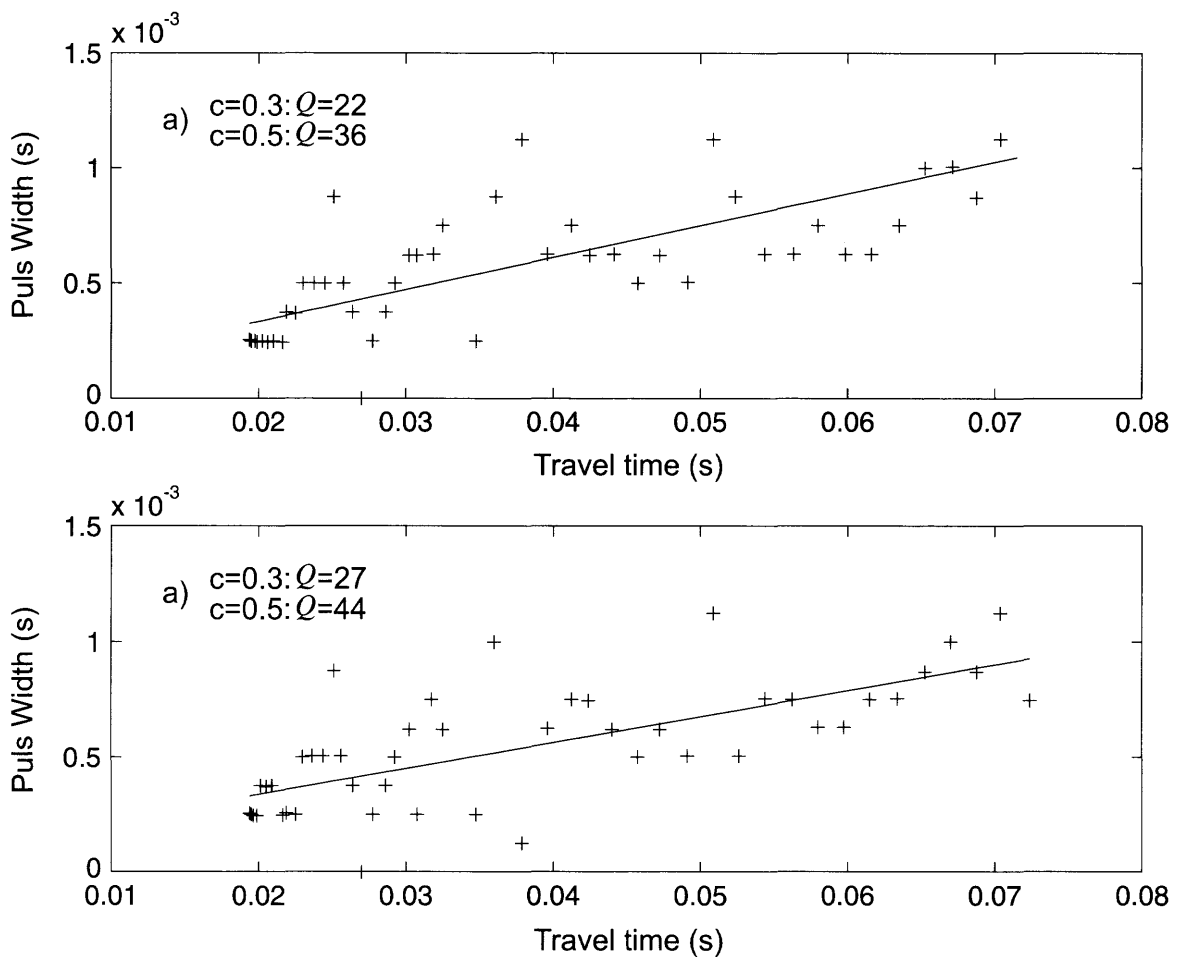


Fig. 2.13 Pulse width as a function of travelttime for seismic pulses generated by a) 50 g and b) 20 g explosive charges. Crosses: observed pulse widths defined by the first zero-crossing and the first maximum of the direct P-wave. Solid: linear least-squares best-fit. Corresponding estimates of Q range from about 20 to 40 (with an estimated standard error of about 10%) depending on the value of the proportionality constant c .

Both Q and its standard error seem to increase systematically with offset (Table 2.2), which could be indicative either of a frequency dependence or significant lateral variations of Q . However, estimating Q for various narrow frequency bands at near offsets did not corroborate this speculation, but rather suggested that systematic increases in Q and its standard error could be caused by decreasing S/N with offset. If the spectral ratio is severely contaminated with noise, this will systematically increase the estimate of Q (spectral-ratio Q is infinite for white noise spectra). Although the overall S/N may still be sufficiently high at far offsets, the higher frequencies may be attenuated below the ambient noise levels. Progressively excluding higher frequencies at larger offsets from the analysis reduces Q and, more importantly, brings the standard errors to values comparable to those measured closest to the source (Table 2.2).

Tab. 2.2 Q values calculated using the spectral ratio method and their standard errors for various sizes of explosive charge, offset ranges, S/N ratios and frequency ranges. Q values with standard errors < 20 are given in bold print.

Offset (m) / S/N ratio	Offset (m) / S/N ratio	Frequency (Hz)	Q	Standard error (%)
Explosives 20 g				
100 / 4000	373 / 15	30 - 1500	43	6
100 / 4000	373 / 15	30 - 800	39	12
100 / 4000	373 / 15	30 - 1200	37	6
103 / 4000	373 / 15	30 - 1500	47	9
103 / 4000	373 / 15	30 - 1100	33	7
100 / 4000	144 / 550	30 - 1500	17	13
100 / 4000	144 / 550	30 - 1100	27	33
100 / 4000	147 / 500	30 - 1500	19	14
100 / 4000	209 / 200	30 - 1500	23	10
100 / 4000	209 / 200	30 - 1200	35	15
144 / 550	373 / 15	30 - 1500	66	16
144 / 550	373 / 15	30 - 1000	41	9
209 / 200	373 / 15	30 - 1500	122	45
209 / 200	373 / 15	30 - 800	53	25
209 / 200	373 / 15	30 - 1000	39	15
218 / 150	373 / 15	30 - 1500	155	50
218 / 150	373 / 15	30 - 500	30	22
Explosives 50 g				
100 / 8000	373 / 50	30 - 1500	39	6
100 / 8000	144 / 2000	30 - 1500	14	12
100 / 8000	144 / 2000	30 - 1300	23	18
100 / 8000	209 / 500	30 - 1500	29	9
100 / 8000	209 / 500	30 - 1200	52	15
144 / 2000	373 / 50	30 - 1500	66	15
144 / 2000	373 / 50	30 - 900	42	17
209 / 500	373 / 50	30 - 1500	88	36
209 / 500	373 / 50	30 - 1200	33	13
218 / 500	373 / 50	30 - 1500	162	51
218 / 500	373 / 50	30 - 1200	63	25
218 / 500	373 / 50	30 - 500	51	32

For comparison we have also applied a slightly modified version of the so-called rise time method of estimating Q to the data recorded from the 20 and 50 g explosive charges. A comprehensive comparison of the spectral ratio and rise time methods is given in Tarif and Bourbié (1987). The rise time method is based on the observation that the low-pass filtering effect of a medium causes the width τ of the seismic pulse to broaden with traveltime t as:

$$\tau(t) = \tau_0 + \frac{c}{Q} \cdot t. \quad (2.4)$$

The constant c ranges from about 0.3 to 0.5, depending on the source and receiver characteristics (Blair & Spathis, 1982). The pulse width was defined as the interval between the onset and the first maximum of the initial P-wave arrival. Using this approach on the 20 g explosive data we obtained Q values between 27 ($c = 0.3$) and 44 ($c = 0.5$); for the 50 g explosive data estimated Q values range from 22 ($c = 0.3$) to 36 ($c = 0.5$) (Figure 2.13). For all estimates the standard error is of the order of 10%. These Q values and their errors are entirely consistent with the results obtained using the spectral ratio method.

We have studied the attenuation of high-quality ($S/N \gg 1$), broad-band (50 - 1500 Hz) seismic data acquired inside a largely intact granite body using the spectral ratio and rise time methods and assuming frequency independence of Q . Our results indicate that Q values of 20 to 60 (with a median value of 35) are representative of the sampled rock mass. For this range of values, standard error estimates based on linear least-squares analyses are 20% or less. Even if the effective uncertainty is greater, it is still low compared to Q estimates from conventional seismic data. We attribute the low uncertainty of the Q estimates to the unusually broad bandwidth and good quality of our data. The Q values obtained are comparable with other estimates from seismic data in near-surface crystalline rocks (Juhlin, 1990, 1995; Li, 1995) and in clay-rich sediments (Schön, 1996; Tonn, 1989). In the investigation areas Zürcher Weinland (Opalinus Clay) and Wellenberg (marl) a similar attenuation is therefore expected. In the crystalline basement of Northern Switzerland, the attenuation should be lower and the propagation characteristics of the seismic waves should be correspondingly better.

2.5 Analysis of the damage caused by explosive charges

In order to determine the damage caused to borehole walls in granite as a result of using explosives as a seismic source, televiwer data registered before and after blasting in borehole BOGS84.041a (1985, July and November 1986) were analysed. Prior to the source test in August 1995, the borehole had already been surveyed in 1985 using a televiwer (Pahl et al., 1989; Albert, 1997). Following the source test, the borehole was surveyed a second time in July 1996. As the shotpoint (100 m) was located on a fault zone, explosives were used again in November 1996 and the borehole surveyed a third time.

2.5.1 Comparison of televiwer measurements from 1985 and July 1996

For the blasting during the source test in August 1995 (shotpoint at 100 m), the televiwer measurement of 1985 is available as a pre-blasting record and the measurement of July 1996 as a post-blasting record (Pahl et al., 1989).

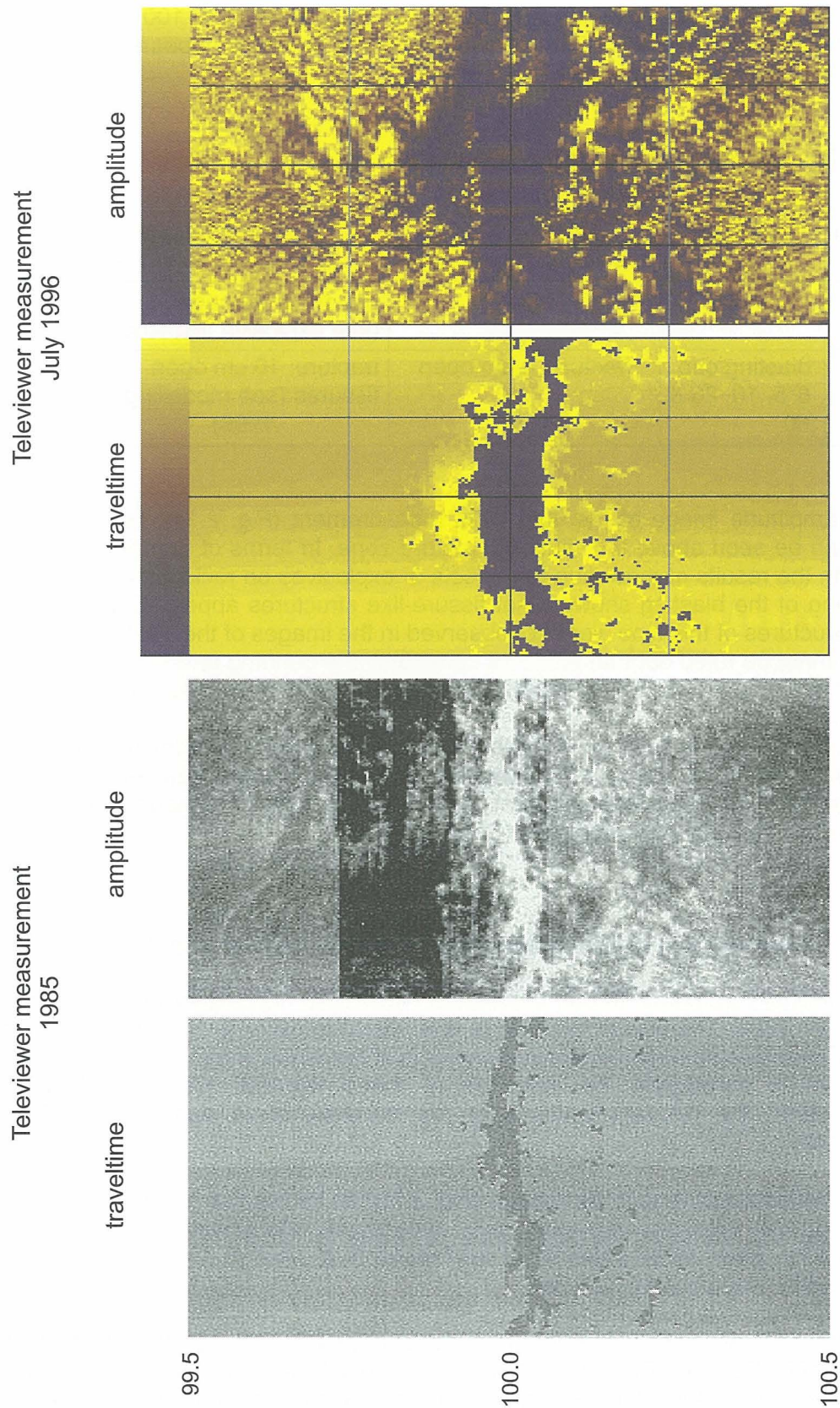


Fig. 2.14

Comparison of traveltime and amplitude images for the televiewer measurements of 1985 (Pahl et al., 1989) and July 1996 (Albert, 1997) in the depth interval 99.4 - 100.5 m.

It is clear in both measurements that there is an open fracture at 100 m (Fig. 2.14). In the traveltimes image of the 1985 measurement, the structure appears to be narrower than in the later measurements.

Tab. 2.3: Use of explosives in the source test

Depth (m)	Charge (g)	Observations televiewer survey 1985	Observations televiewer survey July 1996
20	5	-----	pattern of damage (see explosive test Nov 1996)
100	blasting cap, 6*5, 10, 20 & 50	fracture: 4 cm open	fracture: 10 cm open fissures (see modelling: Song & Kim, 1996)

In the amplitude image of the July 1996 measurement (Fig. 2.14), fissure-like structures can be seen above the widened fracture zone. In terms of form they correspond well with the results of modelling the effects of explosives on rock (Song & Kim, 1996). Modelling of the blasting showed that fissure-like structures appeared at the borehole wall. Structures of this type were not observed in the images of the 1985 measurement, but it cannot be ruled out that artefacts caused by the centring and the lower resolution of the 1985 measurement prevented such structures from being recognised.

Televiewer data from 1996 are available for the shotpoint at 20 m (only 5 g). The borehole section 0 - 37 m was cased during the 1985 measurement (Pahl et al., 1989). The images of the July 1996 measurement show a clear pattern of damage, which was also the case for the later explosives test (Chapter 2.5.2).

2.5.2 Comparison of televiewer measurements from July and November 1996

To obtain more detailed information, 14 explosive charges were detonated on 13th November 1996. The size of the charge was varied in order to determine the dependence of potential damage on this parameter and the shots were positioned on various structures to investigate the influence of these features. On the following day (14.11.1996), the relevant sections of the borehole were again scanned with a televiewer.

If the traveltimes and amplitude images (Fig. 2.15/16) for the two measurements of July and November 1996 are compared, clear shot-related alterations can be seen at most shot depths. Even small amounts of explosives (e.g. shot at 116.2 m with 5 g) produced easily recognisable damage.

However, shot positions with large amounts of explosives do not always show clearly recognisable damage. For example, 50 g of explosives were used at 96 m and the traveltimes do not show any damage. Nor in this case do the amplitudes - only a small decrease in amplitude can be recognised in the image at 96.1 m 180°. However, small amplitude changes of this type can also be found at other depths away from the shot positions.

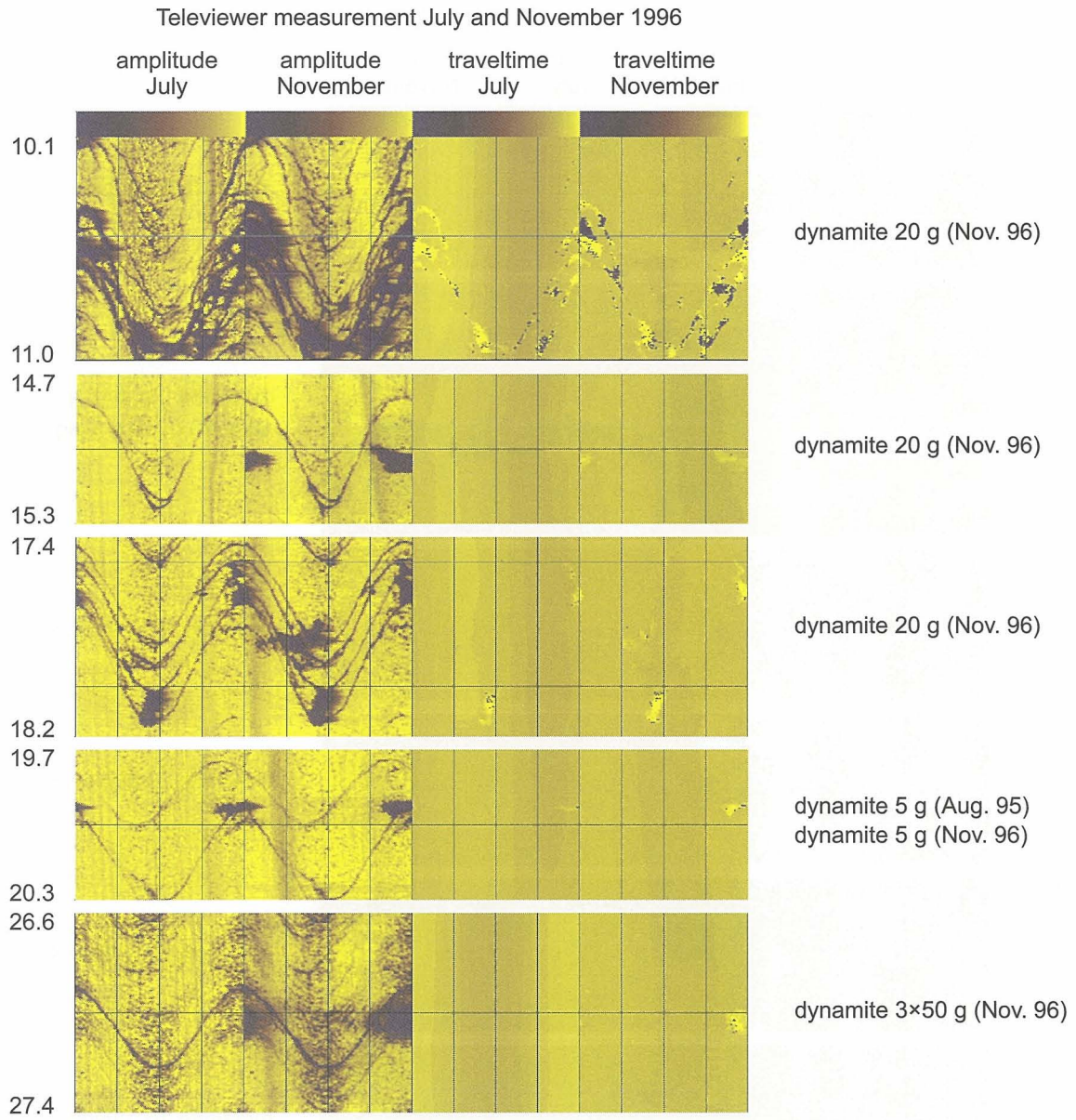


Fig. 2.15 Comparison of traveltime and amplitude images for televiewer measurements of July and November 1996 at the different shot positions between 10 and 30 m.

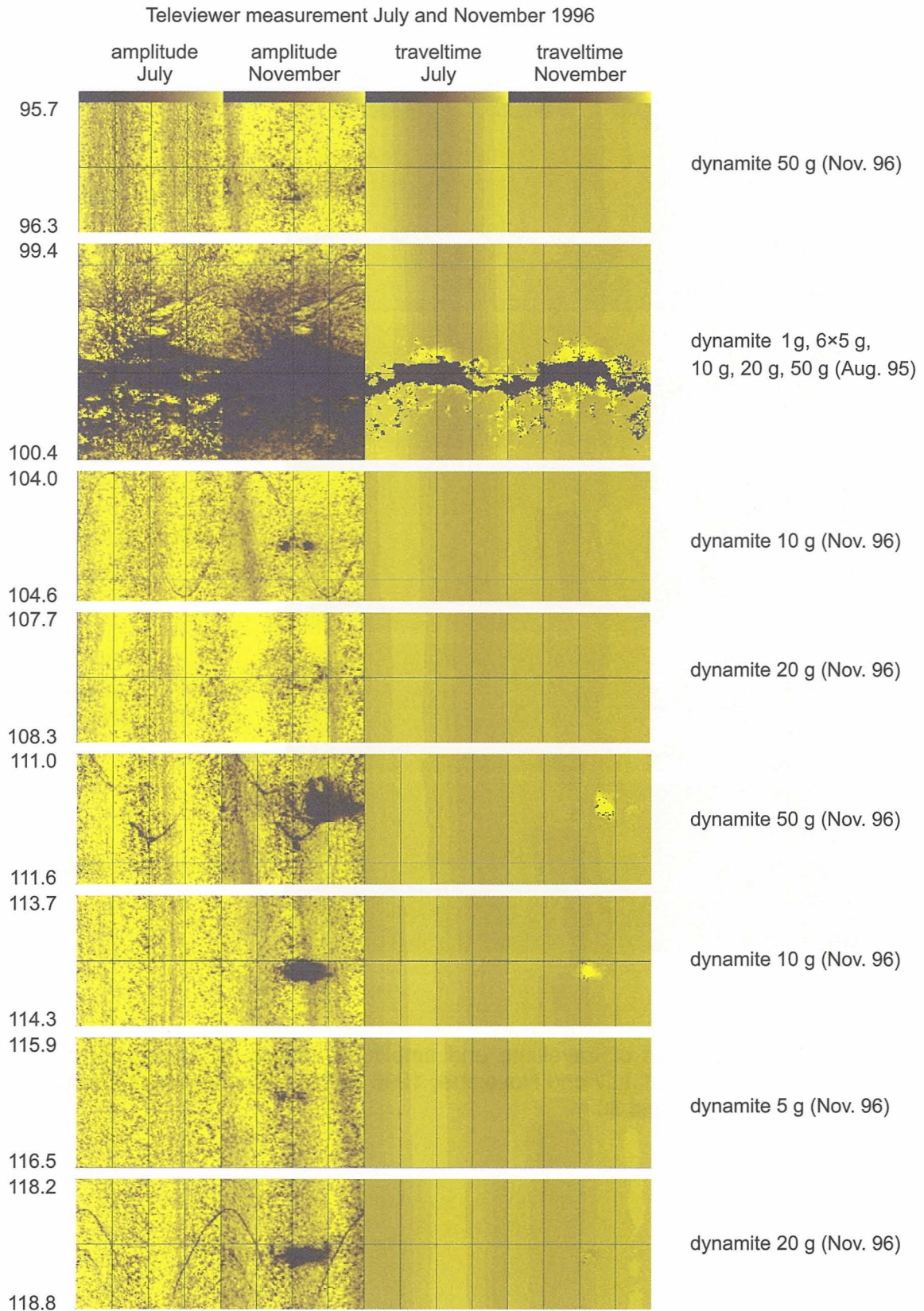


Fig. 2.16 Comparison of traveltime and amplitude images for televIEWER measurements from July and November 1996 at the different shot positions between 90 and 120 m.

Tab. 2.4: Explosives test of 13.11.1996

Depth (m)	Charge (g)	Type of structures	Recognisability
10.7	20	large structure with breakouts	Yes
15.0	20	small structure	Yes
17.8	20	4 parallel structures with breakouts	Yes
20.1	5	small structure	No change in damage at 19.95 m (source test -> 20 m)
27.0	3*20	small structure	Yes
96.0	50	-----	No
104.3	10	small structure	Yes only in amplitude image
108.0	20	-----	No
111.2	50	small structure	Yes
114.0	10	-----	Yes
116.2	5	-----	Yes only in amplitude image
118.5	20	small structure	Yes

The effect of different sizes of explosive charge can be studied using caliber crossplots (Fig. 2.17). If the four shots on small structures (5 g -> 20.1 m, 10g -> 104.3 m, 20 g -> 118.5 m and 50 g -> 111.2 m) are considered (see Table 2.4), it is clear that the degree of damage is dependent on the amount of explosives used. For 5 g no damage was seen in the crossplots, for 10 g there was very slight damage just above the resolution accuracy of the televiewer, for 20 g there was slight but nevertheless clear damage and for 50 g there was a large breakout. The four shots positioned on structure-free zones (5 g -> 116.2 m, 10 g -> 114.0 m, 20 g -> 108.0 m and 50 g -> 96.0 m) show a different picture (Fig. 2.18). Only the shot at 114 m shows distinct damage in the form of a breakout. For the other three positions, the crossplots show only slight damage or none at all. There is no indication (e.g. from core mapping) that the rock at 114 m is mechanically less competent than at the other three positions.

The above discussion on charge size also indicates that there is a relationship between the degree of damage and the presence of structures. If one considers the case of the 20 g shots (108.0 m: no structure, 118.5 m: small weak structure, 15.0 m: small structure, 17.8 m: four parallel small structures and 10.7 m: large structure with breakout), it is clear that marked structures show greater damage than small structures or borehole sections without structures.

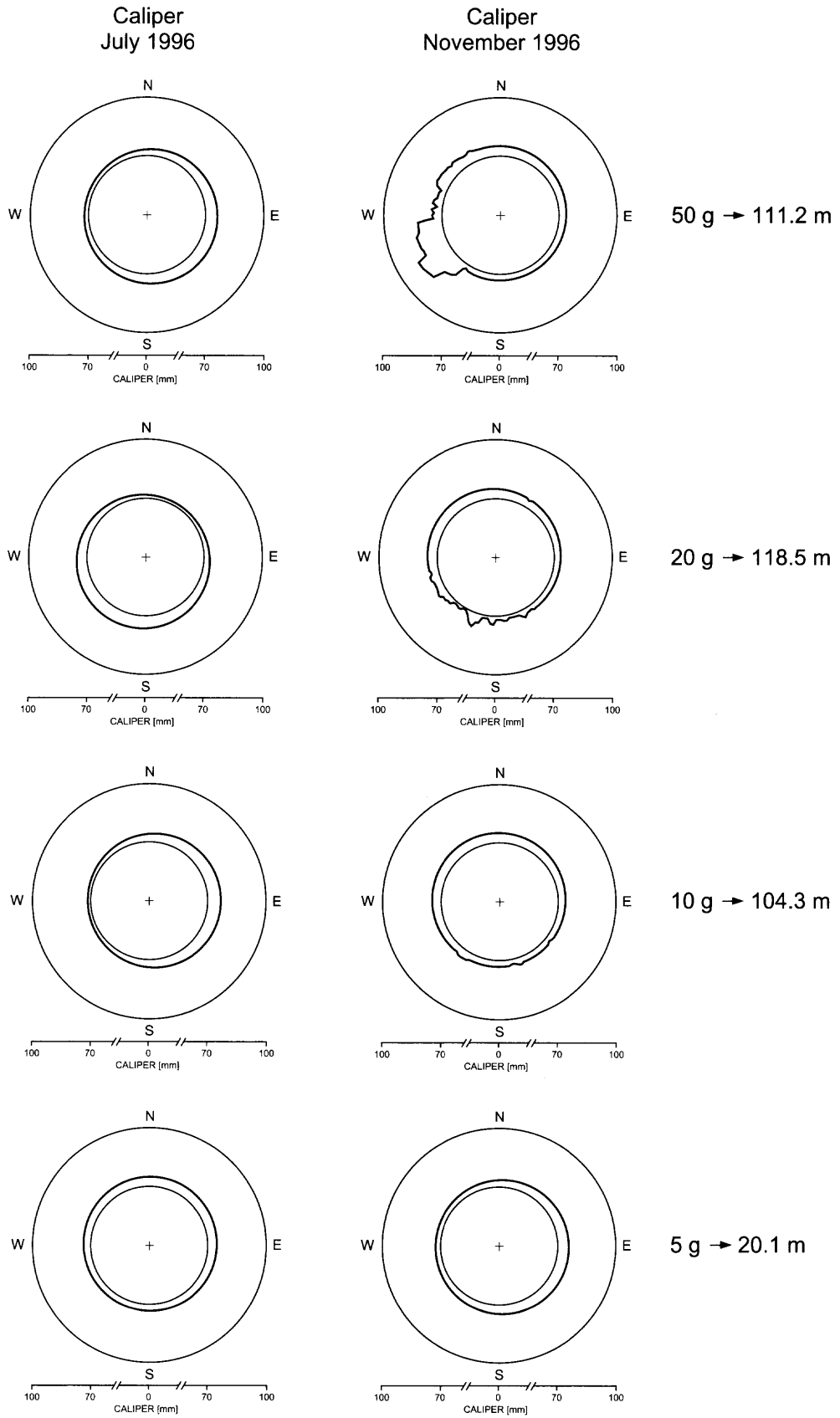


Fig. 2.17 Caliber crossplots for shots at positions with small geological structures.

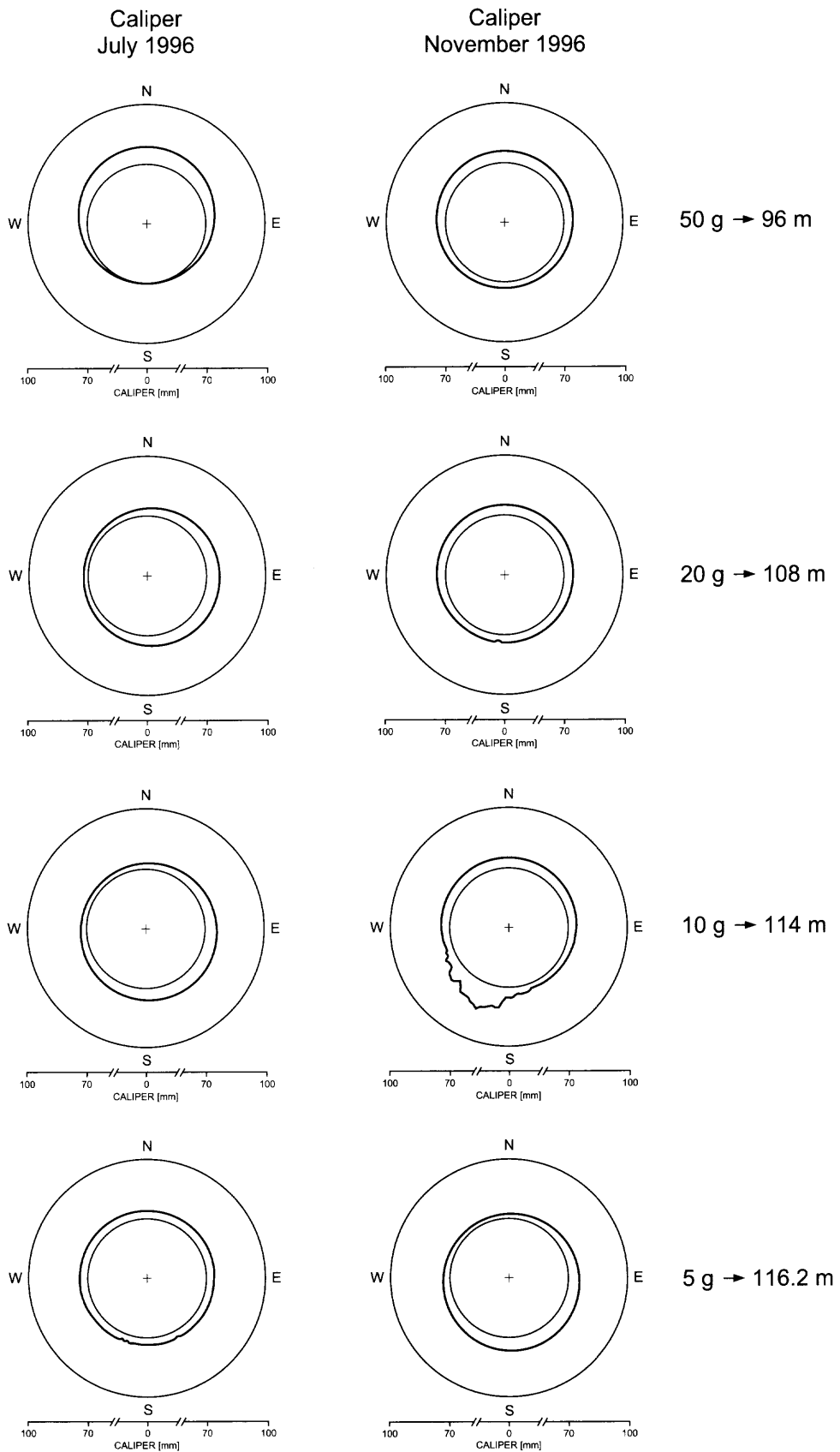


Fig. 2.18 Caliber crossplots for shots at positions with no recognisable geological structures.

Repeated shooting at one position generally leads to greater damage. This is demonstrated very clearly at the 20 m position where 5 g of explosives were used in the source test. The televiewer image and the crossplot of the July 1996 measurement show clear damage at 19.5 m. In the explosives test of 13th November 1996, 5 g were again exploded at 20.1 m. No change was observed in the immediate vicinity of the shotpoint. However, the damage from the source test at 19.95 m showed an increase in size of the observed breakout (depth 19.93 m).

To summarise, it can be said that the size of the charge, the number of shots per position and the presence of structures and any previous damage all have an influence on the extent of the damage to the rock.

2.5.3 Evaluating the direction of damage

The damage caused by explosives in borehole BOGS 84.041a shows clear preferential directions in both measurement fields (see Table 2.5). In the depth interval 10 - 30 m, the dominant azimuth is 315° and in the interval 95 - 120 m it is 200° .

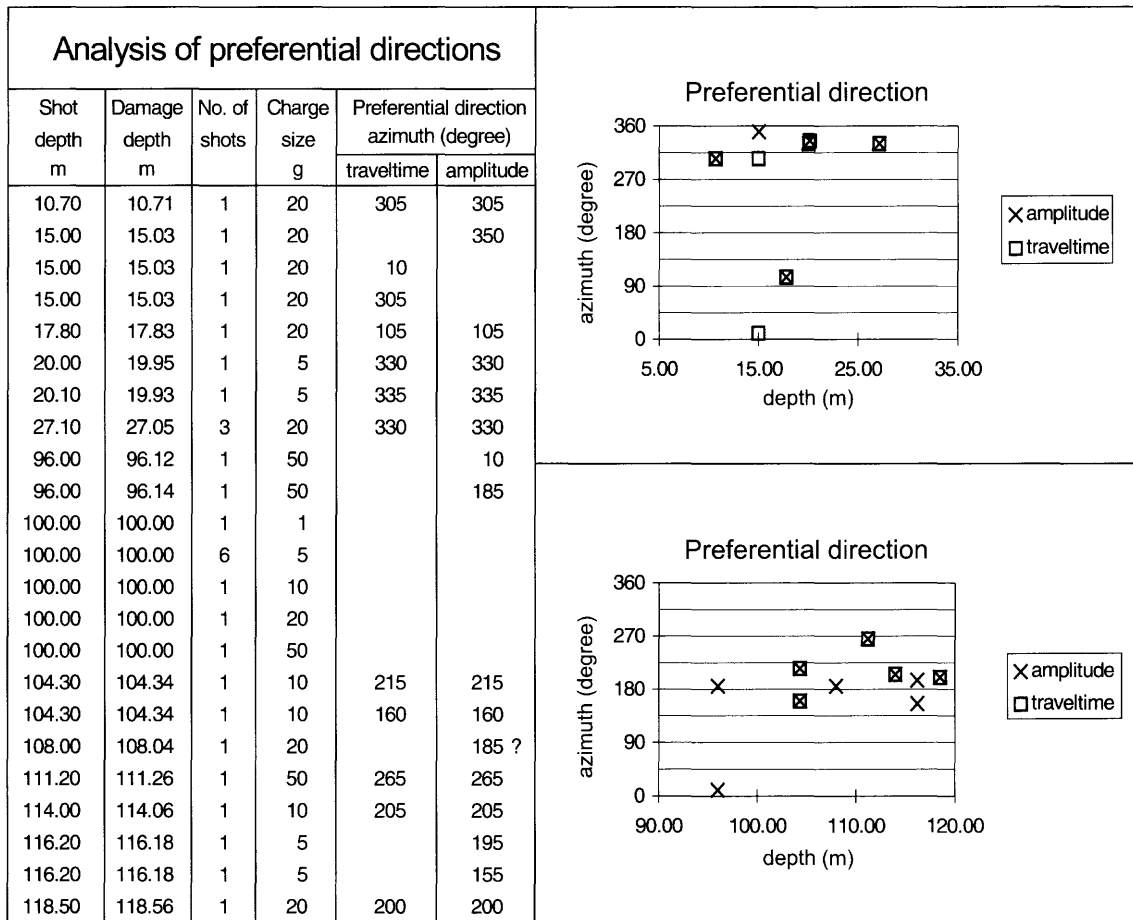
Pahl et al. (1989) give a principal stress direction of $155^\circ/335^\circ$ for the interval 40 - 100 m and a direction of $115^\circ/295^\circ$ for the interval 100 - 172 m. Damage is expected to be perpendicular to the principal stress direction. There is only one shotpoint in the interval 40 - 100 m, at 96 m, and this shows slight alterations in the televiewer amplitudes. In the lower interval (100 - 172 m), the direction agrees very well with the principal stress direction.

The dominant azimuth direction observed in the depth interval 10 - 30 m is 315° and cannot be explained by the principal stress directions (Pahl et al., 1989: from 0 - 40 m $105^\circ/285^\circ$). A further cause of the preferred direction of damage could be a contact of the explosive charge to the borehole wall.

To orientate the measured image, the televiewer also surveys the location of the borehole. In the sections newly measured in 1996, the inclination of the borehole was $\leq 1^\circ$ from the vertical (Albert, 1997). This corresponds to the resolution accuracy of the tool used for a borehole diameter of 146 mm. With such small inclinations, it is no longer possible to derive an azimuth for the borehole inclination from the measured data. The tool simply measures its own movement in the borehole. Given the accuracy of the measuring tool, it can only be said that the borehole is vertical to $\pm 1^\circ$.

The inclination of the borehole is even smaller in the depth interval 10 - 30 m ($\leq 0.5^\circ$ from the vertical; Albert, 1997). Since a borehole azimuth measured with the televiewer in the case of such a small inclination is not reliable, this azimuth should not be compared with the preferential direction of the damage.

Tab. 2.5: Analysis of preferential directions of damage to the borehole wall caused by using explosive charges



2.6 Conclusions on the source test

Various high-frequency borehole and tunnel seismic sources have been tested at the GTS. Small explosive charges (5 - 100 g) produced the strongest seismic signals with the broadest frequency spectrum. Compared with non-destructive sources, the advantage of greater energy production has to be weighed against the fact that even 5 g of explosives can cause damage to a borehole wall in granite. The objective of finding a non-destructive source which would penetrate over large distances at the GTS was not realised. The non-destructive sources which were tested certainly have potential for development but they would not be capable of achieving an energy yield comparable with that of 50 g of explosives.

For tomographic surveys with a maximum ray length less than 400 m at the GTS the non-destructive sources existing today should be powerful enough (s. Fig. 2.10).

In 1997, a newly developed borehole vibrator was tested in the field in the USA and produced more seismic energy than 128 g of explosives which were used simultaneously (Paulson, 1997). This source could represent an alternative to using explosives in deep boreholes drilled from the earth's surface. It cannot be used in tunnel locations. The winch for the hydraulic cable is transported on a 60-t truck.

deep boreholes drilled from the earth's surface. It cannot be used in tunnel locations. The winch for the hydraulic cable is transported on a 60-t truck.

For all sources, the dominant frequency decayed to about 300 Hz or less at source-receiver offsets > 400 m (s. Fig. 2.10). This means that also the resolution of a tomographic survey at the GTS will be lower than expected. Depending on the wavelength, on the ray length and the inversion algorithm (s. below), the reachable resolution can be calculated.

Despite clear differences in the performance of the various sources, the results of this study highlight the importance of the site conditions, in particular the attenuation structure of the rock body under consideration. Q values estimated from direct P-waves generated by the various sources considered in this study ranged from about 20 to 60, with a median of around 35. Such low Q values imply very high attenuation. For example, a 1000 Hz signal will be damped to less than 5% of its original value after propagating for some 200 m (assuming a velocity of 5000 m/s and a Q value of 35). A major geological difference between the rock mass sampled in this study and other hard rock test sites with significantly lower seismic attenuation is the high degree of fracturing at the GTS. Although the mechanisms of seismic attenuation are numerous and complex, it is well known that Q is lowered dramatically by the effects of brittle deformation (Paulsson et al., 1985; Bourbié et al., 1987).

It will therefore be necessary in future tomography projects to obtain information on the damping of seismic waves in the region being investigated before carrying out the tomographic measurements. This will allow the optimum source to be selected and will provide information on achievable resolutions.

The Q values obtained are comparable with other estimates from seismic data in near-surface crystalline rocks (Juhlin, 1990, 1995; Li, 1995) and in clay-rich sediments (Schön, 1996; Tonn, 1989). In the investigation areas Zürcher Weinland (Opalinus Clay) and Wellenberg (marl) a similar attenuation is therefore expected. In the crystalline basement of Northern Switzerland, the attenuation should be lower and the propagation characteristics of the seismic waves should be correspondingly better.

3. TRAVELTIME INVERSION METHODS

The seismic measurements carried out at the GTS in 1985 (US85 experiment, Fig. 3.1) were analysed using the SIRT travelt ime inversion method (Gelbke, 1988). However, with an increasing number of iteration steps, instability problems during the inversion led to various artefacts in the results. The source of this problem has not yet been conclusively identified. It is still unclear whether it is due to inherent problems in the dataset (e.g. surveying inaccuracies in the boreholes, triggering inaccuracies) or the algorithm (not taking into account the anisotropy in the rock). The question is analysed in more detail in the following Chapter with the help of newly developed travelt ime inversion methods which take account of either the anisotropy (Pratt & Chapman, 1992) or borehole path location and triggering inaccuracies as independent parameters (Maurer & Green, 1997).

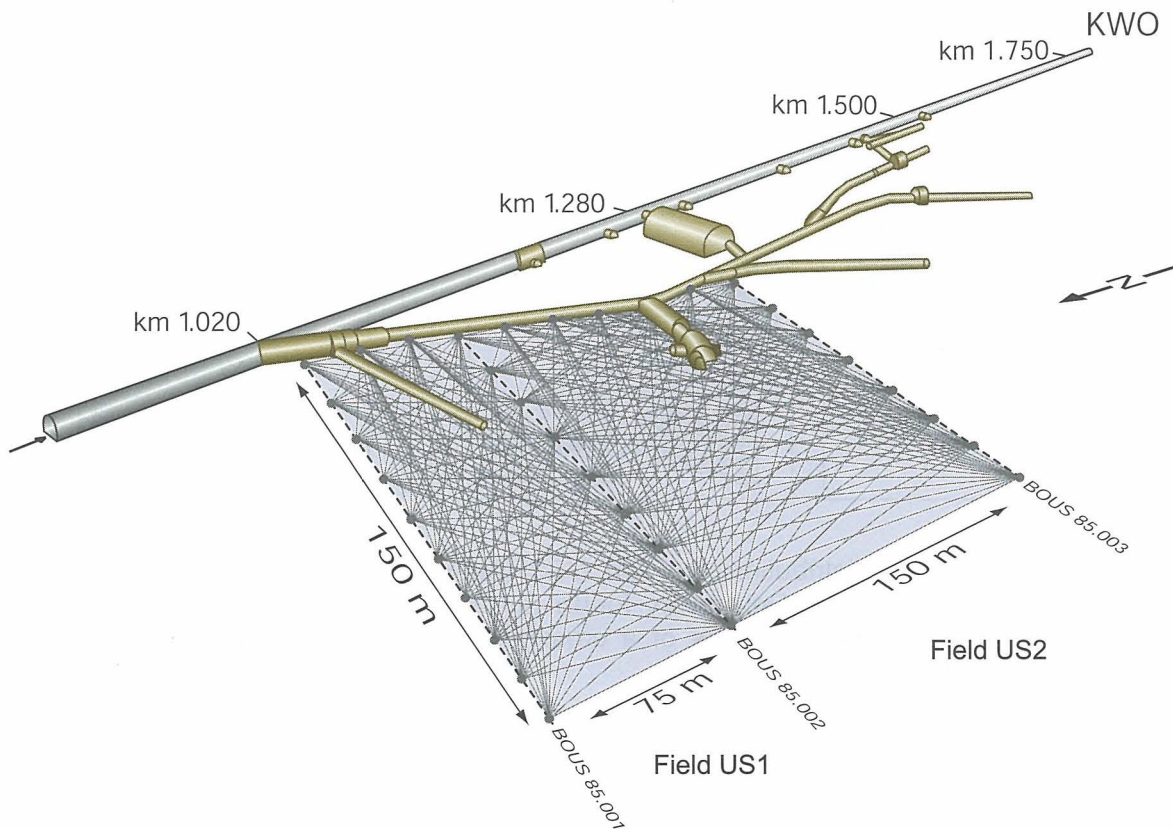


Fig. 3.1 The underground seismic (US) area at the Grimsel Test Site. The areas between the boreholes BOUS85.001 and BOUS85.002, BOUS85.001 and BOUS85.003 and BOUS85.002 and BOUS85.003 have been scanned independently.

3.1 The US85 experiment

In 1985, the underground seismics (US) survey was carried out at the GTS between boreholes BOUS85.001 and BOUS85.003 (Fig. 3.1). Four fields were investigated tomographically (Gelbke, 1988):

Field US1: between boreholes BOUS85.001, 85.002 and the laboratory tunnel
 Field US2: between boreholes BOUS85.002, 85.003 and the laboratory tunnel
 Field US3: between boreholes BOUS85.001, 85.003 and the laboratory tunnel
 Field US4: between the laboratory tunnel and the earth's surface

The data from Fields US1 and US2 were used for the investigations with the newly developed inversion methods. Only the travelt ime inversion which takes into account location uncertainties additionally used the data from Field US3. The following description of the results of the SIRT inversion is therefore restricted to Fields US1 and US2.

These two fields had 271 receiver/transmitter positions. Each of the fields was scanned independently. As an example, Fig. 3.2 shows the seismic rays for every fourth station of Field US2. The geometries contain arrangements of a standard crosshole and two offset VSP measurements. Where the rays of the crosshole and VSP measurements overlap, it was possible to achieve good ray coverage. In contrast, the western sides of the fields show only low ray coverage from the crosshole measurements.

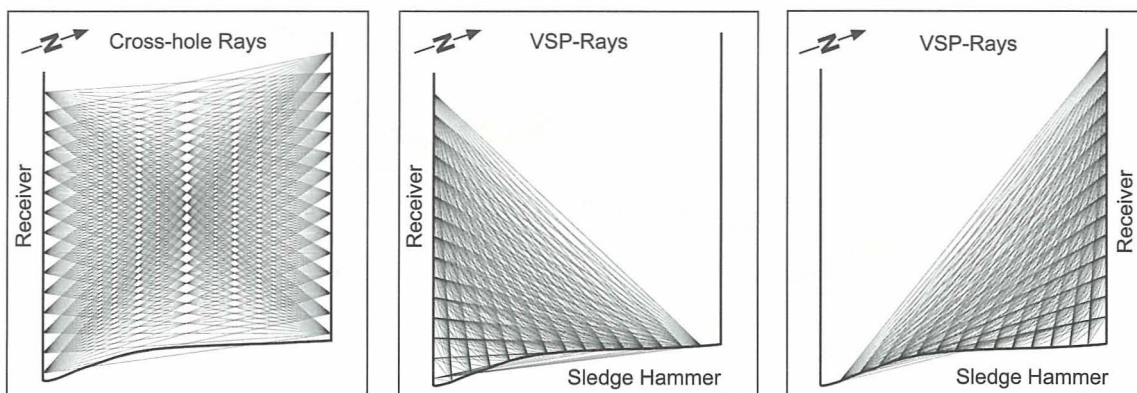


Fig. 3.2 The ray distribution of Field US2 (between boreholes BOUS85.002/BOUS85.003). Only every fourth ray has been plotted. This geometry contains arrangements of a crosshole and two walkaway VSP measurements.

3.1.1 Results of the SIRT inversion

Once the traveltimes from the individual shots had been read (picking), the data were checked and picking errors eliminated.

It was established that the trigger time-points for the borehole source (borehole hammer) and the tunnel source (hand-held hammer) showed slight differences of 0.1 - 0.2 ms (Gelbke, 1988), which is within the reading accuracy of 0.1 ms. Correction factors were determined (hand-held hammer +0.2 ms and borehole hammer +0.3 ms) and applied to the traveltimes.

Velocity variations as a function of ray azimuth were also observed and interpreted as an anisotropy effect (Gelbke, 1988). These are in the order of +/- 1% for an azimuth of the maximum velocity of 330°. Global correction factors were calculated for this anisotropy and applied to the traveltimes.

After 12 (Field US1) and 25 (Field US2) iterations, what was considered to be an optimum result was achieved (Fig. 3.3).

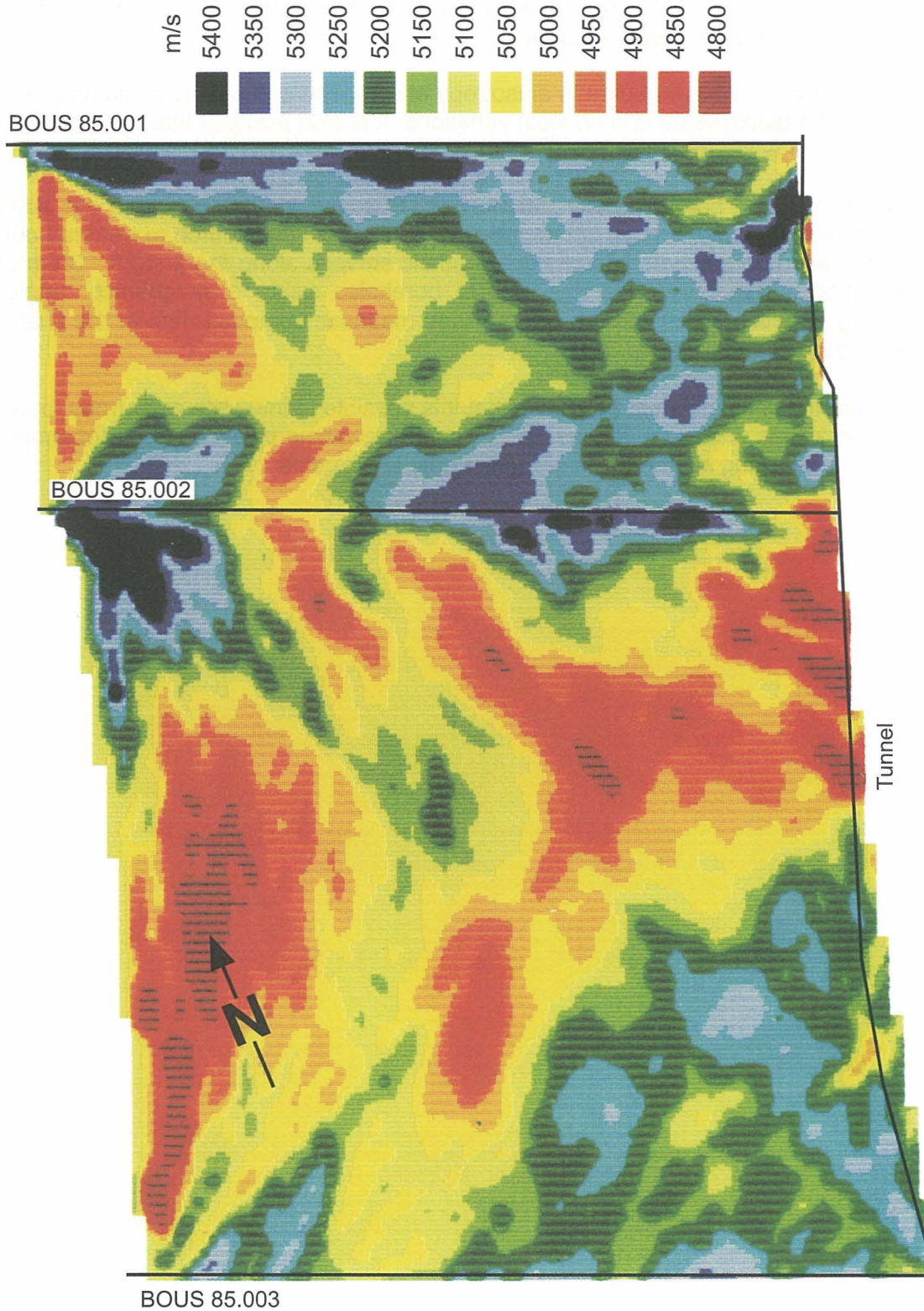


Fig. 3.3

The final result of the SIRT inversion for Fields US1 and US2 (Gelbke, 1988).

3.1.2 Problems of the SIRT inversion

The results obtained were the best possible at the time. However, there were some artefacts, such as the marked drops in velocity in areas of low ray coverage (Fig. 3.3). The attempt to obtain a better result with a larger number of iterations was not marked by success and showed only instabilities.

The reason for this was attributed to anisotropy effects. The corrections could only take into account a global value and no local variations. It is also possible that the triggering inaccuracies affected the quality of the results.

The location of the boreholes BOUS85.001, 85.002 and 85.003 was also not sufficiently accurate to allow a potential negative influence from this source to be ruled out. They are based on accurate line-of-sight geodetic surveys along the first 20 - 30 m of the boreholes, directional changes of the boreholes using a mechanical angle-measuring device from 20 - 30 to ~ 100 m and magnetic compass data in the final ~ 100 to 150 m (SOLEXPERTS, 1986).

In the following sections it will be shown that it is possible to integrate anisotropy, borehole uncertainties and triggering inaccuracies into travelttime inversion as independent parameters, resulting in production of more stable tomograms.

3.2 Anisotropic velocity tomography

Tomographic images produced from seismic transmission surveys have the potential to elucidate geological and geomechanical properties and to image the distribution of these properties. It follows that, if these properties are anisotropic, the seismic properties of the rocks are also likely to be anisotropic. Data processing methods must be used to account for the anisotropy - if this is not done the images will be degraded. In some cases the image degradation can be severe. Borehole mislocation errors are another potential source of image degradation.

Gelbke et al. (1989) estimated the anisotropy at the site as approximately 1%. However this estimate was based on a limited subset of data. Gelbke et al. (1989) also noted that the Field US1 data displayed a level of anisotropy of 2.8%. They were able to remove the anisotropy effect from the data before estimating the velocities. However, their method assumes that the anisotropy is consistent (homogeneous) everywhere within the rock mass.

An alternative, less restrictive approach is to incorporate the anisotropy parameters into the tomographic reconstruction algorithms. This is the basis of the methods developed by Pratt and Chapman (1992).

3.2.1 Method

If sound energy travelled along a simple ray path between a given source and a given receiver, then one could express the relationship between traveltimes t and the velocity distribution $v(x, z)$ as a simple integral

$$t = \int \frac{1}{v(x, z)} dl = \int u(x, z) dl \quad (3.1)$$

where the integral is taken over the ray path connecting the source to the receiver, dl is the incremental distance along the ray and $u(x, z)$ is the "slowness" (i.e. the reciprocal of velocity).

If we consider the slowness field to be represented as a rectangular grid of constant slowness pixels, then the integral equation becomes a summation

$$t_m = \sum_k u_k l_{km} \quad (3.2)$$

where l_{km} is the length of the m th ray in the k th cell. If there are a sufficient number of data measurements, t_m , these traveltimes equations become a set of simultaneous linear equations, with the pixel values u_k representing the unknown quantities. This set of equations may be more compactly written as the matrix equation

$$t = \underset{\sim}{A} \underset{\sim}{u} \quad (3.3)$$

where t is a column matrix containing all traveltimes for all possible source-receiver pairs (i.e. one entry for each ray), u is a column matrix containing one entry for each cell on the grid and \tilde{A} is a large matrix containing the lengths of each ray in each cell.

In tomography the simultaneous equations represented by this matrix equation are solved, or "inverted", to yield u , the slowness in each of the cells sampled by the experiment.

Anisotropic velocity tomography (AVT)

In Pratt & Chapman (1992), the tomographic problem in the presence of anisotropy was considered. They developed a linearisation of this problem and introduced an equation similar to equation (3.3):

$$\delta t = \tilde{A} \delta q \quad (3.4)$$

In this case, the unknown variables incorporate the full anisotropy information required at each cell location and the matrix \tilde{A} contains the required partial derivatives.

According to Pratt & Chapman (1992), for quasi-P waves there are only five physical parameters at a given cell location that control the arrival times in a 2D survey. These five parameters are arranged as a column matrix δq containing five entries for each cell on the grid. The five physical parameters, q_1, q_2, q_3, q_4, q_5 , can be related to more specific parameters, such as those used by Thomsen (1986) to describe the anisotropy of Transversely Isotropic (TI) media. If the tomography problem in equation (3.4) is considered solved, then we may carry out a further transformation to extract the Thomsen parameters at each cell location:

$$\begin{pmatrix} q_1 \\ q_2 \\ q_3 \\ q_4 \\ q_5 \end{pmatrix} \rightarrow \begin{pmatrix} \alpha_o \\ \varepsilon \\ \delta \\ \theta \end{pmatrix} \quad (3.5)$$

The 4 parameters $\alpha_o, \varepsilon, \delta$ and θ represent TI anisotropy in a 2D plane. The velocity α_o is the velocity parallel to the symmetry axis, ε is the fractional difference between α_o and the velocity perpendicular to the symmetry direction, δ can be used to characterise the departure of the slowness curve from an elliptical shape, and θ is the angle between the x_3 axis and the symmetry direction. The anisotropy factor ε is defined such that the velocity perpendicular to the symmetry direction is given by $\alpha_o(1 + \varepsilon)$. Since ε is almost universally positive, the symmetry axis almost always represents the slow direction. The details of the transformation in equation (3.5) are complicated and are given in Pratt & Chapman (1992).

Regularisation

Although equation (3.4) may seem straightforward, in practice it is extremely difficult to solve due to numerically poor conditioning of the matrix \tilde{A} .

This limitation is fundamental in geophysical tomography - the geometrical constraints on the experiment prevent us from obtaining a well-conditioned problem. Instead, we rely on additional constraints to provide adequate "regularisation", turning a poor conditioning problem into a well conditioned one. Clearly, the constraints must be carefully chosen.

We choose to add constraints to the tomographic problem (3.4) that stabilise the problem by inhibiting the "roughness" of the solution. Mathematically, we solve the augmented problem:

$$\hat{\delta t} = \hat{A} \delta q \quad (3.6)$$

where the data vector δt is augmented by the addition of an appropriate number of zeros and the augmented matrix is given by

$$\hat{A} = \begin{pmatrix} A \\ \lambda \tilde{R} \end{pmatrix} \quad (3.7)$$

with the role of λ to be discussed below. The (square) regularisation matrix \tilde{R} is an operator that computes the solution roughness, typically by incorporating difference operators that compute the first or second spatial differences. Thus, equation (3.6) contains additional equations that set the spatial differences of the solutions, δq , equal to zero.

We cannot expect to be able to satisfy all the traveltimes and the additional constraints in equation (3.6) simultaneously. Instead, an astute choice of λ will allow us to choose a range of solutions that will:

- i) Satisfy the traveltimes, but not the constraints (small λ) or
- ii) Satisfy the constraints, but not the traveltimes (large λ)

Examination of the solutions for these two extremes, and for a range of solutions in between, will allow an optimum solution to be selected. Moreover, the full range of solutions provides important information on the uncertainties in the data and in the final solutions.

3.2.2 Parameter test for anisotropic velocity tomography

The first step in solving the anisotropic velocity tomography problem is to generate a suite of results at different regularisation levels, in order to evaluate the traveltimes data quality and to determine optimum parameters for the regularisation. The following section gives the details of these parameter tests.

In order to select a value for λ in equation (3.7), we first solved the traveltime problem using the Field US1 and Field US2 data for a range of values for λ ranging from 0.01 to 3.5. Figures 3.4 (Field US1) and 3.5 (Field US2) display the results of these computations in a compact form. The first figure, Figure 3.4a/3.5a, displays the manner in which the parameter λ controls whether the traveltimes are satisfied (small RMS residuals) or the constraints are satisfied (small RMS roughness) - clearly we cannot satisfy both, but a knee-point can be identified at which both are optimally satisfied. This knee-point occurs at approximately $\lambda = 0.15$. The remaining parts of Figures 3.4 and 3.5 display images from the solutions for $\lambda = 0.05, 0.2$ and 0.8 . The curve labelled "isotropic" represents the values obtained when anisotropy was not incorporated. In this case the residuals are always larger than for the anisotropic solutions.

"Isotropic" velocity images

Once the tomography problem (3.6) is solved, the transformation (3.5) may be carried out at each cell location. The velocity α_o can then be plotted as a tomographic image. However, in cases of anisotropy with variable symmetry axes, it is useful to plot the "isotropic" component of the velocity. This is a parameter (at each cell location) that corresponds to the best fitting isotropic velocity for all directions of propagation. It can be thought of as an average over the possible propagation directions. This parameter, for three values of λ , is shown in Figure 3.4b/3.5b, for both the anisotropic and isotropic case. Clearly, the solutions are unreasonable for the isotropic cases. As λ is increased, the anisotropic solutions are less rough and less noisy. However, if λ is increased too far, the solutions no longer contain detailed information on the velocity heterogeneity.

Anisotropy (ε) images

The images shown in Figure 3.4d/3.5d give an indication of the magnitude of the apparent anisotropy and how this apparent anisotropy is distributed. As described above, ε is the fractional difference between the two perpendicular propagation velocities. It is interesting to note that the general pattern of the anisotropy shown in Figure 3.4d/3.5d is relatively stable, although clearly the images become more smooth as λ is increased. There is a strong increase in apparent anisotropy with depth of the boreholes. For the isotropic solutions, ε is everywhere equal to, or close to, zero due to the effect of the constraints.

Traveltime residuals

It is essential for the purposes of quality control to examine the traveltime "residuals" shown in Figure 3.4c/3.5c. These are computed by predicting the arrival times in the current tomographic solution and subtracting these from the actual picks. The better the fit, the smaller these residuals will be and the more confidence we may place in the results. The larger λ is, the less we will be able to fit the traveltimes and the larger the residuals. However, if we reduce λ too far, we start to fit noisy traveltimes and the images will be corrupted. The panels labelled "isotropic" show how the residuals are systematically distributed when anisotropy is ignored. For all values of λ , if anisotropy is ignored, the residuals show distinct, systematic patterns of red and blue that correlate with propagation direction. Only when anisotropy is incorporated into the algorithm do these patterns disappear.

3.2.3 Results of the anisotropic velocity tomography

On the basis of the information depicted in Figures 3.4 and 3.5, all results were extracted with a value of $\lambda = 0.15$ for Fields US1 and US2 (Pratt, 1995; Worthington & Pessoa, 1994).

Because the traveltime residuals of Field US1 are larger than the survey specification in places, especially where source-receiver pairs are close to the underground tunnel, and because the velocity and anisotropy appear abnormally high in the vicinity of the tunnel, all 5965 traveltimes of Field US1 were systematically evaluated and suspect times were rejected. This was done by rejecting all traveltimes for which either i) the midpoint of the ray was within 20 m of the tunnel or ii) the traveltime residual was larger than +/- 100 μ s. In this fashion, 1619 traveltimes were rejected (Pratt, 1995).

By rejecting suspect traveltimes, we were also able to slightly lower the value of the trade-off parameter λ . This was done for two reasons: First, the elimination of suspect traveltimes makes the inversion more robust and a lower level of regularisation can be used. Secondly, using a lower level of regularisation allows more roughness (structure) to enter the solutions, thus making them appear more compatible with the images for Field US2. A value of $\lambda = 0.05$ was used for all images of Field US1.

The "isotropic" velocity and the anisotropy ε are shown in Figures 3.6 and 3.7 for Fields US1 and 2 together. The velocity images are similar to those given by Gelbke (1988 - Fig. 3.3).

Figure 3.8 displays the orientation of the apparent symmetry axes for both Fields. Each line is drawn to lie along the apparent local symmetry axis and is scaled in length according to the local value of ε . Regions where ε is less than 2% have not been plotted.

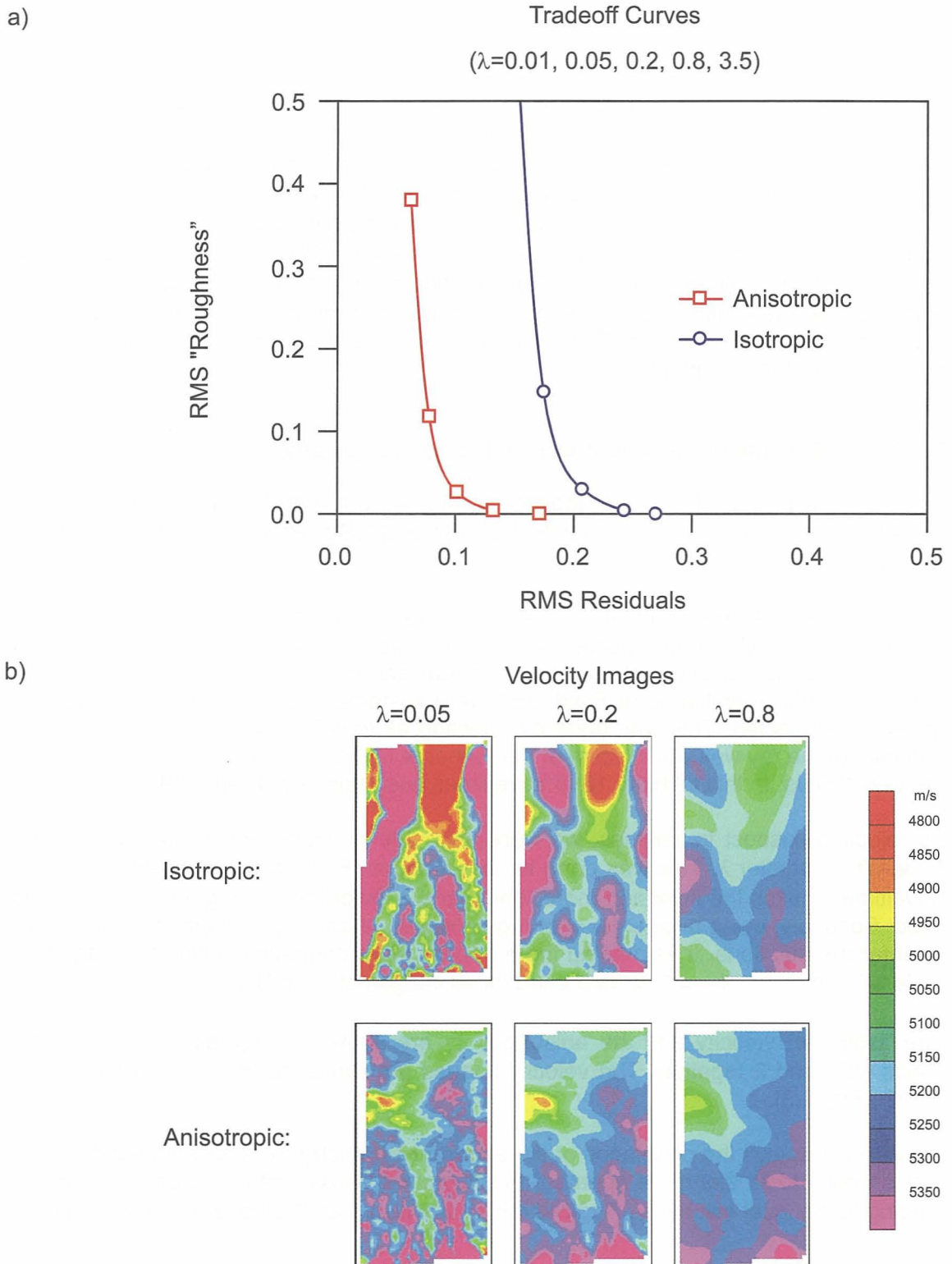
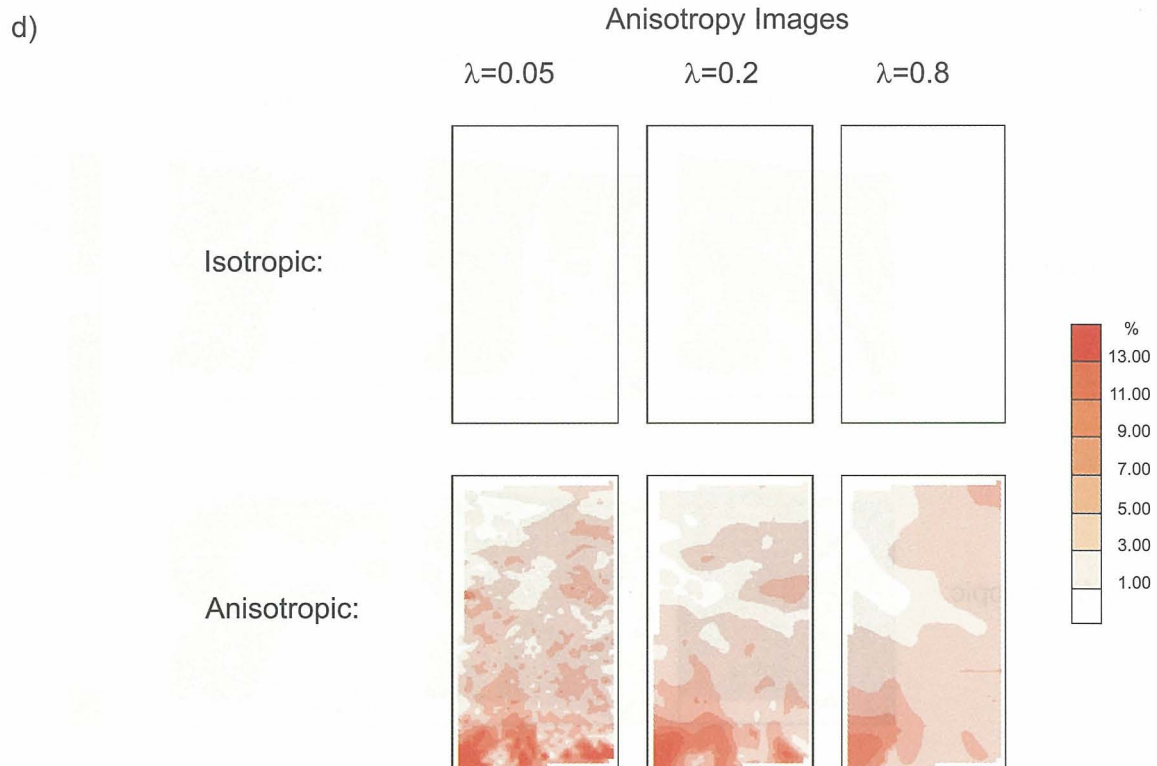
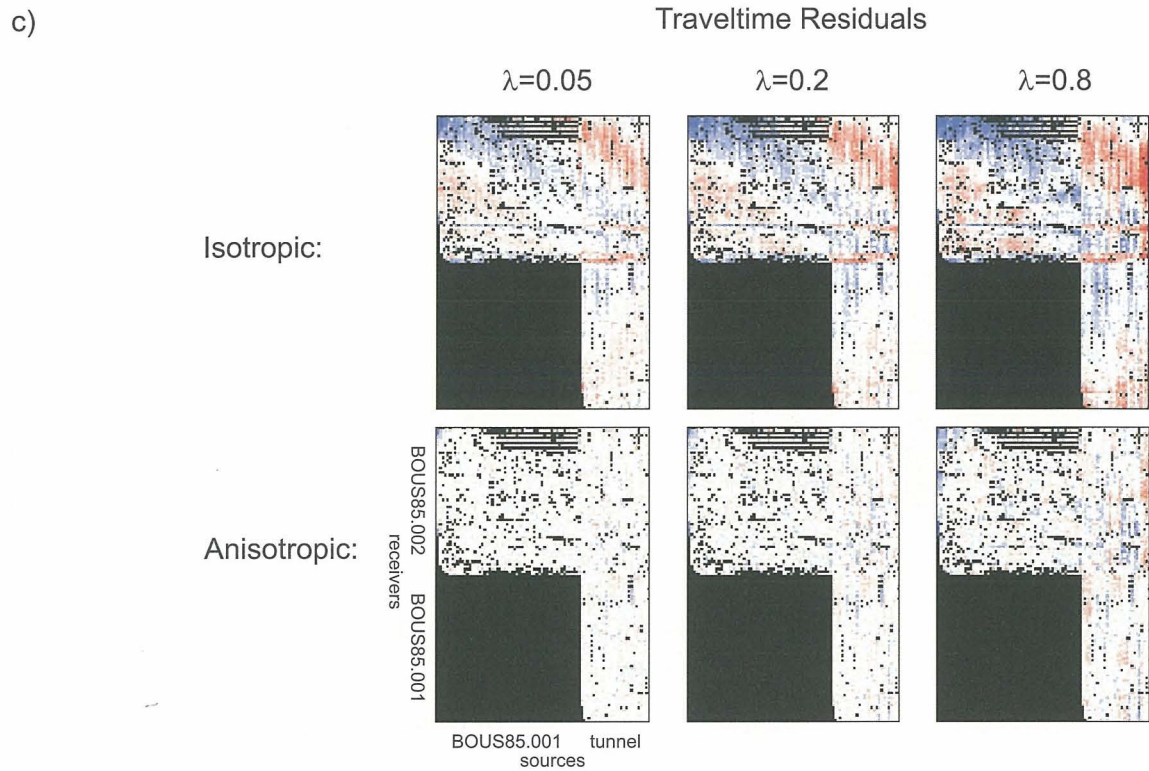


Fig. 3.4 A suite of tomographic results, using variable roughness constraints (λ) for Field US1. a) As λ is increased, the images become less rough, but the data fit degrades. Isotropic images always have higher residuals. b) As λ is increased, the images become less rough and less noisy. The isotropic images are strongly corrupted by anisotropy.



c) Traveltime residuals are shown for all source receiver pairs in relative colour code (red: positive residuals, blue: negative residuals). As λ is increased, the data residuals become larger. The isotropic data residuals display characteristic, systematic patterns. d) The anisotropy is not homogeneous and as λ is increased the images stabilise.

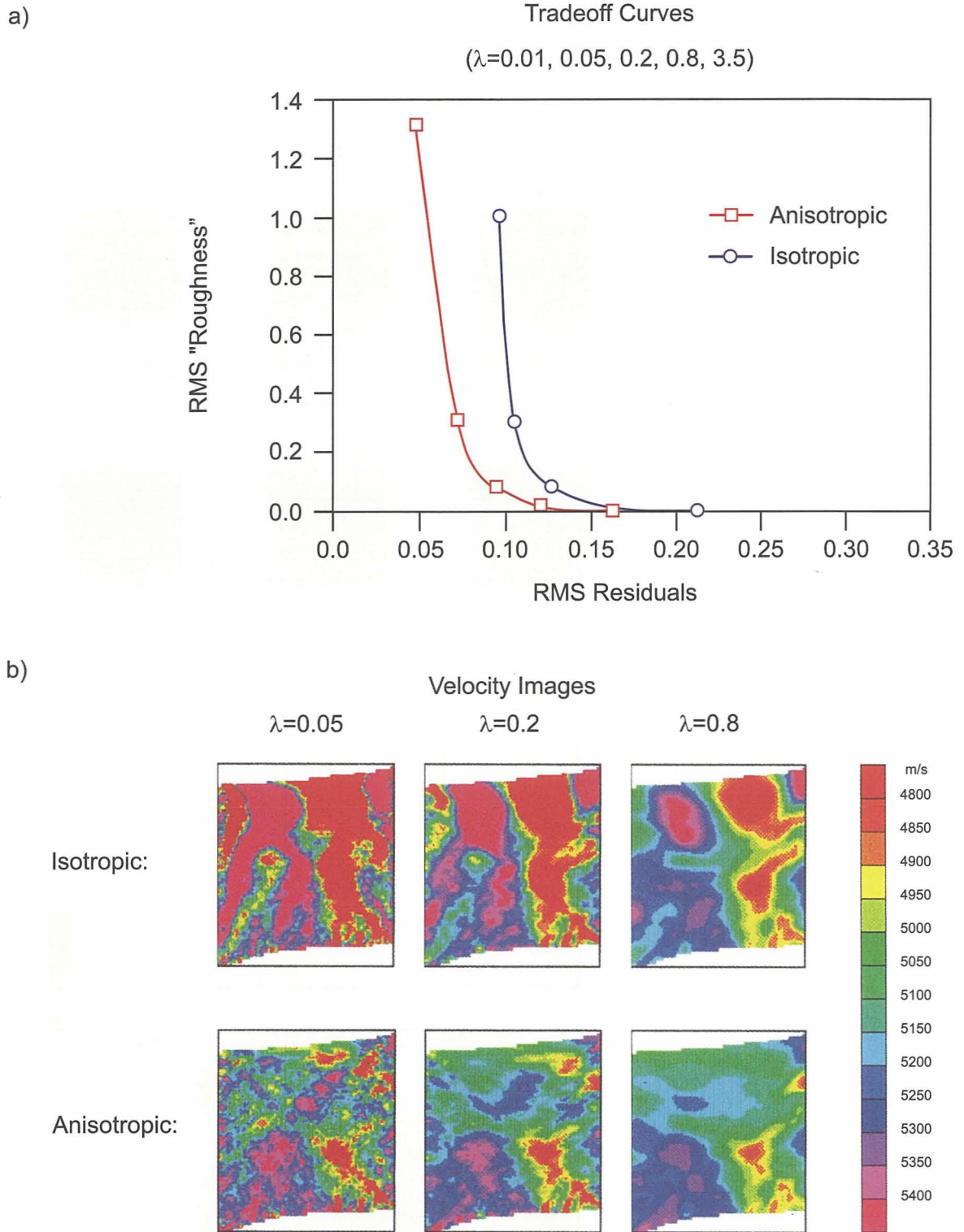
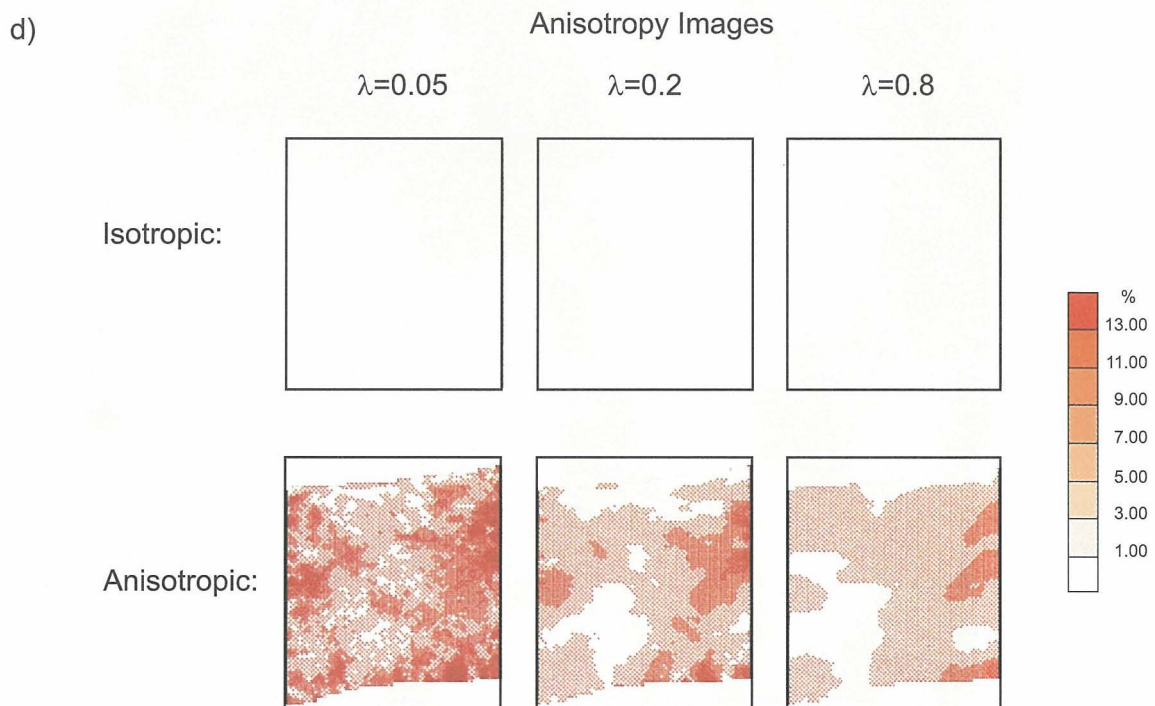
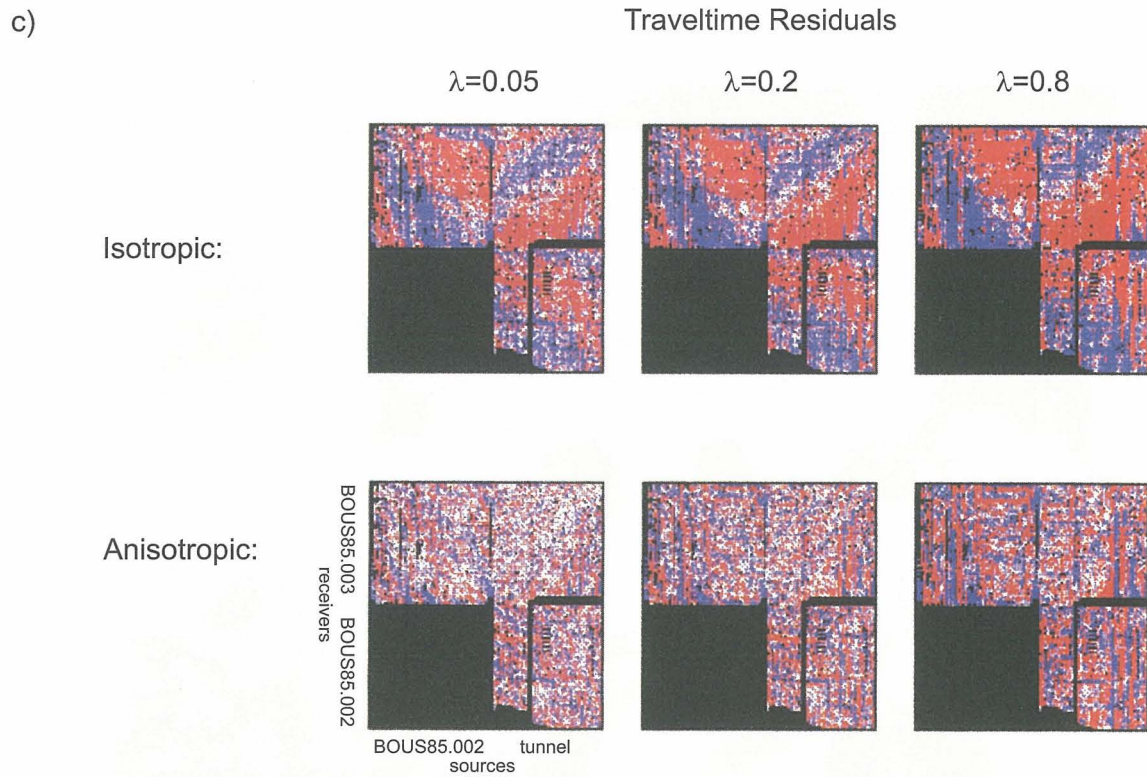


Fig. 3.5 A suite of tomographic results, using variable roughness constraints (λ) for Field US2. a) As λ is increased, the images become less rough, but the data fit degrades. Isotropic images always have higher residuals. b) As λ is increased, the images become less rough and less noisy. The isotropic images are strongly corrupted by anisotropy.



c) Traveltime residuals are shown for all source receiver pairs in relative colour code (red: positive residuals, blue: negative residuals). As λ is increased, the data residuals become larger. The isotropic data residuals display characteristic, systematic patterns. d) The anisotropy is not homogeneous, and as λ is increased the images stabilise.

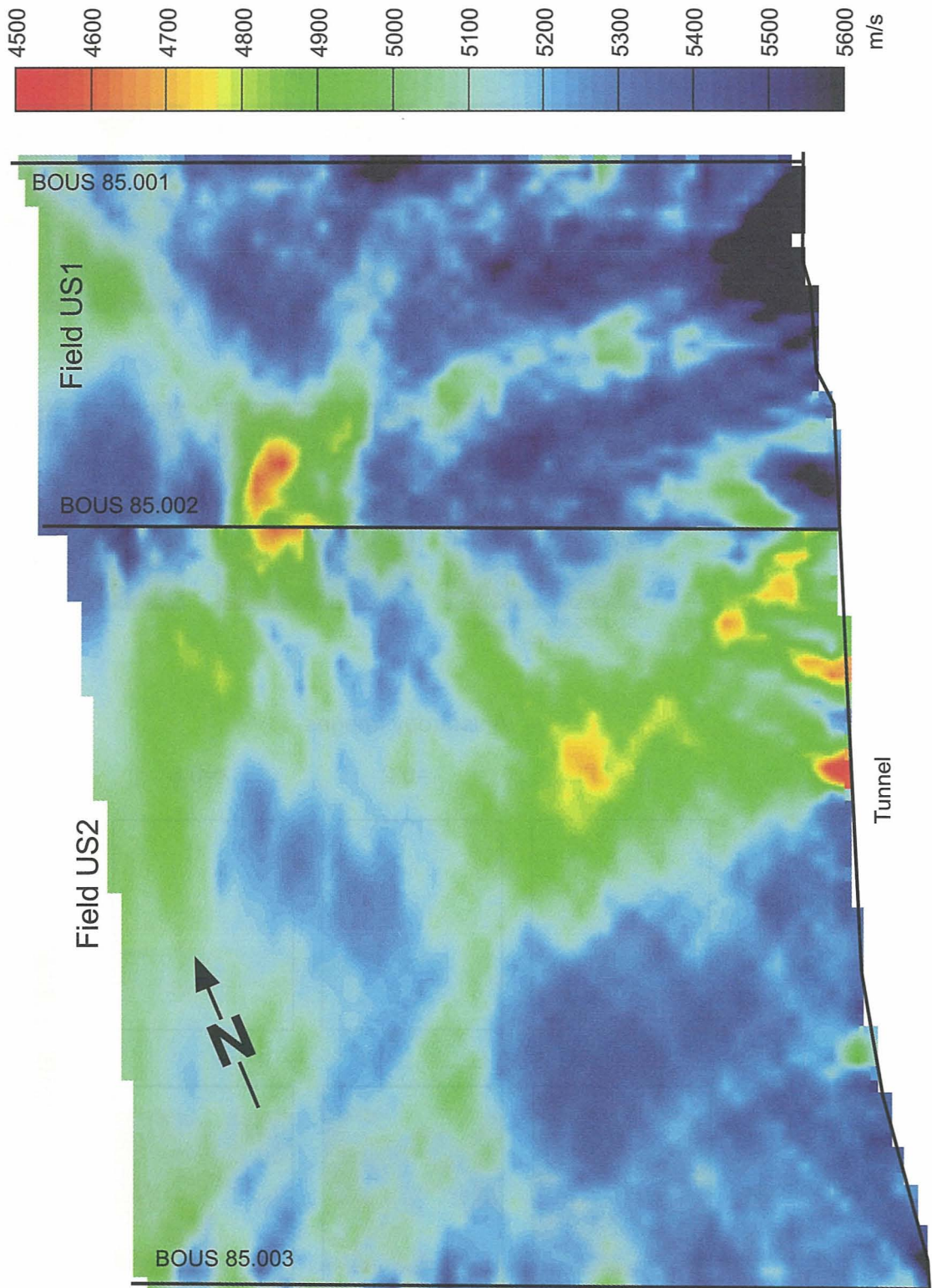


Fig. 3.6

Final velocity image from the anisotropy velocity tomography (AVT) for Fields US1 and US2. This image represents the distribution of the “isotropic” velocity (i.e., the mean velocity in each cell, averaged over all directions).

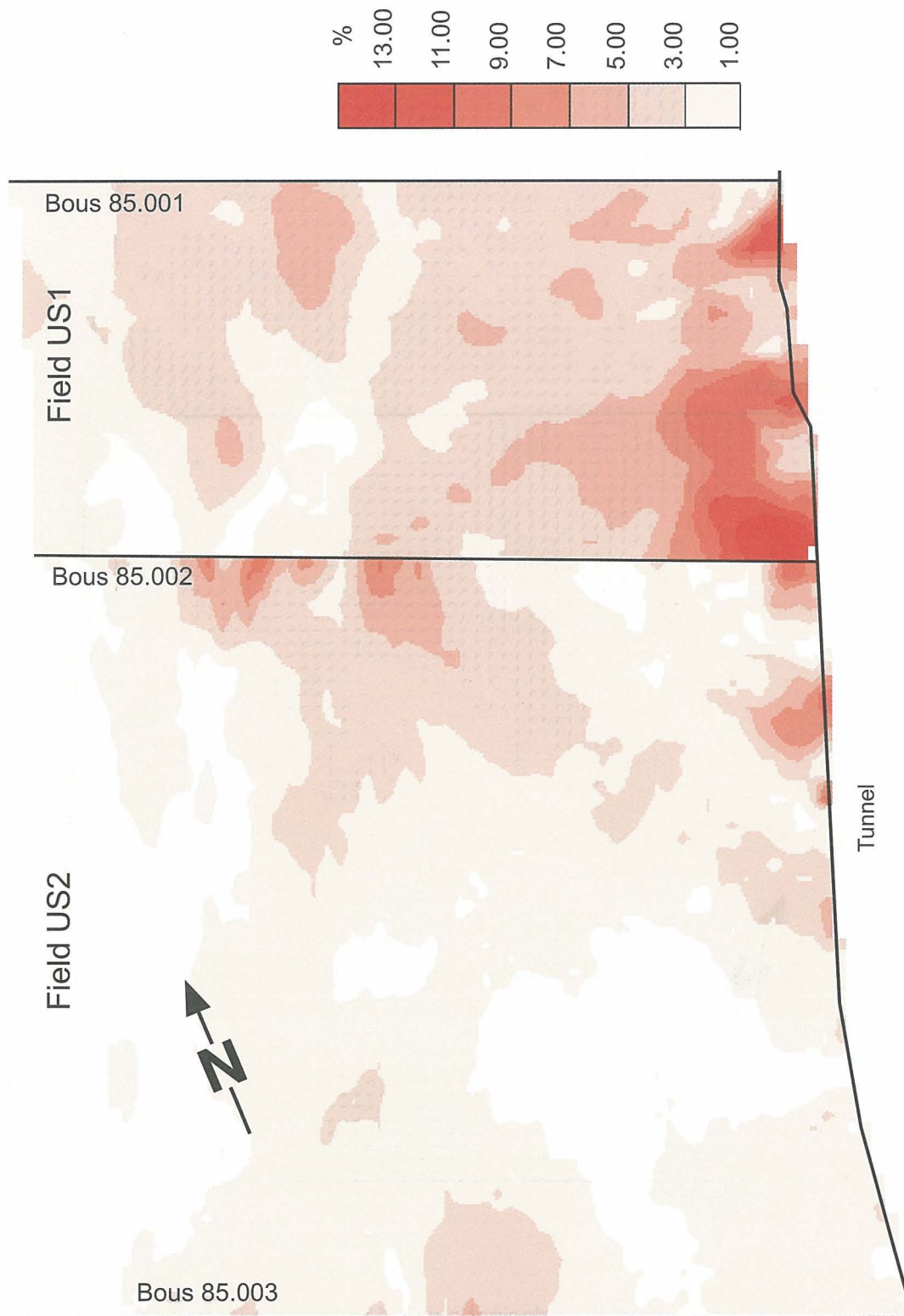


Fig. 3.7

Final anisotropy image from the anisotropy velocity tomography (AVT) for Fields US1 and US2. This image represents the distribution of the ε factor, i.e. the fractional difference between the velocity in the tunnel direction (20°) and the velocity in the borehole direction (290°).

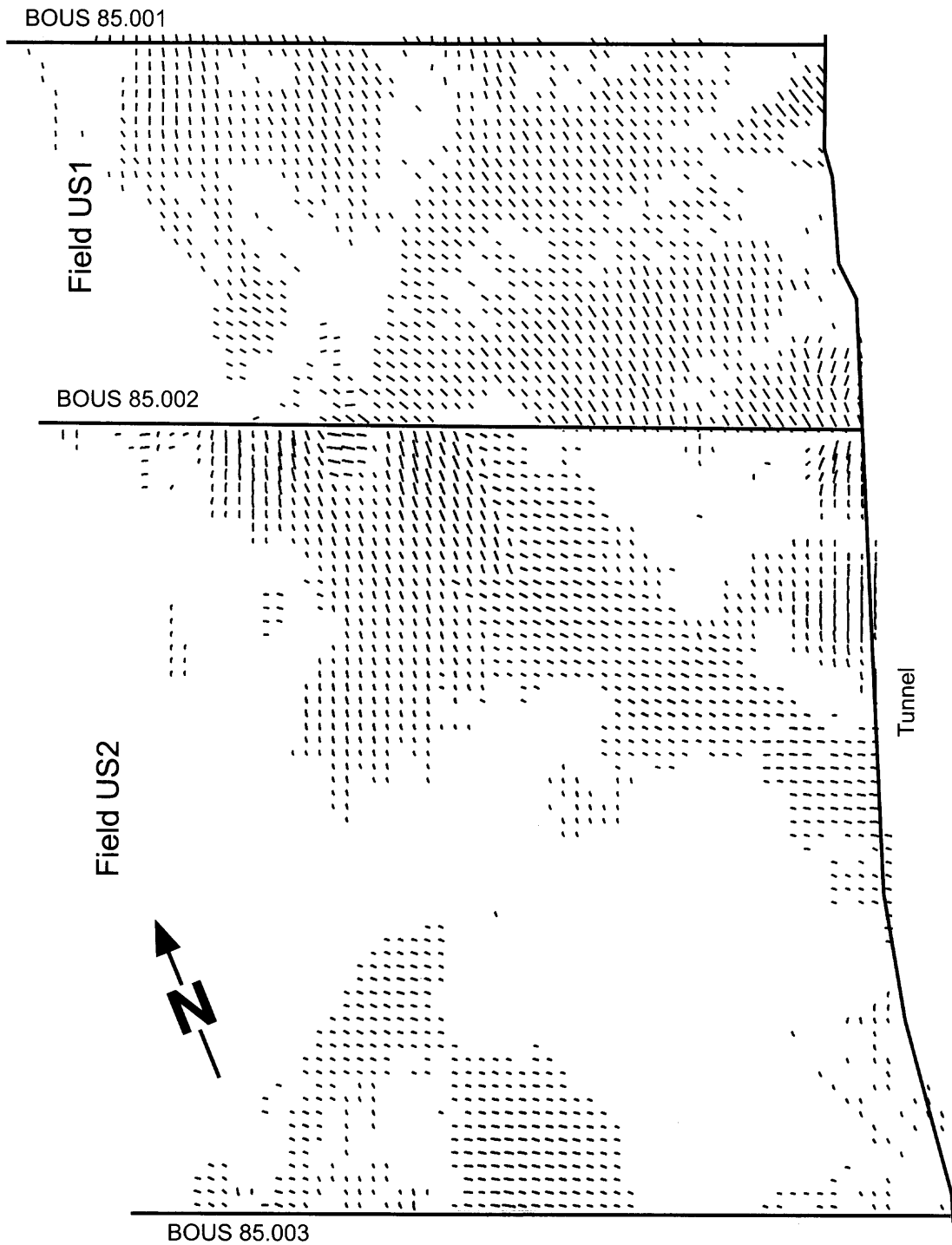


Fig. 3.8

The direction of the principal axes of transverse isotropy symmetry from the anisotropy velocity tomography (AVT) for Fields US1 and US2. If the anisotropy were transverse isotropy, these arrows would indicate the symmetry direction in the plane of the survey. Each arrow is scaled by an amount proportional to the local ϵ factor; where ϵ is less than 2% no arrow is plotted.

3.3 Potential coordinate mislocation in crosshole tomography

In most crosshole studies, velocities are determined from inversions of traveltimes. Traditional crosshole inversion schemes do not account for systematic errors in the data. Here a newly developed inversion algorithm is presented which takes account of borehole path location and triggering inaccuracies as independent parameters (Maurer 1996; Maurer & Green 1997).

The most important class of systematic errors is caused by mislocations of shots and receivers. Although state-of-the-art technologies allow along-borehole coordinates of sources and receivers to be determined with sufficient accuracy, resolution of borehole curvature is generally less reliable. Relative errors in coordinates perpendicular to the general trends of the boreholes can be ~ 1 to 2 %, which may already generate severe artefacts in the tomogram. Other potential errors include variable shot delays, introduced by the use of different source and triggering systems, and constant delays due to uniformly mispicked phase onsets.

A means to account for these systematic errors is the so-called coupled inverse technique, first presented by Aki & Lee (1976) for tomographic investigations of local earthquake data; since hypocentral coordinates and origin times of earthquakes are initially unknown, they must be estimated during the inversion process.

3.3.1 Methodology

For the purpose of investigating potential mislocations a damped linearised iterative inversion scheme (Marquardt, 1970) has been used to repeatedly solve the following normal equations:

$$m_{k+1} = m_k + (G^T C_D^{-1} G + \lambda I)^{-1} G^T C_D^{-1} \Delta d = m_k + G^{-g} \Delta d \quad (3.8)$$

where m_{k+1} denotes the model parameters obtained from the k th iteration, G the Jacobian matrix, G^{-g} the so-called generalised inverse (e.g. Menke, 1984), C_D a diagonal matrix containing the data variances, Δd the differences between calculated and observed data (i.e. the residuals), and λ a damping factor chosen by trial and error.

A finite-difference approximation to the eikonal equation has been used to compute solutions to the forward problem (Vidale, 1988). Compared to two-point ray tracing, this algorithm yields more reliable results in strongly heterogeneous media (Vidale, 1988; Ammon & Vidale, 1993). Velocities were defined on evenly spaced grids and values between the nodes were linearly interpolated. To ensure accurate synthetic traveltimes, grids twice as dense as those employed for the inversion were used to represent the input models.

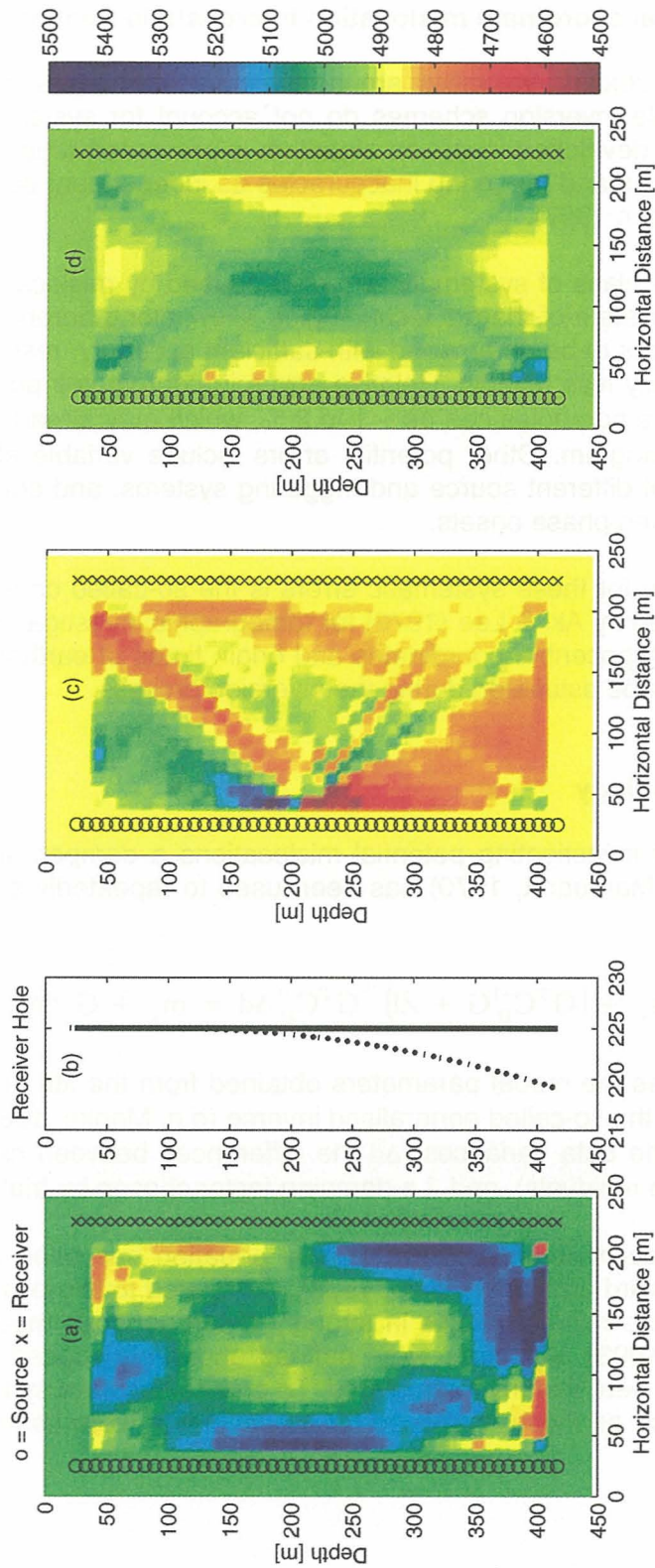


Fig. 3.9

Effects of systematic errors on a constant velocity model (5000 m/s):
 a) Artefacts produced by a slightly curved receiver borehole (shown in b).
 b) Assumed receiver borehole trace (solid straight line) and true borehole trace (dotted line).
 c) Artefacts produced by a constant delay of 0.5 ms for shots deeper than 200 m depth.
 d) Anomaly pattern obtained for an overall delay of 0.5 ms.

Systematic errors may cause timing artefacts that are comparable in magnitude to traveltimes due to true velocity anomalies. Unfortunately, it is often difficult to distinguish between artefacts and real anomalies. This is demonstrated by application of a traditional borehole-to-borehole inversion algorithm (i.e. no account of the possibility of systematic errors) to three simple datasets (Fig. 3.9). Shots located at 50 points along the length of the left hole were recorded by 50 receivers located along the right hole. The velocity model consists of a 5000 m/s homogeneous medium. When no systematic errors are present, the adopted traditional inversion algorithm produces practically perfect results (i.e. a uniform 5000 m/s medium).

Curved Borehole

To calculate the first traveltimes dataset, a slightly curved receiver hole (Fig. 3.9b) was used. In the upper 100 m the hole was linear and the assumed coordinates were correct. With increasing depth, coordinate errors in a direction perpendicular to the borehole were introduced; deviations were in the plane between the boreholes and were proportional to the square of the depth. The resulting tomogram from the traditional inversion (Fig. 3.9a) shows pronounced anomalies (artefacts) between 350 m and 400 m depth and several other velocity perturbations. It is by no means obvious that the anomalies depicted in Figure 3.9a are caused exclusively by receiver mislocations below 100 m depth.

Shot Delays

Figure 3.9c shows the effects of systematic shot delays; for shots at depths greater than 200 m a systematic delay of 0.5 ms was added to the synthetic arrival times. Delays of this order, which represent 1-2 % of the total traveltimes, may occur when different sources or trigger systems are employed. The boreholes in this and the following test were linear and vertical. In isolation, the anomalies in Figure 3.9c would likely be recognised as artefacts. However, they may be difficult to identify when superimposed on a heterogeneous velocity field.

Constant Delay

Inversion results for a dataset that contains a constant delay are shown in Figure 3.9d. Such errors may occur when onsets are systematically mispicked. The relative influence of constant delays depends on the source-receiver distance, such that larger distances are less affected. As shown in Figure 3.9d, these systematic errors lead to a cross-shaped pattern in the tomogram.

Coupled Inversion (CI)

Effects of systematic errors can be reduced by introducing the coordinates of the shots and receivers and the timing delays as additional model parameters. The forward problem can be formulated as:

$$t_{ij} = f(s_i, r_j, \mathbf{u}) + d_i \quad (3.9)$$

where t_{ij} is the arrival time of the initial P-wave from shot s_i recorded at receiver r_j , \mathbf{u} the slowness field and d_i the delay of the i th shot. Shot delays d_i may include the effects of systematically mispicked onsets. In contrast to traditional crosshole applications, the unknown model parameters m (equation (3.8)) consist not only of \mathbf{u} , but also include s , r and d . Unlike local earthquake tomography, receiver positions must also be refined. If a shot and a receiver lie at the same location, they were inverted for a common set of coordinates. As for the slowness derivatives, partial derivatives with respect to shot and receiver coordinates were computed using a finite-difference approximation.

Assumptions and a priori information

Applicability and success of the coupled inversions depend strongly on the experimental geometry. For example, tomographic inversions of local earthquake data require well-constrained hypocenters (e.g. Kissling, 1988). Important parameters that characterise the "quality" of an event include the number of observations and the largest azimuth within which no stations are present (the so-called gap). Generally, only events with a gap less than 180° (inside a network) are considered well-constrained (Kissling, 1988).

Compared with local earthquake investigations, the number of readings per shot in crosshole applications is large. Conversely, the azimuthal coverage is typically poor; due to the geometry of crosshole or even combined crosshole - vertical seismic profiling configurations, it is not possible to achieve gaps of less than 180° for either the shots or the receivers. Nevertheless, there are several reasons why coordinate relocations are practical. First, initial coordinate estimates are usually quite close to the true positions, so that the inversion process most likely reaches the global instead of a local minimum. Secondly, crosshole tomography is a 2D problem in which the sources and receivers lie within the planar velocity field being explored. The under-determined components of such a configuration are much smaller than those of typical local earthquake experiments, which are designed to resolve 3D velocity structures with observational networks positioned on 2D planes (i.e. the earth's surface). An important assumption in the following is that 3D effects are negligible in crosshole data. Furthermore, surveying accuracy in shallow parts of boreholes is generally much better than at greater depths. With the Marquardt inversion scheme this constraint can be implemented by replacing the scalar quantity λ in equation (3.8) with a vector Λ , which may be configured to prevent overly large adjustments to the relatively well-defined shallow coordinates. In the same manner, adjustments of coordinates parallel to the boreholes may be minimised. Finally, that boreholes are usually smoothly varying features offers a further constraint. Within the framework of this study, borehole smoothness has not been applied during the inversion, but instead has been used as a posteriori information to determine the quality of the solution.

3.3.2 Feasibility studies on synthetic data

Before the arrival times observed from the Grimsel experiments were inverted for velocities and borehole coordinates, it was helpful to determine whether there is sufficient information in the datasets to constrain the velocity parameters with the desired resolution and reliability. This was achieved by calculating two synthetic traveltimes datasets for shot-receiver configurations that correspond to the three fields employed in the actual field survey. Actual coordinates used for the forward traveltimes simulations were set to deviate systematically by up to 6 m from the measured coordinates. Figure 3.10 shows the actual and measured shot and receiver locations used for the simulations.

Synthetic Dataset 1: Erroneous borehole locations in a homogeneous medium

First, a homogeneous velocity (5000 m/s) model was employed. If all model parameters were sufficiently constrained, the solution of the coupled inverse problem should adjust the measured coordinates to the actual positions. As shown in Figure 3.11, the

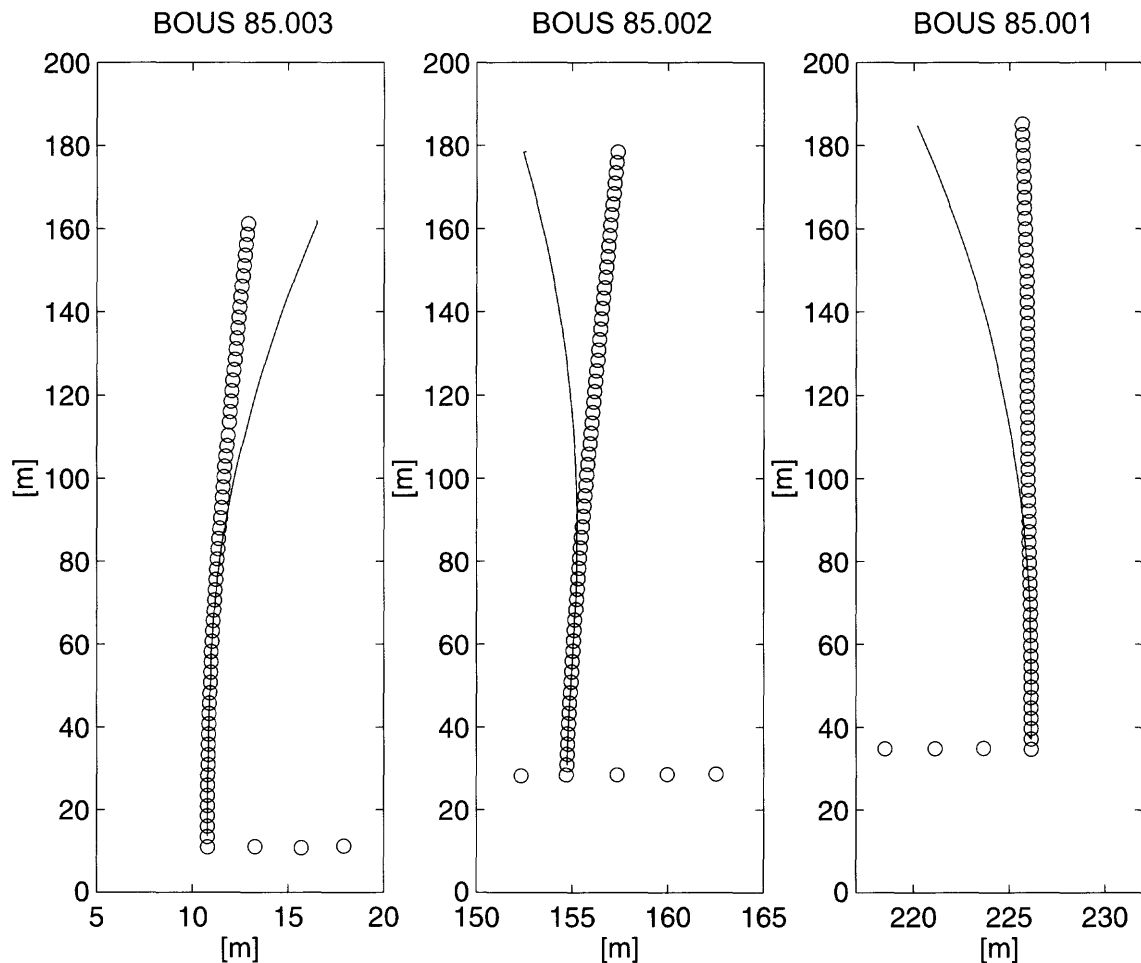


Fig. 3.10 Geometry of boreholes shown with a strong x-axis : y-axis exaggeration (~ 4.75) to highlight the curvature of the boreholes. Measured shot and receiver positions are shown by small circles (from Gelbke, 1988), whereas shot and receiver positions used to compute synthetic traveltimes for the feasibility study are shown by solid lines.

coordinate relocations for all three fields were good. Mislocations of shots and receivers were better than 1 m, whereas initial estimates were wrong by up to 6 m. The best results were obtained when all available data were simultaneously inverted (i.e. fields US1 + US2 + US3). As expected, the true 5000 m/s velocity of the medium was reproduced by the inversion.

Synthetic Dataset 2: Borehole relocations in the presence of realistic velocity anomalies

Maurer (1996) has shown that, for a simple 2-hole configuration exhibiting no pronounced velocity anomalies in the vicinity of the boreholes, only minor trade-offs between velocities and coordinates are expected. By means of our second synthetic experiment, we have sought to determine how well the true coordinates of the Grimsel experiment could be recovered in the case of significant velocity anomalies close to the

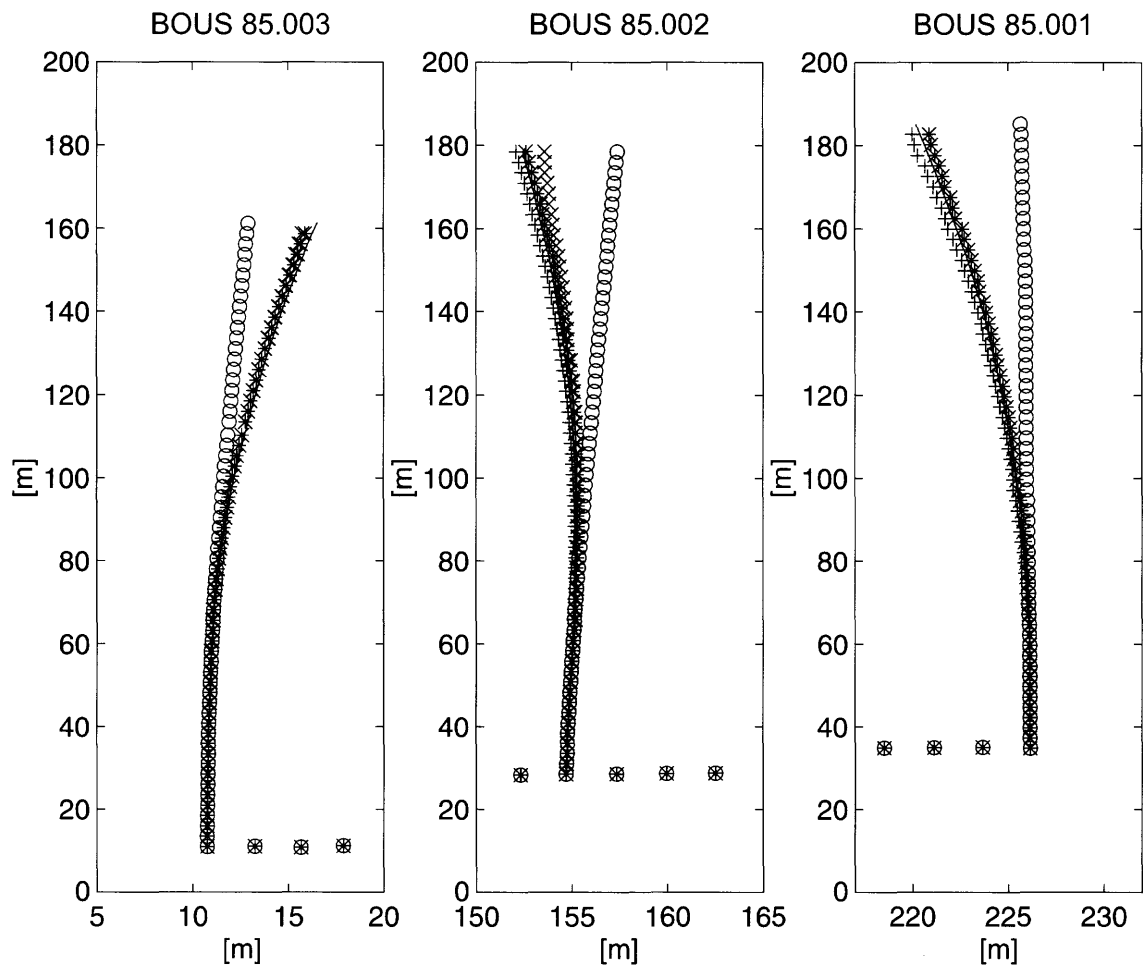


Fig. 3.11 Relocation results for the homogeneous velocity model. Different symbols represent results from the three fields: + = Field US1; x = Field US2; * = Field US3. Due to the good match, it is difficult to distinguish between results of the individual fields.

shots and/or receivers; such anomalies are present in the Grimsel tomograms shown by Gelbke et al. (1989). Figure 3.12 shows the model used for this test. The positive cross-shaped anomaly intersecting borehole BOUS85.002 has been introduced to test the stability of the coupled inversion technique, whereas the low-velocity zone is intended to simulate one of the fracture zones observed at the Grimsel Test Site. Coordinate errors were the same as for the previous synthetic experiment (Fig. 3.10).

Application of a pure velocity inversion (i.e. no account of possible coordinate errors) to these synthetic data results in strongly distorted tomograms (Figs. 3.13a to 3.13c) that include artefacts introduced by the coordinate errors. In all three fields, for the western parts the artefacts are of the same extent and amplitude as the true velocity contrasts. The cross-shaped structure is hardly visible in Field US1 (Fig. 3.13b) and on the right side of Field US3 (Fig. 3.13c).

Modified shot and receiver positions obtained by applying the coupled inversion technique are shown in Figure 3.14. Relocated coordinates for boreholes BOUS85.001 and BOUS85.003 are in good agreement with the actual coordinates, but those determined for borehole BOUS85.002 exhibit some inconsistencies between 60 m and 100 m, with good estimates being provided by the inversion results of Fields US1 and US3 data (plus signs and stars in Fig. 3.14b), and poorer estimates by the inversion results of Field US2 data (crosses in Fig. 3.14b). This effect is due to trade-offs between the velocities and coordinates: the blurred nature of the cross-shaped anomaly in the Field US2 tomogram (Fig. 3.13d) is related to the poorer relocated coordinate estimates (Fig. 3.14b). These trade-offs are probably the result of insufficient intersecting rays within

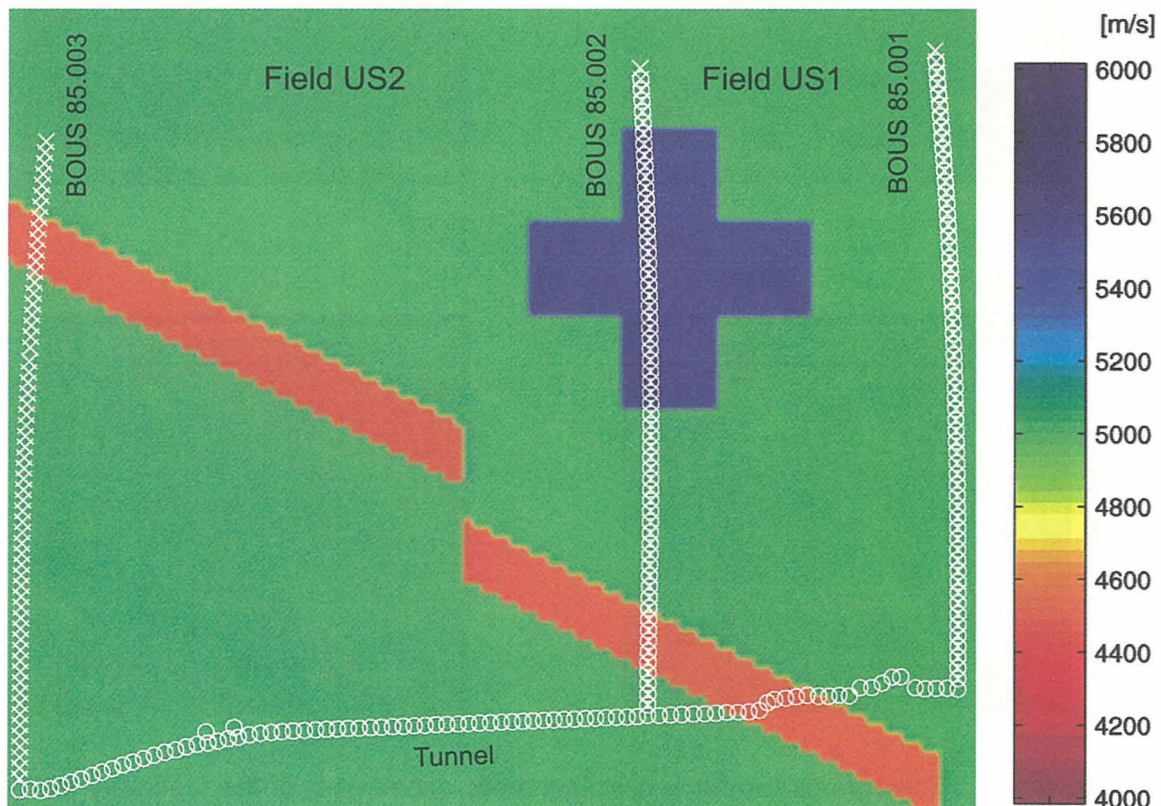


Fig. 3.12 Velocity model used for the second synthetic experiment of the feasibility study. Velocities are in m/s.

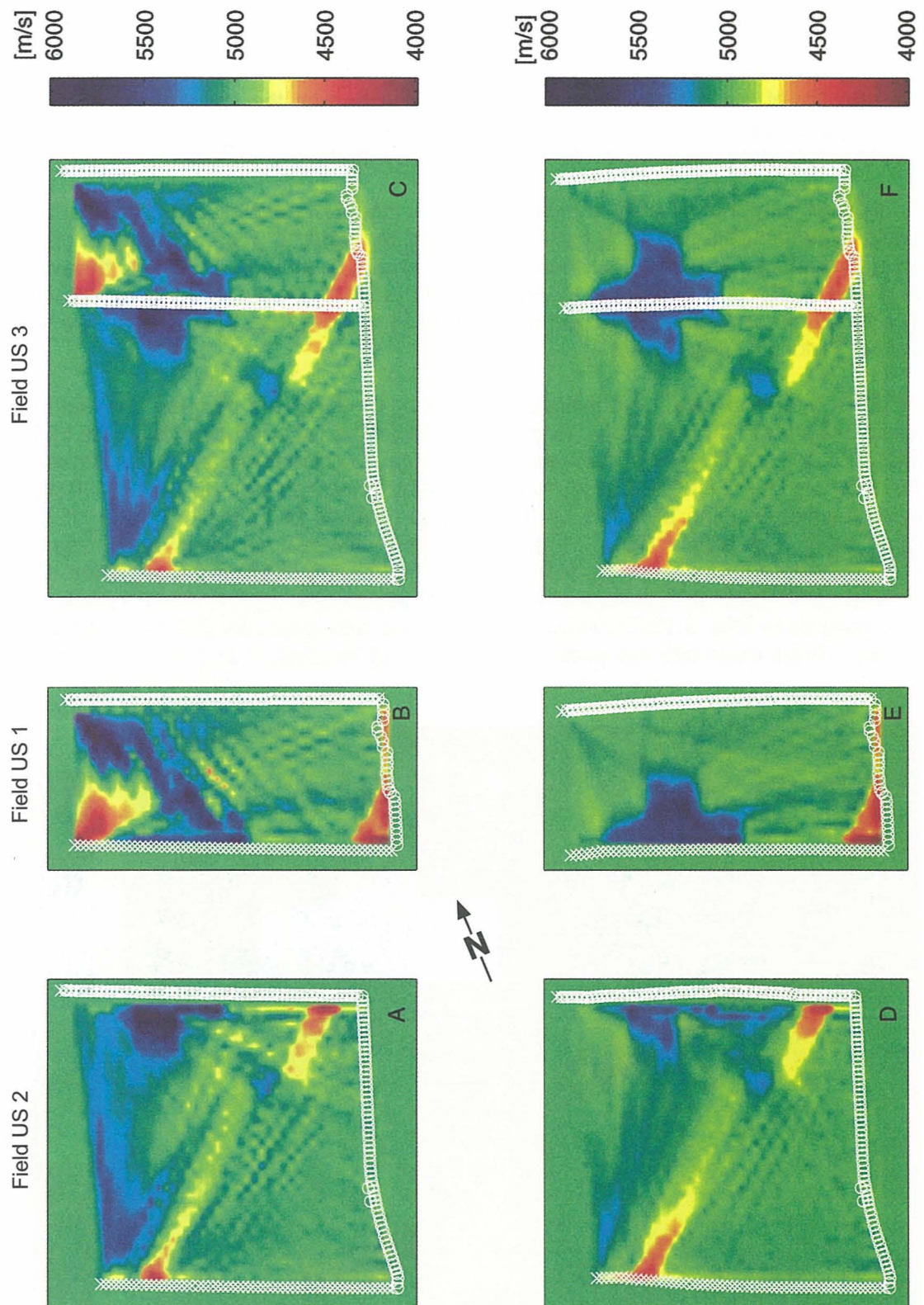


Fig. 3.13 Tomograms for the second synthetic experiment of the feasibility study (input velocity model is shown in Fig. 3.12). The panels a to c show the results of the pure velocity inversions (i.e. no attempt to improve estimates of borehole locations), whereas the panels d to f depict the solutions of the coupled inverse problem. Velocities are in m/s.

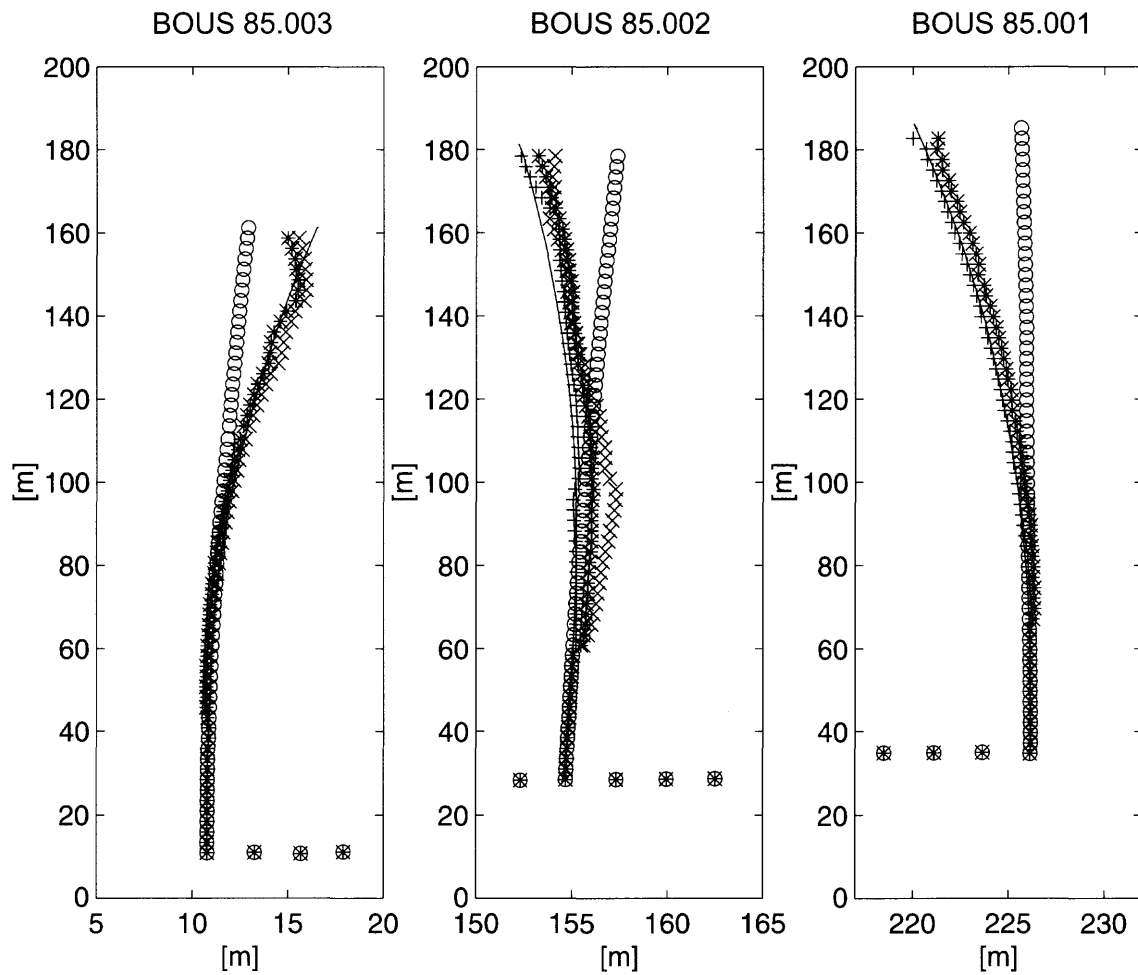


Fig. 3.14 Relocation results of the second synthetic experiment of the feasibility study. Different symbols represent results from the three fields: + = Field US1; x = Field US2; * = Field US3.

Field US2; the smaller distance between boreholes of Field US1 leads to a greater azimuthal coverage of rays than in Field US2 and a correspondingly superior tomographic reconstruction.

The number of intersecting rays between boreholes BOUS85.002 and BOUS85.003 can be enhanced considerably by incorporating additional information from the Field US3 dataset. As a result, the reconstruction of the cross in Field US3 (Fig. 3.13f) and associated relocation results of borehole BOUS85.002 (Fig. 3.14b) are quite good.

The low-velocity zone is well-delineated in all three fields. Since additional data have been included in the Field US3 computations, the resolution of this feature in Figure 3.13f is slightly better than in Figures 3.13d and 3.13e.

Feasibility Study: Summary

Key results of this feasibility study are:

- (a) As for earthquake tomography, shot/receiver coordinates may be treated as variables in crosshole tomographic inversions.
- (b) There seems to be sufficient information in the Grimsel datasets to constrain the important velocity anomalies and the borehole coordinates.
- (c) Pronounced velocity anomalies in the vicinity of boreholes may lead to some trade-offs between borehole coordinates and velocities, such that coordinates are poorly relocated and images of the anomalies are blurred. For the Grimsel experiments, such effects can be detected and partially solved by comparing relocation results from the individual and overlapping fields.
- (d) Since borehole BOUS85.002 is involved in all three inversion fields, its coordinates play a key role in judging the reliability of the coupled inversions.

3.3.3 Inversion results from field data of the Grimsel Test Site

Results of the pure velocity inversions (i.e. no account of possible borehole coordinate errors) and coupled inversions of the Grimsel traveltimes data are shown in Figure 3.15. Due to the averaging of ray velocities in determining the initial homogeneous models for each field, background velocities of the tomograms for the three fields differ slightly from each other (Field US1: 5232 m/s; Field US2: 5132 m/s; Field US3: 5166 m/s). On the basis of the geology we conclude that the 100 m/s difference in average velocity between Fields US1 and US2 is due to the greater degree of fracturing observed in the latter. First-arrival rays from tunnel sources to some near-tunnel borehole receivers traverse the rock mass on the eastern side of the tunnel, thus allowing velocities to be estimated in this region (i.e. velocities east of the three fields in Figs. 3.15a to 3.15f). The exact values of velocity used for the initial model are not critical. For example, nearly identical tomograms to those shown in Figure 3.15 were obtained when the initial velocity was set to 5300 m/s for all fields.

Pure velocity inversions

The left/southern part of the pure velocity tomogram of Field US2 (Fig. 3.15a) is characterised by relatively high velocities (mostly > 5200 m/s) and the right/northern part by generally lower values (mostly < 5100 m/s). Small-scale, large amplitude velocity variations appear along the length of borehole BOUS85.002. Except for broad velocity anomalies in the western part, velocities in the tomogram of Field US1 are fairly chaotic (Fig. 3.15b). The inversion results of Field US3 data (Fig. 3.15c) are very similar to those obtained for the separate Fields US1 and US2. It is noteworthy that for Fields US1 and US2, and for Field US3, velocities on either side of borehole BOUS85.002 only match at the end of this borehole. Since borehole BOUS85.002 does not lie along a mapped geological boundary, this apparent velocity discontinuity may be an indication that the coordinates of its borehole path are wrong.

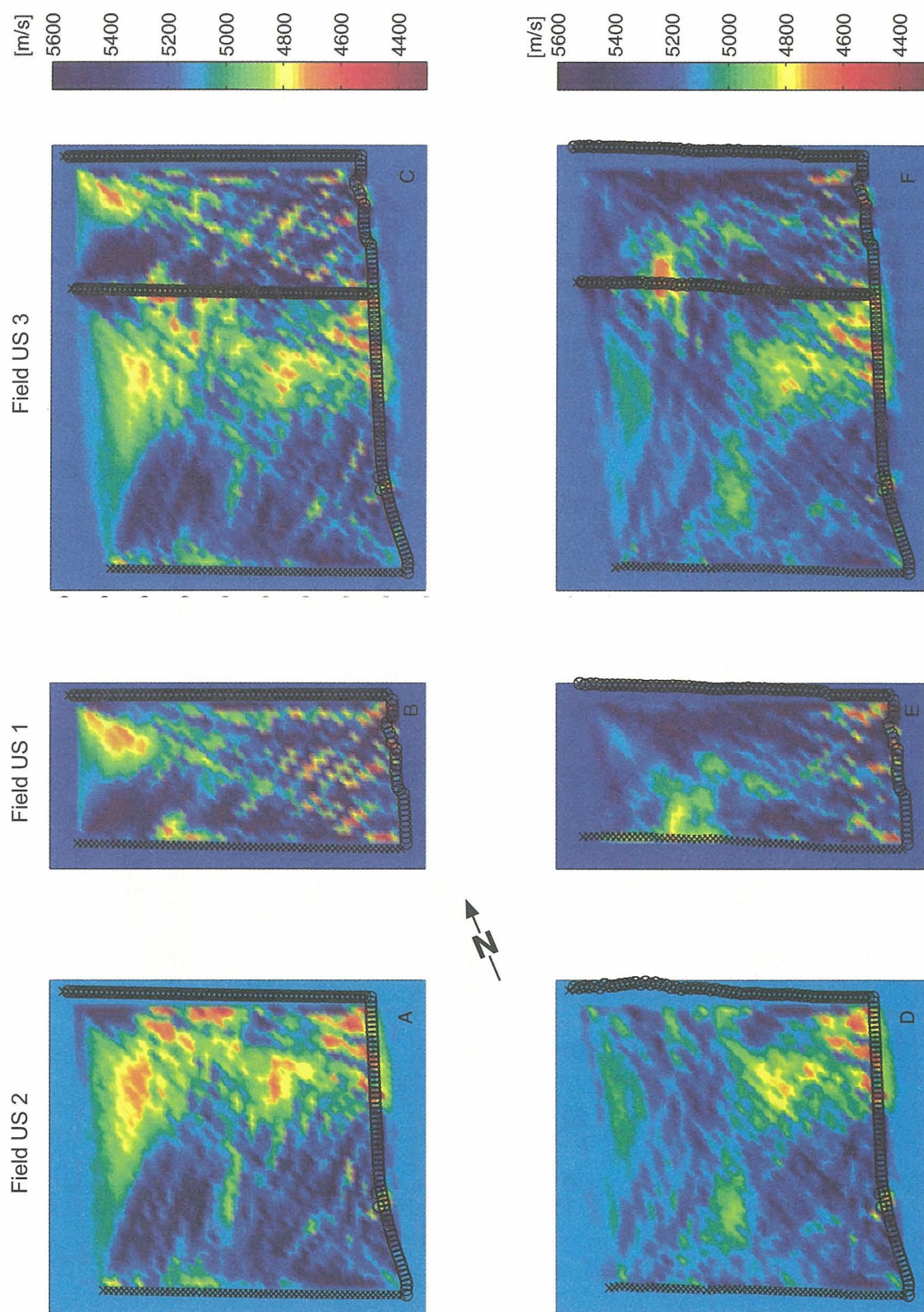


Fig. 3.15 Comparison of tomograms produced by the coupled inversion (CI) derived from the observed Grimsel datasets. The panels a to c show the results of the pure velocity inversions (i.e. no attempt to improve estimates of borehole locations), whereas the panels d to f depict the solutions of the coupled inverse problem. Velocities are in m/s.

Coupled inversions

There are a number of important differences between the velocity tomograms resulting from the coupled inversions (Figs. 3.15d to 3.15f) and those based on the pure velocity inversions (Fig. 3.15a to c). In Figures 3.15d to f, velocity variations in the western part are generally of smaller amplitude, and velocities in Field US1 have a noticeably more systematic pattern. Perhaps the most significant improvement is the continuity of velocities on either side of borehole BOUS85.002, so that the apparent boundary along borehole BOUS85.002 is no longer present (Fig. 3.15f). Due to the slightly different relocations of boreholes computed for the three fields (see next section), there are some noticeable differences between the velocity pattern on the right/eastern side of Field US3 (i.e. between boreholes BOUS85.001 and BOUS85.002) and that in Field US1.

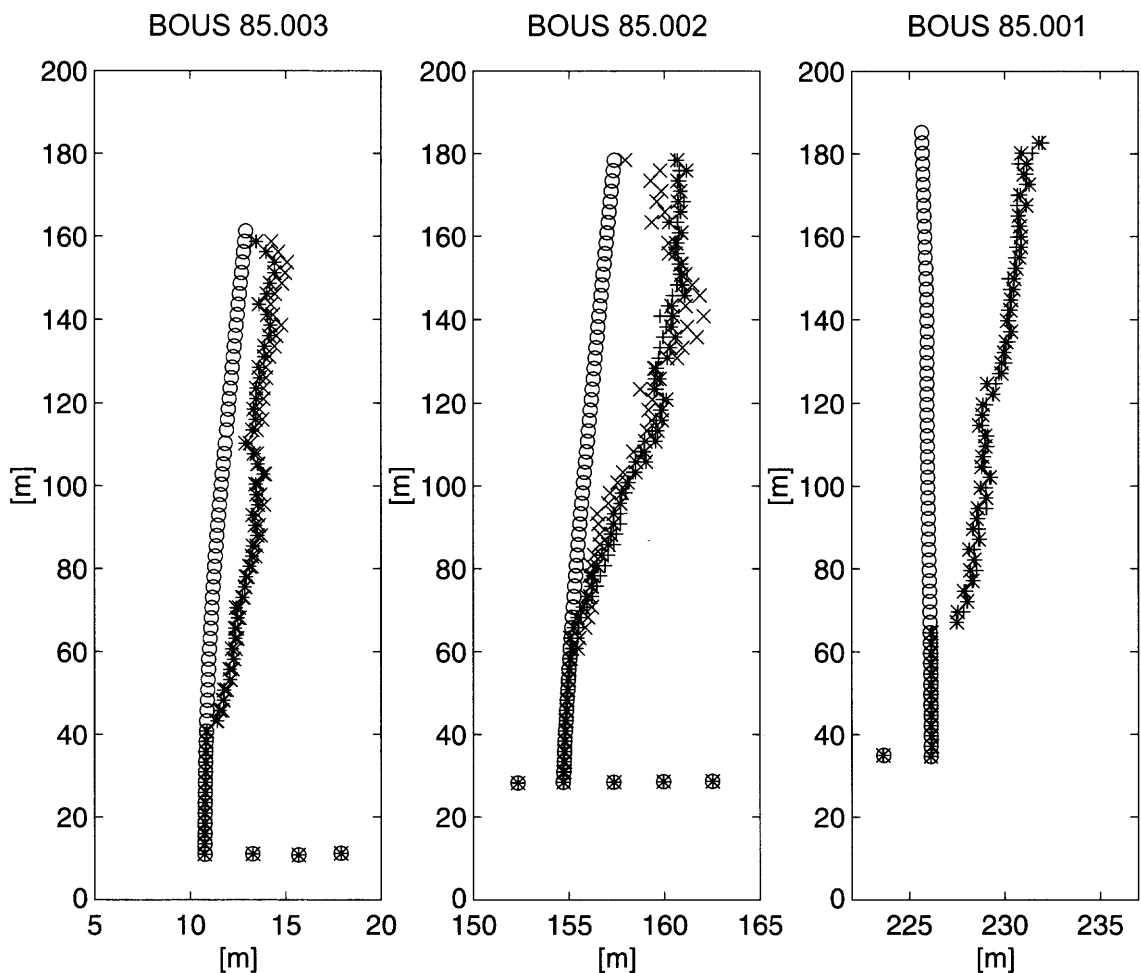


Fig. 3.16 Relocation results of the observed data: + = Field US1, x = Field US2, * = Field US3.

Velocities at grid points outside the original field areas were not changed during the initial coupled inversions (i.e. Figs. 3.15d to f). After the boreholes were relocated, some grid points moved into the investigation fields, so that a variably thin strip of constant velocity values (equal to the input velocity in each case) appears along one or more of the boreholes (e.g. BOUS85.002 in Fig. 3.15d and BOUS85.001 in Figs. 3.15e and f). Velocities along these thin strips may be appropriately adjusted during a second round of inversions in which the relocated coordinates are used as the input coordinates (e.g. Fig. 3.17).

Relocation results

Application of the coupled inversion technique led to the shot and receiver coordinate adjustments shown in Figure 3.16. These adjustments are either quite constant ($y > 80$ m in borehole BOUS85.003; $y > 110$ m in borehole BOUS85.002) or generally increase with distance along the boreholes ($y = 40 - 80$ m in borehole BOUS85.003; $y = 60 - 110$ m in borehole BOUS85.002; most of borehole BOUS85.001), in accordance with the expectation that coordinate accuracy is likely to remain constant or decrease with increasing length along the boreholes. All relocated coordinates lie to the right of the measured coordinates, with maximum adjustments varying from ~ 2 m for borehole BOUS85.003 to ~ 4 m and ~ 5 m for boreholes BOUS85.002 and BOUS85.001, respectively.

The degree to which the different coordinate estimates overlap is remarkable (Fig. 3.16). Relocated coordinates for boreholes BOUS85.001 and BOUS85.002 based on data from Fields US1 and US3, and those for borehole BOUS85.003 based on data from Fields US2 and US3, show nearly perfect matches, such that differences are generally less than a few decimetres. Borehole BOUS85.002 coordinates determined from Field US2 data exhibit some scattering around the positions constrained by data from fields US1 and US3 (Fig. 3.16b). However, the amount of scatter (at most 1 m) is much smaller than the general deviations from the initial locations (up to 4 m). According to the results of the study with synthetic data, the slightly erratic results determined from Field US2 data could be caused by minor trade-offs between velocities and coordinates.

The consistency of the relocation results is good, and the generally smooth nature of the adjusted coordinates is in agreement with the physical requirement that boreholes not exhibit large abrupt directional changes; it should be noted that no a priori smoothness constraints were included in the inversion process. Only for borehole BOUS85.001 (Fig. 3.16c) is an "apparent" discrete change of borehole direction observed. This ~ 1.5 m offset occurs at $y \sim 65$ m. Up to this position (the first 32.5 m of this borehole) the coordinates were fixed at their initial values.

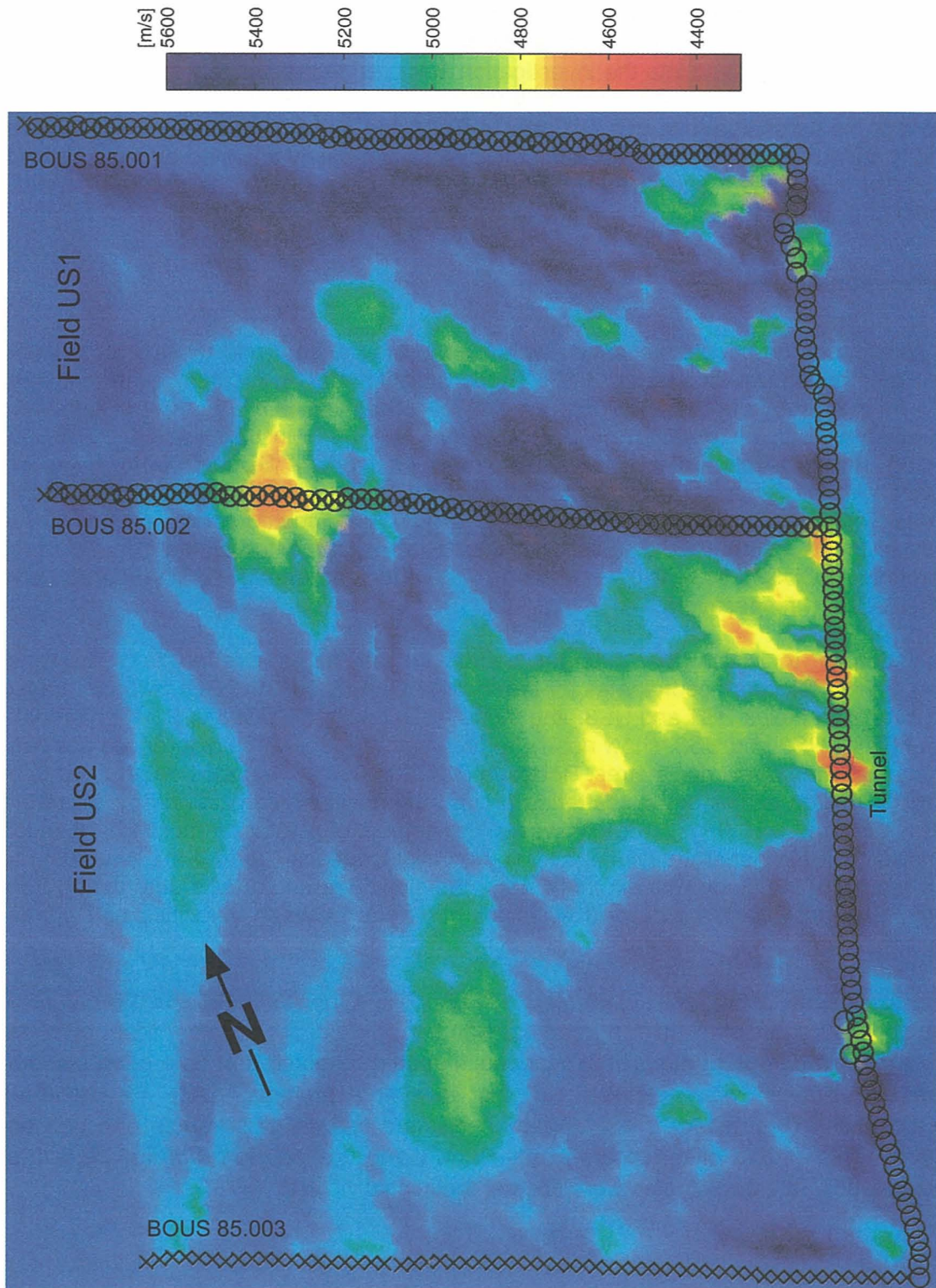


Fig. 3.17 Refined and slightly smoothed version of the tomogram shown in Figure 3.15f. Field US1 lies between boreholes BOUS85.001 and BOUS85.002, Field US2 between boreholes BOUS85.002 and BOUS85.003, and Field US3 between boreholes BOUS85.001 and BOUS85.003. Velocities are in m/s.

Formal model resolutions (diagonal elements of the formal resolution matrices)

To judge the ability of an inversion to resolve a particular model parameter requires consideration of the formal resolution matrix. Since the inverse problem was solved by setting up the normal equations and employing Cholesky decomposition for determining the inverse of the Hessian matrix, calculation of the formal resolution matrix is straightforward (Menke, 1984; Maurer, 1996). Figure 3.18 depicts the diagonal elements of the formal resolution matrix, here defined as the formal model resolutions, corresponding to the velocity tomograms of Figure 3.15. Because there are markedly fewer unknowns involved in the pure velocity inversions than in the coupled inversions, the formal resolution values in Figures 3.18a to c are generally higher than those in Figures 3.18d to f. However, it is significant that the differences between the values in the two sets of figures are quite small and that the patterns of formal resolution estimates are comparable (i.e. adding borehole coordinates as variables has not markedly decreased the resolution of velocities).

Formal resolutions for Field US3 are better than those for the separate inversions of Fields US1 and US2, as would be expected from the superior geometry and increased number of readings employed in the former. They are highest near the centres of the fields, where the densities and azimuth ranges of intersecting rays are greatest, and lowest in the western parts of the fields where they are more limited. It is clear from Figure 3.18 that the cross-shaped fabric connecting the corners of the velocity fields (Fig. 3.15) are artefacts of the recording geometries (see Gelbke et al., 1989 for a figure showing the ray paths employed), and that small-scale variations of velocity in the triangle- to basin-shaped regions in the western parts of all fields are not well resolved. Comparable effects are observed in the synthetic tests of Figures 3.13a to f.

3.3.4 Possible three-dimensional effects and anisotropy

Two different effects could influence the quality of the tomograms, possible 3D effects and anisotropy.

Possible 3D effects

Some features in the tomograms may be caused by velocity anomalies outside the image plane (Mufti, 1995). Since the Grimsel Test Site travelttime tomography includes only first-break information, velocity anomalies with either strong negative contrasts within the image plane or strong positive contrasts outside the image plane would be required for this effect to be a significant problem. Such strong anomalies are neither predicted by the geology nor observed in the various seismic velocity data recorded at the Grimsel Test Site.

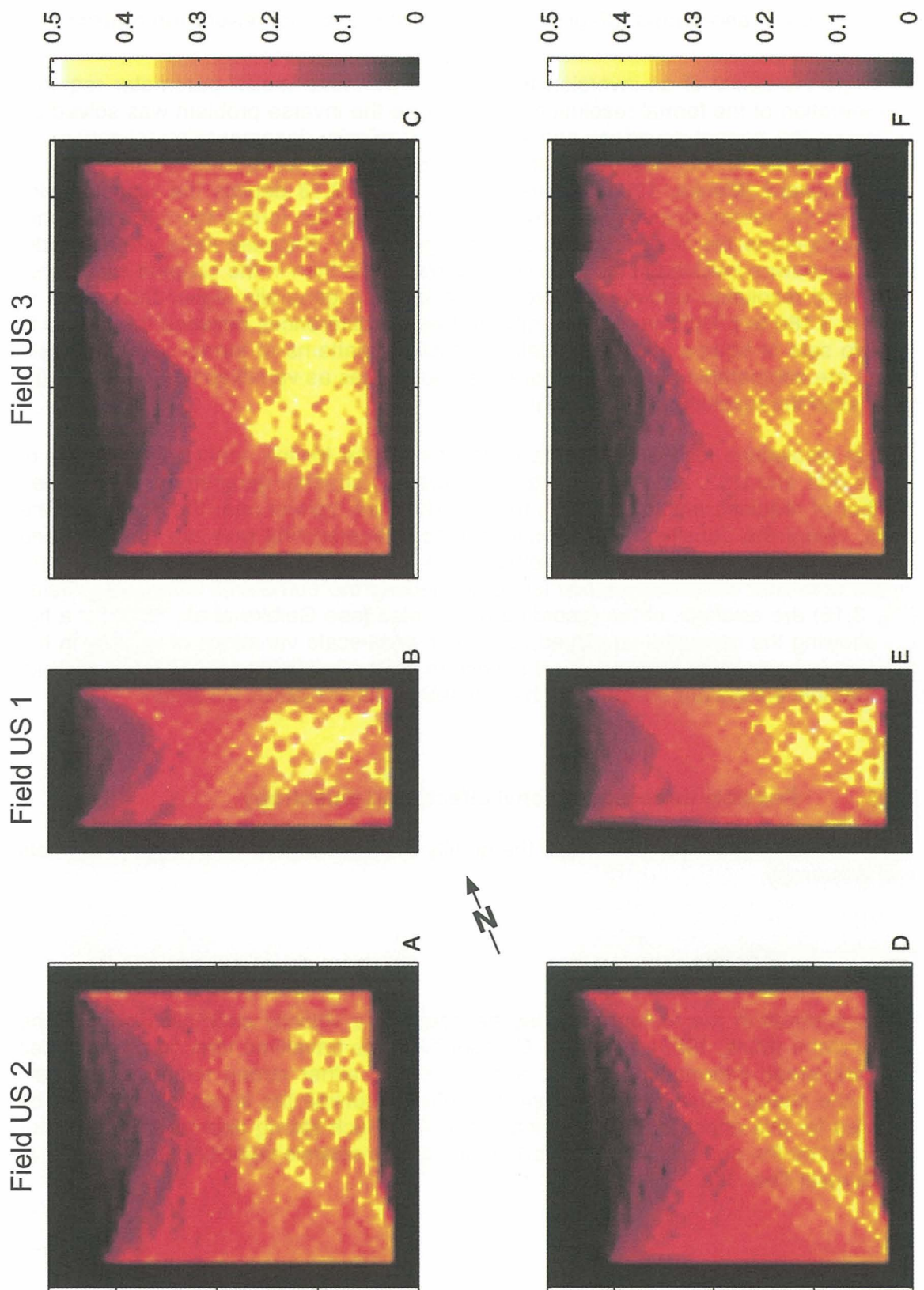


Fig. 3.18 Formal model resolutions (diagonal elements of the formal resolution matrix (Menke, 1984; Maurer, 1996)) of the tomograms shown in Figure 3.15. The values of the diagonal elements indicate whether a particular parameter can be resolved (1 = perfect resolution, 0 = unresolved).

Out-of-plane coordinate errors are as likely as mislocations within the image plane. Fortunately, they have little influence on the results presented here. For example, if a maximum out-of-plane error of 5 m is assumed for sources and receivers separated by 150 m (a value equal to the maximum in-plane separation in this study), the recording distance would be altered by a mere ~ 0.08 m.

Possible anisotropy

In an earlier study by Gelbke et al. (1989), the effects of interpreted uniform velocity anisotropy were removed from the Grimsel traveltimes datasets before they were inverted. The degree (fixed at 1% for the entire investigation site) and direction of anisotropy (northeast-southwest directed maximum velocities) were estimated from velocity versus azimuth plots. Gelbke et al. (1989) corrected tomographic images look quite similar to those shown in Figure 3.15d to f, except in regions more distant from the tunnel (western part of the fields in Fig. 3.15), where Gelbke's velocity anomalies have similarly high amplitudes to those observed in the pure velocity tomograms of Figures 3.15a to c.

Our synthetic model study has demonstrated that the Grimsel traveltimes datasets should provide sufficient constraints for relatively accurate relocations of shot and receiver coordinates and for a reliable determination of velocities over most of the study area. On the other hand, allowing for anisotropy, which has been recognised as an important effect in numerous crosshole tomographic studies (Chapman and Pratt, 1992; Pratt and Chapman, 1992; Pratt et al., 1993; Sams et al., 1993; Williamson et al., 1993; Michelena, et al., 1993, 1995; Pratt and Sams, 1996), this leads to images (Chapter 3.2) that are similar to those produced by the coupled inversions of the Grimsel datasets (Figs. 3.15d to f). In the following, we explore the influence that anisotropy would have on the coupled inversions by applying some simple synthetic examples. In particular, given independent datasets recorded in Grimsel Fields US1 and US2, we wish to determine if uniform anisotropy could produce the effects that led to the borehole relocations shown in Fig. 3.16 (i.e. all relocated coordinates lying to the right of the measured estimates and coincident relocated coordinates for the common borehole BOUS85.002).

Various synthetic datasets have been calculated for homogeneous media characterised by weak anisotropy. For the sake of simplicity and lack of better knowledge, pure elliptical anisotropy has been assumed, so that P-wave velocity V varies as (modified from Thomsen, 1986):

$$V = V_{\max} (1 - \varepsilon \sin^2 (\theta - \phi)), \quad (3.10)$$

where V_{\max} is the maximum P-wave velocity, ε the degree of anisotropy (i.e. fractional difference between the maximum and minimum velocities), θ the azimuth of the wavefront normal (i.e. the ray), and ϕ the azimuth of maximum velocity. The anisotropy factor ε was chosen to be 0.05, corresponding to 5% anisotropy. This value was found to be useful for demonstrating the potential influence of anisotropy on coordinate relocations. Simulations were computed for $V_{\max} = 5000$ m/s and for four different azimuths of maximum velocity: $\phi = 20^\circ, 65^\circ, 110^\circ$ and 155° , which correspond to angles of $0^\circ, 45^\circ, 90^\circ$ and 135° relative to the x-axes of previous figures.

As for the observed Grimsel traveltime data, these synthetic data were inverted for isotropic velocities and coordinate adjustments. A comparison of the relocation results shown in Figure 3.19 with those given in Figure 3.16 demonstrates that weak homogeneous elliptical anisotropy with maximum velocity along $\phi = 65^\circ$ reproduces some of the important features in the observed dataset: the relocated coordinates of all boreholes are on the same side of the measured estimates (compare Fig. 3.19d with Fig. 3.16) and the two estimates of relocated coordinates for borehole BOUS85.002 coin-

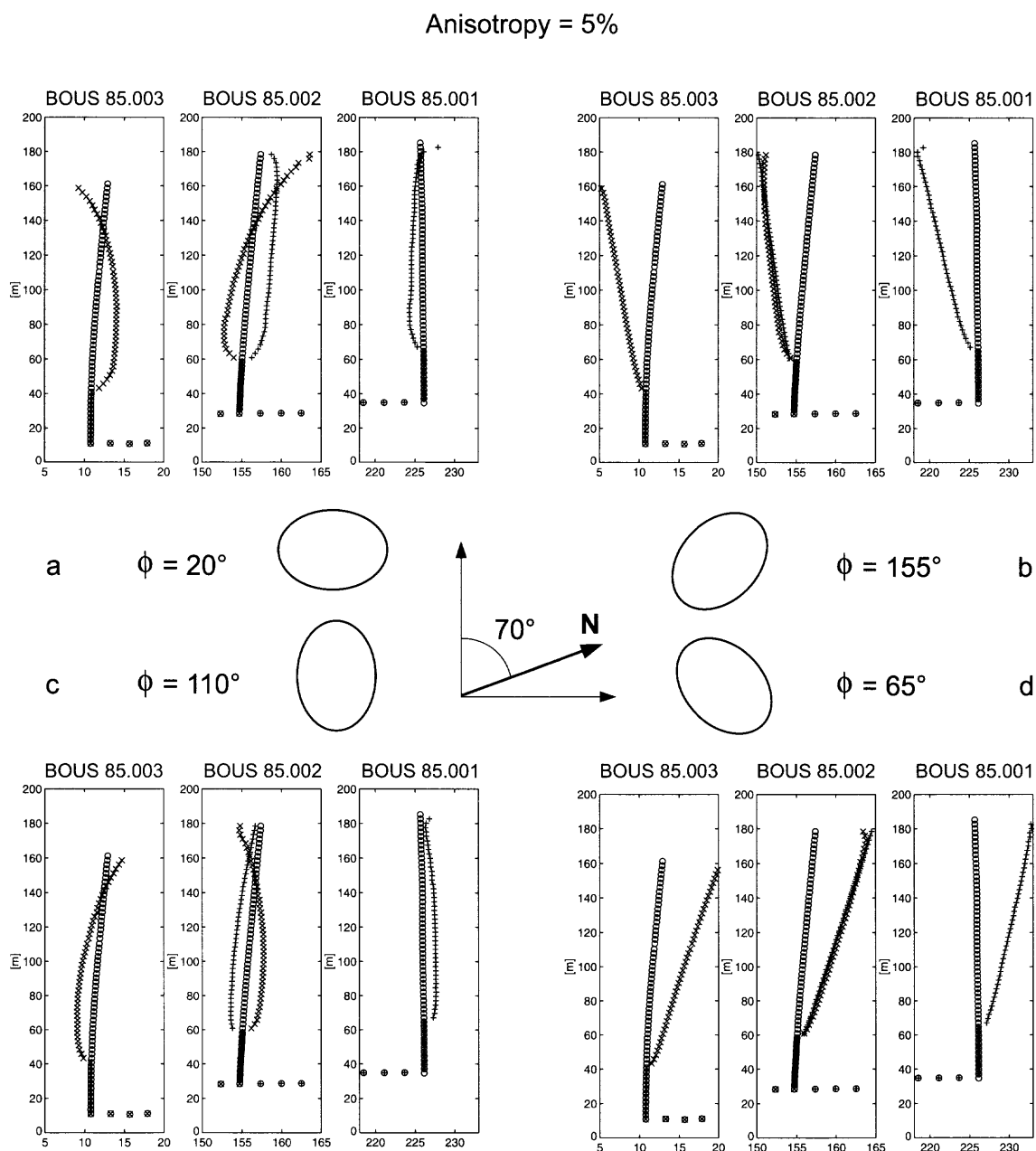


Fig. 3.19

Inversion results of synthetic traveltime data that include an elliptical anisotropy of $\epsilon = -0.05$ and four different azimuths ϕ of the fast axis: 20° , 65° , 110° and 155° , which correspond to angles of 0° , 45° , 90° and 135° relative to the x-axes of other figures. + = Field US1, x = Field US2.

cide. Furthermore, the input homogeneous velocity field is correctly determined by the inversion. However, the varying coordinate adjustments in Figure 3.16 (e.g. maximum of 2, 4 and 5 m for boreholes BOUS85.003, BOUS85.002 and BOUS85.001 respectively) are not reproduced in Figure 3.19d, which, in contrast, shows similar adjustments for all three boreholes. For other orientations of the anisotropy ellipse (Figs 3.19a to c), either the relocated coordinates are on the other side of the measured values, or the two sets of relocated coordinate estimates for borehole BOUS85.002 do not coincide.

3.4 Coordinate errors versus anisotropy

The similarities of the tomographic images (Chapter 3.1, 3.2 & 3.3) together with the results of the synthetic study presented in Figure 3.19 suggest that there may be trade-offs between minor coordinate mislocations and weak velocity anisotropy in the Grimsel traveltimes data. Points that need to be considered in assessing the relative contributions of these two effects are:

- (a) A simple and consistent pattern of borehole relocations results from application of the coupled inversion technique to the Grimsel traveltimes data. The smooth nature of the adjusted coordinates is compatible with the physical requirement that boreholes in relatively homogeneous crystalline rock do not exhibit large abrupt directional changes. Agreement between the two sets of borehole BOUS85.002 coordinate estimates, based on independent data from Fields US1 and US2, is impressive. Although the maximum estimated 4-5 m borehole coordinate adjustments exceed the "expected" 2-3 m (1-2 %) survey accuracy, they are not implausible.
- (b) Synthetic traveltimes variations based on the geometry of the Grimsel boreholes and the estimated dominant northeast-southwest orientation of the anisotropy ellipse (Gelbke et al., 1989) may be modelled by a pattern of borehole adjustments that resemble those obtained for the observed Grimsel traveltimes data (Fig. 3.19d). The fact that coupled inversions of traveltimes data, affected by northeast-southwest oriented anisotropy, produce matching coordinate estimates for the common borehole BOUS85.002 is a remarkable coincidence; computations using significantly different orientations of the anisotropy ellipse do not reproduce the pattern of relocated coordinates based on the observed Grimsel traveltimes data.
- (c) Although the pattern of relocated coordinates in Figures 3.19d and 3.16 is similar, there is one significant discrepancy: adjustments in all three boreholes are simple and of comparable magnitude in Figure 3.19d, whereas for the observed data of Figure 3.16 the pattern of adjustments is different for each borehole and their magnitudes vary by more than a factor of two between boreholes BOUS85.001 and BOUS85.003.
- (d) The northeast-southwest direction of anisotropy estimated by Gelbke et al. (1989) parallels some important geological fabrics (fracture and shear zones) observed within the Grimsel Test Site.
- (e) There is a small but significant discrete step in the relocated receiver coordinates of borehole BOUS85.001 at 32.5 m along the borehole (Fig. 3.16c). It is near to

this location that receiver coordinate damping markedly changes. There are two possible explanations for the discrete offset. The shallow receiver positions may have been fixed at erroneous locations. Alternatively, the observed offset may be explained by the effects of anisotropy; Figure 3.19d shows a similar discrete offset between the first part of the borehole BOUS85.003 (the first 32.5 m) which were fixed and the rest of the borehole which were relocated.

- (f) The tomogram which represents the amount of anisotropy (Fig. 3.7) shows a clear transition from Field US2 to Field US1 at borehole BOUS85.002. The poor agreement can be explained by uncertainties in the borehole path coordinates.

There seems to be little doubt that minor coordinate mislocations and, at the same time, a weak anisotropy are both critical factors in the Grimsel traveltimes dataset. However, to completely separate the effects of slightly erroneous source and receiver coordinates from those originating due to weak northeast-southwest oriented elliptical anisotropy will be difficult on the basis of traveltimes data alone. For future borehole-to-borehole and tunnel-to-borehole experiments, it will be important to design the source-receiver geometries such that the effects of systematic errors may be distinguished from the influences of anisotropy. For example, at the Grimsel Test Site, this could be achieved by means of tests employing additional boreholes oriented at $\sim 45^\circ$ to the other boreholes.

4. WAVEFIELD INVERSION

Seismic traveltimes tomography, though robust and efficient, is limited in the resolution that it can achieve. Wave equation methods have better resolution but are generally non-quantitative. Wavefield inversion offers the prospect of high-resolution quantitative inversion of seismic data, and the frequency domain is naturally efficient for such problems. Song et al. (1995) developed a frequency domain full wavefield non-linear iterative inversion (WFI).

The objective of a joint project of Imperial College and Nagra was to apply this wavefield inversion to real data recorded at the Grimsel Test Site (Fields US1 and US2) in order to achieve reconstruction with higher resolution than that from traveltimes tomography.

Because of the particularities of the Field US1 and US2 data, such as the large size of the model, inclusion of VSP data, existence of anisotropy and elasticity, synthetic tests are necessary before final application to the real data. A first synthetic test is the inversion of acoustic data for an isotropic medium. This is to examine what can be achieved for the Grimsel model in an ideal case. The second step is to fully process an elastic wave dataset computed by a third party, to use this processing to identify an optimal pre-processing sequence for the real data, and finally to fully process the Field US1 and Field US2 data. All three of these objectives have been met. The final results presented in this Chapter represent a significant improvement in the resolution of the velocity images when compared to all previous methods used on these data (such as those provided by traveltimes tomography: Chapter 3). We are convinced that the wavefield method used in this project is unique in its ability to extract the wavelength scale features of the velocity variations.

4.1 Methodology

The inverse problem can be formulated as a least-squares optimisation (Tarantola 1984, 1987; Song & Worthington 1995; Song et al. 1995), i.e. the minimisation of:

$$S(m) = \frac{1}{2} (P_{\text{obs}} - P(m)) * C_p^{-1} (P_{\text{obs}} - P(m)) \quad (4.1)$$

where P_{obs} is a vector of the observed data, with the frequency domain components corresponding to the source-receiver pairs, $P(m)$ is the vector of the estimated data for the current model m , C_p is the covariance operator in data space, and $*$ represents the adjoint operator. The gradient of $S(m)$ with respect to the model space m is:

$$\mathbf{g} = \frac{\partial S}{\partial m} = -L * C_p^{-1} \delta P \quad (4.2)$$

where L^* is the adjoint of the Fréchet derivative of $P(m)$, and $\delta P = P_{\text{obs}} - P(m)$ denotes the data residuals. For the constant density acoustic wave equation the only relevant model parameter is the velocity, and the gradient δv^+ is a vector in the dual space of the velocity. The direction of steepest descent is then obtained by applying an appropriate

model covariance operator, C_m (Tarantola, 1987), and this defines a possible direction for upgrading the model:

$$\mathbf{v}_{i+1} = \mathbf{v}_i + \alpha_i C_m \delta \hat{\mathbf{v}}_i \quad (4.3)$$

Here α_i is a step length chosen carefully to give optimum convergence.

The Fréchet derivative operator is then defined by the Born approximation:

$$\delta P = L \delta v \quad (4.4)$$

and the expression for the gradient is correspondingly (Song et al., 1995):

$$\delta \hat{v}(r) = \frac{\omega^2}{\pi v_0^3(r)} \sum_{k_y} \Delta k_y \sum_s [P_b(r, k_y) \cdot P_0^*(r, k_y)] \quad (4.5)$$

where

$$P_b(r, k_y) = \sum_g \delta \hat{P}(r_g) G_{2.5}^*(r; r_g, k_y) \quad (4.6)$$

This represents backpropagation of weighted pressure residuals from receiver positions and correlation of the result with the original forward modelled wavefield for each source.

The wavefield inversion procedure is summarised by the following steps:

1. The procedure is initiated from some appropriate starting model. This will usually be obtained using traveltimes tomography.
2. A single or multiple temporal "imaging" frequency is chosen and the Fourier component of the data at this frequency is extracted from the recorded time domain data, yielding one (complex) frequency component for each source-receiver pair in the data. Usually the data will be pre-processed to remove shear waves and other late arrivals by time domain windowing and the amplitudes will be normalised in some fashion before computing the Fourier components.
3. A forward finite difference simulation is run in the current velocity model. A frequency domain method (Pratt, 1990, improved by Jo et al., 1996) is used to simulate the data at the imaging frequency only. In contrast to a time domain approach, this approach is much better suited for forward modelling for a large number of source positions.
4. Data residuals are formed by subtracting the frequency domain data from step 2 from the modelled data from step 3. (If these residuals are small, the process has converged.)
5. A "descent direction" in the model parameters is sought that will reduce the residuals in step 4. This descent direction, or "gradient vector", can be very efficiently computed with a single additional modelling step, in which the time reversed data residuals are used as sources in the computation. The product of this "backpropagated" wavefield with the original wavefield forms an image of the anomalous velocity regions, in a manner analogous to seismic migration.

6. A "step length" is obtained that allows us to scale the gradient vector from step 5 in velocity units, and provides an optimal reduction in the residuals. The gradient vector is then scaled and subtracted from the current model to form an updated (improved) velocity model.
7. Iteration is done by returning to step 2, until achieving an acceptable fit at the current imaging frequency. Generally between 5 and 10 iterations are run at a given imaging frequency.
8. Then steps 2 through 7 with selection of imaging frequencies from within the bandwidth of the data are repeated. The choice of frequency interval is largely governed by the width of the time window used to pre-process the data. The final image will contain information from all imaging frequencies chosen during the inversion procedure. Because a wave theory is used in the imaging process, the smoothing effects of diffractions on the traveltimes are effectively unravelled during the imaging procedure.

There are several critical choices to be made during the inversion procedure outlined above. These include selecting an appropriate pre-processing sequence for the input data, choosing an appropriate sequence of imaging frequencies, and choosing an appropriate level of regularisation to apply to each gradient vector as it is computed, in order to stabilise the procedure. Each of these choices will be illustrated later in this Chapter with reference to the processing of the real data.

4.2 Results with synthetic data

In order to validate the wavefield inversion approach in a realistic model, and to provide a control dataset that could be used to test the effect on the imaging of various processing parameters, it was decided to build a velocity model that mimics some of the expected velocity variation at the Grimsel Test Site. The model simulates the Field US2 area. The size of the area is about 145 m by 150 m, with a background velocity of 5.2 km/s and a number of velocity perturbations between 10 and 20 %. The model is depicted in Figure Fig. 4.1a. The large low velocity zone in the lower right-hand section of the model represents the known presence of lamprophyre dykes that intersect the tunnel wall (the bottom of the figure) and the thin, dipping features represent the known fracture directions at the site. There is a low velocity zone situated at the top of the model. This zone lies within a region with poor coverage, and will serve to illustrate the image degradation of features not well covered by the data. A low velocity perturbation in the region of the tunnel represents possible excavation damage. The largest frequency used in the model was 1000 Hz, at which the smallest wavelength in the model is about 5 m. The frequency domain modelling method of Jo et al. (1996) is used, which requires that the grid contains 3 to 4 grid points (in each direction) per wavelength. Therefore acoustic wave propagation in the model was simulated using a grid of $126 \times 134 = 16,884$ nodes.

Because the acoustic modelling method described in the previous paragraph is the same as used in the wavefield inversion process, it was important to also generate a synthetic dataset with the same model, using an elastic wave modelling code. This is because it was unknown how the method would be affected by the presence of elastic modes, such as direct and mode converted shear waves. The data for this test were provided by Professor M. Korn at the University of Leipzig. These data are full 2D, two component simulations of the displacement field. At the time the modelling was carried

out, it was not possible to generate equivalent elastic wave data at Imperial College for the large number of source positions involved. In the meantime, Štekl & Pratt (1998) have developed an elastic modelling capability using the same rotated operator approach used by Jo et al. (1996) for the acoustic wave equation, and now the modelling can be carried out at Imperial College.

In both acoustic and elastic simulations, sources and receivers were placed to simulate the actual Field US2 survey. Sixty sources were placed along the tunnel location and

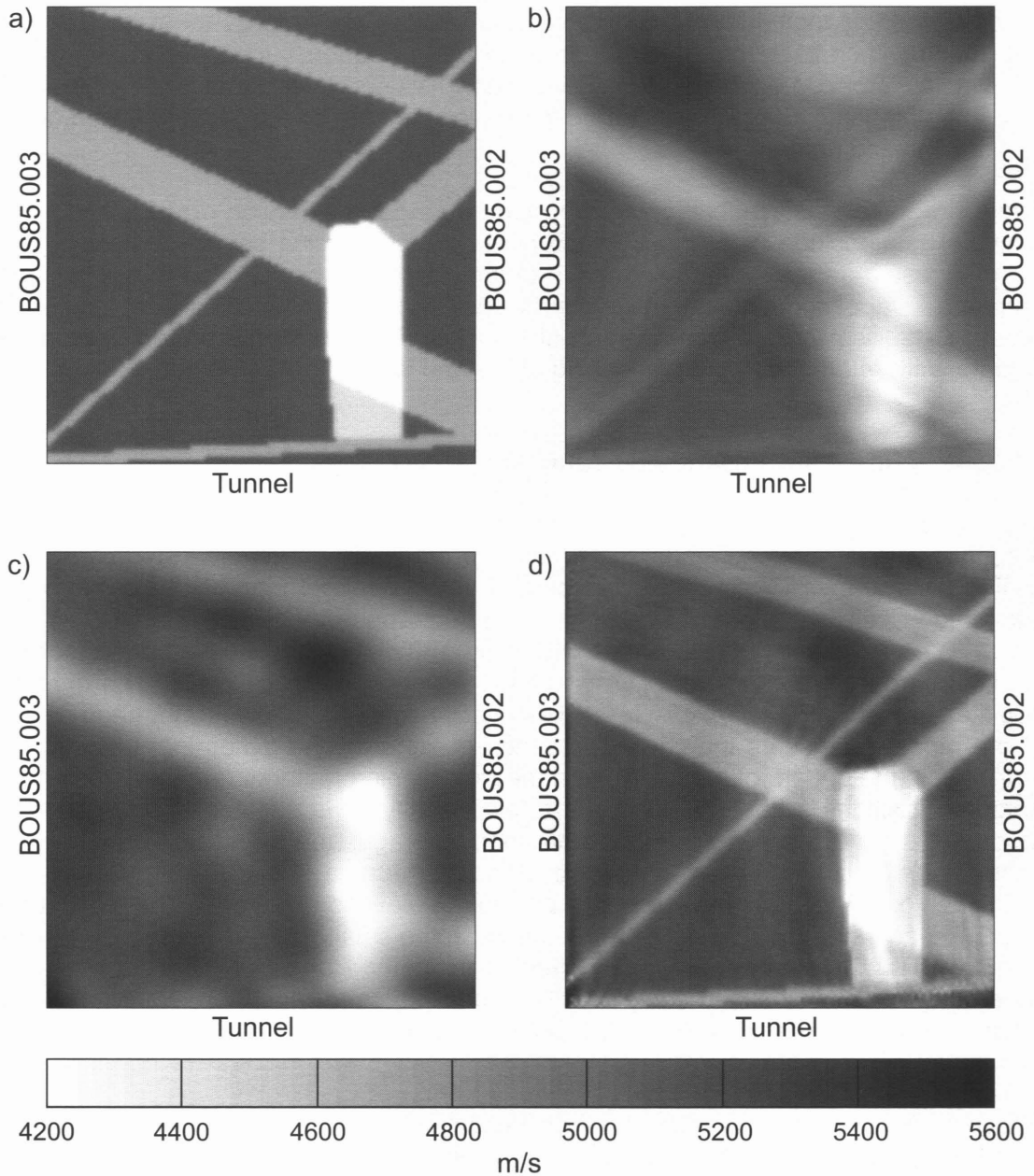


Fig. 4.1 Acoustic wavefield inversion of synthetic acoustic data. a) Model of schematic velocity distribution in Field US2. b) Traveltime tomography result obtained from manual picking of elastic synthetic time domain data. c) Acoustic wavefield inversion result, using 100 Hz data. d) Acoustic wavefield inversion result using 1000 Hz data.

sixty further sources were placed in borehole BOUS85.002, and receivers were located in both boreholes. A simulated crosshole dataset was recorded between BOUS85.002 and BOUS85.003, and two VSP datasets were recorded from the tunnel to each of boreholes BOUS85.002 and BOUS85.003. All source and receiver spacings were 2.5 m. All simulations were run in two dimensions (2D). Because of the advantage of working in the frequency domain, Imperial College was able to generate acoustic data at only a limited number of imaging frequencies (100 Hz through 1000 Hz, in 100 Hz steps). The elastic data were generated in the time domain.

4.2.1 Acoustic synthetic data: imaging results

Figure 4.1b shows an image obtained from synthetic data using traveltimes tomography. Because only the elastic synthetic data (s. Chapter 4.2.2) were simulated in the time domain, only these elastic synthetic data could be used to generate traveltimes by manual picking. The traveltimes image is a good representation of the true model, but is somewhat smeared in the two 45 degree directions. This smearing effect is a direct consequence of the limited aperture of the survey and of the limited resolution of the traveltimes method. The resolution of a traveltimes reconstruction is not expected to reconstruct anomalies much smaller than the first Fresnel zone in size (Williamson 1991; Williamson & Worthington 1993), given approximately as $\sqrt[3]{L\lambda}$ where L is the propagation distance and λ is the wavelength. Here, for a frequency of 1000 Hz, λ is about 5 m. For a propagation distance of 100 m, this gives a Fresnel zone width of approximately 20 m. We have thus been able to reconstruct the larger velocity anomalies, but there is only a faint hint of the thin, dipping velocity anomaly. There is a severe imaging problem associated with the low velocity zone at the top of the image.

Figure 4.1c shows the result of using four iterations to reconstruct the velocities from the 100 Hz data alone. Even at this very low imaging frequency, with a wavelength of about 50 m, the reconstruction is comparable to the traveltimes reconstruction. It is less successful at reconstructing the thin simulated fracture zone running from the bottom left to the top right corner, but more successful at reconstructing the anomaly at the top of the image. The image is consistent with the expectations from theoretical considerations, which predict a resolution length of approximately half a wavelength (Song & Worthington, 1995).

Figure 4.1d shows the image obtained using all imaging frequencies between 200 Hz and 1000 Hz. The lower limit was chosen with reference to the real data, which contained no useful signal below 200 Hz. The image was formed using 6 frequency components of the data: 200, 300, 500, 700, 800 and 1000 Hz. Each frequency component was used for a maximum of 5 iterations before moving to the next frequency, using the current image as a starting model for the next frequency. The final frequency was used for 10 iterations. The individual frequency components were iterated upon until convergence, defined as the point beyond which the algorithm could no longer reduce the misfit function.

In Figure 4.1d it is evident that there is considerable improvement with respect to the traveltimes image shown in Figure 4.1b. In particular, the exact geometry of the low velocity "dyke" at the bottom right is perfectly resolved, and all simulated fracture zones have been recovered. The magnitudes of the velocity values are very close to the "true" velocity values.

Figure 4.2 shows the results of a number of tests in which the survey geometry was deliberately restricted. The effects of carrying out only a crosshole survey (Figure 4.2a), only the two VSP surveys (Figure 4.2b) or only one of the two VSP surveys (Figure 4.2c and Figure 4.2d) are shown. It is evident that the crosshole survey is the least important in resolving the simulated dyke feature, but contributes significantly to the imaging of the fractures. Only when all three surveys are combined (as in Figure 4.1d) are all features of the model optimally resolved. The extra cost in computation is minimal.

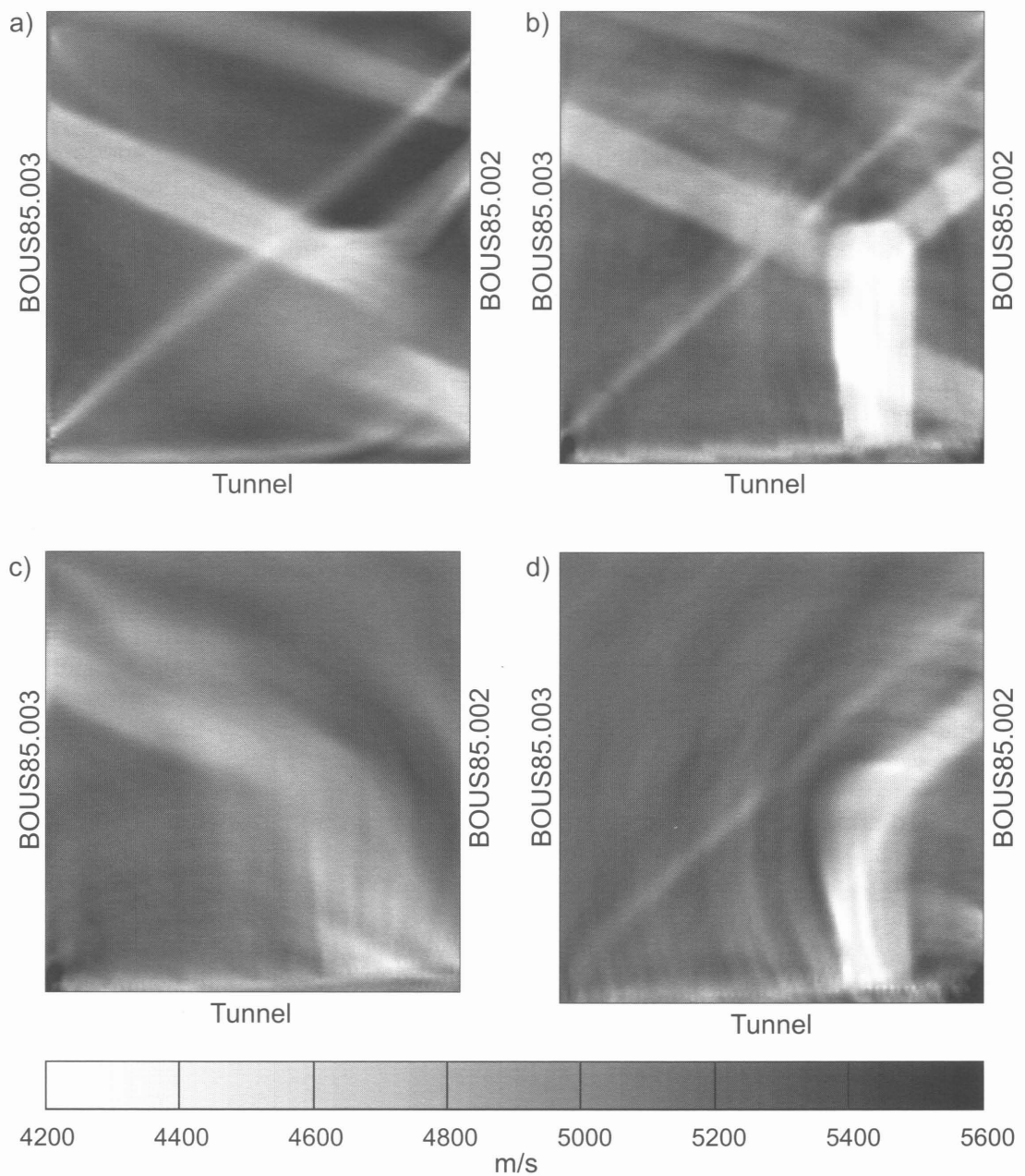


Fig. 4.2: Acoustic wavefield inversion of synthetic acoustic data: Tests of survey geometry. a) Crosshole data, b) both VSP datasets, c) left-hand VSP d) right-hand VSP, all formed using 1000 Hz data, as in Figure 4.1d).

4.2.2 Elastic synthetic data: imaging results

After the successful test of the wavefield inversion with an acoustic synthetic dataset we can continue with testing the inversion on more realistic elastic synthetic data. This dataset was generated by Prof. Korn of Leipzig University, using a time domain finite difference method. The velocity model used for this numerical experiment is identical to that used for the acoustic wave study of the previous section, and is shown again in Figure 4.3a. The data are two-component displacements, and may be considered to be roughly equivalent to two-component geophone data.

In order to process these synthetic data, in preparation for the processing to be used for the real data, the following pre-processing steps were undertaken:

- i) Project the two-component geophone data onto a local coordinate system defined by straight ray paths.
- ii) Window the projected wavefield first arrivals in time using an exponentially tapered time window 15 ms wide, starting 5 ms before the picked arrival time.
- iii) Trace-normalise the windowed data to remove trace-to-trace amplitude variations.
- iv) Use traveltimes tomography to produce a starting model for wavefield inversion.

In the following paragraphs we summarise the reasoning behind the application of each of these steps.

Data projection is used to transform the two component displacement data into single component data. This is required since the inversion software models only acoustic, compressional waves, and hence requires data that represent equivalent pressure field variations. By geometrically projecting the two components onto the straight ray direction we enhance the compressional waves and partly eliminate the shear waves. This step was largely successful in eliminating most of the shear wave energy in the synthetic elastic data.

Data windowing should ensure that only the first arrival, transmission wavefields are in the data. Transmission data are more suitable for wavefield inversion than reflections. Windowing also serves to exclude remaining shear wave energy from the data.

Trace normalisation is not generally necessary, but the amplitude variations in the field data of the Grimsel Test Site make this step essential when processing the real data. We therefore included this step with the synthetic data in order to assess the effect, detrimental or otherwise, on the inversion scheme.

In order to initialise the wavefield inversion scheme, it is necessary to begin with an adequate starting model. This model should be capable of describing the time domain data to within a half of the dominant period, in order to avoid fitting the wrong cycle of the wavefields. The lower the frequency, the less accurate the starting model need be; however all real data are band limited and thus a certain accuracy is required of the starting model. In the real data, the lowest frequencies are corrupted by an unacceptable amount of noise. We therefore chose to generate an accurate initial model using traveltimes tomography and proceed with the wavefield inversion using the higher frequencies.

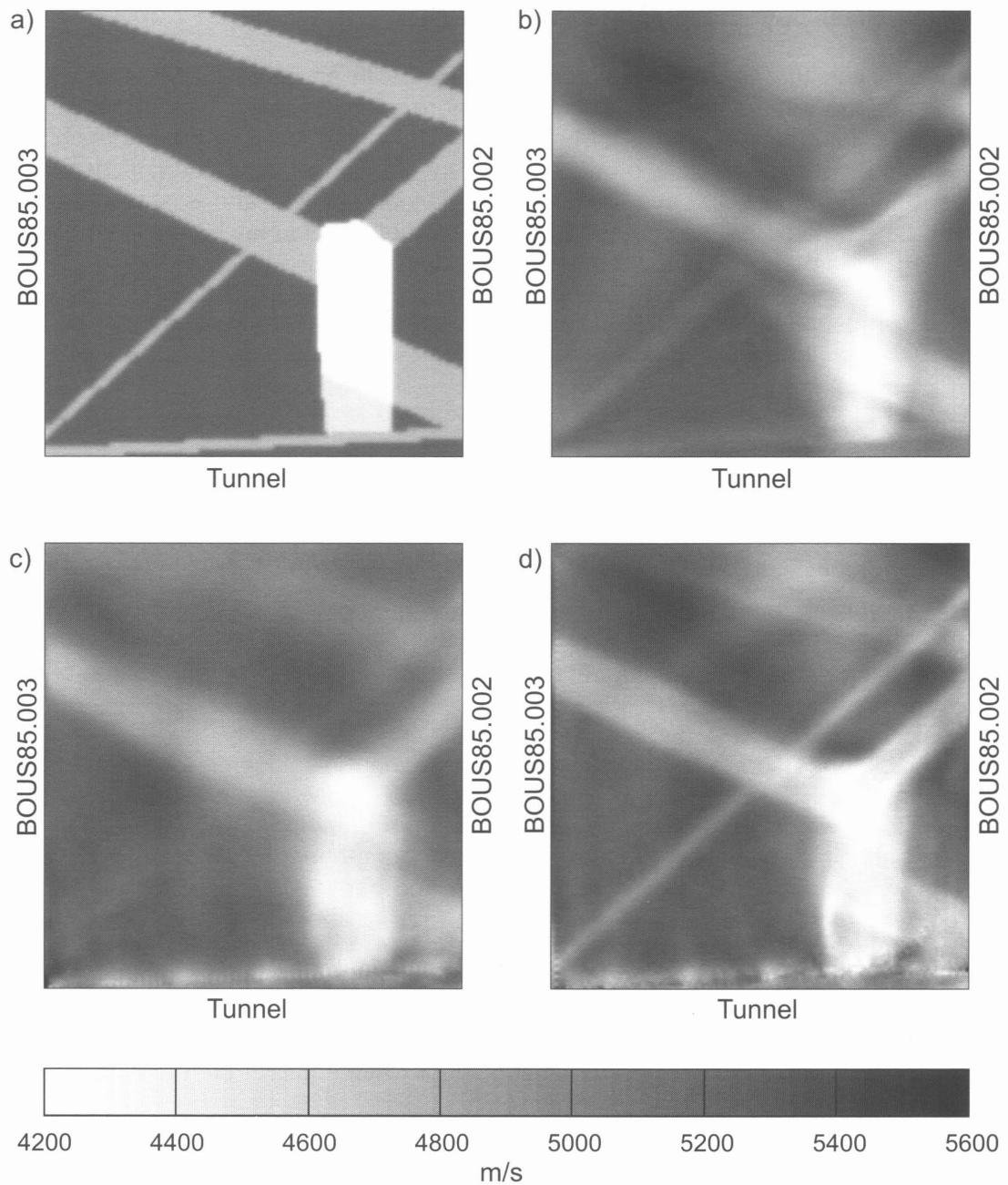


Fig. 4.3: Acoustic wavefield inversion of synthetic elastic data. a) True model (same as in Figure 4.1a), b) traveltime inversion, c) acoustic inversion of original data d) acoustic inversion of windowed, normalised data.

Traveltime tomography using the synthetic data

All arrival times in the full synthetic dataset were picked and used to produce a velocity image using the anisotropic velocity tomography (s. Chapter 3.2). On the synthetic dataset here the velocity image has been calculated only for the isotropic case. The result is shown in Figure 4.3b and is identical with the result shown in Figure 4.1b.

Wavefield inversion of non-preprocessed synthetic data

Wavefield inversion was carried out of the projected synthetic data in order to verify the processing approach for the field data. The result of wavefield inversion for the non-preprocessed synthetic data is shown in Figure 4.3c. As with the acoustic wave data, these images were formed using 6 frequency components of the data: 200, 300, 500, 700, 800 and 1000 Hz, using the same convergence strategy as before. In Figure 4.3c it is evident that there is some improvement with respect to the travelttime image shown in Figure 4.3b. In particular, the exact geometry of the low velocity "dyke" at the bottom right is better resolved, and there is a subtle improvement in the geometry of most of the features. Moreover, the magnitudes of the velocity values are closer to the true velocity values of the model. Nevertheless, this image so far is just about comparable in resolution to the travelttime image.

Wavefield inversion of trace-normalised synthetic data

In order to investigate whether the inaccurate amplitude simulation of the acoustic inversion method is adversely affected by the elastic wave amplitudes in the synthetic data, and furthermore to verify completely the approach for processing field data (see below), wavefield inversion was carried out of trace-normalised synthetic data. This was necessary for the field data due to high amplitude variations - here the normalisation as a pre-processing step was verified. As the image in Figure 4.3d shows, the final result is a significant improvement over the result from the non-normalised data. All important features are better recovered than from the non-normalised data. While inverting these data we found that the convergence rate was higher for the normalised dataset. The result confirms that the main source of information in transmission data is in the wavefield itself and not in the trace-to-trace amplitude variations. It will be appreciated that amplitude pre-processing is important in this case, since elastic wave amplitudes are affected in a different manner than acoustic amplitudes.

It is clear from this examination (Fig. 4.3) that smaller anomalies, completely overlooked by travelttime tomography, are completely recovered and correctly positioned by wavefield inversion for all anomalies that lie in the region with good coverage. It is, however, possible to obtain false anomalies in the regions with poor coverage (at the top of the model), where the travelttime result has generated a low velocity anomaly. This anomaly is transferred into the full wavefield result by using the travelttime tomogram as an initial guess. This can be avoided in synthetic studies, in which, in most cases, we can start the wavefield inversion from a homogeneous model. However, when working with real data it is usually impossible to use sufficiently low frequency data, so that a better initial guess is required.

In conclusion, once the data have been trace-normalised, wavefield inversion produces images in which the low velocity anomalies are much better resolved than on the travelttime tomographic image, and the velocity values are closer to the ones in the model. It is important to point out that this is a significant test of the method, as the data were generated by an independent third party using an elastic wave simulation. The inversion software uses an acoustic wave method, which ignores elastic effects, and the images justify the use of this approximation. These synthetic tests are therefore more realistic than those presented in the previous section, in which synthetic data were generated, but using exactly the same acoustic software as used in the inversion.

4.3 Inversion of field data

Having successfully demonstrated the wavefield inversion technique on elastic synthetic data, and having verified many of the pre-processing techniques required, we now turn our attention to the real data. The most significant problem with the real data identified in Song & Worthington (1995) was the trace-to-trace amplitude variation. An example of this amplitude variation is shown in Figure 4.4, in which the common source VSP data can be seen to have serious amplitude variations from one receiver to the next. We saw in the previous section that the synthetic, third party, elastic wave data could be successfully processed by normalising each seismic trace separately according to its maximum amplitude. As we shall see in this section, the problems arising from the amplitude variations in the real data have been entirely solved by trace-normalisation of the data.

The pre-processing flow for the real data, with one exception, was identical to the pre-processing used for the elastic synthetic data. The full procedure was:

- i) Project the two-component geophone data onto a local coordinate system defined by straight ray paths.
- ii) Window the projected wavefield first arrivals in time using an exponentially tapered time window 15 ms wide, starting 5 ms before the picked arrival time.
- iii) Trace-normalise the windowed data to remove spurious trace-to-trace amplitude variations.
- iv) Use traveltimes tomography to produce a starting model for wavefield inversion.
- v) Separate the unknown source behaviour into distinct physical "groups". Four individual groups were used for the Field US2 VSP data, and one additional group was used to represent all of the Field US2 crosshole data. Figure 4.5 shows in which manner these groups were identified for the Field US2 data. For Field US1, although on some shot gathers alternate receiver traces were correlated better with each other than adjacent receiver traces (see Figure 4.6), the identification of separate source groups was not possible. Instead, for Field US1, all VSP sources were assumed to have the same behaviour and all crosshole sources were assumed to have the same behaviour.

The additional step here, not used with the synthetic data, was the manner in which the unknown source behaviour was separated into distinct groups and solved for. For the synthetic data we solved for the source behaviour, but we treated the entire dataset as if it came from a single physical source. The field data are known to contain significant source-consistent static time shifts (as commented on by Gelbke et al., 1989). An example of these static time shifts is shown in Figure 4.5.

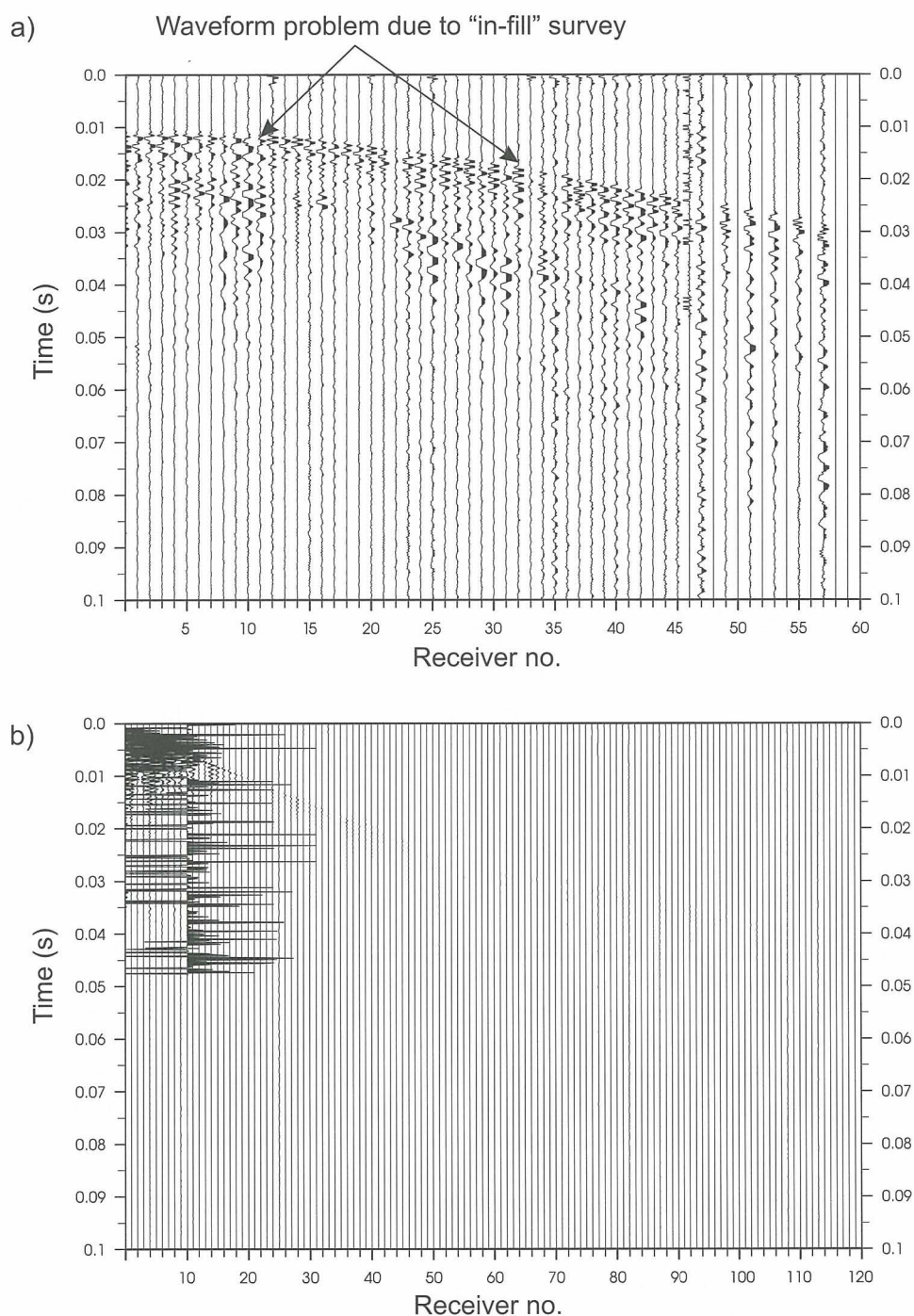


Fig. 4.4: Two representative source gathers of VSP data from Field US2, as true amplitude displays. a) A VSP source gather with large offset. The spurious variation of amplitude from trace to trace is evident, as is the lack of consistency of alternate traces. The data were recorded in two passes, with intermediate traces recorded during a later "in-fill" survey. b) A near offset VSP source gather, on which the dramatic change in amplitude with receiver depth is evident. These variations in amplitudes cannot be modelled using the 2D acoustic method. As described in the text, in order to invert these data a normalisation was applied separately to each trace.

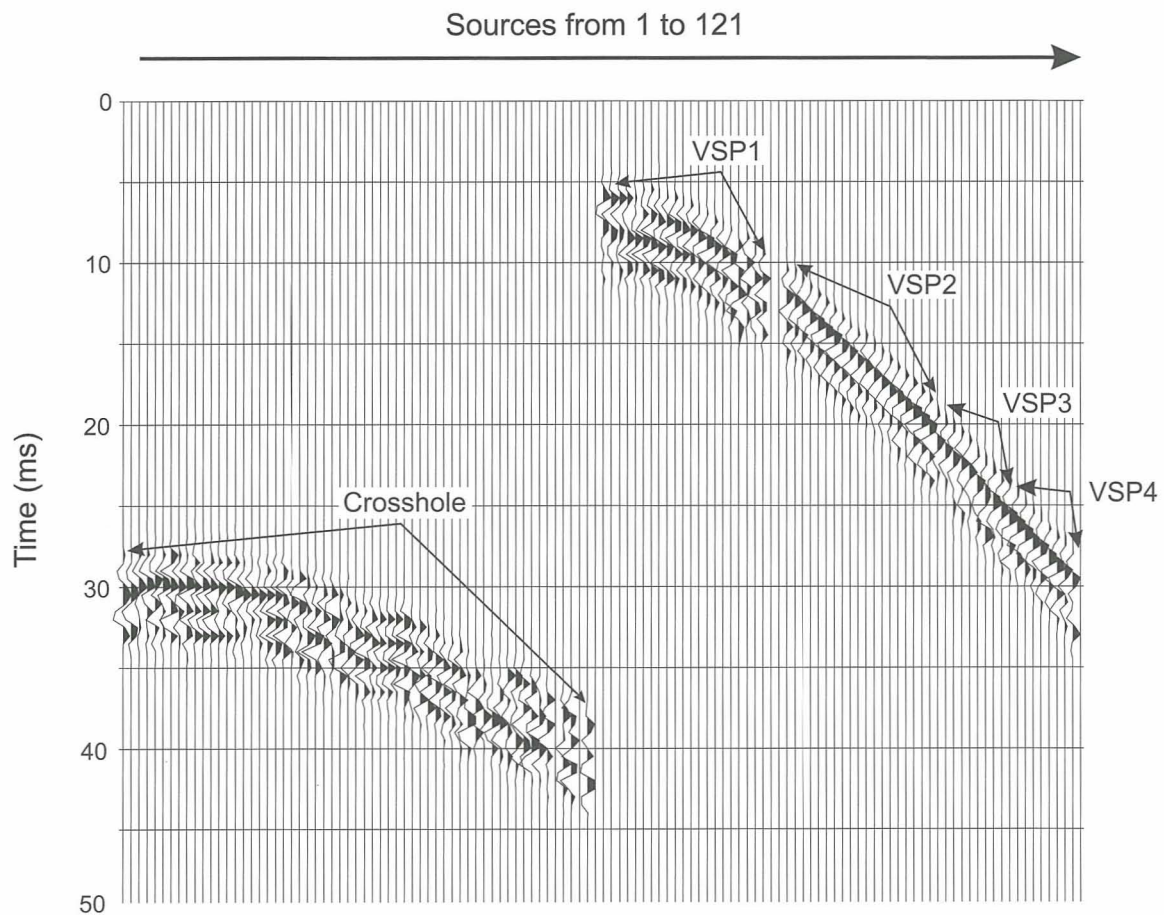


Fig. 4.5: A representative common receiver gather of the Field US2 data. The receiver was in borehole BOUS85.003. The first portion of the gather was recorded with sources in borehole BOUS85.002, and thus represents a portion of the crosshole data. The second section was recorded with sources in the tunnel, and thus represents a portion of the VSP data. The data have been windowed and trace-normalised. The random static shifts in the crosshole data and the systematic static shifts in the VSP data are evident. The labels indicate the VSP source groups that were identified, in order to solve for the source-consistent static shifts.

The source-consistent static time shifts were included into the inverse problem by using 4 separate VSP source "groups" for the Field US2 data, and solving for 4 separate source functions. Using more than one source group does not significantly affect the uniqueness of the inversion approach, but it is essential that these source-consistent errors be accounted for. There are also random source and receiver static shifts in the crosshole data that are not accounted for. The random nature of these latter problems causes a decrease in the signal to noise level of the final images (see next section), but does not cause a significant systematic deterioration of the images. For the Field US1 data, it was not possible to identify separate source groups, and instead all Field US1 VSP data are treated as if they originate from a single source - again it is assumed that the source variation is essentially random between sources. However, the Field US1 inversions did allow for a different behaviour between the crosshole sources and the VSP sources.

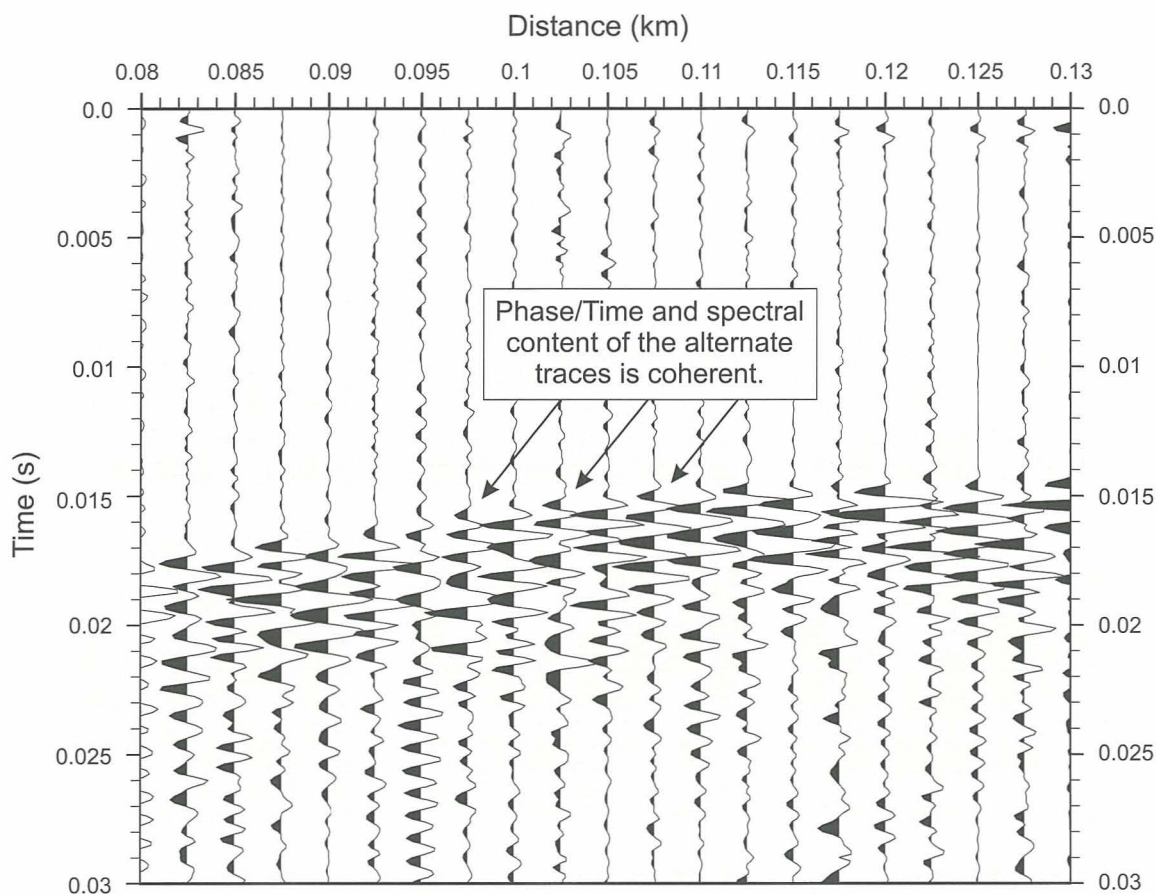


Fig. 4.6: A small section of the Field US1 seismic wavefield data, from shotpoint 121 (crosshole data). This demonstrates the data problems referred to in the text - every alternate trace contains a small phase shift, possibly due to slightly different instrumentation specifications between the initial and "in-fill" surveys.

4.3.1 Isotropic wavefield inversion

All the wavefield inversion images computed were initiated using a starting model obtained from isotropic image of the anisotropic velocity tomography, as described in Chapter 3.2.

After initial tests a further decision was made to attempt to control remaining noise in the images by applying a constraint on the roughness of the solutions (we term this a "smoothing constraint"). This constraint is similar to the constraint used by Pratt & Chapman (1992) for travelt ime tomography (Chapter 3.2). The objective is to form images that contain no unnecessary structure - the only structure that should appear in the images is the structure required to fit the data.

From the pre-processed field data for Field US2 a series of full wavefield inversion results with various levels of smoothing parameters were generated. The resulting images are shown in Figure 4.7.

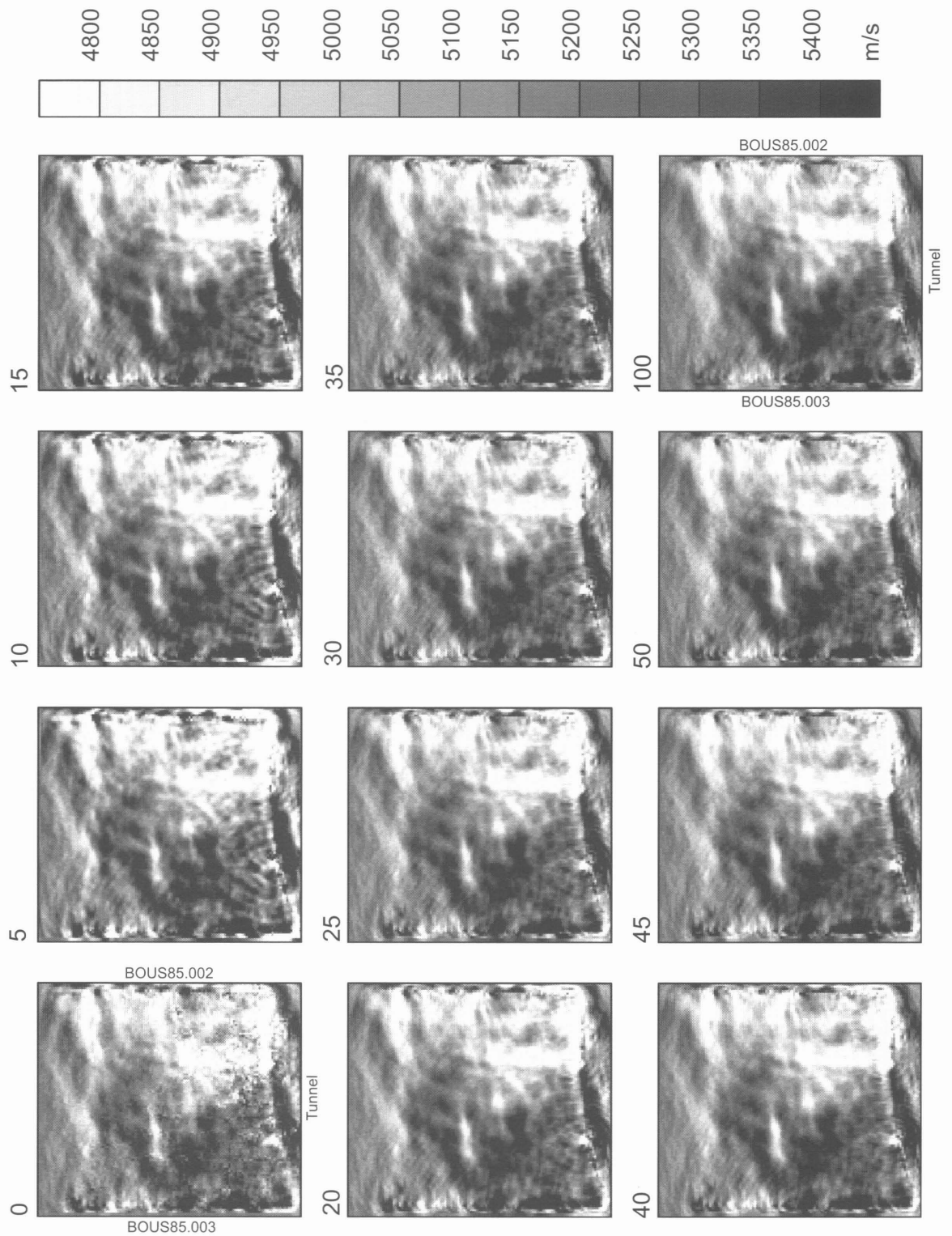


Fig. 4.7: Isotropic full wavefield inversion results for Field US2, with various values of smoothing parameter increasing from 0 to 100.

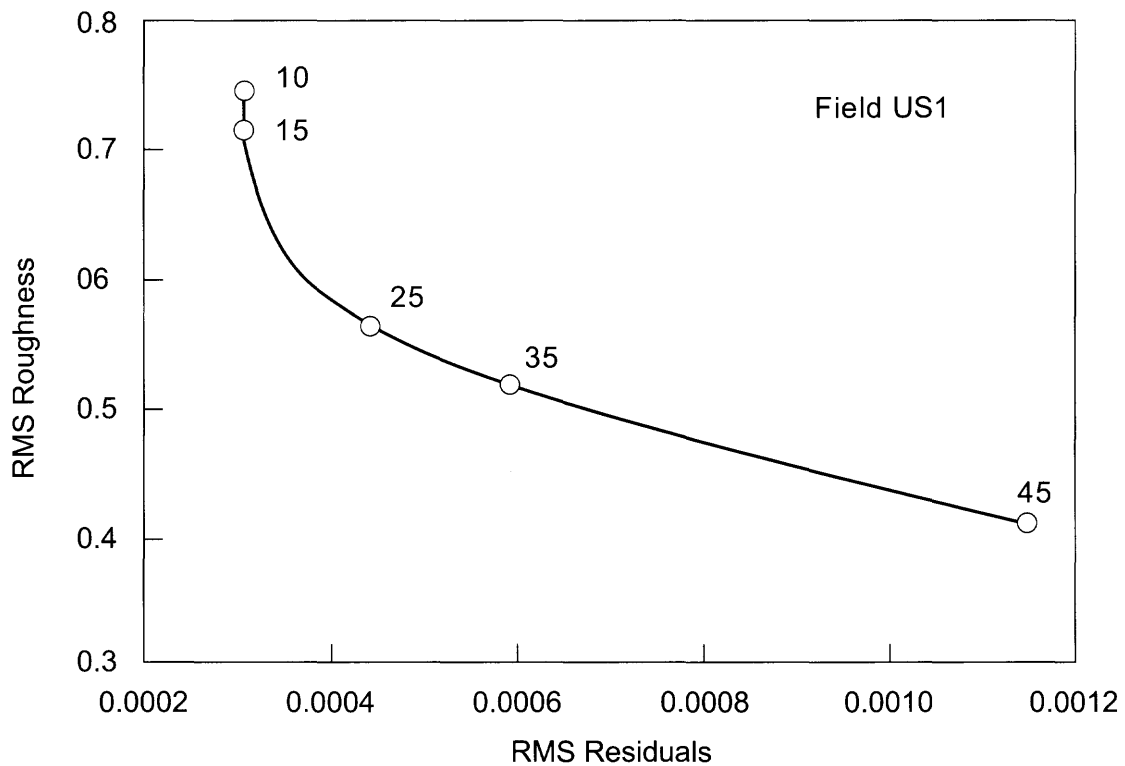
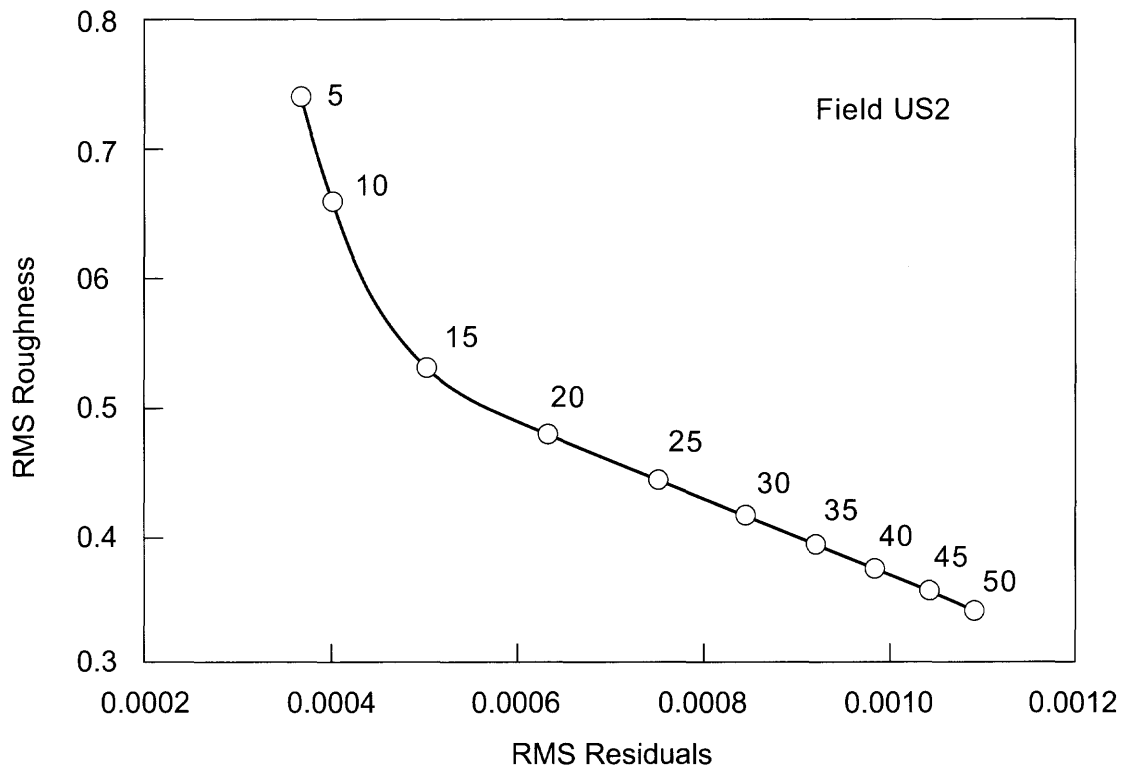


Fig. 4.8: Trade-off curve showing RMS roughness vs. RMS residuals for a suite of smoothing parameters (top panel is for Field US2, bottom panel is for Field US1).

In order to select an appropriate regularisation level, the RMS residuals and RMS roughness for each of these images were also computed and plotted against each other (Figure 4.8). As Pratt & Chapman (1992) have advocated for traveltimes tomography in the past (s. Chapter 3.2), we select an image that simultaneously fits the data as well as possible (low residuals) and is as smooth as possible (low roughness). We seek a "knee-point" on the trade-off curve, which, in this case, indicates a smoothing parameter of about 15. A similar set of tests were carried out for the Field US1 data; these are also shown in Figure 4.8.

The Field US1 data were somewhat more difficult to process than the Field US2 data, and hence a slightly higher smoothing parameter might have been appropriate. However, in the interest of consistency, the same level of smoothing parameter was used for the wavefield inversion of both datasets (i.e. a value of 15). Therefore the Field US1 images will have a slightly higher noise level than the Field US2 images. This noise level manifests itself as oscillations in the velocity values and is more prevalent near the source and receiver locations. Although we could damp these oscillations by using a larger smoothing level, the resulting images would not necessarily be any more accurate. The higher noise level is a combination of the increased sensitivity to source static terms (due to the smaller physical distances in Field US1) and the higher noise level in the field data.

Source-consistent statics

It was important to verify the method used to account for source-consistent static shifts. As described above, to account for these static shifts in the Field US2 data the VSP data were divided into 4 source "groups", each assumed to have a separate source behaviour (these groups were identified in Figure 4.5). Also a fifth group was included to collectively represent all crosshole sources. In order to evaluate this approach the resultant (inverted) time domain source signatures were examined (Štekl & Pratt, 1996). Each of these signatures was estimated independently from the data alone - it is reassuring that the wavefields of the VSP source signatures were consistent and that most of the differences are due only to a time shift. This consistency tends to verify this approach.

The evidence for anisotropy

The Field US2 isotropic results show a large variation in velocities from the left-hand edge of the images to the right-hand edge (Fig. 4.7). This variation is correlated with the distributions of the ray paths from the two VSP surveys, which give us cause to question the quality of the image. In order to shed light on this question, we show in Figures 4.9 & 4.10 images that represent the frequency domain data for a single frequency component of the Field US2 data and Field US1 data (900 Hz in this example). Because each source-receiver pair yields only a single complex number at each frequency, we can display the real parts of these data as "maps", indexed by the source and receiver numbers (see Figures). Figure 4.9a and 4.10a shows the residuals of the original data (following pre-processing and Fourier transformation), and Figure 4.9b and 4.10b shows the residuals following the isotropic inversion procedure. If we had matched the data perfectly, these residuals would be zero everywhere. Noise will corrupt the residuals, but one would expect a random distribution of the noise on the residual images. Instead, the residuals show much the same patterns as the original data, although reduced in amplitude. Thus we see that much of the data variation remains unexplained by the best isotropic results.

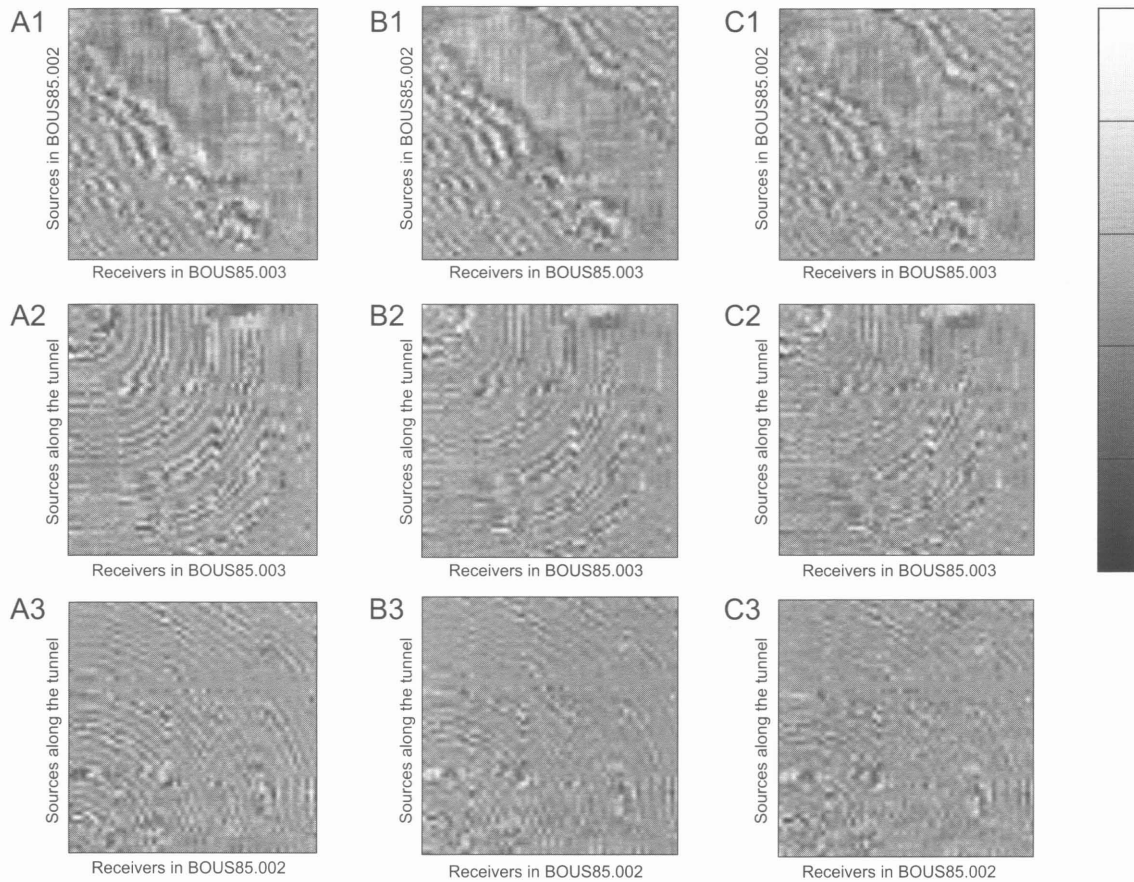


Fig. 4.9: Frequency domain data for Field US2, 900 Hz. a) Original data (following pre-processing and frequency transformation, b) residuals following isotropic wavefield inversion, c) residuals following correction for 2 % anisotropy. In all figures, each pixel represents the real part of the complex valued Fourier component for a single source - receiver pair in the survey, with sources arranged along the vertical axis and receivers arranged along the horizontal axis. Panel 1 corresponds to the crosshole data and panels 2 and 3 correspond to the two VSP surveys. The grey scale is a relative amplitude.

In many other studies of both Field US1 and Field US2 using travelt ime tomography it has proven necessary to account for a small level of anisotropy. We believe that the variation in velocities in the images and the remaining residual levels in the data are both best explained by the seismic anisotropy of the rocks. The anisotropy at the Grimsel Test Site is expected to be relatively low. Previous estimates from the seismic traveltimes have shown an overall level from 1 % to 3 %, with a slow axis dipping 45° from the top right corner to the bottom left corner. By using our knowledge of the full wavefield modelling software, we would expect that the errors in the modelling code are of the order of 1 % and that the inversion errors will be at least an additional few percent. If the errors of the method are of the same order as the anisotropy level, why does the anisotropy affect the images so strongly? The answer lies in the systematic distribution of the ray directions in the data. The main ray directions in the VSP da-

tasetts are, in this case, almost exactly matched with slow and fast velocity axes. Thus we have a large amount of data covering the main part of the survey which is correlated with either the slow or the fast velocities.

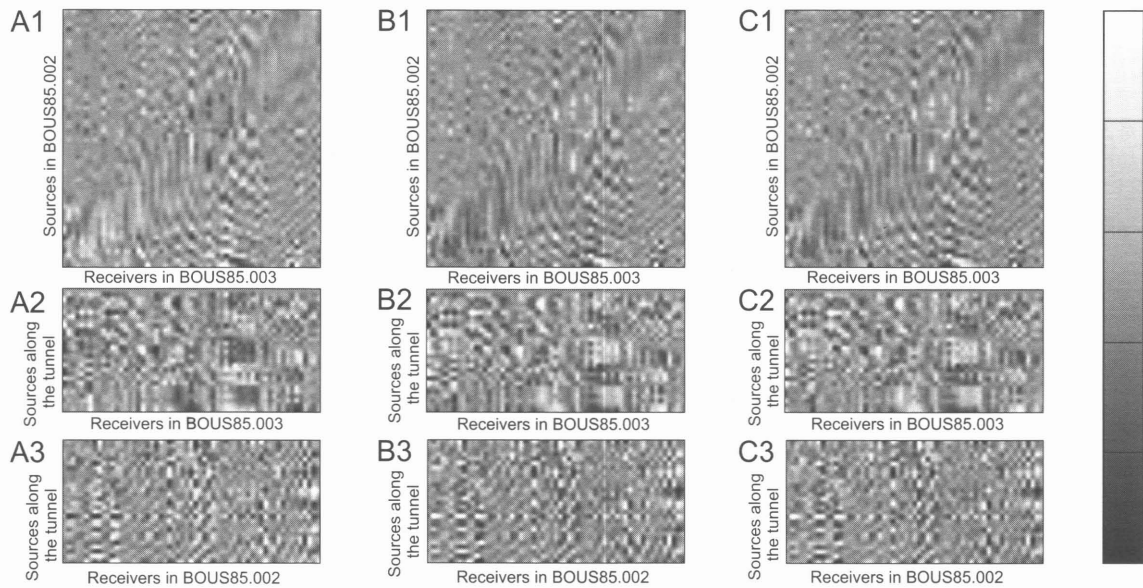


Fig. 4.10: Frequency domain data for Field US1, 900 Hz. a) Original data (following pre-processing and frequency transformation), b) residuals following isotropic wavefield inversion, c) residuals following correction for 2 % anisotropy. In all figures, each pixel represents the real part of the complex valued Fourier component for a single source - receiver pair in the survey, with sources arranged along the vertical axis and receivers arranged along the horizontal axis. Panel 1 corresponds to the crosshole data and panels 2 and 3 correspond to the two VSP surveys. The grey scale is a relative amplitude.

In order to test this explanation, we generated a synthetic, homogeneous, elliptically anisotropic model (with 3 % anisotropy and the slow axis dipping 45° from the top right corner to the bottom left one). Using this anisotropic model, we generated a full wavefield dataset using the exact Field US2 source-receiver configuration. The homogeneous (isotropic) velocity that was perturbed was $V_p = 5.2$ km/s. We then inverted these data using the isotropic inversion scheme. The result is shown in Figure 4.11 and suffers from the same left-right velocity distribution problem identified on the isotropic images computed from the real data (Figure 4.7). The synthetic inversion result shows the isotropic velocity in the central region where we have coverage from both the VSP datasets and from the crosshole datasets. In the regions covered by only a single VSP dataset, the image compensates for the mismatch by creating a low (or high) velocity anomaly.

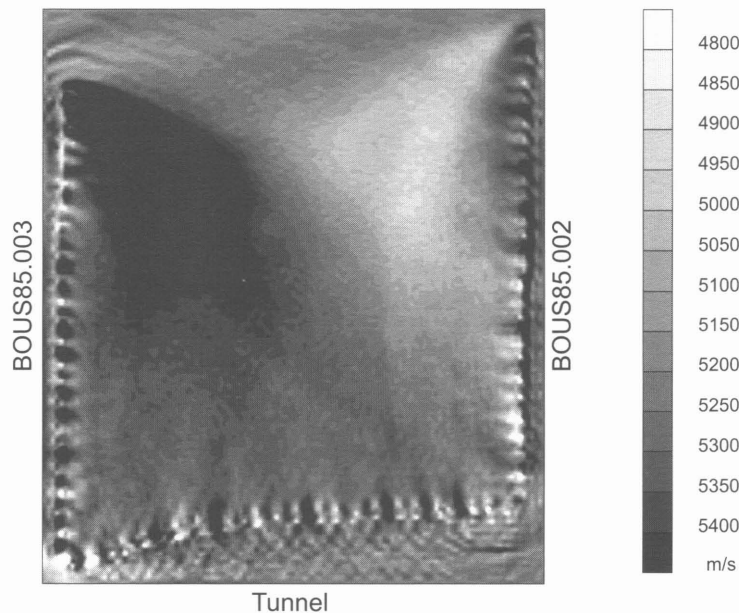


Fig. 4.11: Isotropic inversion of a synthetic dataset from a homogeneous, anisotropic model.

4.3.2 Anisotropic wavefield inversion

In order to compensate for the strong anisotropy effect evident from our synthetic tests, we have carried out inversions of the Field US2 and the Field US1 data by assuming a constant level of elliptical anisotropy of 1, 2 and 3 %. In each case the slow axis was chosen as in the previous synthetic study to be consistent with the orientation used in most of the travelttime tomography studies at the site, i.e. dipping 45° from the top right corner to the bottom left corner. The images are shown in Figures 4.12 and 4.13. Although the strong left-right variation of velocities is reduced as the anisotropy is increased (especially for the Field US2 results), it is not clear from these images which is the correct background level of anisotropy. In order to help the selection of this parameter, we also computed the RMS residuals for each of these images. The results are shown in Figure 4.14. For Field US2, a level of 3 % anisotropy gives residuals that are as far from the solution as the isotropic result is. For Field US1, the results are less sensitive to the level of anisotropy, although the isotropic result clearly produces the largest residuals. It appears from both plots that the optimum result will have $\sim 1.8 - 1.9$ % anisotropy. It is significant that we obtained essentially the same minimum for both the Field US1 and the Field US2 data.

The data residuals for the Field US2 images following the correction for a 2 % anisotropy level are shown in Figure 4.9c. The data residuals no longer display the strong systematic distributions observed in the isotropic case. Figure 4.10 shows a similar study of the frequency domain data from Field US1. It is much more difficult to detect the anisotropy effects in the Field US1 data, due to the high noise level and less infor-

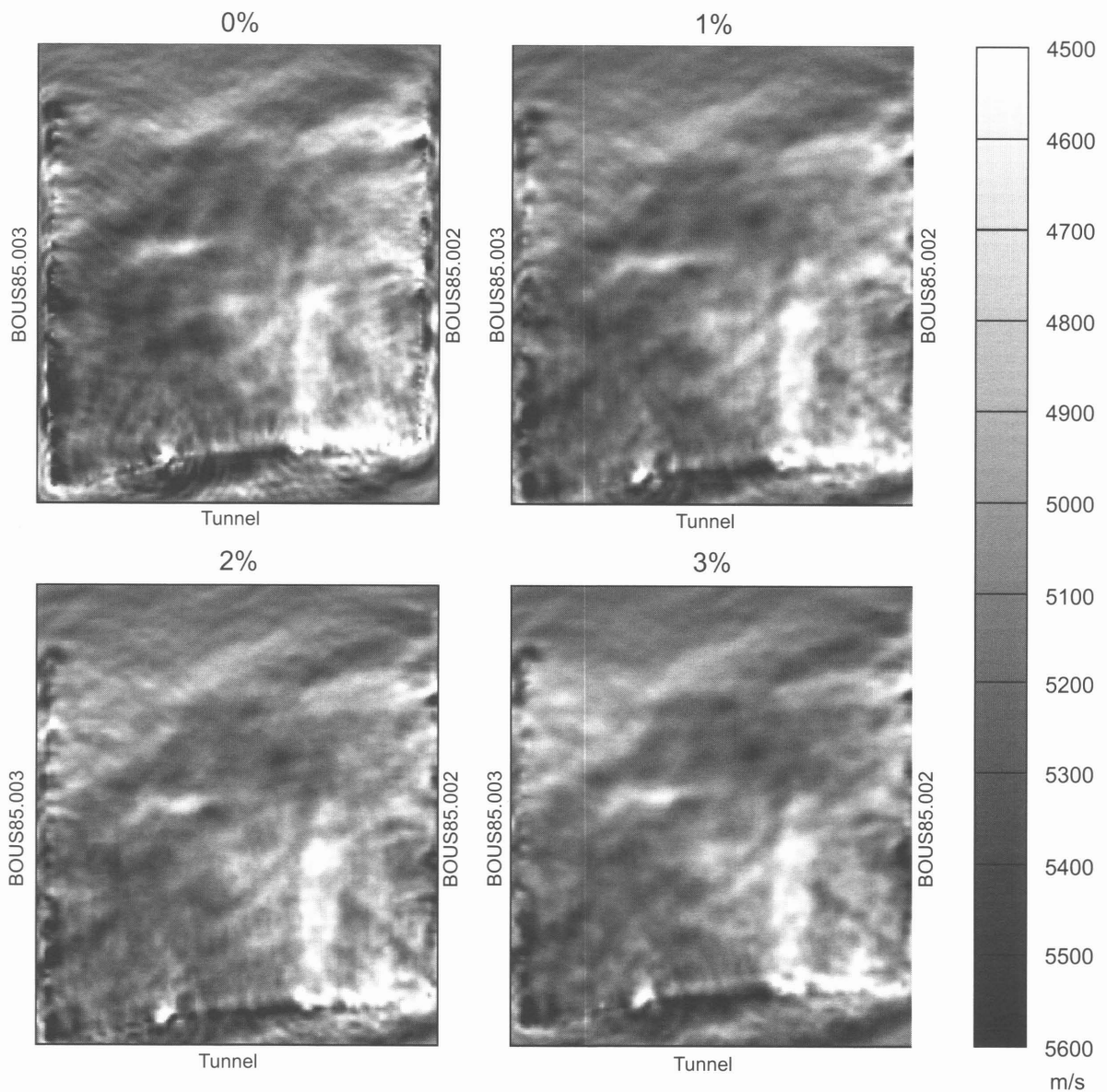


Fig. 4.12: Anisotropic full wavefield inversion results for Field US2 with 0, 1, 2 and 3 % elliptical anisotropy.

mation from the VSPs. This noise is largely due to source and receiver statics, in some cases caused by slight differences between the original survey and the "in-fill" survey. These statics manifest themselves as vertical stripes on the images in Figure 4.10.

Figure 4.15 shows the final anisotropic wavefield inversion results. The left-right velocity distribution of the isotropic Field US2 result has largely disappeared. These results of Field US1 and Field US2 show some correlation where they overlap at borehole BOUS85.002: on a broad scale, regions with high and low velocities can be followed

across BOUS85.002, with a consistent increase in velocity away from the tunnel. On a finer scale, there are some inconsistencies, largely due to the effects of noise in the Field US1 data.

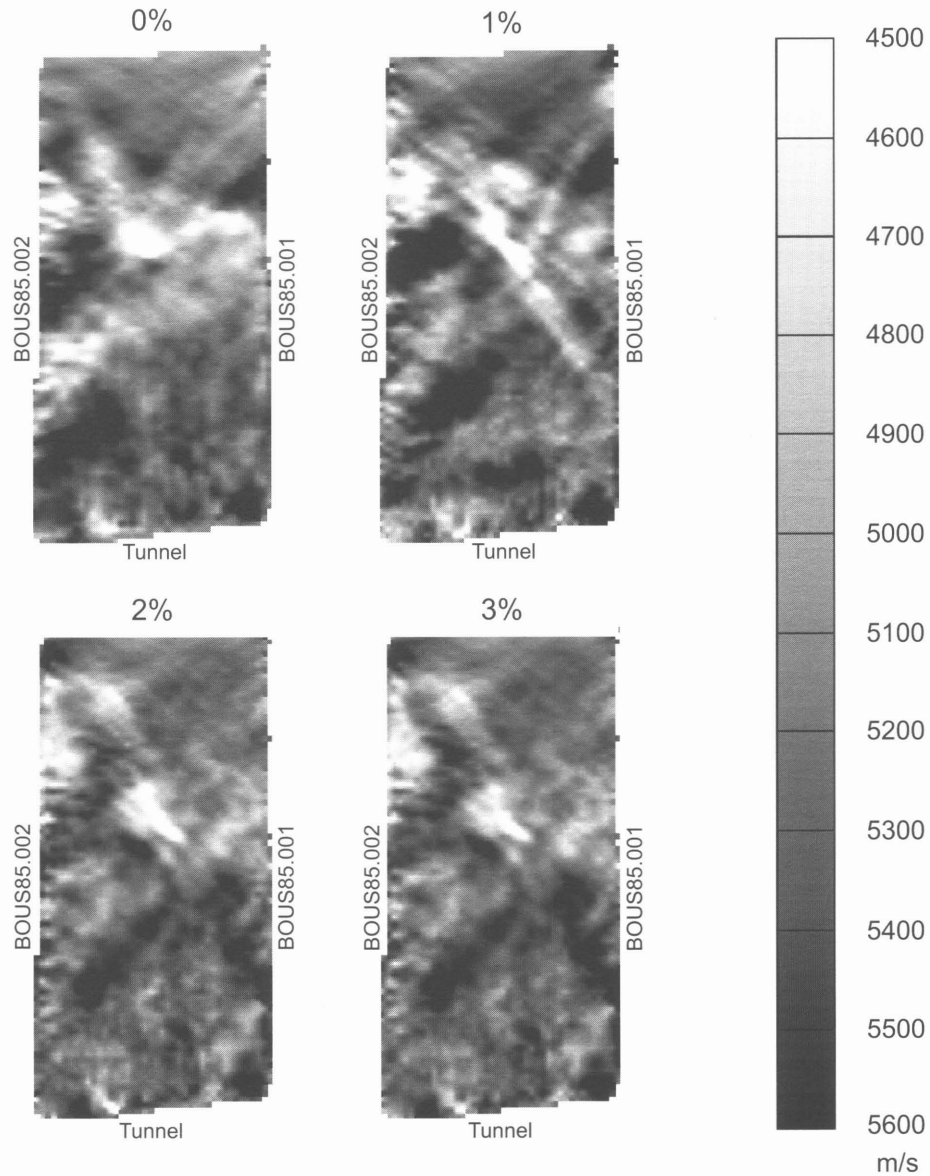


Fig. 4.13: Anisotropic full wavefield inversion results for Field US1 with 0, 1, 2 and 3 % elliptical anisotropy.

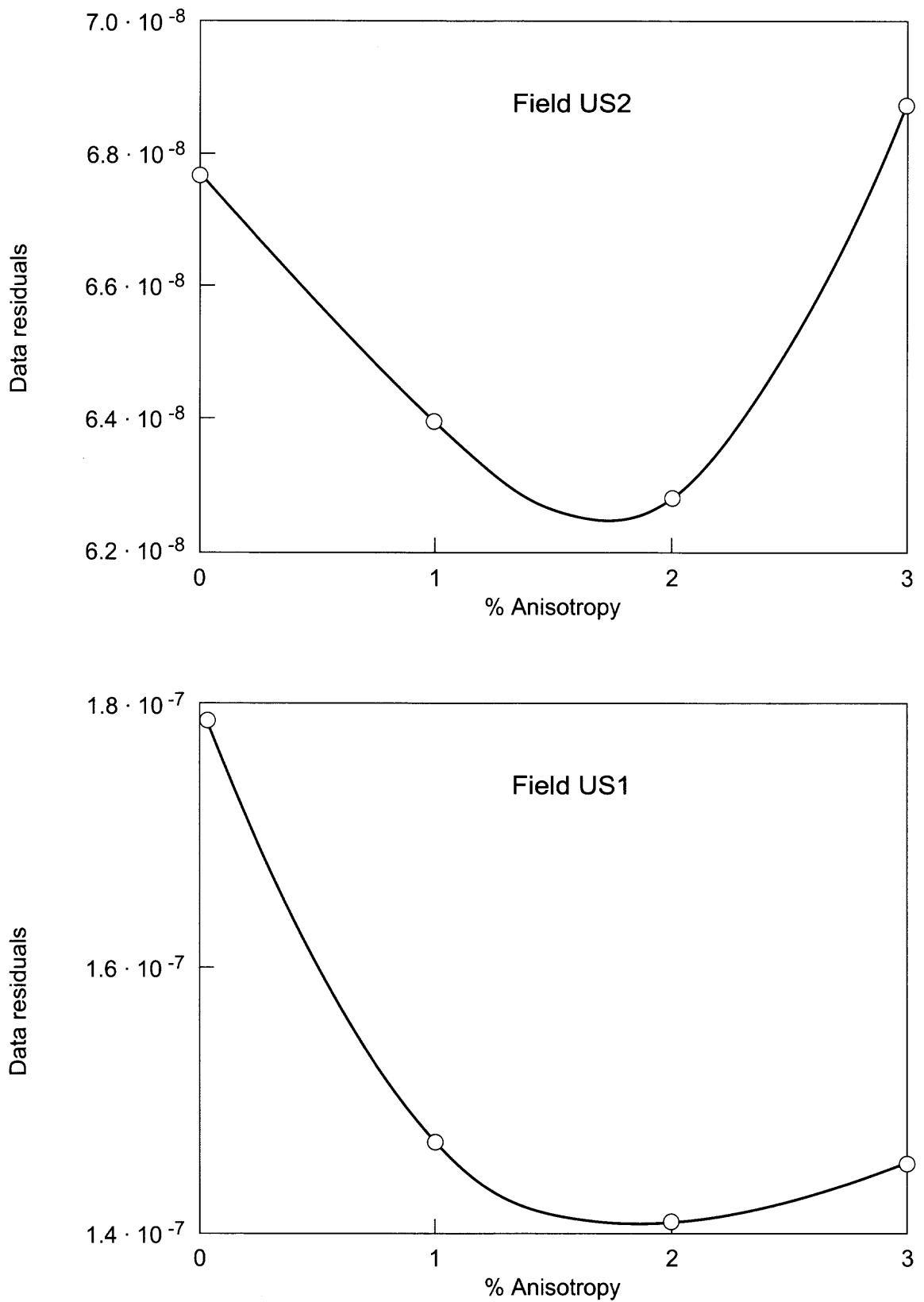


Fig. 4.14: RMS residuals for each of the tested anisotropy levels. Top panel is for Field US2, bottom panel is for Field US1.

4.4 Conclusions on full wavefield inversion

In this Chapter we have achieved three major objectives:

- i) We have demonstrated the possibility to generate high-resolution acoustic wavefield inversion images in a controlled test using synthetic elastic data;
- ii) We have identified a successful pre-processing sequence for the field data that handles the poor signal-to-noise levels, the large amplitude variations and the significant static time shifts and have demonstrated the efficacy of these methods on the synthetic data;
- iii) We have successfully obtained reliable and interpretable images using wavefield inversion from the real Field US1 and Field US2 data. The final images show the expected improvement in resolution and will enhance the detailed characterisation of the Test Site. We are convinced that the wavefield inversion is unique in its ability to extract the wavelength scale features of the velocity variations. No other technique known to us is capable of extracting these features (s. Chapter 5).

As a result of studying these data, we have identified a number of developments in the imaging technique that should deliver yet more accurate and better resolved velocity images in the future. The most important development will be to extend the method to a full elastic wavefield inversion. This development will allow the use of shear wave energy in a constructive fashion and should lead to shear wave velocity images in addition to improved compressional wave velocity images. Štekl & Pratt (1998) have already developed equivalent forward modelling methods for the elastic problem; the use of these in an imaging algorithm awaits future development. Such an extension would also lead eventually to an anisotropic, elastic imaging technique. Ultimately, we anticipate that an anisotropic wavefield imaging method would enable us to allow for the spatially variable nature of the anisotropy in highly stressed crystalline rocks (such as at the Grimsel Test Site), and would lead to corresponding improvements in image reliability.

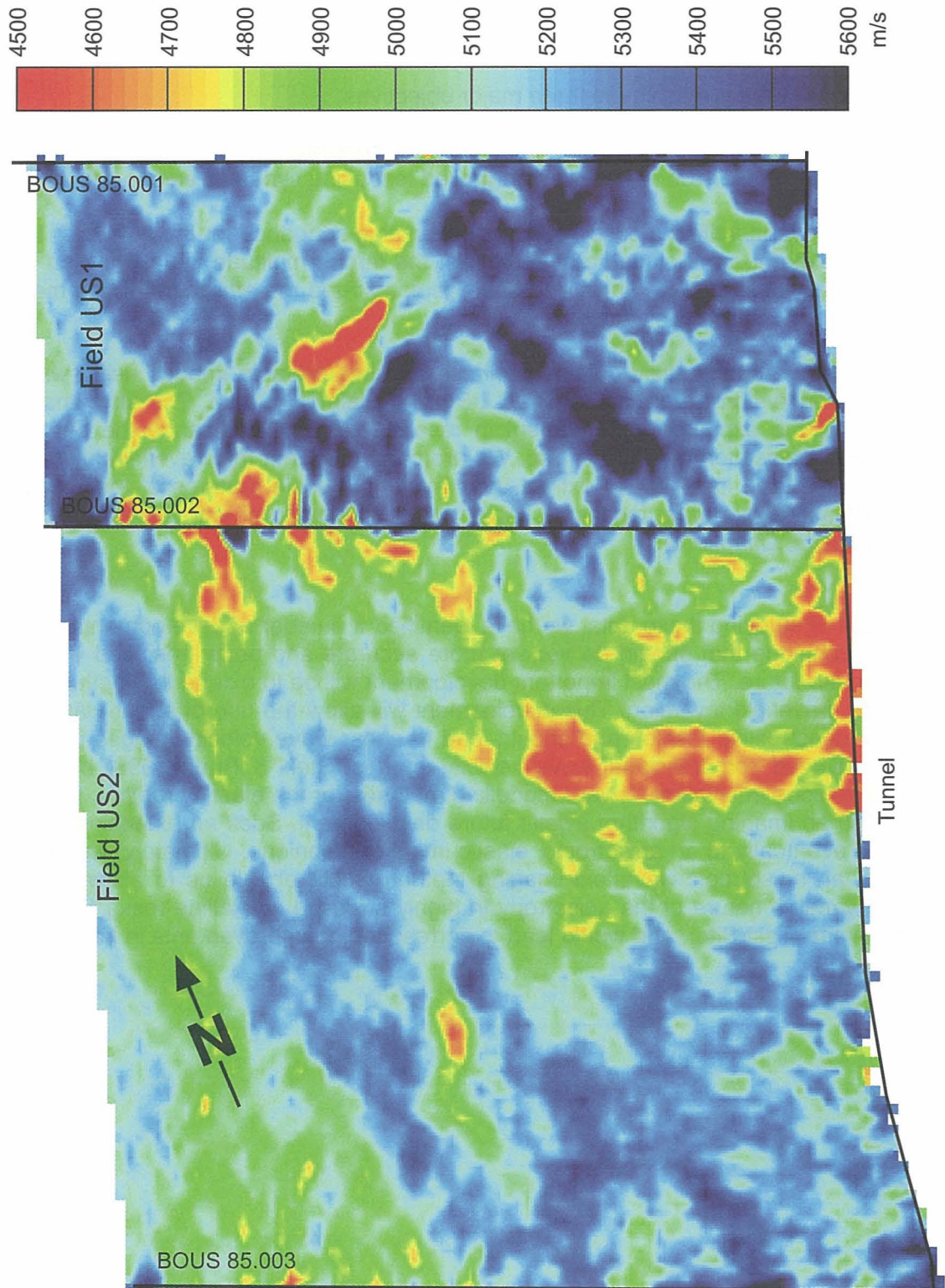


Fig. 4.15: Final wavefield inversion images from Fields US1 and US2, using 2 % elliptical anisotropy.

5 VALIDATION OF TOMOGRAMS

In addition to the existing SIRT tomograms (Gelbke, 1988, Fig. 3.3), this project produced new traveltimes and wavefield tomograms for Fields US1 and US2 (anisotropic velocity tomography (AVT): Fig. 3.6, coupled inversion (CI): Fig. 3.17 (including Field US3 data), wavefield inversion (WFI): Fig. 4.15). The individual tomograms are similar in many respects, but when considered in detail they show marked differences. This section aims to answer the question on which tomogram best describes Fields US1 and US2.

The procedure consists of a number of steps. Firstly, the tomogram results for the neighbouring Fields US1 and US2 are compared individually for each inversion technique. The tomograms are then correlated with the results of borehole measurements (sonic logs). Finally, the tomograms are compared with available geological information.

5.1 Conformity of Field US1 and US2 tomograms at borehole BOUS85.002

Fields US1 and US2 were inverted separately for all inversion techniques. Data from Field US3 were taken into account only in the case of coupled inversion (Chapter 3.3). For the purpose of the present comparison, however, only the data from Fields US1 and US2 are considered. Nevertheless, to include data from Field US3 would improve the quality of the tomograms for all inversion methods (as shown for the coupled inversion – Chapter 3.3) but a consistency check at the position of the borehole BOUS85.002 will then no longer be possible.

The datasets inverted separately for Fields US1 and US2 show no overlap and no parameters were used which, on inversion, transferred information from one field to the other. The inversions of the two fields were thus carried out completely independently. At the interface between the two fields - borehole BOUS85.002 - the separately inverted results should conform within the range of accuracy. This provides an internal consistency check of the inversions.

Even the SIRT inversion (Fig. 3.3/Chapter 3.1) showed a good agreement of the two fields at borehole BOUS85.002. In general, similarly high and low velocities are observed on both sides of the borehole. Only the directions of the anomalies appear to change at the location of the borehole, with an angle change of approx. 90° being observed repeatedly. Since the direction of the anomalies often corresponds to the diagonal of the two fields, it can reasonably be presumed that these are data processing artefacts.

The AVT inversion (Fig. 3.6/Chapter 3.2) also shows a good agreement for the velocities at the boundary of the two fields. Both the zones of high and low velocities and the directions of the anomalies can be followed well across borehole BOUS85.002. The boundary between the fields is clearly recognisable only for small-scale anomalies and velocity variations. These variations are particularly noticeable when the velocity distribution along the borehole taken from the tomograms is compared (Annex 5). Conformity is not as good when the anisotropy images are compared (Fig. 3.7 & 3.8). While the directions of anisotropy correlate very well (Fig. 3.8), the amounts of anisotropy (Fig. 3.7) show very little overlap. As discussed in Chapter 3.4, it is not always possible

to separate anisotropy effects and mislocations on the basis of traveltimes data. The poor agreement for the amounts of anisotropy along the borehole could therefore be explained by mislocations of the US boreholes.

The coupled inversion (Field US1 & US2: Fig. 3.15d & e / Chapter 3.3) also shows good conformity. Zones of high and low velocity and directions of anomalies can be followed across the borehole. The smaller anomalies in the Fields which are in the direction of the field diagonal and are assumed to be artefacts have no influence on the anomalies or velocity zones which can be followed across the borehole. The overlap is improved by taking into account the rays of Field US3 which were registered across borehole BOUS85.002 (see Fig. 3.15f & 3.17). The relocation of the borehole BOUS85.002 fits well in this result.

At first sight, the wavefield inversion (see Chapter 4/Fig. 4.15) shows a clearly higher resolution than the results of the traveltimes inversions. This is also clear at the boundary between the two fields where the wavefield inversion shows a good correlation. Zones of high and low velocities and directions of anomalies can be followed across borehole BOUS85.002. The frequency of anomalies and velocity variations appears to be higher along the borehole in both Fields. This is particularly clear in Field US1. This can be interpreted as an artefact of the field edges (Chapter 4).

The consistency check of inversion results for Fields US1 and US2 carried out in this section shows a good agreement of the velocity distribution along borehole BOUS85.002 for all inversion techniques. The direction change at the position of the borehole observed in the SIRT inversion could be eliminated in all the techniques developed and tested as part of the work presented in this report.

5.2 Validation with new geometry data

For the coupled inversion (Fig. 3.17/Chapter 3.3), it is possible to validate the relocated source and receiver positions. Relocation revealed clear deviations (up to 4%) of the locations of the boreholes BOUS85.001, 85.002 and 85.003, according to which all boreholes were shifted towards the north (Fig. 3.16). It should be possible to check this result with a new geometry survey of the borehole paths.

Only one surveying system for horizontal slim hole boreholes is currently available which promises an absolute accuracy of 0.1%. In 1994, this optical surveying instrument was used to check the borehole locations (Fig. 5.1; Albert, 1994). The difference in measurements resulting from just introducing the tool into the boreholes and removing it was however already more than 2% (in the tomographic plane about 1%). Other systematic inaccuracies were presumed to exist and the results were therefore not used for validation purposes.

A company is currently developing a tool based on gyroscopic and inertial systems which should also be capable of achieving the desired accuracy of 0.1%. It is planned to survey the three US boreholes using this tool.

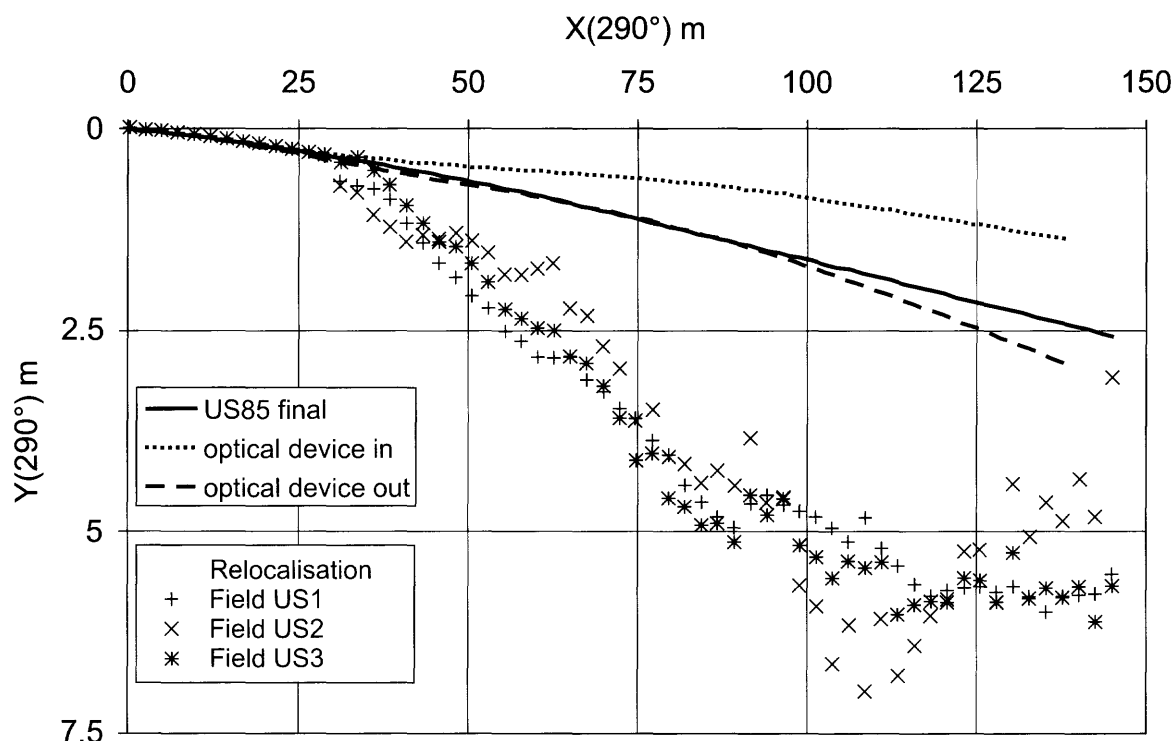


Fig. 5.1: Geometry surveys in BOUS85.002 and relocalisation results from coupled inversion (Fig. 3.16).

5.3 Validation with sonic data

The tomograms give the distribution of seismic velocities in the fields under consideration. Seismic velocities along boreholes can be read directly from the tomograms and presented in the form of a borehole log. Seismic velocities were measured directly in several boreholes using sonic tools. In this section, the sonic velocities are compared with the velocities obtained from the tomograms.

Before the comparison is made, the results of the sonic measurements in Fields US1 and US2 are summarised in the following section. The comparison is done with absolute velocity values (Chapter 5.3.2) and relatively by correlating velocity anomalies (Chapter 5.3.3).

5.3.1 Summary of sonic velocities in the area of the tomography Fields US1 & US2

Seismic velocities were measured in a large number of boreholes at the Grimsel Test Site (Prakla-Seismos, 1981: BOSB 80.001 - 80.006; Holub, 1984: BOWT 84.009 & 84.010, BOVE 84.011; BPB, 1985: BOUS85.001 - 85.003; Möri & Bossart, 1997: BOBK85.004/86.001, 85.008 & 86.003 and Häring, 1996: FEX95.001 & 95.002).

Boreholes BOUS85.001 - 85.003 (dip: -15°) delimit the tomography Fields US1 and US2. Boreholes BOBK85.004/86.001, 85.008 and 86.003 were drilled from the BK cavern above the US2 field at an angle of -35° and penetrate the field. Boreholes

FEX95.001 and 95.002 are almost horizontal (-1°); they lie above the tomography planes and can easily be projected onto them (Fig. 5.2).

Borehole BOSB80.001 lies above the US2 plane in the region of the BK cavern (Keusen et al., 1989). With the exception of this borehole, all the boreholes in the area of the tomography experiment have mean velocities which correlate well with the velocities determined from the tomograms (Tab. 5.1). The results from the 6 boreholes BOSB80.001 - 80.006 are around 10% higher (on average 5600 to 5200 m/s for the Aare Granite and the granodiorite) than measured in the tomography fields. This discrepancy also found its way into Keusen et al. (1989), without being investigated more closely. The most likely explanation is a wrong correction of the time-keeping instrument of the acoustic log of Prakla-Seismos (Prakla-Seismos, 1981). The results were corrected because an error was presumed to have occurred. If the effect of the correction is reversed, the results then agree well. Since it cannot be ruled out that further errors are present in the measurements from the boreholes BOSB80.001 - 80.006, these results are not taken into account any further.

Table 5.1 gives the average measured velocities in the boreholes in the area of the tomography planes.

Filtered sonic logs are used for the comparison with the tomograms. The filter length is 2.5 m, which corresponds to the receiver and shotpoint spacing in the measurement (Gelbke, 1988) and around half the wavelength of the seismic waves.

Fig. 5.2 gives the velocity distribution from the sonic logs presented as a tomogram. The general velocity trends indicate that the highest velocities are in the north (BOUS85.001 and FEX95.001). Borehole BOBK85.008, which was drilled through a negative velocity anomaly observed in all tomograms (Chapter 3 and 4), shows very low velocities.

Tab. 5.1: Overview of results of sonic measurements in boreholes BOBK85.004 / 86.001, BOBK85.008, BOBK86.003, FEX95.001, FEX95.002 and BOUS85.001, 85.002 and 85.003.

	Vp sonic m/s				Vp sonic filtered m/s				Depth m
	minimum	maximum	average	deviation	minimum	maximum	average	deviation	
BK85.004/86.001	4353	5547	5137	215	4616	5411	5138	177	88.90
BK85.008	3776	5282	4855	337	4106	5248	4855	297	48.90
BK86.003	3581	5581	5132	291	4585	5478	5131	196	68.10
FEX95.001	4541	5633	5321	138	4936	5536	5321	103	76.00
FEX95.002	4684	5611	5135	120	4877	5492	5136	92	132.10
BOUS85.001	4367	5888	5299	171	4764	5754	5299	144	149.90
BOUS85.002	3662	6106	5165	248	4434	5544	5165	181	149.90
BOUS85.003	4101	5779	5218	176	4708	5424	5218	134	149.90
Total	3581	6106	5184	232	4106	5754	5184	192	863.70

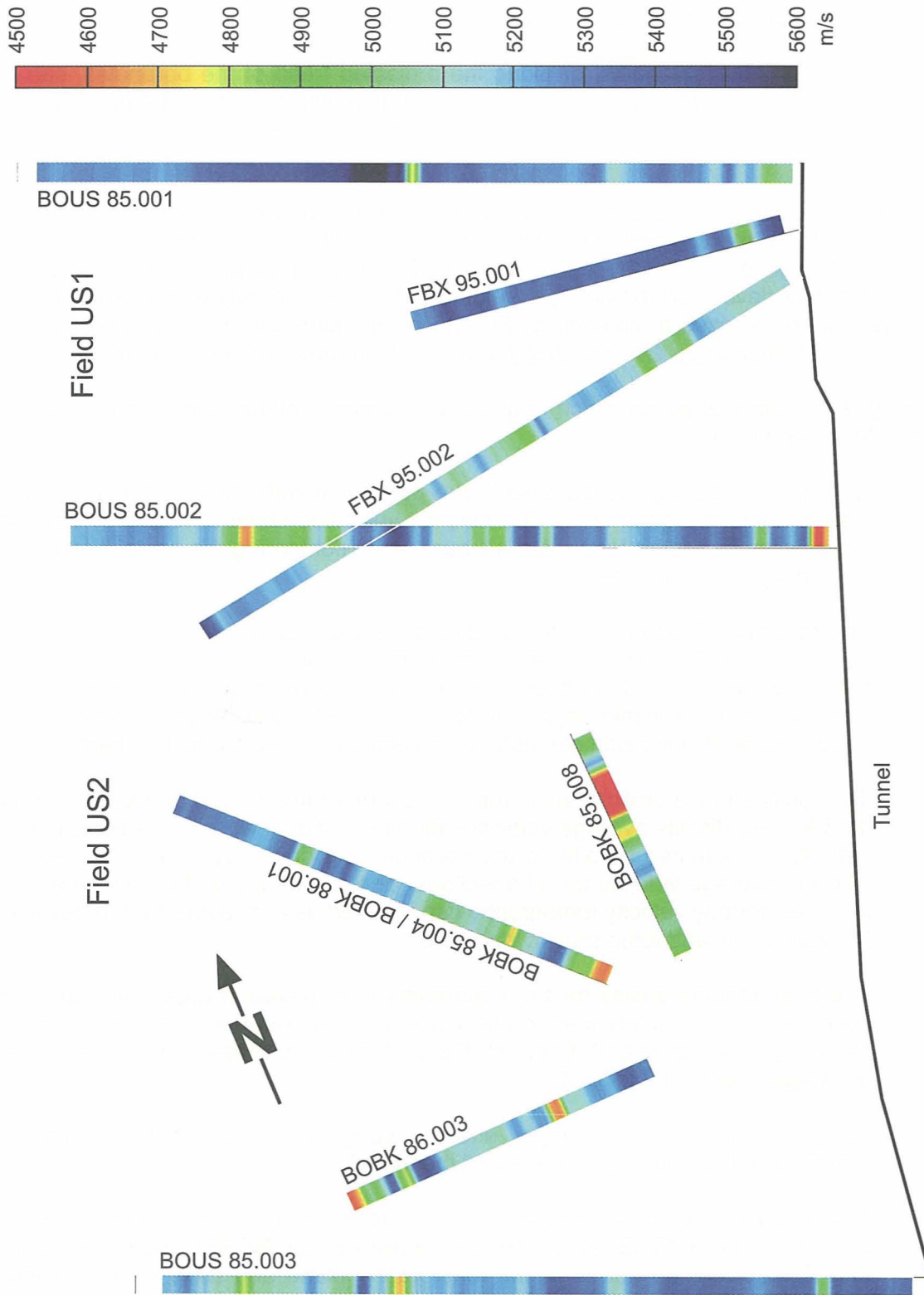


Fig. 5.2 Sonic logs from boreholes BOBK85.004/86.001, BOBK85.008, BOBK86.003, BOUS85.001, BOUS85.002, BOUS85.003, FBX95.001 and FBX95.002. The sonic logs were smoothed along the vertical projected trends of the boreholes onto the tomography plane; the colour code is the same as for the tomograms.

5.3.2 Correlation of sonic & tomogram velocity logs

Velocities along the boreholes, or along the projected trend of the boreholes, can be read from the tomograms and compared with actual measurements in the boreholes. In this section, the velocities along the boreholes and their projections are compared with one another.

In order to evaluate the different inversion results, the tomograms of the SIRT inversion (Gelbke, 1988), the two new traveltimes inversions (AVT & CI: Chapter 3) and the full wavefield inversion (WFI: Chapter 4) were used for the comparison. The full wavefield inversion was developed for isotropic velocity fields and can only be corrected for the whole field in the case of anisotropy. For the comparison, all four calculated cases - isotropic, 1% anisotropy, 2% anisotropy and 3% anisotropy - were considered.

Firstly, some general points which may have a negative influence on the comparison have to be mentioned:

- Seismic tomography measurements are performed with different signal frequencies to sonic measurements. The seismic velocities show a frequency dependence which has to be taken into account when comparing the sonic results with the tomography velocities.
- The resolution is dependent on the different signal frequencies and on the inversion methods. Traveltimes inversion methods can obtain a resolution of the first Fresnel zone (10 m - 30 m depending on the wavelength and on the propagation distance of the seismic rays / Williamson, 1991; Williamson & Worthington, 1993), wavefield inversion can obtain a resolution of a wavelength (Chapter 4).
- The rocks show a velocity anisotropy. The tomograms (Fig. 3.3, 3.6, 3.17, 4.12, 4.13 & 4.15) display average velocities for all directions, while in the sonic log the velocity is measured parallel to the borehole and does not have to correspond with the average velocity for all directions. The anisotropy of the rock measured in the anisotropy velocity tomography can be used as a measure for the deviation between sonic and tomographic velocities.
- The best imaging quality for the tomograms is achieved in areas with good ray coverage. Due to differences in accessibility, it was not possible to achieve the same ray coverage in both fields (cf. Fig. 3.2). The formal resolution based on ray coverage is given in Fig. 3.18.
- Many inversions show edge effects along field boundaries (boreholes BOUS85.001, 85.002 and 85.003 and the tunnel).
- The boreholes which can be used for the velocity comparison in the central sections of the fields (BOBK85.004/86.001, BOBK85.008, BOBK86.003, FEX95.001 and FEX95.002) do not lie in the tomography plane and have to be projected onto it. The distance between the borehole and the tomography plane has to be taken into account in the comparison (see Chapter 5.1).

The comparison was done using composite logs (Fig. 5.3 and Annex 1-8). These logs present the sonic logs and the velocities from the tomograms together for comparison purposes.

Even a first glance reveals that the velocities derived from the inversion results (tomogram log) correctly reproduce the sonic velocities (sonic log) with a deviation of 5-10%. The sonic and tomogram logs show different wavelengths over depth (Fig. 5.3 and Annex 1-8). The SIRT gives the lowest frequency image, which also corresponds to the lowest resolution. The two new travelt ime inversion methods AVT and CI show a higher frequency image than the SIRT inversion. Particularly in boreholes BOUS85.001, 85.002 and 85.003, the wavefield inversion shows very high frequency oscillations in the measuring point grid, with high velocity values (up to 10%). These have already been identified as artefacts (Chapter 4). The oscillations cannot be recognised in Fields US1 and US2 as their amplitudes are low.

The sonic logs normally show only small velocity anomalies (< 5 m, corresponding to a wavelength of the seismic signals from the tomographic measurements of 1985: Gelbke, 1988). Numerous small anomalies are not reproduced by the velocity logs of the inversion results, which is not surprising given the resolution of the inversion techniques.

Only a few large-scale (≥ 5 m) velocity anomalies show deviations of more than 5% from the average value (Table 5.2). These anomalies should be imaged at least by inversion.

Tab. 5.2: Velocity anomalies with a lateral extent of more than 5 m and negative velocity deviations of at least 5% (corresponding to approx. 260 m/s) from the average value. The depths in the boreholes and the deviations in per cent are given.

Anomalies (depth (m): velocity deviation (%))			
BOBK85.004/86.001	0 - 8 m: \approx 5-10%		
BOBK85.008	32-40 m: \approx 15-20 %	43-49 m: \approx 10 %	
BOBK86.003	60-68 m: \approx 5-10%		
FEX95.001			
FEX95.002			
BOUS85.001			
BOUS85.002	0 - 5 m: \approx 10%	64-69 m: \approx 5%	95-115 m: \approx 5-10%
BOUS85.003			

The borehole BOBK85.008 shows the most marked negative velocity anomaly (between 32 and 40 m), together with other anomalies with a smaller velocity contrast. Compared with other boreholes, this borehole generally has very low velocities (see also Table 5.1). For the sonic tool used (one transmitter and two receivers), the accuracy of the absolute velocity values is not better than 3%.

Only the tomogram of the full wavefield inversion with 2% anisotropy correction (best possible correction, see Chapter 4.3) is capable of reproducing the anomalies in borehole BOBK85.008 accurately (Fig. 5.3). For this borehole, the other three full wavefield tomograms show either marked anomalies but with the wrong location (isotropic case and 3% correction) or anomalies (1% correction) where the velocity contrast is too small. The small values of the anisotropy corrections show clear differences in this comparison, which confirms the sensitivity of the algorithm to anisotropy effects. The results of the traveltimes inversions for this borehole also show large-scale lowering of velocity (from approx. 25 m to final depth) and thus reproduce the trend accurately. However, it is impossible to resolve the length of the anomalies in detail, which could be due to the resolution of the traveltimes inversions being too low. In general, the values from the velocity logs obtained from inversion results are higher than the sonic velocities (by around 2-3%, except for the anomaly between 32 and 40 m), which is within the accuracy of the absolute velocity determination of the sonic tool.

The anomaly mentioned in Table 5.2 for borehole BOBK85.004/86.001 (0-8 m) is not reproduced in any of the tomogram logs. In the area of the anomaly the borehole is more than 10 m from the tomography plane; the anomaly is located at the start of the borehole in the excavation disturbed zone of the BK cavern. Local influences of the excavation disturbed zone, which cannot be projected onto the tomography plane, certainly have a considerable impact on the intensity of this anomaly. The anomaly in borehole BOBK86.003 is reproduced only by the wavefield inversion. It is located in a section of Field US2 which did not have good ray coverage (see also Fig. 3.18) and could not be imaged optimally. The two more prominent of the three anomalies in borehole BOUS85.002 (0 - 5 m & 95 - 115 m) are reproduced by the traveltimes inversions. The velocity variations of the logs of the SIRT inversion (Fields US1 and US2) are too low. The AVT and CI traveltimes inversions successfully reproduce the two anomalies. In the case of the wavefield inversion, the strong oscillations at the field boundaries make it impossible to say anything about the correlation between the sonic log anomaly and the tomogram log anomaly.

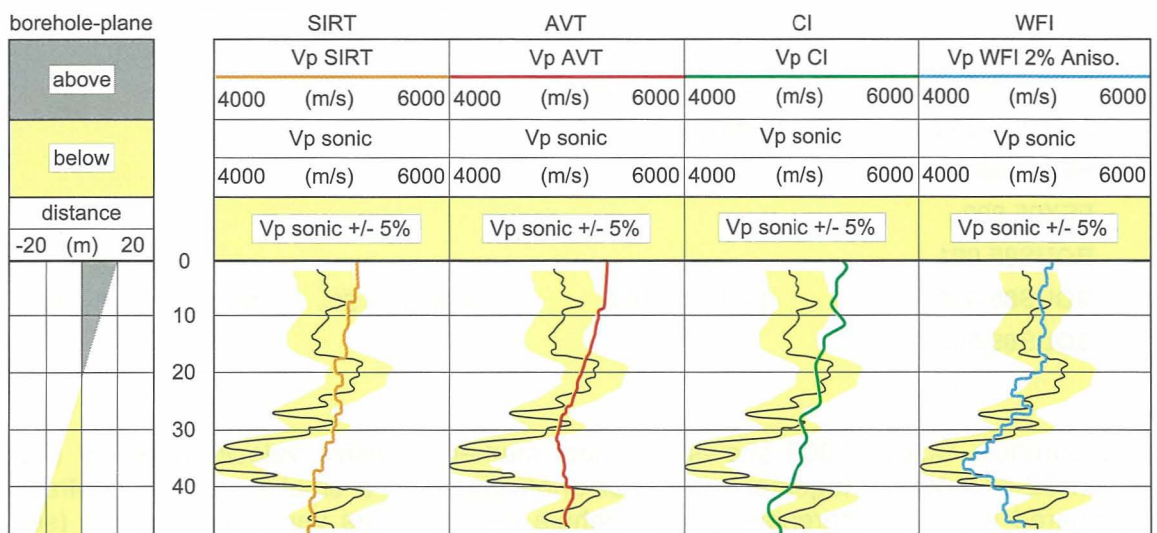


Fig. 5.3 Composite log for borehole BOBK85.008. Besides the sonic logs, the velocities read from the different tomograms along the projection of borehole BOBK85.008 are presented.

5.3.3 Correlation of sonic & tomogram velocity images

In Chapter 5.3.2, the tomograms were correlated with sonic velocities using logs with absolute velocity values. Such a quantitative comparison is a hard validation criterion. However, for structural information from tomography, a qualitative comparison on the basis of relative velocity anomalies in the vicinity of the borehole or its projection is sufficiently reliable.

Firstly, the sonic logs are superimposed on the tomograms (Figs. 5.4, 5.5, 5.6 and 5.7). The comprehensive information on velocity from borehole measurements can also be presented as a tomogram. The boreholes are projected vertically onto the tomography plane and the sonic velocities are presented along the borehole trace with the colour coding of the tomogram (Fig. 5.2). The sonic data were filtered (see above) to produce images which are comparable with the tomograms.

Compared to other tomographic measurements, there is a wealth of borehole data in the US85 field. Despite this, it is still difficult to correlate the sonic anomalies of the individual boreholes with one another without additional information.

The projected trace of the borehole FEX95.002 crosses borehole BOUS85.002. It is clear that the two boreholes show different values at their intersection point. Even if another type of projection is used, there are still discrepancies. The vertical spacing of the two boreholes at the projected intersection point is approx. 25 m. The lateral extent of the velocity structures at the intersection point is apparently smaller than the vertical spacing of the boreholes. In the following comparison of sonic data in the form of tomograms (log image) with inversion results, the distance of the boreholes to the tomography plane has to be taken into account in each case.

The SIRT inversion (Fig. 5.4/see also Figs. 3.3 and 5.2) shows a good correlation of the larger-scale velocity variations for the boreholes BOUS85.001, BOUS85.002, BOUS85.003, BOBK85.008, FEX95.001 and FEX95.002 in Field US1. Small-scale variations (< 5 m) are not reproduced. No correlation is observed for boreholes BOBK85.004/86.001 and FEX95.002 in Field US2. This is due inter alia to the prominent decreases in velocity in the area of low ray coverage (the western section of the two fields), which has already been identified as an artefact (Chapter 3.1).

The anisotropic velocity tomography (Fig. 5.5: see also Fig. 3.6 and 5.2) shows a good correlation of the larger-scale velocity variations for all boreholes, with the exception of FEX95.002 in Field US2. Small-scale variations (< 5 m) are reproduced only occasionally, and then only in outline. The lack of correlation for borehole FEX95.002 in Field US2 can be explained by the vertical distance (> 25 m) of the borehole from the tomography plane.

The coupled inversion (Fig. 5.6: see also Figs. 3.17 and 5.2) shows a good correlation of larger-scale velocity variations for all boreholes, with the exception of FEX95.002 in Field US2. Small-scale variations are only occasionally reproduced, and then only in outline.

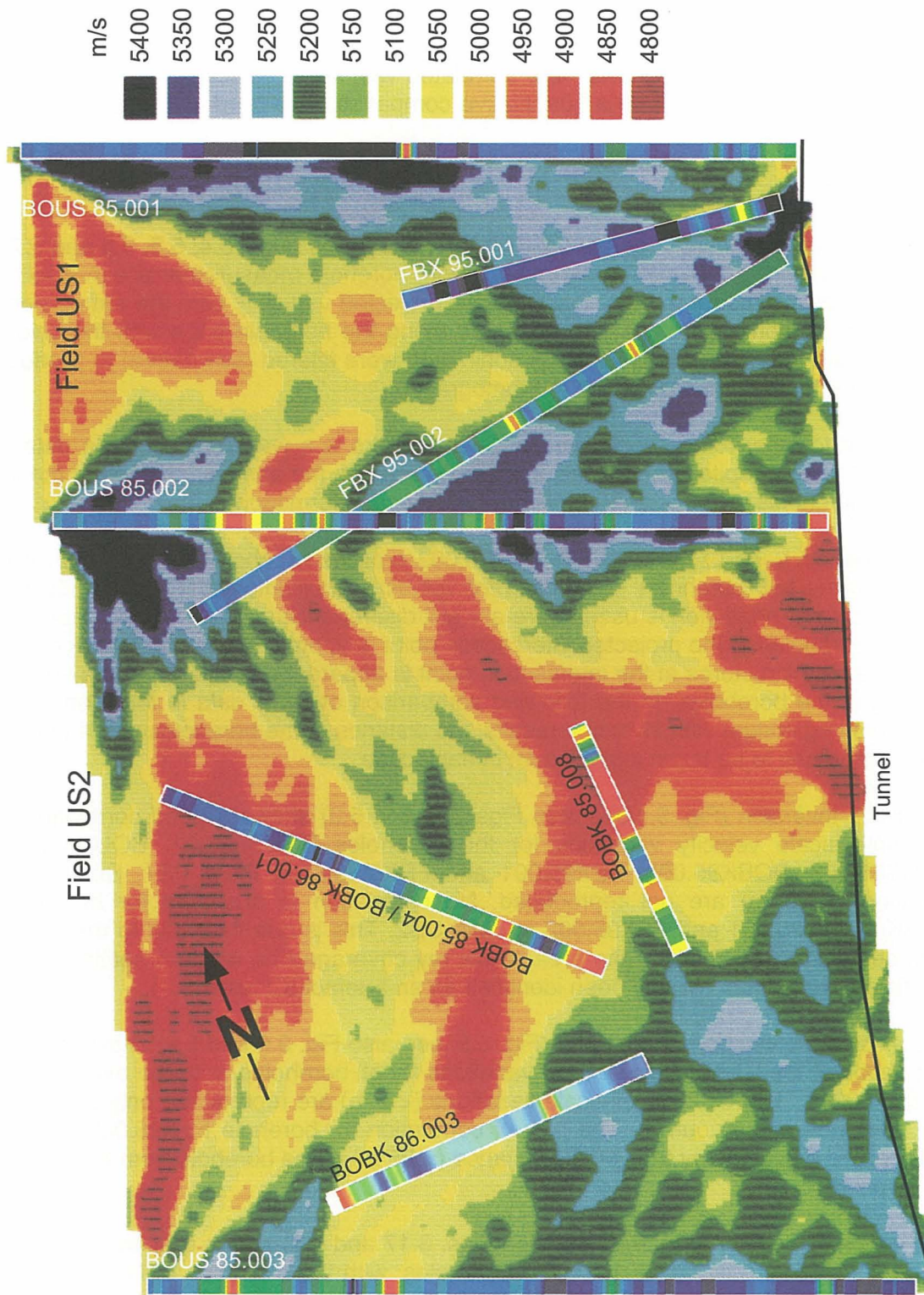


Fig. 5.4 Comparison of the SIRT inversion with the sonic velocities. The velocity image was superimposed with the colour-coded sonic logs (see Fig. 5.2).

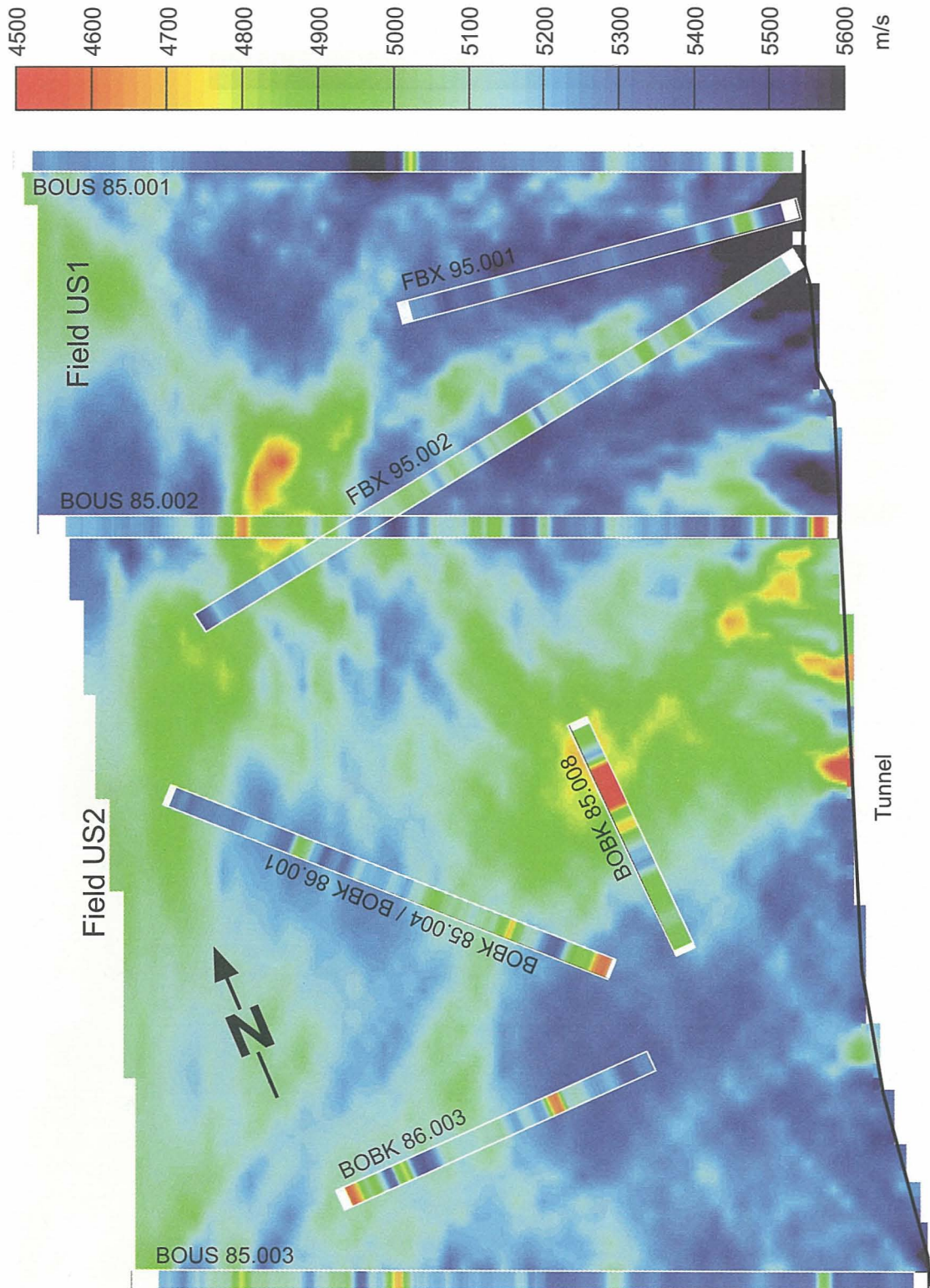


Fig. 5.5 Comparison of the AVT inversion with the sonic velocities. The velocity image was superimposed with the colour-coded sonic logs (see Fig. 5.2).

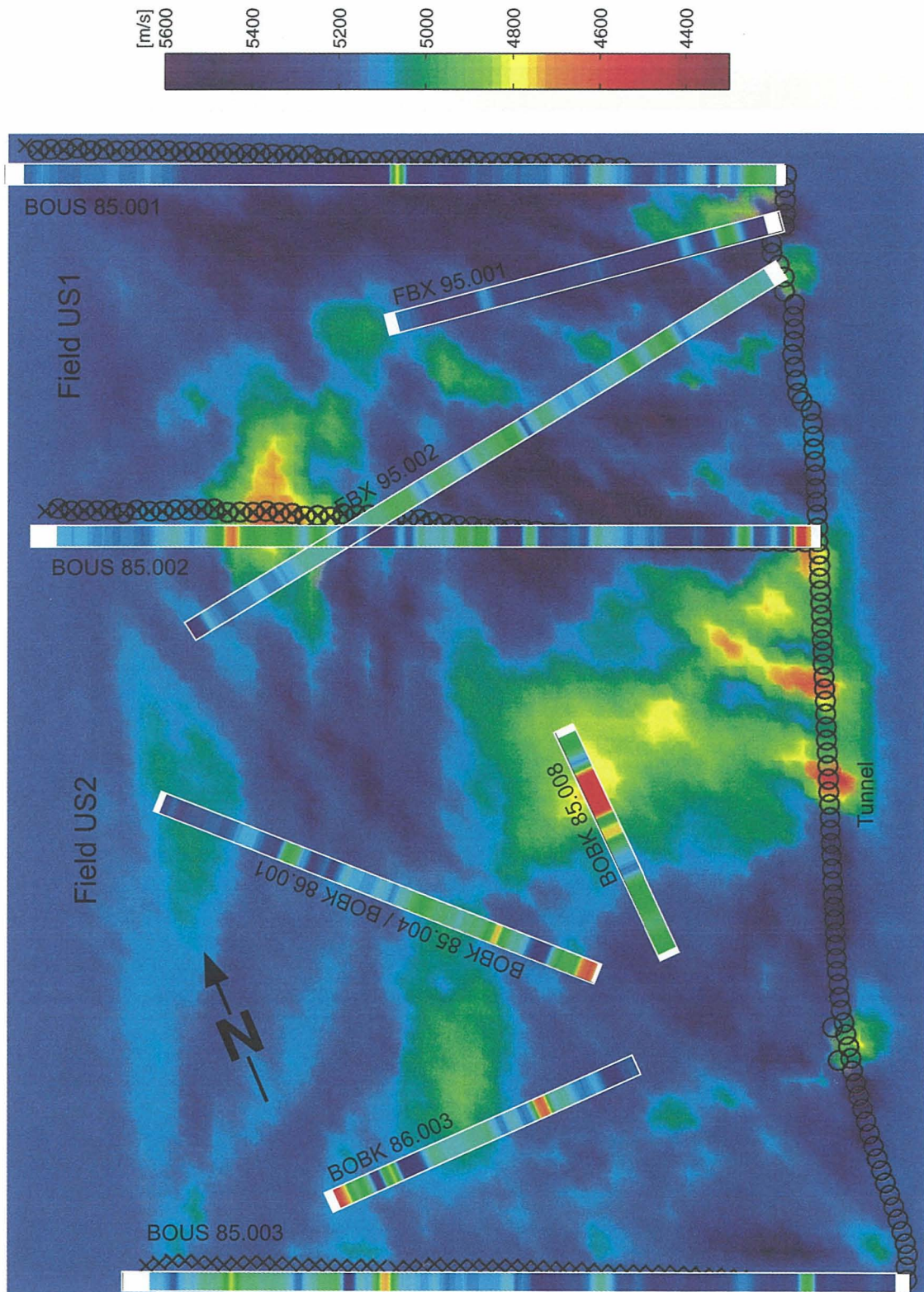


Fig. 5.6 Comparison of the CI inversion with the sonic velocities. The velocity image was superimposed with the colour-coded sonic logs (see Fig. 5.2).

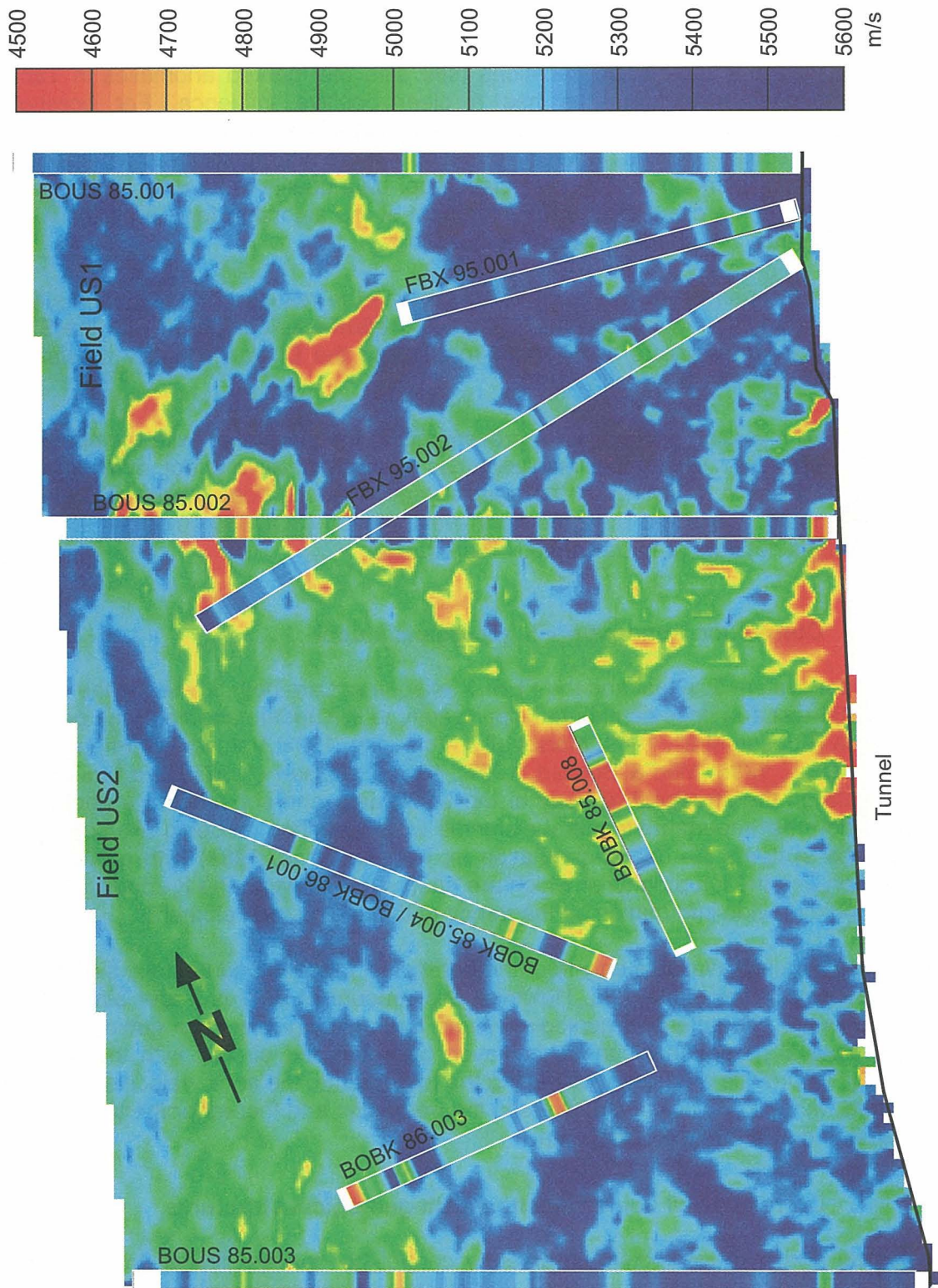


Fig. 5.7

Comparison of WFI inversion with the sonic velocities. The velocity image (with an anisotropy correction of 2%) was superimposed with the colour-coded sonic logs (see Fig. 5.2).

The wavefield inversion (Fig. 5.7: see also Figs. 4.15 and 5.2) shows a good correlation for all boreholes except BOUS85.001 and FEX95.002 in Field US2; this is also partly true for the smaller-scale variations (see also the marked anomalies in Table 5.2). The higher resolution thus has a clear positive influence. For borehole BOUS85.001, the tomogram and the log image correlate well up to around 70 m. The generally high sonic velocities between 70 and 150 m are not reproduced. Whether this is due to an insufficient anisotropy correction, poor data quality or an error in the inversion procedure is not clear. Further development of the algorithm for the elastic wave equation (Chapter 4.4) should answer this question.

A qualitative comparison of the sonic velocities with the results of the new travelttime inversions shows clear improvements for both procedures as compared with the SIRT inversion. The AVT appears to be more robust and the CI has a better resolution. However, the differences are only slight.

The wavefield inversion also shows improvements in the correlation with the sonic velocities for Field US2. The higher resolution has a clearly positive effect, even where it is no longer possible to distinguish between inversion-induced oscillations and the image of the geology. In Field US1, the north-west section (BOUS85.001 from 70 m) in particular does not appear to be correctly reproduced.

5.4 Correlation tomogram <-> geological model

The fracture system flow test and the FEBEX experiment are both located in the region of the US85 test and have contributed significantly to the understanding of the geology of the area (Keusen et al., 1989; Marschall & Vomvoris, 1993; Vomvoris & Frieg, 1991; McKinley et al., 1996; Möri & Bossart, 1997). Möri & Bossart (1997) have brought together data on the structural geology of the US85 area and constructed a geological model. The most important structural elements were identified as being two conjugate shear zone systems (S- and K-orientation, s. Keusen et al., 1989) with partly brittle reactivation and the lamprophyres which are often sub-parallel to the K zones. Tomography should provide information on the trends of these structural elements.

Geological data are available only from the boreholes, caverns and tunnels, similarly to the situation with the sonic data. However, the amount of data is larger since more boreholes were characterised geologically and hydrogeologically. The geological and hydrogeological parameters cannot, however, be compared directly with the seismic velocities. To provide a basis for validating the tomograms, the sonic velocities are first compared with the geological structures in the boreholes and thereafter the tomograms are correlated with the geological data.

5.4.1 Correlation of sonic velocities with geological structures

Geological and hydrogeological parameters cannot be derived directly from seismic velocities. Besides mineral composition, the seismic velocities describe the mechanical stability of the rocks. Shear zones, for example, have different mechanical - and therefore seismic - parameters to the intact rock and it is therefore possible, generally to correlate shear zones with seismic parameters (Albert, 1995).

Sonic and geological data are available for the boreholes described above (see Annex 1-8).

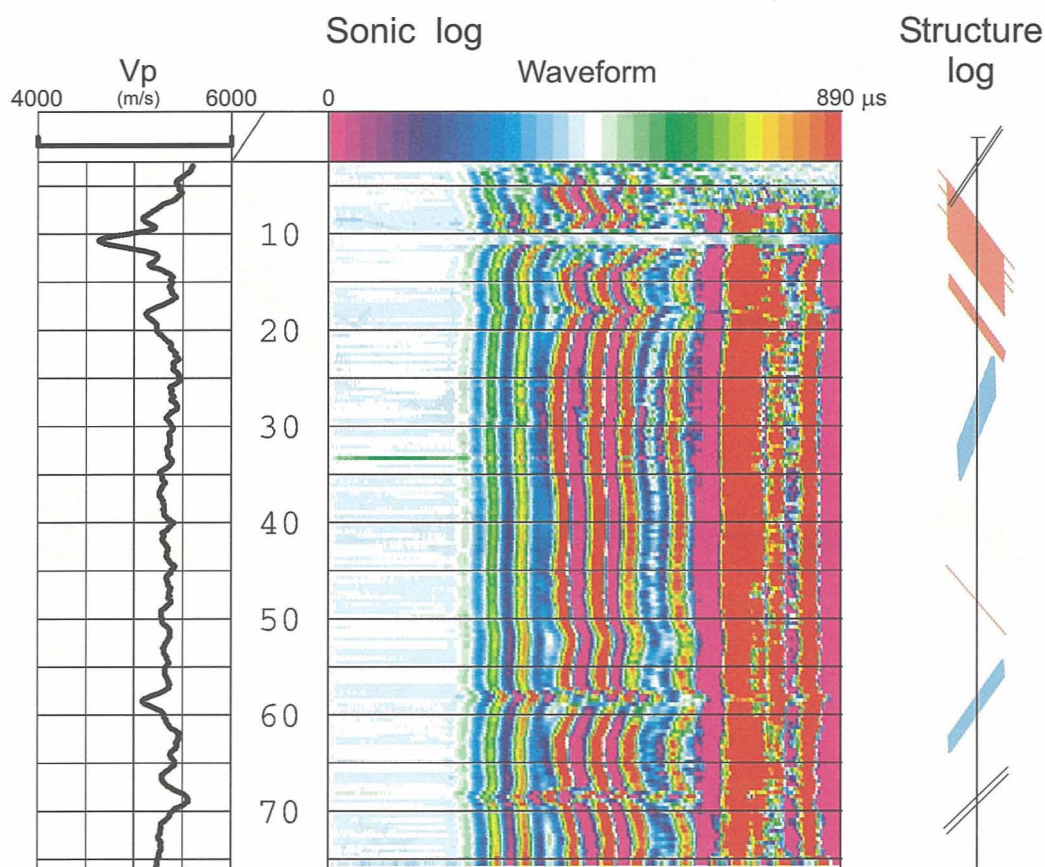


Fig. 5.8 Comparison of geological structures (S-zone: red, K-zone: blue and lamprophyre: grey) with the sonic logs (waveform and velocity: V_p) for borehole FEX95.001.

The sonic log for borehole FEX95.001 (Fig. 5.8), for example, shows an almost homogeneous velocity of approx. 5400 m/s and a few negative (10, 18 and 58 m) and positive (2 and 69 m) anomalies. Anomalies can also be observed at these positions in the sonic wave trains. The negative velocity anomalies correlate well with the S- and K-zones while lamprophyres can be found at the positive anomalies. The marked anomaly at 10 m also showed a water inflow point. However, not all S- and K-zones and lamprophyres can be linked with velocity anomalies, with small zones in particular showing no anomaly.

To summarise, the following relationships have been identified between sonic velocities and geological structures in GTS Fields US1 and US2 (Möri & Bossart, 1997):

- S-structures are often responsible for low velocities in the sonic logs and are generally recognised by the logs.
- K-structures are also generally associated with low velocities but are not recognised as frequently as S-structures by the sonic logs.
- Lamprophyres generally cause an increase in velocity in the sonic logs.
- Hydrothermally altered and cataclastically deformed zones with a high biotite content are frequently associated with low velocities.
- Quartz veins and alpine tension joints can either increase or decrease the velocity.

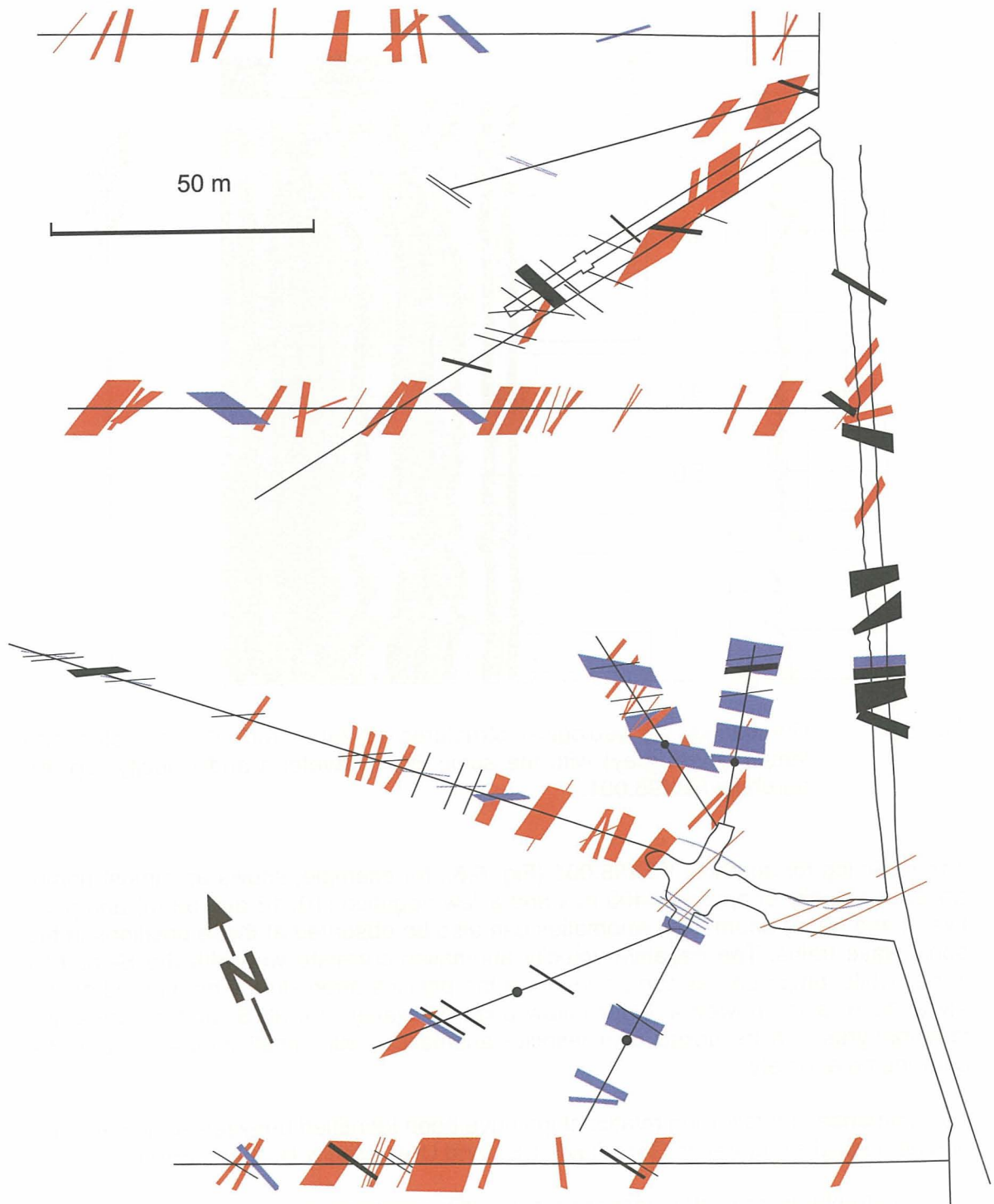


Fig. 5.9

Plan with the geological interpretation of structural elements (S-zone: red, K-zone: blue and lamprophyre: grey). Projection of the borehole information onto the tomographic plane.

Marked velocity anomalies frequently occur where structures intersect (see Fig. 5.9). The fact that lamprophyres are associated with higher velocities may appear surprising at first. This was also observed by Keusen et al. (1989) and can be explained on the basis of the mineralogical composition of the lamprophyres.

5.4.2 Correlation of the tomograms with geological structures

It has to be borne in mind when comparing the tomograms with the geological structures that only those structures which have a thickness equivalent to around one wavelength of the seismic signal (or the first Fresnel zone for traveltime tomography) are resolved in the tomograms. In this respect, structure is taken to mean not only a water inflow point with a thickness of perhaps 1 mm, but also the whole mechanically disturbed zone which shows lower seismic velocities. Further, only the S- and K-structures should be compared with the tomograms. The lamprophyres often show slight velocity increases, but can also be associated with velocity decreases, which makes them difficult to characterise seismically.

Möri & Bossart (1997) projected the geological structures mapped in the boreholes onto the tomography plane (Fig. 5.9) and then inter- and extrapolated the data between the boreholes and the tunnel to produce a structural geology model of Fields US1 and US2 (Fig. 5.10). When the projection of the geological structures (Fig. 5.9) and the structural model (Fig. 5.10) are superimposed on the tomograms (see Annex 9-12), the impression is that the tomograms correlate only partly with the geological structures. This is not surprising since the sonic velocities in the boreholes did not correlate for every geological structure. If only those geological structures which are clearly imaged in the sonic logs are taken into account in the correlation, the following conclusions can be reached:

- For the SIRT inversion (Fig. 3.3, Annex 9), the prominent structures correlate partly with wide (≥ 10 m) velocity decreases. However, geological structures are not always responsible for the decreases in velocity.
- For the AVT (Fig. 3.6, Annex 10), three anomalies (BOBK85.008: 30-48 m and BOUS85.002: 0-10 m & 100-120 m) correlate clearly with geological structures. Marked decreases in velocity ($V_p < 4800$ m/s) always coincide with geological structures.
- For the CI (Fig. 3.17, Annex 11), many of the geological structures are reproduced, as is the case for the AVT inversion. One clear velocity decrease (BOBK86.003 at 30-40 m) occurs at a location where there is no geological structure.
- The wavefield inversion (Fig. 4.15, Annex 12) shows the best correlation. Not only prominent structures correlate with velocity decreases. Along boreholes BOUS85.001 and 85.002 in Field US1 there are a few velocity decreases (< 4800 m/s) which do not correlate with geological structures. This can be explained by the oscillations along the field boundaries, which have already been discussed. The correlation is better at the boundaries of Field US2. The only velocity decrease along borehole BOUS85.003 which cannot be correlated with a geological structure is located at a depth for which the sonic log shows a velocity decrease.

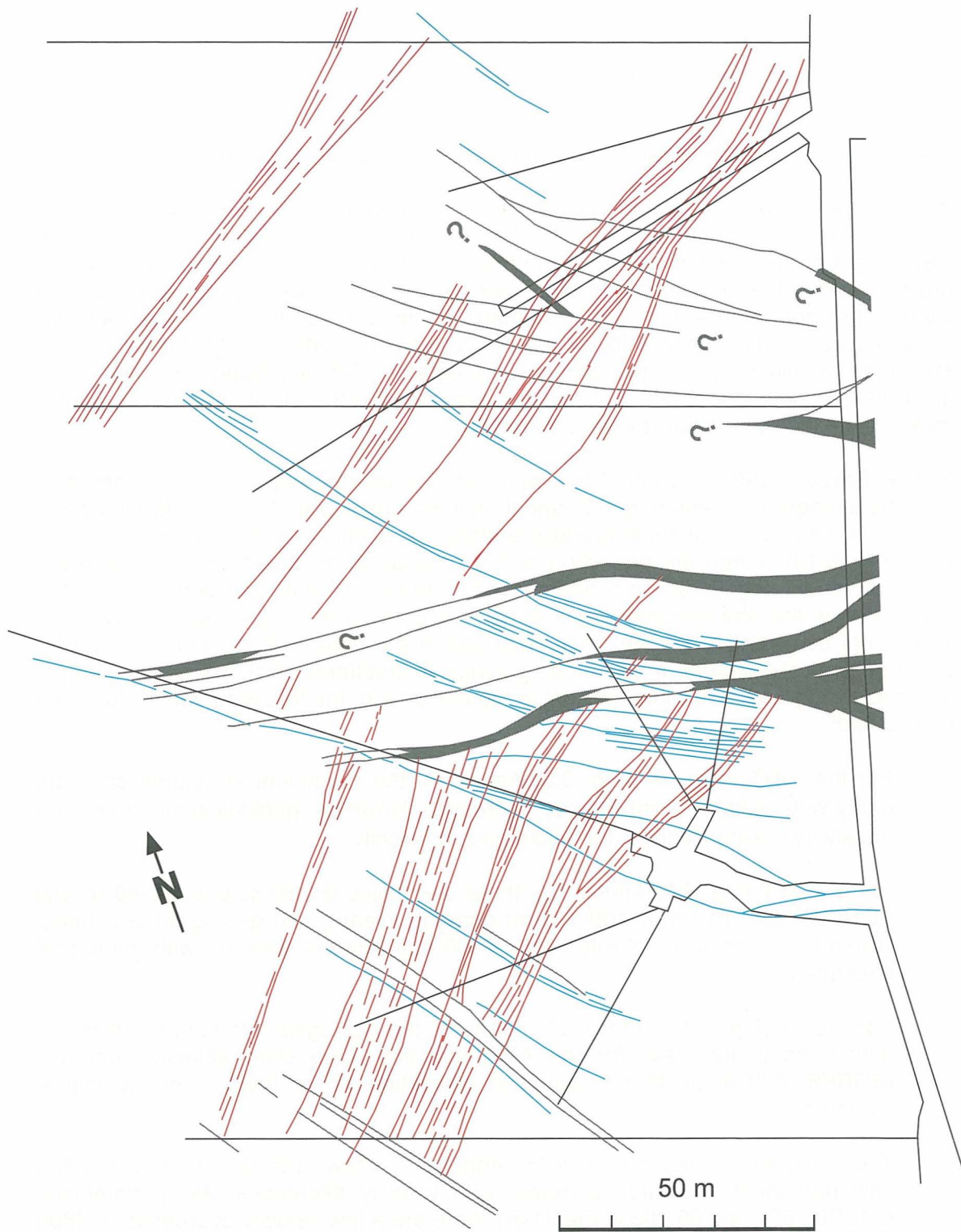


Fig. 5.10 Interpretation of structural elements (S-zone: red, K-zone: blue and lamprophyre: grey) based on geological and hydrogeological data (Möri & Bossart, 1997).

Generally, all the tomograms show the most prominent velocity anomalies at the same locations. This allows a weighting of the geological structures independent of inversion technique.

The clearest fault zones are expected between the BK cavern and borehole BOUS85.002 (clearly evidenced in borehole BOBK85.008). This area - with its sequence of lamprophyres, S- and K-structures - is easily recognisable by any visitor in the laboratory tunnel. Geological extrapolation into Field US2 is not easy. In Möri & Bossart's (1997) geological model (Fig. 5.10), the area is notable mainly due to the question marks. It is certainly permissible to extend the fault zones visible in the tunnel along the velocity decreases in the tomograms for a geological interpretation (Fig. 5.11).

A further velocity decrease, which is imaged mainly in the traveltimes inversions, is located at approx. 100-120 m in borehole BOUS85.002. In this case the wavefield inversion shows less clear decreases which are overlain by oscillations. These oscillations have already been identified in Chapter 4 as artefacts. Geological structures were indeed found in this section of BOUS85.002, but not as many as expected on the basis of the velocity decreases in the traveltimes inversions. No particular importance is assigned to this zone in the geological model.

Linking these two zones of reduced velocity with one another and interpreting further velocity decreases in terms of direction is dependent on the selected tomogram and is not essential.

When making this interpretation, it should not be forgotten that the velocity contrasts in Fields US1 and US2 are very small and that, in terms of tomographic resolution, the geological structures encountered are generally small. Modelling the effects of mislocations and triggering inaccuracies (see Chapter 3.3) shows similar velocity anomalies to those which are due to geology.

5.5 Overall evaluation of the inversion techniques

New inversion techniques have been developed and tested as part of this project. Compared to the SIRT inversion, the two new traveltimes inversions (AVT and CI) produce a more stable image with less artefacts which correlates better with measured sonic velocities and geological structures. The difference between AVT and CI is small; the AVT image has a poorer resolution, but is more reliable in terms of structure identification. A combination of the two techniques may improve the image quality.

The wavefield inversion produces the best resolution and the best correlation with sonic results and geological evidence, but it also produces the image with the most artefacts. The reliability of the interpretation is reduced by strong oscillations mainly at the field boundaries and by sensitivity to the selected anisotropy correction. Reliability of the interpretation will only be improved by further developing this algorithm for the elastic wave equation, taking into account the anisotropy.

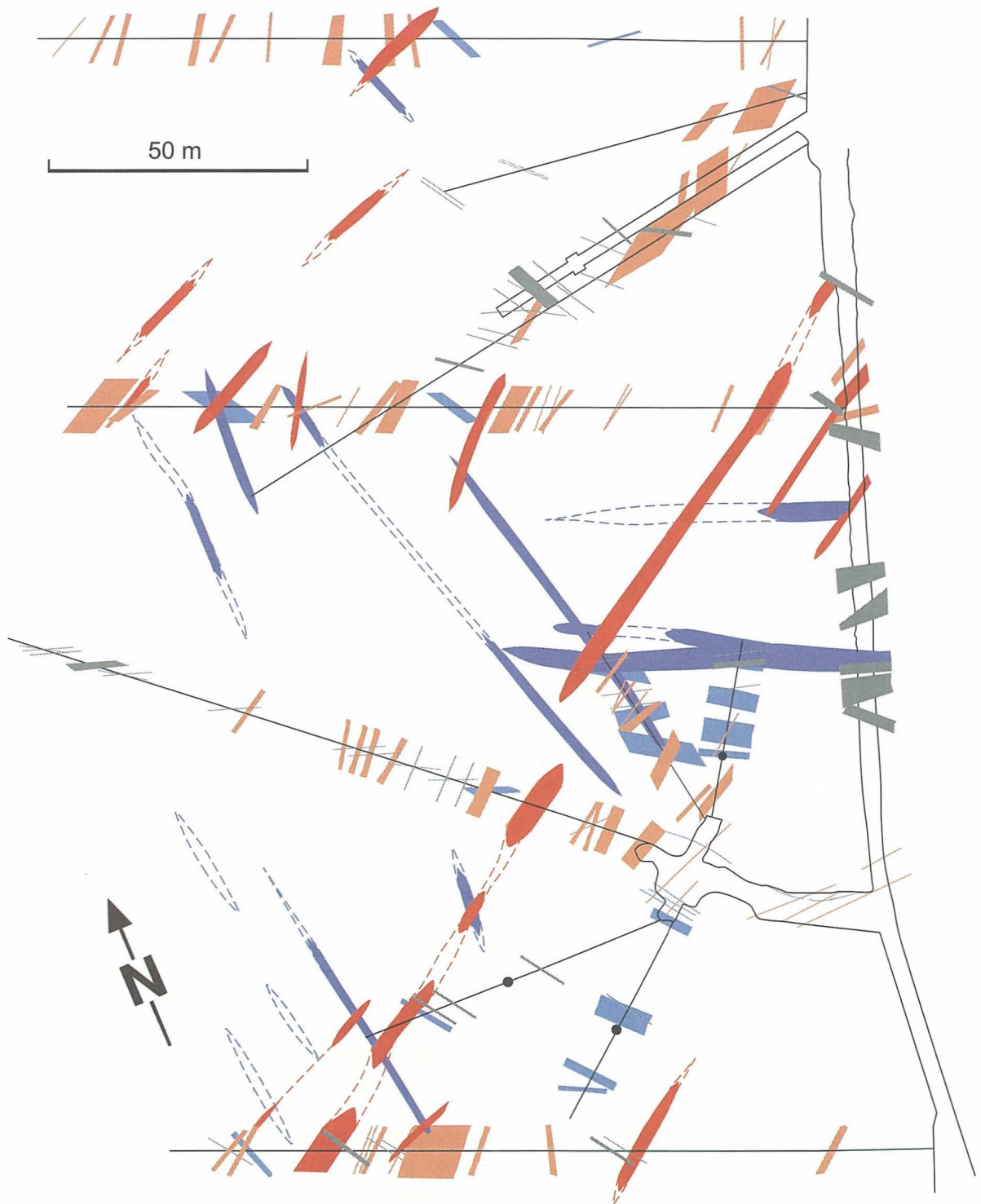


Fig. 5.11 Geological interpretation of AVT, CI and WFI tomograms (S-zone: red and K-zone: blue).

6. CONCLUSIONS ON NEW INVERSION METHODS

Both the anisotropy velocity tomography (AVT) and coupled inversion (CI) methods have produced tomograms which are clearly more stable and have fewer artefacts than the SIRT inversion. The velocity images of the two new traveltimes inversions differ only slightly and, within the range of achievable resolution, agree well with available sonic data. They also provide additional information such as anisotropy images and relocation of shot and receiver positions. This information is helpful in evaluating and interpreting inversion results, even if it has to be assumed that location errors in the anisotropy images as well as the anisotropy in the relocation result will be imaged. Combining the two techniques would bring more certainty, but the resulting velocity image would not be significantly different.

An important point to bear in mind when evaluating inversion techniques is that it is not only their stability and freedom from artefacts which is important, but also their resolution. In principle, the resolution of the traveltimes inversions is restricted to the first Fresnel zone (Williamson 1991; Williamson & Worthington 1993). It is thus dependent on the wavelength of the seismic signal and on the ray length and, consequently, the geometry of the measurement field. In Field US2, for example, the maximum resolution reached with traveltimes tomography is 20 - 25 m. Wavefield inversion (WFI) was tested as a means of getting round this restriction. WFI (Song et al., 1995) is based on the acoustic wave equation and seismic waves are therefore calculated only approximately. The inversion results showed a verifiable increase in resolution up to one wavelength (approx. 5 m). However, the WFI also has many artefacts such as oscillations and a very marked sensitivity to the selected global anisotropy correction. These two factors make interpretation significantly more difficult. Only by considering the elastic wave equation and anisotropy as a free parameter can the procedure be improved to the stage where it is robust and interpretable tomograms can be produced.

In order to test newly developed, high-resolution inversion techniques such as, e.g., a WFI which is based on the elastic wave equation and takes anisotropy into account, a new field dataset should be used. Particularly for the WFI (Chapter 4), it has become clear that the data registered at the Grimsel Test Site in 1985 are not sufficient for a high-resolution inversion technique (Chapter 4.3). For this reason, among others, the data for Field US3 were not taken into account for all the inversion techniques presented here.

In planning future tomography projects, the question of the necessary resolution will be decisive for the selection of inversion techniques and the necessary quality control of field acquisition.

REFERENCES

- AKI, K., and LEE, W. K. H. (1976): Determination of three-dimensional velocity anomalies under a seismic array using first p arrival times from local earthquakes. - *J. Geophys. Res.*, 81, 4381-4399.
- ALBERT, W. (1994): Lagevermessung der Tomographiebohrungen im FLG. - unpublished report, Nagra, Wettingen.
- ALBERT, W. (1995): Petrophysical parameters – an indication of rock permeability ?, *Nagra bulletin*, 26, 26-37.
- ALBERT, W. (1997): Sprengstoff als seismische Bohrlochquelle: Welche Schäden an der Bohrlochwand treten auf ?, - unpublished report, Nagra Wettingen.
- AMMON C.J., and VIDALE J. (1993): Tomography without rays. – *Bull. Seismol. Soc. Am.*, 83 (2), 509-528.
- ASTURIANA DE ZINC S.A., DEUTSCHE MONTAN TECHNOLOGIE, ESCUELA TECNICA SUPERIOR DE INGENIEROS, DE MINAS DE MADRID, and BRITISH GEOLOGICAL SURVEY (1998): Development of tomographic systems for mining, mineral exploration and environmental purposes. – EU Project BE-7508, in press.
- BLAIR, D. P., and A. T. SPATHIS (1982): Attenuation of explosion-generated pulse in rock masses. - *J. Geophys. Res.*, 87, 3885-3892.
- BLÜMLING, P., and SATTEL, G., (1988): Tomographic Investigations: *Nagra Bull.* 1+2, 1988, 35-40, Nagra Wettingen.
- BOURBIÉ, T., COUSSY, O. and ZINSZNER, B. (1987): *Acoustics of Porous Media.* - Gulf Publishing, Houston, Texas.
- BPB (1985): Logs from the boreholes BOUS85.001, 85.002 & 85.003.
- BÜHNEMANN J. (1996): Feldtest hochfrequenter seismischer Quellen in kristallinem Gestein. - Unpublished report, Nagra Wettingen.
- BÜHNEMANN J., and HOLLIGER K. (1998): Comparison of high-frequency seismic sources at the Grimsel Test Site, Central Alps, Switzerland. – *Geophysics*, 63, p. 1363 - 1370.
- CHAPMAN, C.H., and PRATT, G.R. (1992), Traveltime tomography in anisotropic media--I. - Theory: *Geophys. J. Intl.*, 109, 1-19.
- DYER B., and BARIA R. (1994): Development of the CSMA Mark II high temperature borehole sparker source. - unpublished report CSMA.
- EMSLEY, S., GUERENDEL, P., and ROBSON S. (1994): The 2D-interpretation of the tomogram data from the RCF-area Sellafeld. – Nirex Report S/94/007, Nirex.

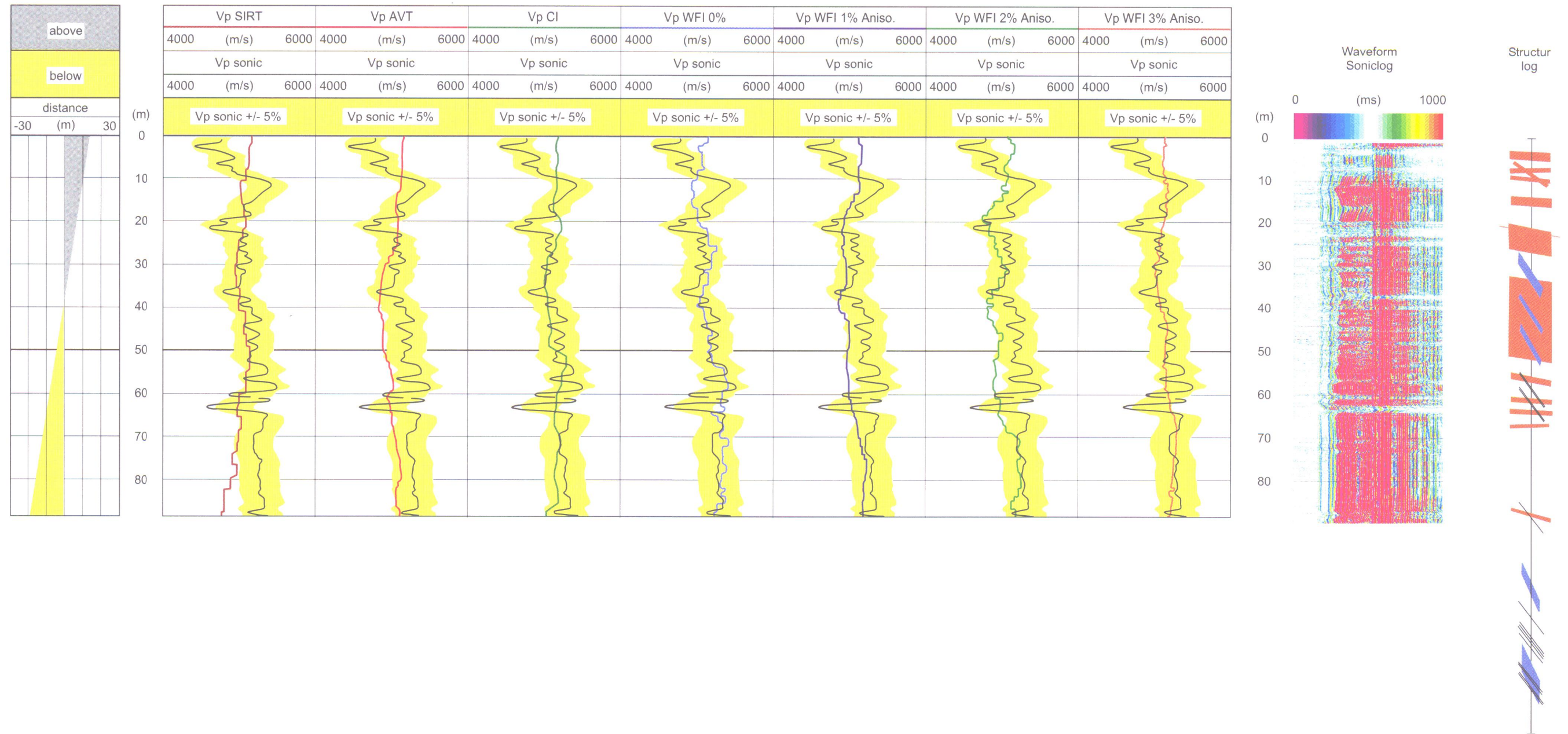
- GELBKE C. (1988): Felslabor Grimsel: Seismische Durchschallungstomographie.- Nagra technical report NTB 88-06, Nagra Wettingen.
- GELBKE, C., MIRANDA, F., and SATTEL, G. (1989): Results of a seismic transmission tomography survey at the Grimsel Rock Laboratory. - *The Log Analyst*, July-Aug., 1989, 243-260.
- GREEN, A.G., and MAIR, J.A. (1983): Subhorizontal fractures in a granitic pluton: their detection and implications for radioactive waste disposal. - *Geophysics*, 48, 1428-1449.
- HÄRING M.O. (1996): GTS/FEBEX: Supervision and interpretation of geophysical investigations Boreholes FBX 95.001 and FBX 95.002, Unpublished report, Nagra, Wettingen.
- HAYLES, J.G., SERZU, M.H., LODHA, G.S., EVERITT, R.A., and TOMSONS, D.K. (1996): Cross-hole seismic and single-hole geophysical surveys to characterise an area of moderately fractured granite. - *Can. J. Expl. Geophys.*, 32, 6-23.
- HOLLIGER, K. and BÜHNEMANN, J. (1996): Attenuation of broad-band (50-1500 Hz) seismic waves in granitic rocks near the earth's surface. - *Geophys. Res. Lett.*, 23, 1981-1984.
- HOLUB (1984): Bericht über geophysikalische Bohrlochmessungen im Felslabor Grimsel, Bohrlochmessungen in der BOVE 84.011, BOWT 84.009 und BOWT 84.010. - unpublished report Geotest.
- JO, C. H., SHIN, C. S., and SUH, J. H. (1996): Design of an optimal 9 point finite difference frequency-space acoustic wave equation scheme for inversion and modelling. - *Geophysics*, 61, 529-537.
- JOHNSTON, D. H., M. N. TOKSÖZ, and A. TIMUR (1979): Attenuation of seismic waves in dry and saturated rocks II. Mechanisms. - *Geophysics*, 44, 691-711.
- JUHLIN, C. (1995): Imaging of fracture zones in the Finnsjön area, central Sweden, using the seismic reflection method. - *Geophysics*, 60, 66-75.
- JUHLIN, C. (1990): Seismic attenuation, shear wave anisotropy and some aspects of fracturing in the crystalline rock of the Siljan Ring area, central Sweden, PhD Thesis, 167 pp. - Uppsala University, Uppsala.
- KEUSEN, H.R., GANGUIN, J., SCHULER, P., and BULETTI, M. (1989): Felslabor Grimsel, Geologie. - Nagra technical report NTB 87-14, Nagra, Wettingen.
- KISSLING, E. (1988): Geotomography with local earthquake data. - *Rev. Geophys.* 26, 659-698.
- KRAGH, E., CHAPMAN, C., EMSLEY, S., and DODDS, K. (1996): Anisotropic travelttime tomography in a hard-rock environment. - *First Break*, 14, 391-397.
- LI, X.-P. (1995): Estimation of apparent attenuation of crystalline rocks in the KTB area using VSP data. - *Scientific Drilling*, 5, 199-216.

- MARQUARDT (1970): Generalised inverse, ridge regression, biased linear estimation and non-linear estimation. - *Technometrics*, 12, 591-612.
- MARSCHALL P., VOMVORIS S., BOSSART P., CORREA N., GUYONNET D., HEINEMANN-GLUTSCH B., HURTIG E., JOHNS R., KOHL T., KUHLMANN U., MÜRI F., and RYBACH L. (1993): Grimsel Test Site, Developments in hydro-testing, fluid logging and combined salt/heat tracer experiments in the BK-site (phase III). - Nagra technical report NTB 93-47, Nagra, Wettingen
- MAURER H.R. (1996): Systematic errors in seismic crosshole data: application of coupled inverse technique. - *Geophysical Research Letters*, Vol. 23, No. 19, p. 2681-2684.
- MAURER H.R., and GREEN A.G. (1997): Potential coordinate mislocations in cross-hole tomography: results from the Grimsel Test Site, Switzerland. – *Geophysics*, 62, p. 1696-1709.
- MC KINLEY I., KICKMAIER W., DEL OLMO C., and HUERTAS F. (1996): The FEBEX project: Full-scale simulation of engineered barriers for a HLW repository. – *Nagra bulletin*, 27, 56-67.
- MENKE, W. (1984): *Geophysical data analysis: discrete inverse theory*. - Academic Press Inc.
- MICHELENA, R.J., HARRIS, J.M., and MUIR, F. (1995): Crosshole tomography estimation of elastic constants in heterogeneous transversely isotropic media. - *Geophysics*, 60, 774-783.
- MICHELENA, R.J., MUIR, F., and HARRIS, J.M. (1993): Anisotropic travelttime tomography. - *Geophys. Prosp.*, 41, 381-412.
- MILLER, R.D., PULLAN, S.E., STEEPLES, D.W., and HUNTER, J.A. (1992): Field comparison of shallow seismic sources near Chino, California. - *Geophysics*, 57, 693-709.
- MILLER, R.D., PULLAN, S.E., WALDNER, J.S., and HAENI, F.P. (1986): Field comparison of shallow seismic sources. - *Geophysics*, 51, 2067-2092.
- MÖRI A., and BOSSART P. (1997): Visualisierung und Interpretation der geologischen Strukturen aus den Bohrungen der Felder US-1 und US-2. - unpublished report, Nagra Wettingen.
- MUFTI, I.R. (1995): Pitfalls in crosshole seismic interpretation as a result of 3D effects. - *Geophysics*, 60, 821-833
- PARKER, J.C., PELTON, J.R., and DOUGHERTY, M.E. (1993): A versatile shotgun source for engineering and groundwater seismic surveys. - *Geophysics*, 58, 1511-1516.
- PAHL A., HEUSERMANN St., BRÄUER V., and GLÖGGLER W. (1989): *Rock Stress Investigations*, Nagra technical report NTB 88-39. Nagra, Wettingen.

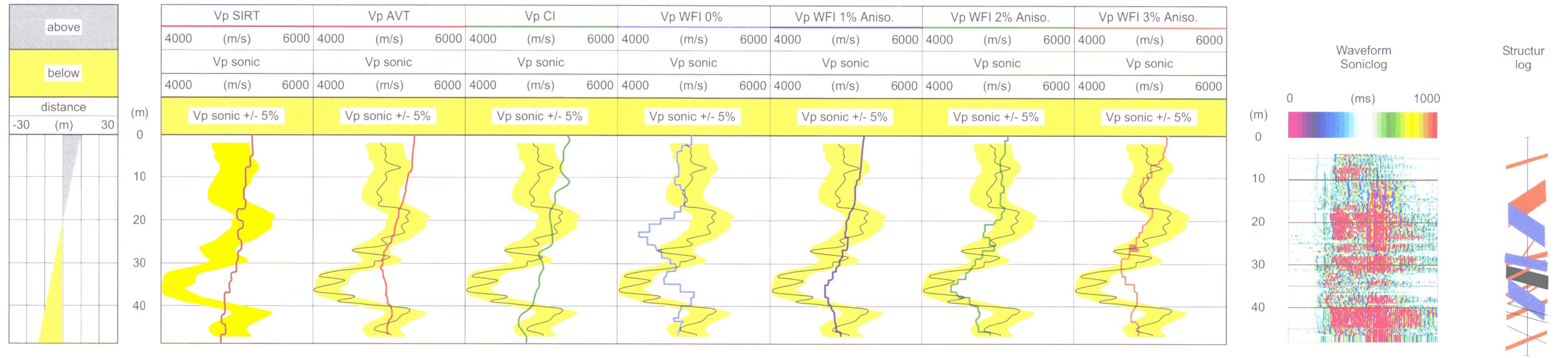
- PAULSSON, B.N.P. (1997): Results from the downhole vibrator survey at UPRC Carthage fracture site, unpublished paper. - Paulsson Geophysical Services Inc.
- PAULSSON, B.N.P., COOK, N.G.W., and MCENVILLY, T.V. (1985): Elastic-wave velocities and attenuation in an underground granitic repository for nuclear waste. - *Geophysics*, 50, 551-570.
- PRAKLA-SEISMOS (1981): Sondierbohrungen Juchlistock-Grimsel Band 3, geophysikalische Untersuchungen. Unpublished report. Nagra, Wettingen.
- PRATT R.G. (1995): Anisotropy velocity tomography for "field 1" tomographic data at the Grimsel Rock Laboratory. Unpublished report. Nagra, Wettingen.
- PRATT R.G. (1990): Frequency-domain elastic wave modelling by finite differences: A tool for crosshole seismic imaging (short note). - *Geophysics*, 55, no. 5, 626-632.
- PRATT, R. G., MCGAUGHEY, W. J., and CHAPMAN, C. H. (1993): Anisotropic velocity tomography: a case study in near-surface rock mass. - *Geophysics*, 58, 1748-1763.
- PRATT, R.G., and CHAPMAN, C.H. (1992): Traveltime tomography in anisotropic media--II. - *Applications: Geophys. J. Intl.*, 109, 20-37.
- PRATT, R.G., and SAMS, M.S. (1996): Reconciliation of crosshole seismic velocities with well information in a layered sedimentary environment. - *Geophysics*, 61, 549-560.
- PULLAN, S.E., and MACAULEY, H.A. (1987): An in-hole shotgun source for engineering seismic surveys. - *Geophysics*, 52, 985-996.
- RECHTIEN, R.D., HAMBACHER, K.L., and BALLARD, R.F. (1993): A high-frequency sparker source for the borehole environment. - *Geophysics*, 58, 660-669.
- SAMS, M.S., WORTHINGTON, M.H., KING, M.S., SHAMS KANSHIR, M. (1993): A comparison of laboratory and field measurements of anisotropy. - *Geophys. Prosp.*, 41, 189-206.
- SCHLUMBERGER (1992): Schlumberger cross-well system, unpublished paper. Schlumberger.
- SCHÖN, J.H. (1996): Physical properties of rocks. - Pergamon.
- SKOLNIK, M.I. (1990): Radar Handbook, 2nd Edition. - McGraw Hill, New York.
- SOLEXPART (1986): Felslabor Grimsel: Bohrlochlagevermessung - geodätisch, - mit Deflekto-Dex, - mit Multishot und Koordinatenberechnung der Bohrungen: BOUS85.001, BOUS85.002, BOUS85.003, Koordinatenberechnung der Kurzbohrungen BOUS85.013 bis 85.100. - unpublished report Solexpert.
- SONG J., and KIM K. (1996): Micromechanical Modeling of the Dynamic Fracture Process During Rock Blasting. - *Int. J. Rock Mech. Min. Sci. & Geomech. Abstr.*, 33, No. 4, 387-394.

- SONG Z.M., and WORTHINGTON M. (1995): Full wavefield inversion for the Grimsel Test Site, annual report (21.3.94 - 20.3.95). - Unpublished report. Nagra, Wettingen.
- SONG Z.M., WILLIAMSON, P.R., and PRATT R.G. (1995): Frequency-domain acoustic-wave modeling and inversion of crosshole data: Part II-inversion method, synthetic experiments and real-data results. - *Geophysics*, 60, 796-809.
- ŠTEKL I., and PRATT R.G. (1996): GTS: Isotropic and anisotropic full wavefield images of field 2 from Grimsel Test Site, annual report (March 1995 - March 1996). - Unpublished report. Nagra, Wettingen.
- ŠTEKL I., and PRATT R.G. (1998): Accurate viscoelastic modeling by frequency-domain finite differences using rotated operators. - *Geophysics*, 63, 1779-1794.
- TARANTOLA A. (1984): Inversion of seismic reflection data in the acoustic approximation. - *Geophysics*, 49, 1259-1266.
- TARANTOLA A. (1987): *Inverse problem theory: Methods for data fitting and parameter estimation*. Elsevier.
- TARIF R., and BOURBIÉ T. (1987): Experimental comparison between spectral ratio and rise time techniques for attenuation measurements. - *Geophys. Prosp.*, 35, 668-680.
- TAYLOR, J. R. (1982):, *An Introduction to Error Analysis*. - University Science Books, Mill Valley, California.
- THOENEN, J.R., and WINDES, S.L. (1942): Seismic effects of quarry blasting. - U.S. Bureau of Mines Bull. 442.
- THOMSEN, L. (1986): Weak elastic anisotropy. - *Geophysics*, 53, 1954-1966.
- TONN, R. (1989): Comparison of seven methods for the computation Q . - *Phys. Earth Planet. Inter.*, 55, 259-268.
- VASCO, D.W., PETERSEN, J.E., and MAJER, E.L. (1995): Beyond ray tomography: wavepaths and Fresnel zones. - *Geophysics*, 60, 1790-1804.
- VIDALE, J. (1988): Finite-difference calculation of traveltimes. - *Bull. Seism. Soc. Am.*, 78, 2062-2076.
- VOMVORIS S., FRIEG B., GUYONNET D., KELLEY V., LAVANCHY J.-M., LÖW S., and MISHRA S. (1991): Grimsel Test Site, Interpretation of crosshole hydraulic tests and a pilot fluid logging test for selected boreholes within the BK-site. - Nagra technical report NTB 91-09, Nagra, Wettingen
- WHITAKER, S.H. (1987): Geoscience research for Canadian Nuclear Waste Management Program. - *Radioactive Waste Management and Fuel Cycle*, 8, 145-196.

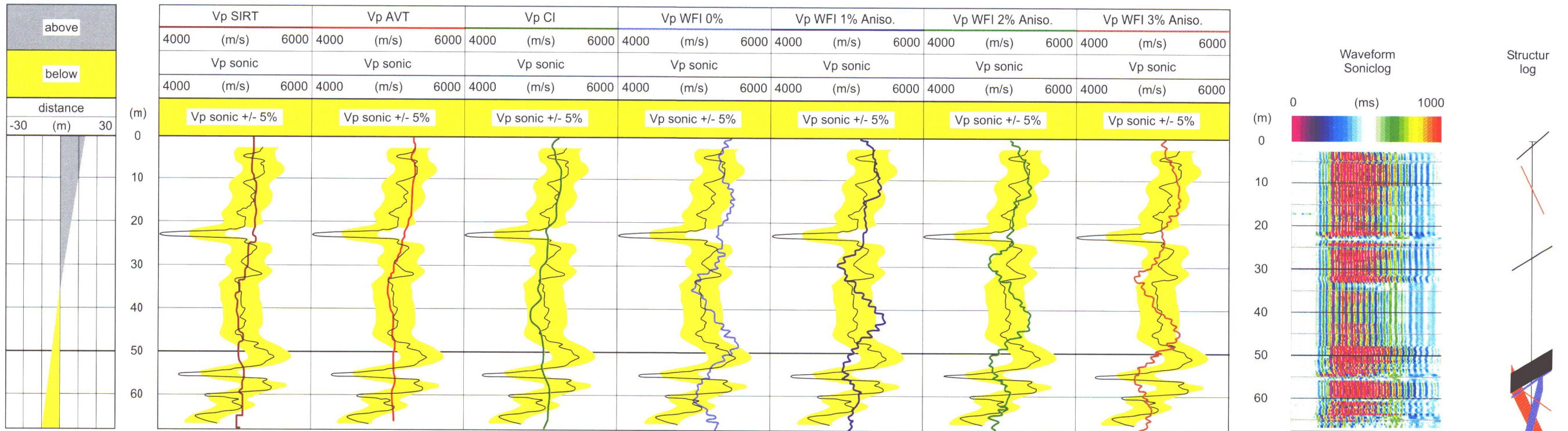
- WHITE, R. E. (1992): The accuracy of estimating Q from seismic data. - *Geophysics*, 57, 1508-1511,.
- WILLIAMSON, P.R. (1991): A guide to the limits of resolution imposed by scattering in ray tomography. - *Geophysics*, 56, 202-207.
- WILLIAMSON, P.R., SAMS, M.S., and WORTHINGTON, M.H. (1993): Crosshole imaging in anisotropic media. - *The Leading Edge*, 12, 19-23.
- WILLIAMSON, P.R., and WORTHINGTON, M.H. (1993): Resolution limits in ray tomography due to wave behaviour. - *Numerical experiments: Geophysics*, 58, 727-735.
- WORTHINGTON M.H. and PESSOA M. (1994): GTS: Seismic traveltime tomography at the Grimsel Rock Laboratory. - Unpublished report. Nagra, Wettingen.
- WU, R. and TOKSOZ, M.N. (1987): Diffraction tomography and multisource holography applied to seismic imaging. - *Geophysics*, 52, 11-25.
- YILMAZ Ö. (1987): Seismic data processing. - Soc. of Expl. Geophys., Tulsa, Oklahoma, USA.



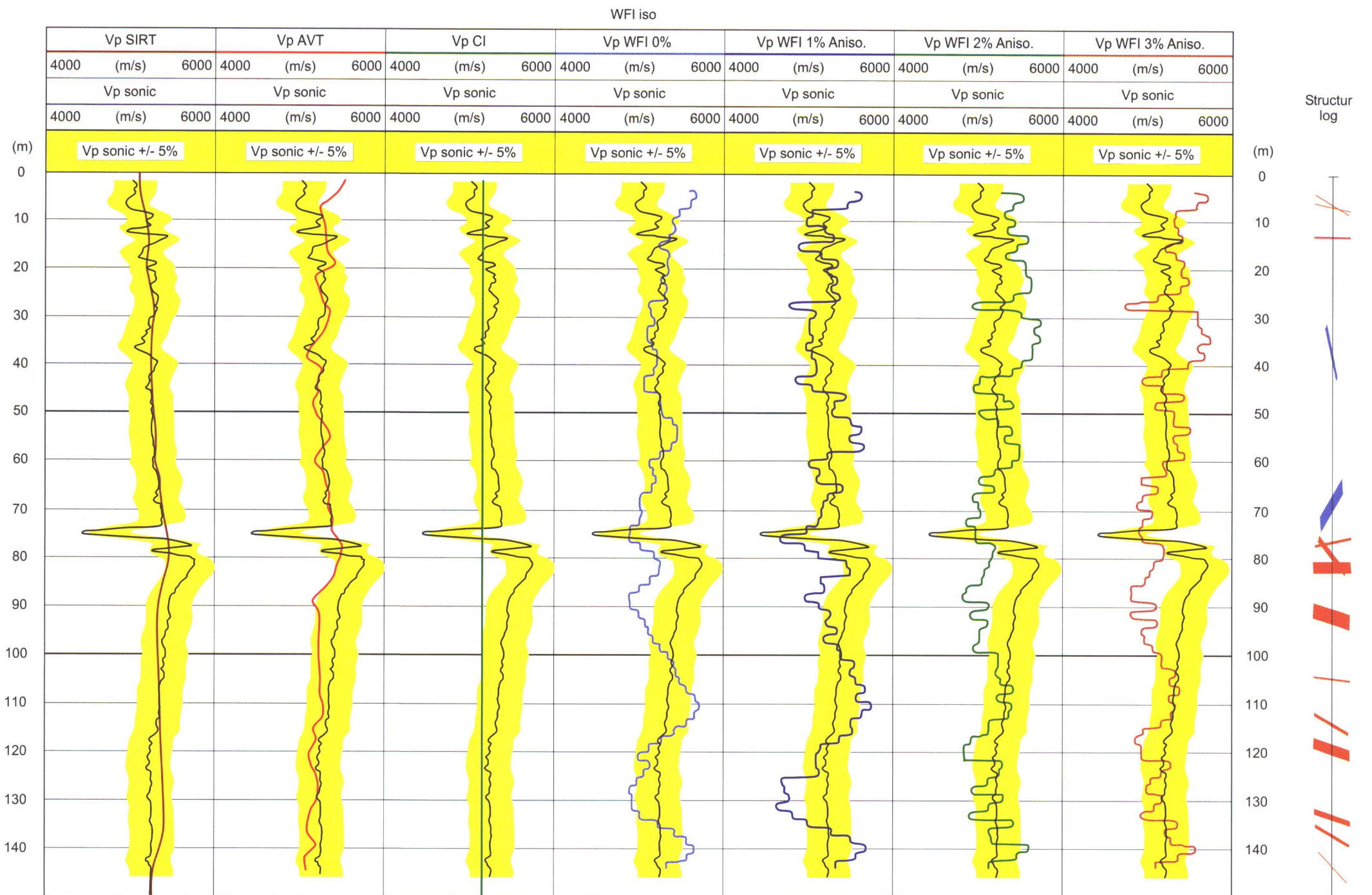
Annex 1: Composite log for borehole BOBK85.004/86.001. The composite log gives the sonic velocities, the tomogram velocities along the vertical projection of the borehole for the SIRT, AVT and CI traveltim inversions and for the isotropic WFI inversion, 1%, 2% and 3% anisotropy correction, the sonic wavefields and the geological structures.



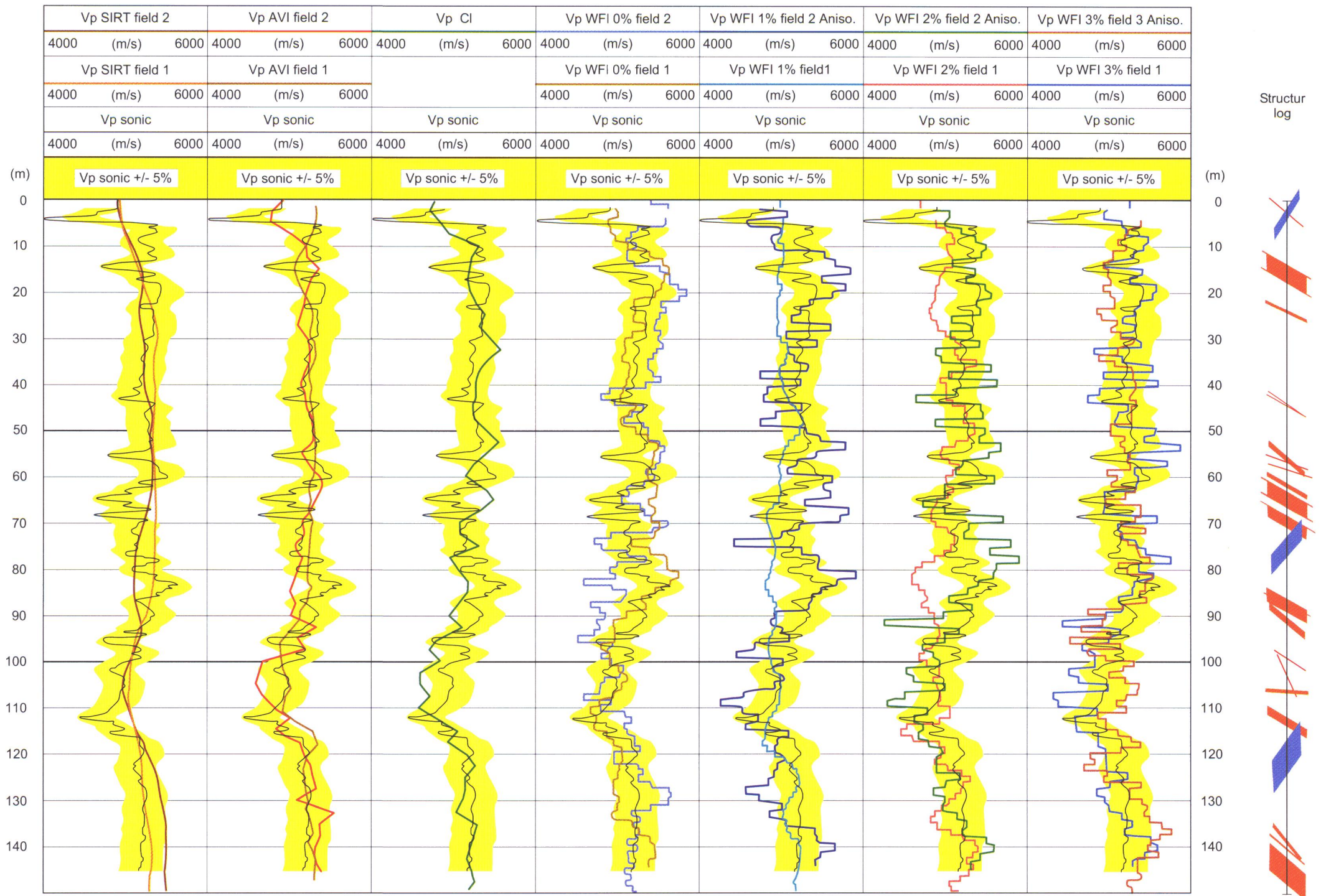
Annex 2: Composite log for borehole BOBK85.008. The composite log gives the sonic velocities, the tomogram velocities along the vertical projection of the borehole for the SIRT, AVT and CI travelt ime inversions and for the isotropic WFI inversion, 1%, 2% and 3% anisotropy correction, the sonic wavefields and the geological structures.



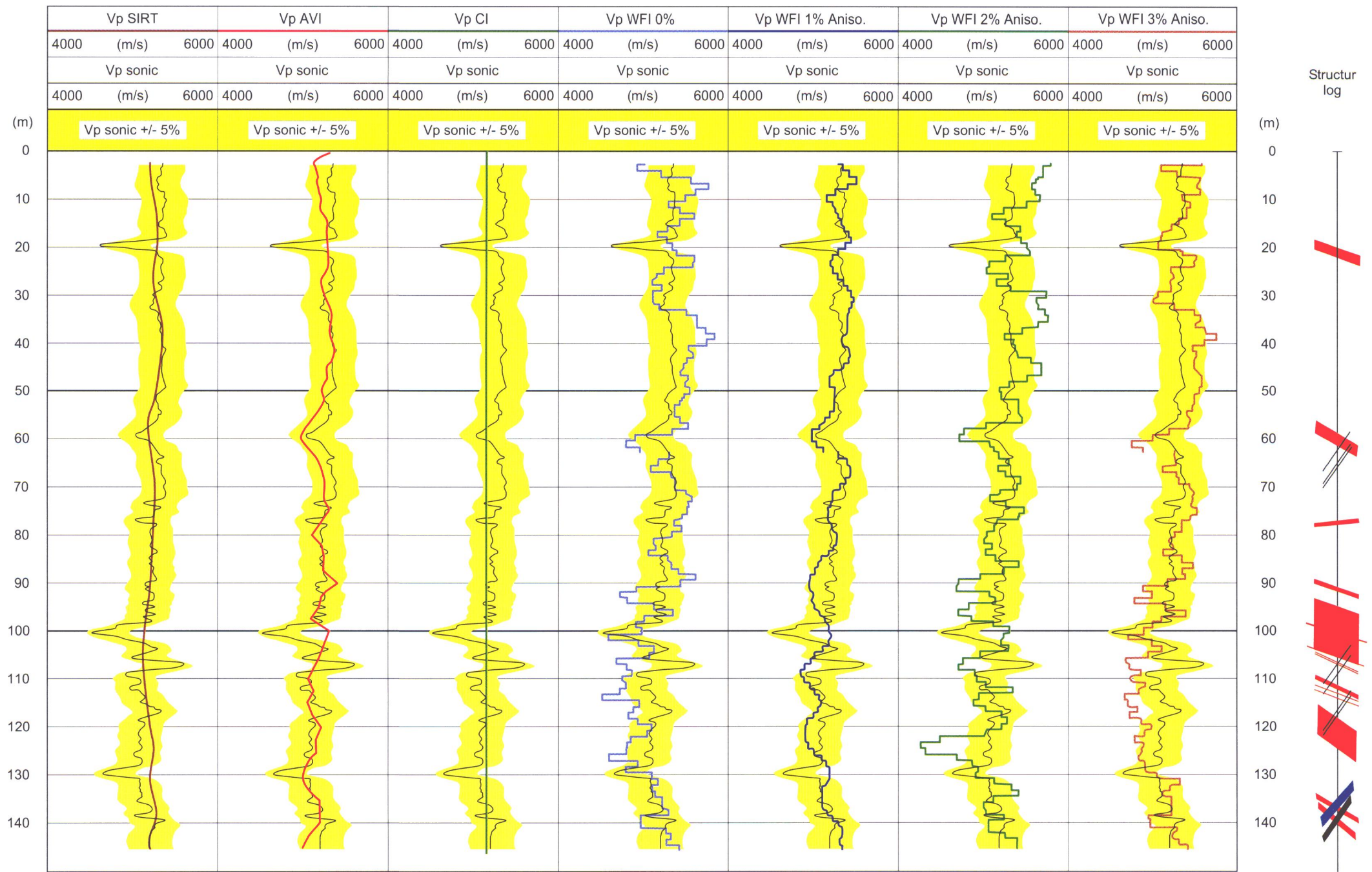
Annex 3: Composite log for borehole BOBK86.003. The composite log gives the sonic velocities, the tomogram velocities along the vertical projection of the borehole for the SIRT, AVT and CI traveltimes inversions and for the isotropic WFI inversion, 1%, 2% and 3% anisotropy correction, the sonic wavefields and the geological structures.



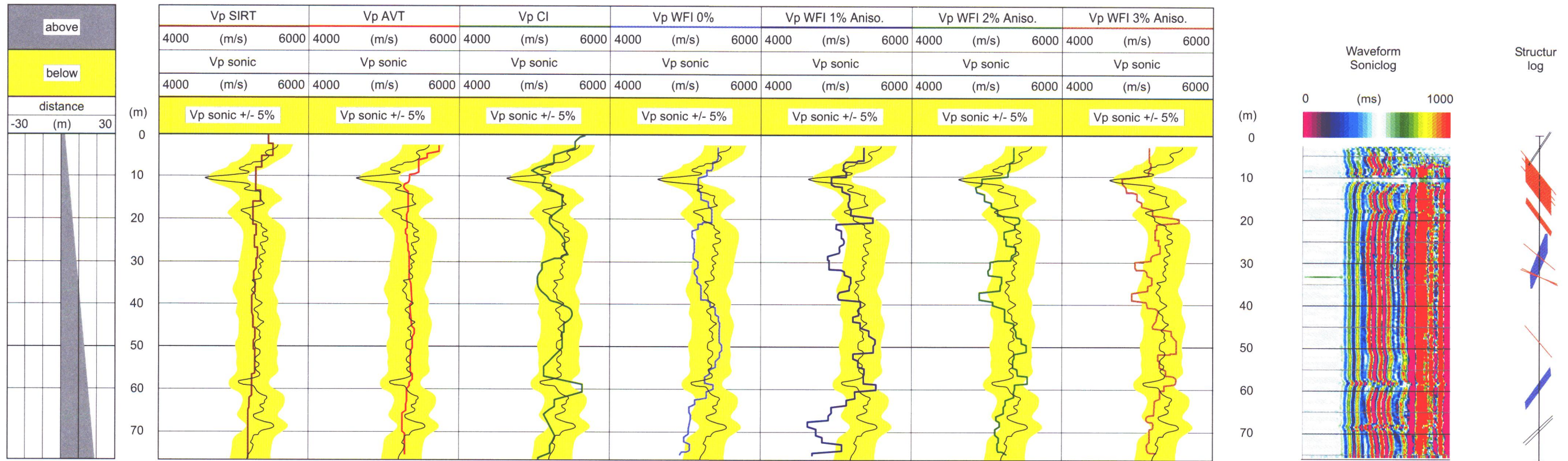
Annex 4: Composite log for borehole BOUS85.001. The composite log gives the sonic velocities, the tomogram velocities along the borehole for the SIRT, AVT and CI traveltimes inversions and for the isotropic WFI inversion, 1%, 2% and 3% anisotropy correction, the sonic wavefields and the geological structures.



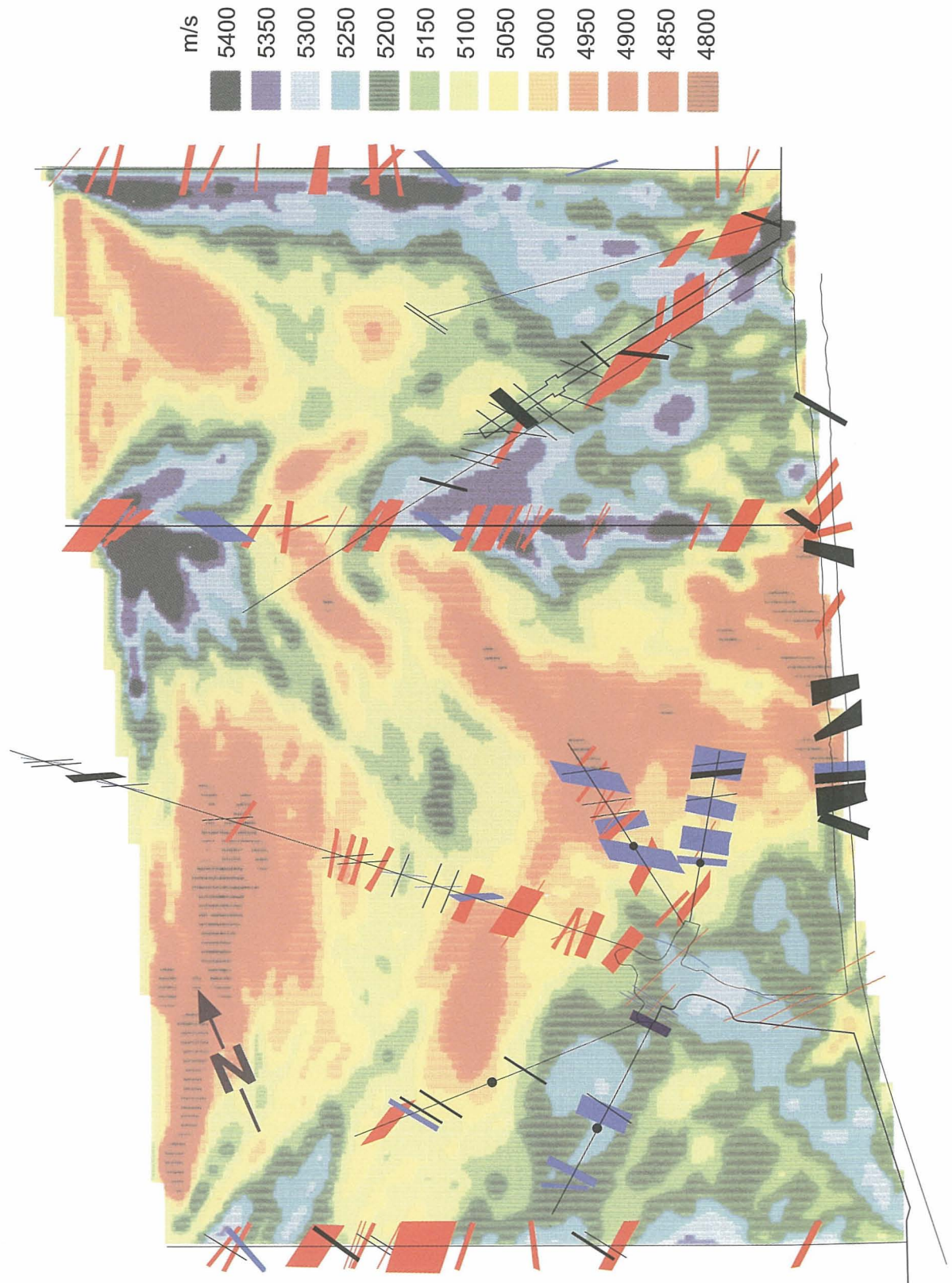
Annex 5: Composite log for borehole BOUS85.002. The composite log gives the sonic velocities, the tomogram velocities along borehole for the SIRT, AVT and CI travelttime inversions and for the isotropic WFI inversion, 1%, 2% and 3% anisotropy correction, the sonic wavefields and the geological structures.



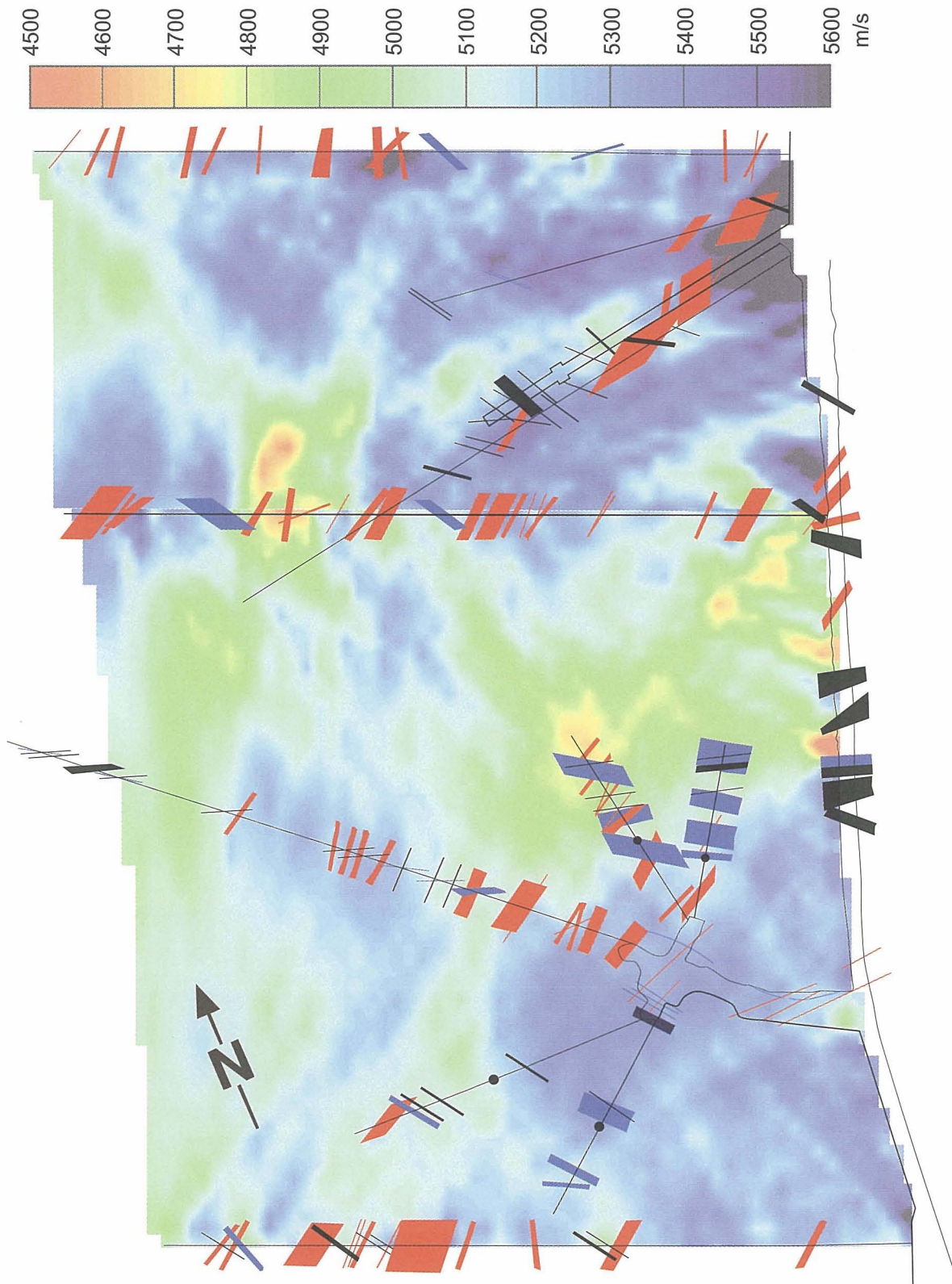
Annex 6: Composite log for borehole BOUS85.003. The composite log gives the sonic velocities, the tomogram velocities along the borehole for the SIRT, AVT and CI traveltime inversions and for the isotropic WFI inversion, 1%, 2% and 3% anisotropy correction, the sonic wavefields and the geological structures.



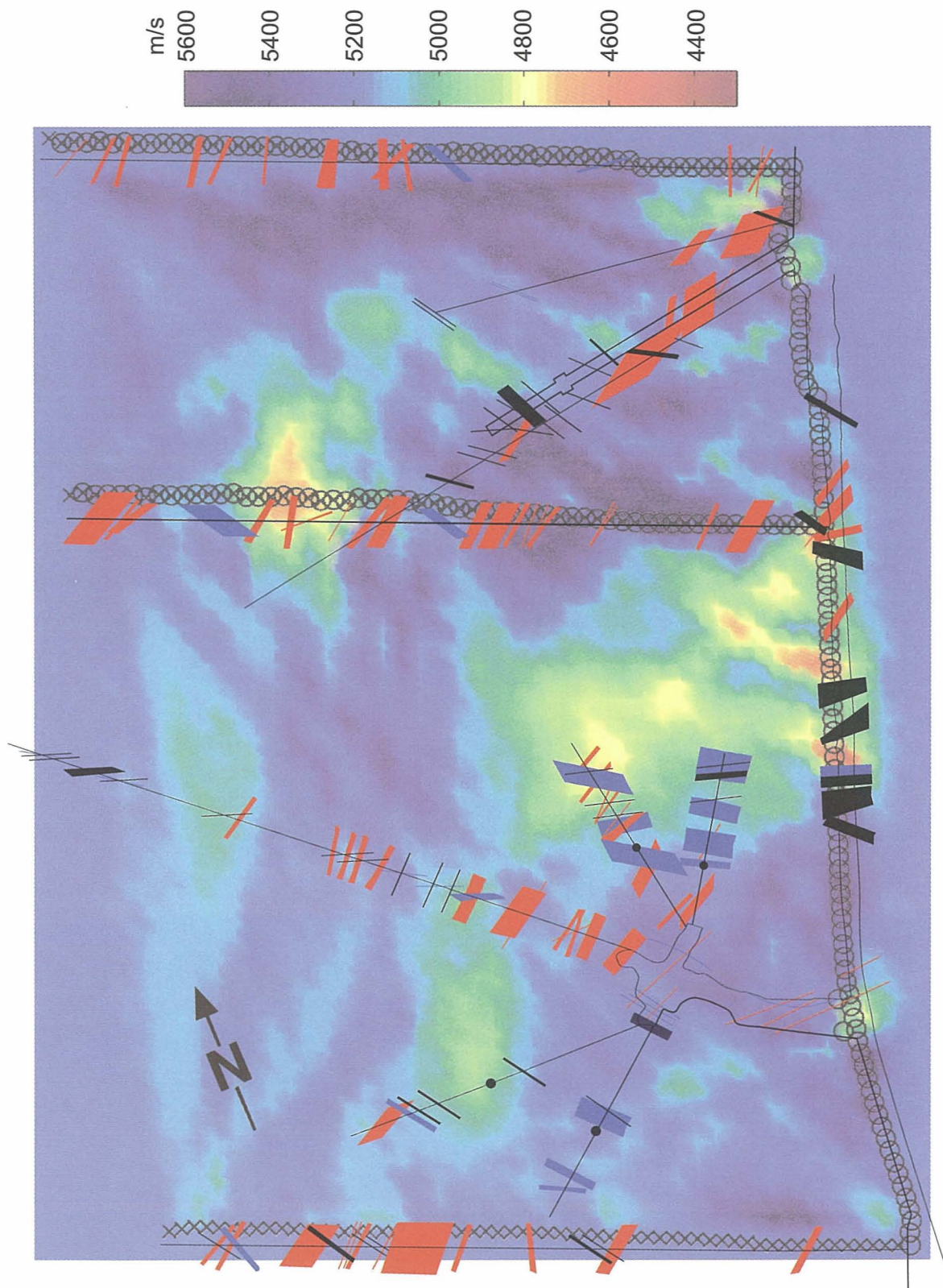
Annex 7: Composite log for borehole FEX95.001. The composite log gives the sonic velocities, the tomogram velocities along the vertical projection of the borehole for the SIRT, AVT and CI travelt ime inversions and for the isotropic WFI inversion, 1%, 2% and 3% anisotropy correction, the sonic wavefields and the geological structures.



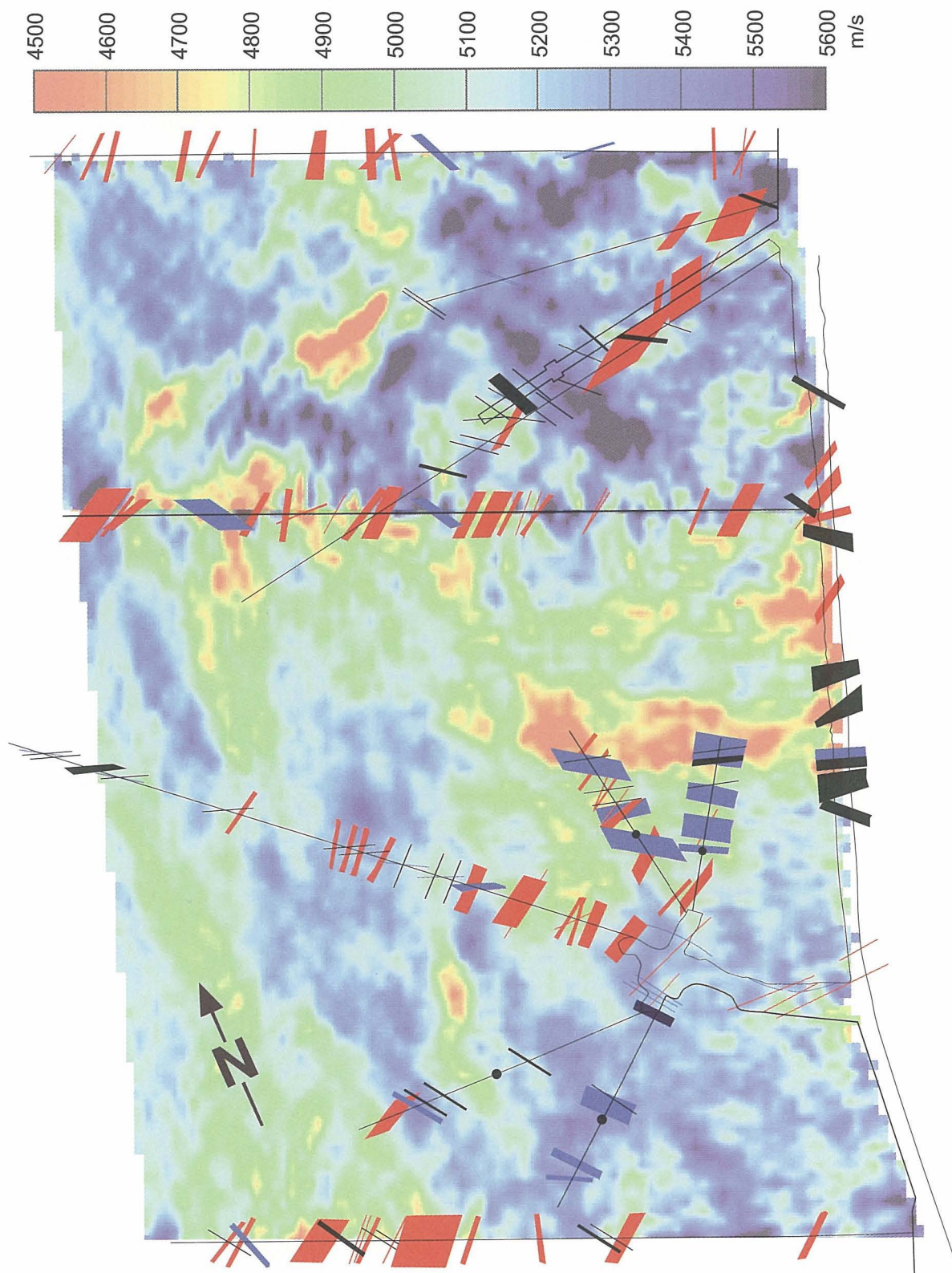
Annex 9: Overlay of the geological structures (Fig. 5.9) on the SIRT tomogram (Fig. 3.3).



Annex 10: Overlay of the geological structures (Fig. 5.9) on the AVT tomogram (Fig. 3.6).



Annex 11: Overlay of the geological structures (Fig. 5.9) on the CI tomogram (Fig. 3.17).



Annex 12: Overlay of the geological structures (Fig. 5.9) on the WFI tomogram (Fig. 4.15).